Procédé de séparation par formation sélective d'hydrates de gaz pour la valorisation du biogaz

Luiz Paulo Sales Silva

2016 SACLY021

THESE DE DOCTORAT
DE
L'UNIVERSITE PARIS-SACLAY
PREPAREE A
L'ECOLE NATIONALE SUPERIEURE DE TECHNIQUES AVANCEES

ECOLE DOCTORALE N° 579
Sciences mécaniques et énergétiques, matériaux et géosciences

Spécialité de doctorat : Génie des Procédés

Par

M. Luiz Paulo Sales Silva

Procédé de Séparation par Formation Sélective d'Hydrates de Gaz pour la Valorisation du Biogaz

Thèse présentée et soutenue à « Palaiseau », le « 15 décembre 2016 » :

Composition du Jury :

M. Bertrand Chazallon	Professeur, Université de Lille 1	Rapporteur
M. Paolo Stringari	Chargé de Recherche, Mines ParisTech	Rapporteur
M. Daniel Broseta	Professeur, Université de Pau	Président
M. Philippe Arpentinier	Docteur, Air Liquide	Examinateur
M. Didier Dalmazzone	Professeur, Ensta ParisTech	Directeur de thèse
M. Moncef Stambouli	Professeur, CentraleSupelec Paris	Co-directeur de thèse
M. Walter Fürst	Docteur, Ensta ParisTech	Invité

Remercîments

Je suis convaincu que la réussite d'un projet de thèse est un grand partie due aux interactions vécues entre le thésard et son environnement tout au long de la période du doctorat.

Ainsi, je remercie premièrement mon directeur de thèse Didier Dalmazzone de m'avoir confié un sujet de recherche autant passionnant que défiant. Je tiens également à remercier son encadrement par les discussions et accompagnements du projet ainsi que pour la confiance portée sur mes résultats. Je remercie mon co-directeur de thèse Moncef Stambouli pour sa gentillesse, sa disposition et pour ses conseils toujours constructifs. Je remercie Philippe Arpentinier étant qu'encadrant industriel de ce projet. Merci pour sa disponibilité et professionnalisme et pour avoir enrichi ce projet avec sa vision du monde industriel.

Mes remerciements s'adressent également à Bertrand Chazallon et Paolo Stringari pour avoir accepté d'être rapporteurs et pour leur participation au jury pendant la soutenance. Je remercie Daniel Broseta d'avoir accepté d'être le président de mon jury de thèse. Ainsi, je remercie tous les membres du jury pour les discussions très intéressantes et constructives que nous avons eues au cours de la soutenance.

Je remercie Walter Fürst qui, au démarrage du projet, figurait comme Directeur de l'UCP. Merci de m'avoir accepté comme doctorant au sein de son laboratoire et d'avoir accompagné le déroulement du projet.

Je remercie tout équipe des enseignant-chercheurs du groupe Génie de Procédés de l'UCP. Je remercie Elise Provost pour son aide au démarrage du projet, surtout dans pour la technique de GC. Je remercie Patrice Paricaud pour les agréables échanges scientifiques et pour l'opportunité d'avoir travaillé dans des projets bien valorisés. Je remercie également Johnny Deschamps pour les agréables et souvent comiques discussions ainsi que pour ses nombreuses aides dans les réparations des équipements. Je remercie aussi l'actuel Directeur de l'UCP, Laurent Catoire.

Je remercie les membres d'Air Liquide, notamment Anne-Laure Lesort et Antonio Trueba, pour leur participation tout au long du projet et ses précieux conseils.

Je remercie l'IDEX Paris Saclay et Air Liquide pour le financement de ce projet.

Un merci tout spécial à ceux qui sont devenus plus que des collègues de travail, mais de véritables amis : Ramy Ghosn, Aurélie dos Santos et Amokrane Boufares. Merci pour votre patience, votre compréhension et surtout pour votre capacité d'écoute. Les moments passés avec vous ne seront jamais oubliés.

Enfin, je souhaite remercier ma famille au Brésil qui supporte toujours l'éloignement. Une pensée spéciale à mon père Vicente dont malheureusement sa lumière s'est éteinte durant la période de la thèse. Merci à ma mère Nivalda pour sa dédicace et soutient tout au long de ma vie.

En tant qu'un méfiant croyant du déterminisme, je remercie à tous ceux qui ont contribué de manière directe et indirecte à la réussite de ce projet.

Finalement je dédie ce travail à deux sources d'énergie (deux soleils, simplement) qui ont été sans aucun doute ma plus forte motivation : Liza (Lili ou *gatinha*) et Raphaël (*malandro*).

CONTENTS

List of Figures

List of Tables

Nomenclature

List of symbols

A	Surface Area
AARD	Average Absolute Relative Deviation
Ci	Number of Cage Type *i* per Water Molecule in Unit Cell
DSC	Differential scanning calorimetry (DSC)
EoS	Equation of State
f	Fugacity
g	Gas
GSHF	Gas Separation by Hydrate Formation
GEFTA	German Society for Thermal Analysis
H	Henry's constant
k	Constant Rate Transfer
*K**	Combined Rate Constant For The Diffusion Adsorption Processes
m	Mass
MW	Molecular Weight
n	Number of Moles
N	Number of Molecules
NAvo	Avogadro's number, 6.023 x 1023 molecules/mol
p	Pressure
PSA	Pressure Swing Adsorption
PWS	Pressure Water Scrubbing
RD	Relative Deviation
Rolsi^{TM}	Rapid on-Line Sampler-Injector
S	Separation Factor
SRK	Soave-Redlich-Kwong
t	Time
T	Temperature
TBAB	Tetra-n-Butylammonium Bromide
TBAC	Tetra-n-Butylammonium Chloride
TBAF	Tetra-n-Butyl Ammonium Fluoride
TBPB	Tetra-n-Butylphosphonium Bromide
TBPC	Tetra-n-Butylphosphonium Chloride
TBPO	Tributylphosphine Oxide
THF	Tetrahydrofuran
THP	Tetrahydropyran
v	Molar Volume
V	Volume
VOC	Volatile Organic Compounds
w	Mass Fraction
x	Mole Fraction at Liquid Phase
*x**	Solubility of Gas In Liquid Phase

y	Mole Fraction at Gas Phase
z	Mole Fraction
Z	Compressibility Factor

Greek letters

α	Scanning Rate
β_i^j	Mole Fraction of Compound i at Stage j after the Equilibrium
ΔH	Dissociation Enthalpy
θ	Cage Occupancy Rate
υ	Hydration Number
ρ	Density
λ_i	Extensive Property of the Pure Compound i
$\lambda_{mixture}$	Mixture Extensive Property
ω_i^j	Mole Fraction of Compound i at Stage j in the Flow Entering Stage j

Subscript

0	Initial
cell	Hydrate Unit Cell
d	Diffusion
D	Additive
end	Inflection Point at Dissociation Peak
eq	Equilibrium
f	Final
i	i^{th} Unknown Variables
M	Measured
p	Particle
r	Adsorption
S	Standard
step	Step in Stepwise DSC Protocol
W	Water

Superscripts

j	j^{th} Unknown Variables
G	Gas Phase
H	Hydrate Phase
L	Liquid Phase
T	Total

INTRODUCTION

In the perspective of limited access to fossil energy sources, renewable energy becomes an alternative pathway and one of the most researched topics in these last years. One of these alternatives is the biogas produced from anaerobic digestion of biomass.

According to the European Biomass Association, in Europe, "biomass currently accounts for 2/3 of renewable energy and will play a key role in achieving the target approved by the renewable energy directive of 20% of final energy consumption based on renewable sources by 2020" [1]. In Germany, biomass accounted for approximately 8.2% of the primary energy demand in the year 2013. By 2050, Germany aspires to cover 80% of its electricity consumption from renewable energy [2].

Examples of biofuels produced from biomass include bioethanol, biodiesel and biogas. Currently, Germany is the world leader in the deployment of biogas technology and plays the leading role in the European biogas market [3]. The number of biogas plants in Germany increased from 1050 in 2000 to 7850 in 2013. With respect to overall biogas production, Germany is followed by the United Kingdom, France, Italy and the Netherlands [4].

Biogas is a gas mixture which results from the anaerobic digestion of organic matter. This phenomenon happens in presence of various groups of microorganisms in an oxygen-free environment. It is a natural process that occurs in many conditions such as watercourses, sediments, waterlogged soils and the mammalian gut [5].

In our society, anaerobic digestion is used as a biological treatment for municipal, industrial or farm waste. In fact, it represents a powerful and important tool for waste management and it is an alternative for energy production. It makes possible to treat the residues that pollute the environment, to reduce the volume of waste in the landfills and as a result produce simultaneously a valuable energy product (biogas) and high quality organic biofertilizers [6-7].

The sources of organic matter as well as the conditions of the media are the key factors that determine biogas composition. In general, biogas from agricultural waste contains about 60 % in volume of methane gas (CH_4), 38 % in volume of carbon dioxide (CO_2), between 0.2 and 1 % of hydrogen sulfide (H_2S) and 1 % of other compounds in trace amounts, such as N_2, O_2 and some volatile organic compounds (VOC) [8-10]. The two first gases (CH_4 and CO_2) can

be valued in several industries if they are recovered. To achieve this goal, it is first necessary to remove the other biogas constituents (from here called pollutants). In this context, H_2S is the main target to eliminate because it is a toxic gas and at same time, an acid that can cause corrosion of the equipment. After the removal of pollutants, the couple CH_4/CO_2 must be separated. Once separated, methane can be used to produce energy by combustion, or as feed gas for steam methane reforming or directly injected in natural gas network [2, 11]. Carbon dioxide can be used in industry as a fluid refrigerant, as a raw material for industrial applications, or as an ingredient in soft drinks in food industry.

One of the classical methods used for separating CH_4 and CO_2, in order to upgrade biogas, is the absorption in a chemical solvent (ammonia for example) or pressurized water (pressurized scrubbing water – PSW). Other techniques include separation in adsorption columns (pressure swing adsorption – PSA) and separation by membranes. All these techniques have advantages and disadvantages in terms of ratio quality of outgoing biogas / cost of the process, which still leads seeking either a better optimization of the process, or new separative techniques adapted to biogas. One of these new processes is the gas separation by hydrate formation (GSHF) [12-13].

Gas hydrates or clathrate hydrates are crystalline compounds formed by a combination of guest molecules and a network of water molecules. They are formed under suitable condition of high pressure and low temperature [14]. In these conditions, water molecules linked by hydrogen bonds form polyhedral cavities that are able to trap small molecules. The whole structure of gas hydrates is stabilized by Van der Waals' interactions between the trapped molecules and the network of water molecules [14].

The GSHF consists in separating compounds from a gas mixture by selectively trapping gas molecules in the cavities of the structure formed by water molecules. The method relies on the physical interactions between the guest molecules and the host structure. In other words, the separation is driven by the difference of affinity between the gas molecules of the mixture with the cavities of hydrate. Depending on thermodynamic conditions of the system, a given gas can have different affinity to the hydrate phase. This process was previously studied in the context of ANR SECOYHA project that showed the technical feasibility of GSHF applied in post-combustion CO_2 capture processes from power plant flue gas.

The use of thermodynamic promoters, such as ammonium/phosphonium quaternary salts, can reduce the hydrate formation pressure leading to a gain of energy efficiency for the process.

Moreover, they can improve the selectivity of one gas into the hydrate phase, thus further increasing the efficiency of the process.

Since GSFH is a process based on phase transition, the knowledge of the phase diagram of the (gas + promoter + water) system is essential to evaluate, design and optimize the process. Nevertheless, in literature related to hydrate-based CO_2 capture from CO_2+CH_4 mixtures, only few equilibrium data are available in a limited range of promoter composition. New promoters with potential to improve the efficiency of the process have been proposed recently. However, most of these new promoters were never tested for GSHF of CO_2+CH_4 mixture. Besides, the available works in literature using thermodynamic promoters were carried out at relative high pressure (>2.5 MPa) and low temperature (<278 K).

Therefore, the aim of this research project was to study the feasibility of GSHF process as a new technique for biogas upgrade. The specific objectives of this work were: at first to evaluate the GSHF process using only water by simulation process; if necessary, select new promoters having potential to improve the efficiency of the process and determine the hydrate formation conditions of these promoters in presence of CO_2, CH_4 and CO_2+CH_4 mixture in a composition near to biogas; test these promoters in experimental GSHF process at laboratory scale in an instrumented reactor at mild pressure and temperature conditions; evaluate the kinetic and thermodynamic effects of each promoter in the GSHF process.

This manuscript is divided in six parts, being five *Chapters* and the conclusion. In *Chapter 1* an overview of biogas, clathrate hydrates and their applications is presented. *Chapter 2* shows the study of process simulation of biogas upgrading by hydrate formation. The equipments and the experimental procedures used during this research project are described in *Chapter 3*. The fourth *Chapter* is devoted to the experimental results of phase equilibria study involving the selected thermodynamic hydrates promoters. *Chapter 5* presents and discuss the results obtained from the experiments in instrumented reactor for biogas upgrading using the GSHF process in presence of thermodynamic promoters. Finally, in the last part the general concluding remarks are presented followed by some perspectives for further studies in hydrate-based process.

Chapter 1

Biogas and Gas Separation by Hydrate formation: an overview

Résumé

Ce chapitre commence en présentant les principaux concepts de la production, de la composition et des techniques d'épuration du biogaz. Ensuite, le concept de l'utilisation des hydrates clathrates dans un procédé de séparation de gaz est proposé. Un aperçu général des hydrates clathrates, en termes de définition, structures, propriétés et conditions de formation, est donné. Les diagrammes de phase des systèmes d'hydrates formés avec des promoteurs thermodynamiques, le dioxyde de carbone, le méthane et le mélange des ces deux gaz sont particulièrement discutés. Les aspects cinétiques du phénomène de nucléation sont également abordés. Enfin, nous discutons les travaux de la littérature portant sur le procédé de séparation de gaz par la formation des hydrates (GSHF) appliqué au mélange CO_2+CH_4 pour lequel peu de promoteurs ont été testés. Ainsi, la possibilité d'explorer d'autres promoteurs dans le procédé GSHF est une des principales motivations de ce travail.

Abstract

This chapter starts by presenting the main concepts of biogas production, composition and upgrading techniques. Then, the use of clathrate hydrate in a gas separation process is proposed. An overview of clathrate hydrates, including the definition, structure, properties and formation conditions, is given. The phase diagrams of hydrate systems formed with thermodynamic promoters, carbon dioxide, methane and the mixture of both gases are specially discussed. The kinetics aspects of nucleation phenomenon are explained as well. Finally, we discuss the available works on literature about gas separation by hydrate formation (GSHF) process for CO_2+CH_4 mixture, observing that few promoters were tested. Exploring other promoters in such process is then one of the main motivations of this work.

1.1 Biogas

Biogas is a renewable source of energy obtained from decomposition of organic matter by microorganisms at anaerobic conditions (oxygen-free). It is mainly composed by methane (CH_4) and carbon dioxide (CO_2). Biogas is odorless and colorless gas and it burns with clear blue flame similar to that of LPGgas [15]. This gas has a significant production potential for the next years. It is expected that in 2020 EU-countries will be supplied with 20 % in bioenergy, from which at least 25 % will be originate from biogas produced from wet organic materials, such as animal manure, whole crops silages, wet food and feed wastes [16].

The production and utilization of biogas in integrated systems (*Figure 1.1*) of renewable energy production, resources utilization, organic wastes treatment and nutrient recycling and redistribution, generate intertwined agricultural and environmental benefits, such as [16-17]: renewable energy production; cheap and environmentally healthy organic waste recycling; less greenhouse gas emission, specially methane compared to traditional manure management or landfills; substitute for fossil fuels; high quality digestate that can be used as a fertilizer; less nuisance from odors and flies; economical advantages for the farmers.

Moreover, the waste management from anaerobic digestion process is largely used to stabilize the organic matter in wastewater solids, reduce pathogens and odors, and reduce the total solids by converting part of the volatile solids fraction into biogas [6-7, 15]. In these facilities, the resulted product contains stabilized solids, as well as some available forms of nutrients such as ammonia-nitrogen that is used as fertilizer in agricultural applications. The application of the anaerobic treatment process in waste management includes septic tanks, sludge digesters, industrial wastewater treatment, municipal wastewater treatment, hazardous waste management (aromatic and halogenated compounds), and agricultural waste management [15].

The resulted biogas from waste management facilities is in majority composed by methane and carbon dioxide. Methane can be utilized as an energy source in combined heat and power plants, as a vehicle fuel, or as a raw material in the industry [17]. Biogas can be used on a production site, or it can be distributed through the gas grid and it can also be liquefied. For heat and electricity production there is a wide range of technologies available for biogas utilization such as the traditional gas boiler, internal combustion engine (ICE), gas turbine, and fuel cell [18].

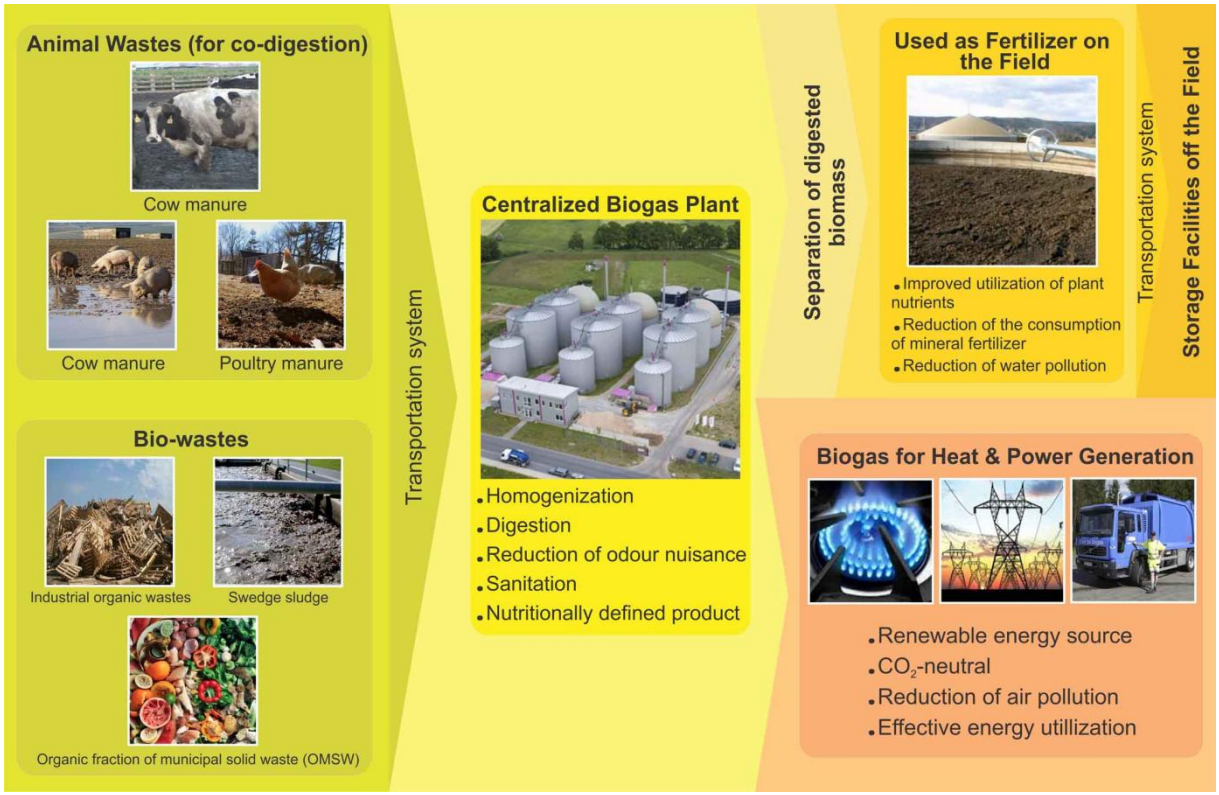

Figure 1.1. The main streams of the integrated concept of a centralized biogas plant [19].

The carbon-neutral character of biogas as a source of renewable energy represents a competitive alternative for energy production both by its energy efficiency and by its environmental impact. Vehicle fuel produced from biogas from manure, wastes and also from energy crops fulfils the EU sustainability requirement from 2017 onwards, reducing greenhouse gas (GHG) emissions by 60% as compared to fossil [20]. Besides, replacing fossil fuel by biogas also gives a perspective on reducing particles and nitrogen oxide emissions [21].

The main utilization of biogas in Europe is for generating heat and electricity. Some of the produced heat is used within the biogas plant as process heating and the remaining heat is distributed through districts heating systems to consumers. The produced power is sold to the grid. In some countries, like Sweden, the produced biogas is upgraded to bio-methane which is utilized as vehicle fuel [8, 22].

Concerning the biogas plants, they are classified in two categories based on the type of digested substrates, the technology applied, or the size of the plant. The first one is the large scale, joint co-digestion plants and the second is the farm scale plants. However, there are no major differences between these two categories regarding the technology used [19].

In France, the potential development of biogas is important. It is estimated that in 2030, 56 TWh will be produced from this source, which corresponds to the energetic consumption of nearly 3 million homes. About 90% of biogas production will be from agricultural field [23].
Holm Nielsen *et al.* [16] have listed some strategies that must be developed in order to increase the utilization of biogases. Some of these strategies include programs to stimulate recycling of organic resources/organic wastes, especially of wet organic wastes; improvements of the present technologies and reduced cost; R&D on small scale systems, going from economy of scale to economy of numbers; improved post-treatment and separation technologies, aiming to overcome transport constraints; finding and implementing new post-treatment technologies; programs for active implementation and dissemination of biogas technologies and knowledge transfer to other countries around the world; an overall policy to stimulate green electricity production from renewable sources and to encourage use of renewable in combined heat and power systems.

1.1.1 Production and composition

Biogas is produced by micro-organisms from anaerobic decomposition of different organic materials and in different environments including sludge digesters in wastewater treatment plants, food waste, manure and energy crop digesters, and landfills. Therefore, the actual composition of biogas varies between these different sources of organic matter as well as the individual sites due to changes in the process conditions [18].

The anaerobic decomposition phenomenon consists in degradation of organic matter by a complex mixture of symbiotic microorganisms under oxygen-free conditions. They transform organic materials into biogas, nutrients and additional cell matter, leaving salts and refractory organic matter. Raw biogas typically consists of methane (60%), carbon dioxide (40%), water vapor and trace amounts of hydrogen sulfide (H_2S), oxygen (O_2), nitrogen (N_2) and volatile organic compounds [18, 22, 24]. In nature this process occurs in environments such as marshes, ponds, swamps, paddy fields, lakes, hot springs, landfills, sewage digesters, oceans and intestinal tracts of humans and animals.

The degradation of organic materials into biogas occurs from four key biological and chemical stages: hydrolysis, acidogenesis, acetogenesis and methanogenesis (*Figure 1.2*). During the first stage the large, complex insoluble substrates including polysaccharides, proteins and lipids are hydrolyzed into smaller molecules by several hydrolytic

microorganisms. Indeed, in this stage, the microorganisms secret some hydrolyzing enzymes such as cellulase, cellobiase, xylanase, amylase, protease, lipase that "break" the complex molecules into smaller units [25]. For example, hydrolysis of cellulose by the enzyme complex cellulase yield glucose, hemicellulose degradation results in monosaccharides such as xylose, glucose, galactose, arabinose and mannose [26].

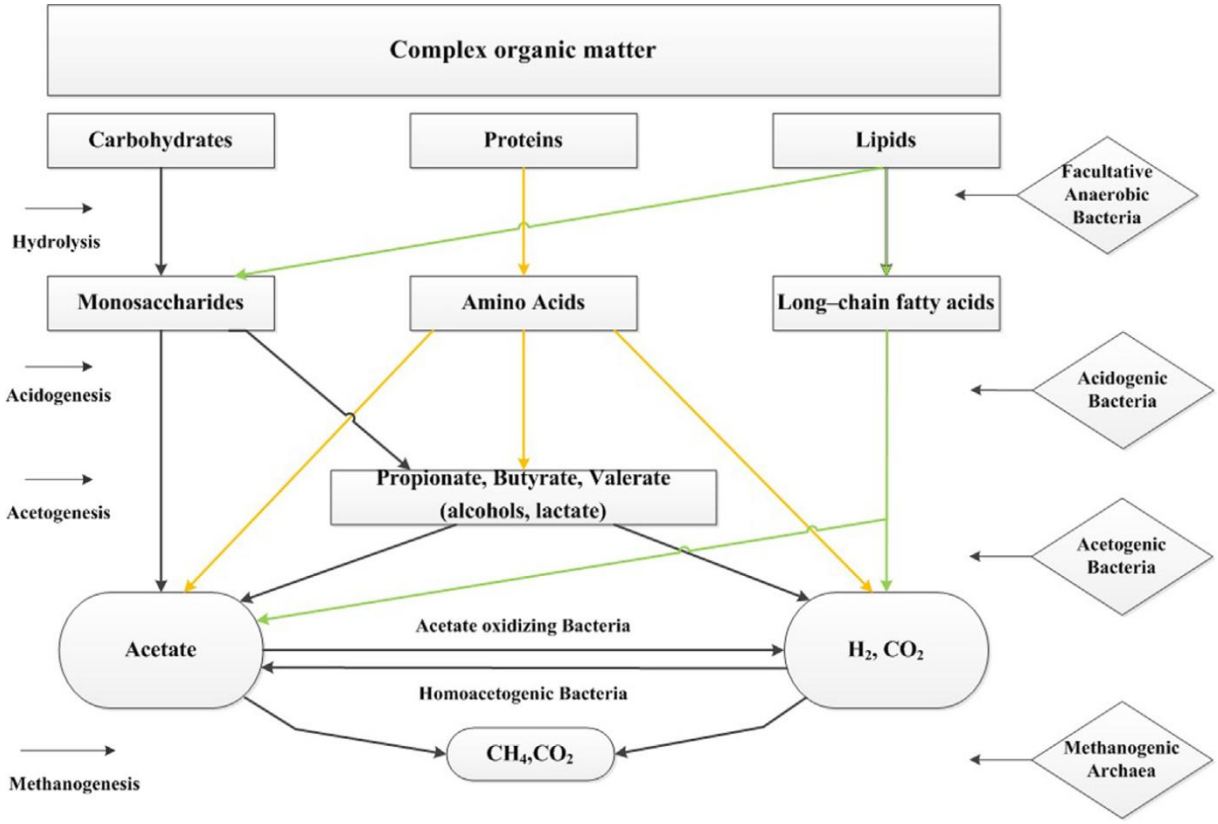

Figure 1.2. Schematic representation of anaerobic decomposition [15].

The resulted molecules from hydrolysis (mainly, sugars, long-chain fatty acids and amino acids) become now substrates for fermentative microorganisms (*Streptococcus*, *Lactobacillus*, *Bacillus*, *Escherichiacoli*, Salmonella). The acidogenesis stage then starts and organic acids, such as acetic, propionic, butyric and other short-chain fatty acids, alcohols, H_2 and CO_2 are produced by fermentation or by anaerobic oxidizers [15]. Acidogenesis is usually the fastest reaction in the anaerobic conversion of complex organic matter in liquid phase digestion [27].

The third stage of anaerobic digestion is acetogenesis. In this stage, the increase of hydrogen concentration in the liquid phase promotes the accumulation of electron sinks, such as lactate ethanol, propionate, butyrate and higher volatile acids. These molecules cannot be consumed directly by the methanogenic bacteria and should be degraded further by the acetogenic bacteria [28]. Therefore, these bacteria convert the electron sinks to further acetate, carbon

dioxide and hydrogen. Glucose is converted to acetate and ethanol is converted to acetic acid and release molecular hydrogen [15].

Finally, methane is produced by methanogenic microorganisms in anoxic conditions. It is produced by two ways: reduction of carbon dioxide with hydrogen (hydrogenotrophic methanogenesis) or conversion of acetic acid to carbon dioxide and methane (aceticlastic methanogenesis) [15]. The hydrogenotrophic methanogenesis is the most common metabolic pathway where one molecule of CO_2 and four molecules of H_2 are converted to one molecule of methane and two molecules of water. In the second path, the aceticlastic methanogenesis, acetate is directly converted to methane. The carboxyl group of the acetate is oxidized to CO_2 where by the methyl-group is reduced to methane and carbon dioxide [29]. The remaining indigestible material constitutes the digestate.

Depending on the kind of substrates the methanogenic potential is different and the composition of biogas is variable. Rasi *et al.* [22] studied the biogas composition and variation in three different biogas production plants. Methane, carbon dioxide, oxygen, nitrogen, volatile organic compounds (VOCs) and sulphur compounds were measured in samples of biogases from a landfill, sewage treatment plant sludge digester and farm biogas plant. *Table 1.1* shows the obtained results. The highest methane content occurred in the gas from the sewage digester while the lowest methane and highest nitrogen contents were found in the landfill gas during winter. The investigation of presence of VOCs in this biogas production plants (*Figure 1.3*) showed that biogas from farm is more "clean" which can indicate that upgrading process from this kind of biogas may be easier.

Table 1.1. Biogas composition from different producing plants [22].

	Biogas		
	Landfill	Sewage digester	Farm biogas plant
CH_4 (mol%)	47-57	61-65	55-58
CO_2 (mol%)	37-41	36-38	37-38
O_2 (mol%)	< 1	< 1	< 1
N_2 (mol%)	< 1-17	< 2	< 1-2
H_2S (ppm)	36-115	b.d.	32-169
Benzene (mg m^{-3})	0.6-2.3	0.1 -0.3	0.7-1.3
Toluene (mg m^{-3})	1.7-5.1	2.8-11.8	0.2-0.7

b.d.—Below detection limit 0.1 ppm.

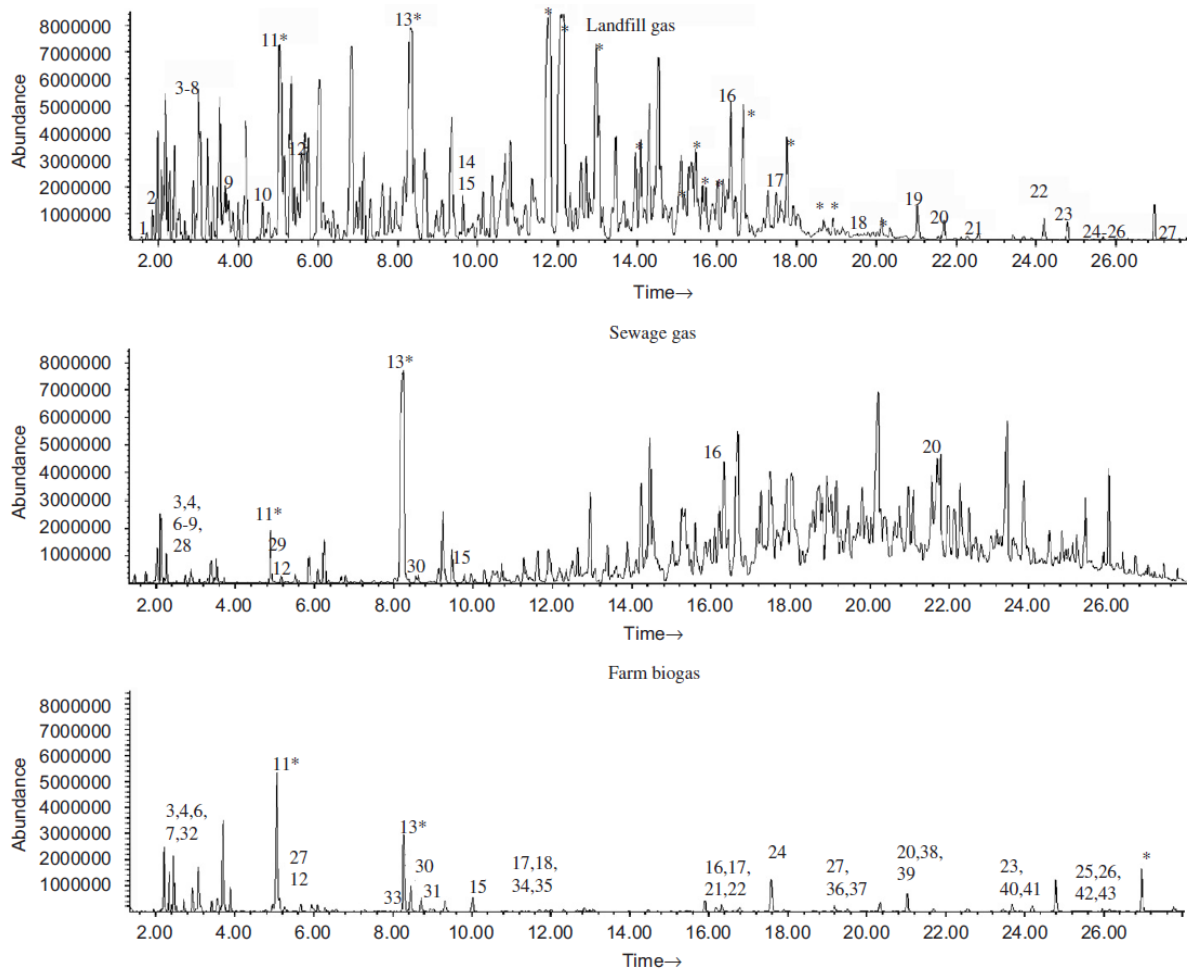

Figure 1.3. Total ion current chromatograms (TIC) of VOCs from landfill gas (above), sewage digester gas (middle) and farm biogas (below) [22]

1. 1-Chloro-1-fluoroethane (1.71), Ethyl chloride (1.80)
2. Dichlorofluoromethane
3. Methylene chloride
4. Carbon disulphide
5. 1-Chloropropane
6, 8. Thiols
7. Trimethylsilanol
9. 1,2-Dichloroethene
10. 1,1,1-Trichloroethane
11. Benzene
12. Hexamethyldisiloxane
13. Toluene
14. Tetrachloroethylene
15. Hexamethylcyclotrisiloxane
16. Octamethylcyclotetrasiloxane
20. 2,4-bis(trimethylsiloxy) benzaldehyde
26. Decamethyltetrasiloxane
28. 1-Propanethiol
29. Thiophene
30, 31. Methylthiophenes
32. DMS
33. DMDS
34, 35. Ethylthiophenes
17, 18, 19, 21, 22, 24, 27, 36, 37, 38, 39, 40, 41, 42, 43. Alkyl disulphides (C3–C10)
23, 25. Alkyl trisulphides (C6)
*Aromatic hydrocarbons

Rasi *et al.* [22] attributed the lower content and variation of VOCs in farm biogas compared to landfill and sewage digester to the probably more homogenous material (manure and confectionery by-products) in the farm biogas plant. Although much waste material is recycled, wastes in landfills still contain wide range of different kind of materials and probably even some hazardous waste from time when it was not separately collected. In the sewage treatment plant biogas production takes place in a stable environment but the source of the treated material is both industrial and household.

Landfill gas is used for heat and electricity production in many countries, but its use for vehicle fuel production is considered in many cases to be too complicated and thus expensive because it contains trace compounds, such as sulphur, chloride and silicon compounds [30].

More recently Rasi *et al.* [18] provided a review about the importance of trace compounds in biogas. They suggested that methane and hydrogen sulphide contents have had the most influence when energy utilization application has been considered. With more advanced processes the quantity and quality of trace compounds is also more important. As observed from their previous work biogas from agricultural waste contains less trace compounds, thus methane content becomes the most important parameter to evaluate. *Table 1.2* lists methane content in biogases from agricultural wastes and we observe that from the different sources biogas presents methane content around 65 %. In terms of hydrogen sulphide content, biogas from fruits and vegetables presented the value of 300 ppm which was the highest value compared to other biogases [31].

Table 1.2. Methane content in biogases from agricultural wastes.

	CH_4 [%]	Ref.
Corn silage	68 - 73	[32-33]
Grass silage	55 -72	[32, 34]
Beet pulp	62-69	[32]
Whey	62-70	[32, 35]
Fruits and vegetables	56 - 63	[31, 36]
Municipal food wastes	65-70	[24]

Ryckebosch *et al.* [37] made an extensive review about main compounds that must be removed in order to upgrade biogas. They also described the possible impact of each impurity (*Table 1.3*) and the possible techniques that can be used to remove them.

Table 1.3. Biogas impurities and their consequences [37].

Impurity	Possible Impact
water	Corrosion in compressors, gas storage tanks and engines due to reaction with H_2S, NH_3 and CO_2 to form acids
	Accumulation of water in pipes
	Condensation and/or freezing due to high pressure
Dust	Clogging due to deposition in compressors, gas storage tanks
H_2S	Corrosion in compressors, gas storage tanks and engines
	Toxic concentrations of H_2S (> 5 $cm^3.m^{-3}$) remain in the biogas
	SO_2 and SO_3 are formed due to combustion, which are more toxic than H_2S and cause corrosion with water
CO_2	Low calorific value
Siloxanes	Formation of SiO_2 and microcrystalline quartz due to combustion; deposition at spark plugs, valves and cylinder heads abrading the surface
Hydrocarbons	Corrosion in engines due to combustion
NH_3	Corrosion when dissolved in water
O_2/air	Explosive mixtures due to high concentrations of O_2 in biogas
Cl^-	Corrosion in combustion engines
F^-	Corrosion in combustion engines

1.1.2 Main biogas upgrading techniques

The most common way to valorize biogas is upgrading it to biomethane. For that, the removal of other constituents, such as carbon dioxide, hydrogen sulphide, water, is necessary. Here we will describe briefly four well-established techniques to transform biogas to biomethane: absorption in amines; pressure water scrubbing (PWS); pressure swing adsorption (PSA); and membrane separation. The utilization of each technique depends on the necessary quality conditions of the incoming gas, the technique's efficiency and operational bottlenecks.

Generally, biogas upgrading aims at: (1) a cleaning process, in which the trace components harmful to the natural gas grid, appliances or end-users are removed, (2) an upgrading process, in which CO_2 is removed to adjust the calorific value and relative density in order to meet the specifications of the Wobbe Index [11, 16].

Absorption in amines

This technique involves biogas-liquid mass transfer in which CO_2 will be selectively removed from gas phase by using CO_2-reactive absorbents such as alkanolamines (monoethanolamine, diethanolamine, methyldiethanolamine, etc.). Indeed, there is a chemical reaction between

absorbed substances and the solvent [11]. The formation of intermediate chemical species (CO_3^{2-}, HCO^{3-}) mediated by the exothermic reaction of the absorbed CO_2 with the chemical reagents present in liquid phase results in an enhanced CO_2 absorption capacity and process operation at maximum CO_2 concentration gradients [37]. This technology consists of a packed bed absorption unit coupled to a desorption unit equipped with a reboiler, which simplifies process configuration compared to their physical absorption counterparts (*Figure 1.4*). The process is operate in a countercurrent flow configuration. The methane loss is estimated to be less than 0.5 % in a plant with a capacity of 300 Nm^3/h (rawgas) [8]. However, a downside of this technology relates to energy consumption, as a large amount of high-temperature heat is needed to regenerate chemical solvents [38].

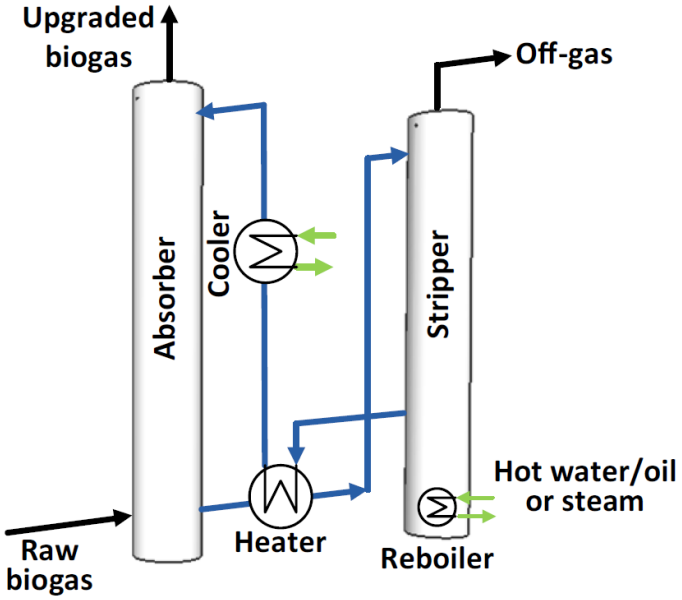

Figure 1.4. Biogas upgrading by absorption in amines [11].

Pressure water scrubbing (PWS)

This process is based on physical absorption, where the solvent is water. The principle takes into account the highly different solubility in water between CH_4 and CO_2, the second having a much higher value compared to the first. Besides, hydrogen sulphide can be also removed since its solubility in water is even higher than CO_2. Nevertheless, H_2S is poisonous and once dissolved in water can cause corrosion problems, thus a biogas pre-treatment for H_2S removal is generally recommended [38]. PWS is nowadays a mature technology, which accounts for approximately 41 % of the global biogas upgrading market, being considered the upgrading method less sensitive to biogas impurities [39]. The pressure operating process in absorption column (*Figure 1.5*) is often at 6-10 bar, although pressures in the range of 10–20 bar are

also used [37]. In flash column, the process is operated at 2-4 bars, which allows releasing a CO_2 rich gas phase (80–90 % CO_2 and 10–20 % CH_4) that returns to inlet process. Water decompression to atmospheric pressure in the desorption column, often assisted by air injection, results in the final regeneration of the absorbent that is returned to the absorption unit. The amount of water required (m^3 h^{-1}) depends on the water pressure and temperature [38]. PWS can achieve biomethane with CH_4 content of about 80-99 % depending on the volume of non-condensable gases such as N_2 and O_2 that cannot be separated from CH_4. Concerning CH_4 loss, manufacturers guarantee 2 % with exhaust gas recirculation, although losses of 8–10 % have been measured under regular operation, as a consequence of the non-optimized operation of the flash column [8].

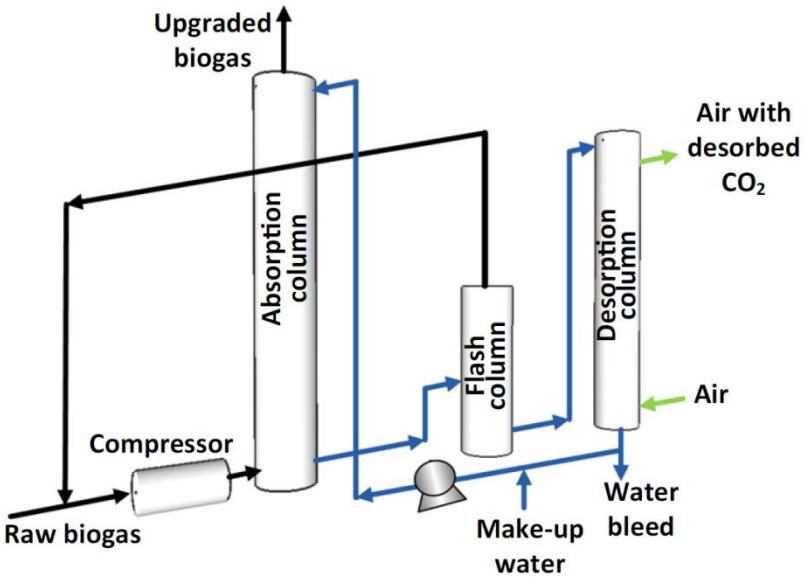

Figure 1.5. Biogas upgrading by pressure water scrubbing (PWS) [11].

Pressure swing adsorption (PSA)

PSA process is based on the selective adsorption of gas molecules into porous adsorbents with a high specific surface area. This solid surfaces are normally activated carbon, silica-gel, activated alumina, zeolite and polymeric sorbents [17, 37]. In PSA process, molecular size exclusion and adsorption affinity constitute the separation mechanisms of the technique. Therefore, CH_4 can be separated from N_2, O_2 and CO_2, since the CH_4 molecule is larger than the other gas molecules [38]. However, H_2S must be removed in a pre-treatment because the adsorption material used in PSA adsorbs H_2S irreversibly. In general adsorption is a discontinuous process, but the application of multiple adsorption vessels transforms the discontinuous process into a continuous one (Figure 1.6). While one column is adsorbing the

CO_2 molecules from the bulk CH_4 stream, the other adsorption vessels are regenerated [40]. The adsorption stage is often operated at 4-10 bars in order to increase CO_2 retention inside the adsorbent material. When the vessel becomes saturated with CO_2, the blow down phase starts by filling the next vessel (previously regenerated) with the exiting gas. The saturated column is depressurized till ambient pressure and purged with upgraded biogas to complete the regeneration of the adsorbent bed. The outlet biomethane contains CH_4 with a purity ranging from 95 to 98 % [38, 41].

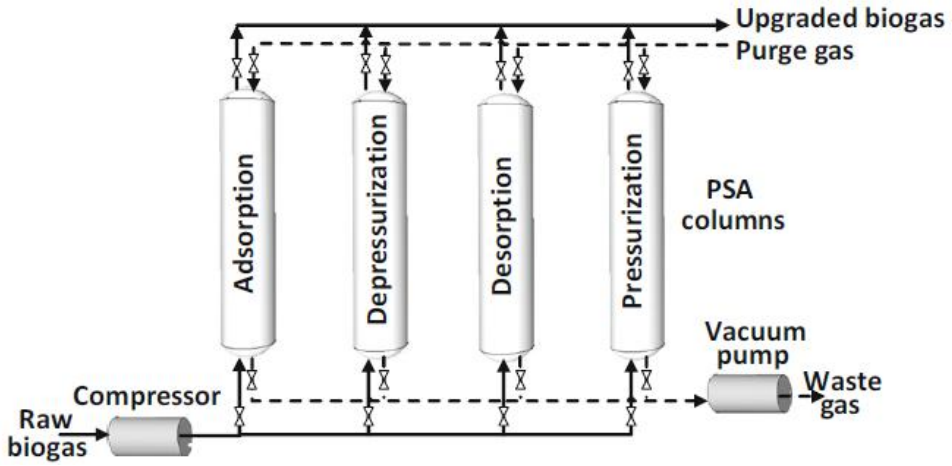

Figure 1.6. Biogas upgrading by pressure swing adsorption (PSA) [11].

Membrane separation

This technology relies on the principle of selective permeation of some constituents of biogas through a semi-permeable membrane. For biogas upgrading, CO_2 and H_2S pass through the membrane to the permeate side, while CH_4 is retained on the inlet side. Since some CH_4 molecules may also pass through the membrane, achieving a high purity of CH_4 may involve large losses of CH_4 [38, 40]. Membrane separation is in fact a mature technology (with a market share of 10 %) commercialized either in high pressure gas–gas modules or low pressure gas–liquid modules [41]. Gas–gas units are manufactured under different configurations: single-pass membrane unit or multiple stage membrane units with internal recirculation of permeates and retentates (*Figure 1.7*) [11]. As a result, the final CH_4 content in outlet gas stream will depend on the membrane configuration used. Two stages gas-gas unit with recirculation of the permeate from the second membrane module provides CH_4 recoveries of 98-99%. For further purity more complex designs with recirculation of both the permeate from the second stage and the retentate from the filtration of the permeate of the first module is required [11]. The operating pressure can vary from 6 to 20 bars [21, 39].

Although the process is capable of removing small concentrations of H_2S, pre-treatment to remove the majority of H_2S prior to membrane separation is recommend [41].

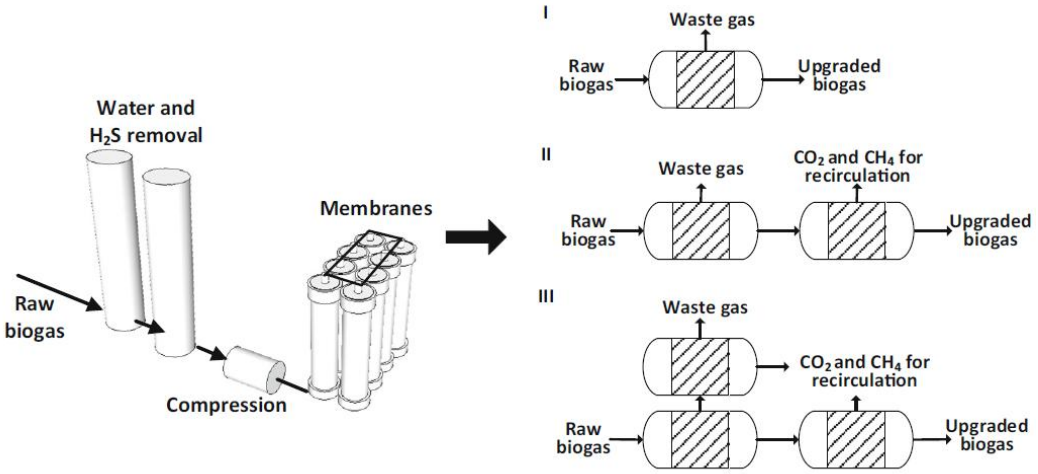

Figure 1.7. Biogas upgrading by membrane separation; different configurations of units: I single-pass membrane unit, II multiple stage membrane units with internal recirculation of permeate and III internal recirculation of retentates [11].

In resume all these techniques have their advantages and drawbacks (see *Table 1.4*). However, it is important to seek for other processes that make it possible to transform biogas to biomethane. In recent years a new process based on selective gas capture by hydrate formation have showed interesting results [12, 42-48]. The basic mechanism of the separation process is selective partition of the target component between the hydrate phase and the gaseous phase. In next *Sections* we will define clathrates, more specifically the gas hydrates and their properties and present the works in literature that promote applications of these compounds.

Table 1.4. Advantages and disadvantages of different biogas upgrading techniques [37].

Technique	Advantages	Disadvantages
Absorption in amines	High efficiency (> 99 % CH_4)	Expensive investments
	Cheap operation	Heat required for regeneration
	Very low CH_4 losses (0.1 %)	Corrosion
	Regeneration	Precipitation of salts
	More CO_2 dissolved per unit of volume (compared to water)	
PWS	High efficiency (> 97% CH_4)	Expensive investments
	Easy in operation	Expensive operation
	Regeneration possible	Clogging due bacterial growth
	Low CH_4 losses (< 2%)	
PSA	Highly efficient (95 - 98% CH_4)	Expensive investments
	Compact technique	Expensive operation
	Also for small capacities	Extensive process control needed
Membrane	Simple construction	CH_4 losses
	Simple operation	Little operational experience
	Small gas flows treated without proportional increase of costs	Multiple steps required (modular system) to reach high purity
	High reliability	

1.2 Clathrate hydrates

The discovery of gas hydrates is normally attributed to the English chemist Sir Humphrey Davy. He studied the hydrate of chlorine in the early 19th century and observed that this ice-like solid is formed at temperatures higher than the freezing point of water [14, 49].

A clathrate is a compound in which a molecule of one substance (guest) is enclosed in a structure built from molecules of another substance (host). When the structure is composed by water molecules the compound is called clathrate hydrate. A clathrate gas hydrate is then a compound where gas molecules are trapped in a structure built by water molecules [49].

More specifically, clathrate gas hydrates is a group of ice-like, crystalline, non-stoichiometric compounds, formed by a combination of guest molecules and a network of water molecules. They are formed under suitable conditions, at high gas pressures and at low temperature [14]. In these compounds, water molecules linked by hydrogen bonds form polyhedral cavities that are able to trap molecules. The whole structure of gas hydrates is stabilized by Van der Waals' interactions between the trapped molecules and the network of water molecules [14, 49]. Depending on the structure formed, liquid guest such as tetrahydrofuran and cyclopentane can also form clathrate hydrates [14, 50].

Another group of clathrates are the so called semi-clathrate hydrates. In these compounds water molecules forms lattices with tetra-alkylammonium/alkylphosphonium salts or trialkylamine or trialkylphosphine oxides [50-51]. They were first identified by Fowler *et al.* [52] and later their structures were analyzed applying X-ray diffraction [51, 53]. In these solids, the nitrogen or phosphorus atoms from salts and the nitrogen/phosphorus atoms and oxygen atoms from oxides occupy the lattice sites of the structure. The alkyl chains act as a guest filling the cages formed by water molecules [54]. They are stable at ambient pressure and at temperatures as high as 30 °C [51, 55]. In these structures some small dodecahedral cages are available and can encage small gas molecules, such as CH_4, CO_2 and H_2S [56-58].

Recently, clathrate hydrates have been studied in many innovating industrial applications, such as natural gas storage and transport [59-66], sequestration of carbon dioxide with *in situ* methane hydrate decomposition [59, 62, 67-70], hydrogen storage [71-74], separation of carbon dioxide from the flue gas [12, 48, 75-79], refrigeration [80-86] and biogas upgrading [12, 87-91].

1.2.1 Structures and properties

The structures of clathrate gas hydrates are composed by five polyhedral cages formed with water molecules (*Figure 1.8*). The description of each cage is made by n_i^{mi}, where n_i is the number of edges in face type "*i*", and *mi* is the number of faces with n_i edges.

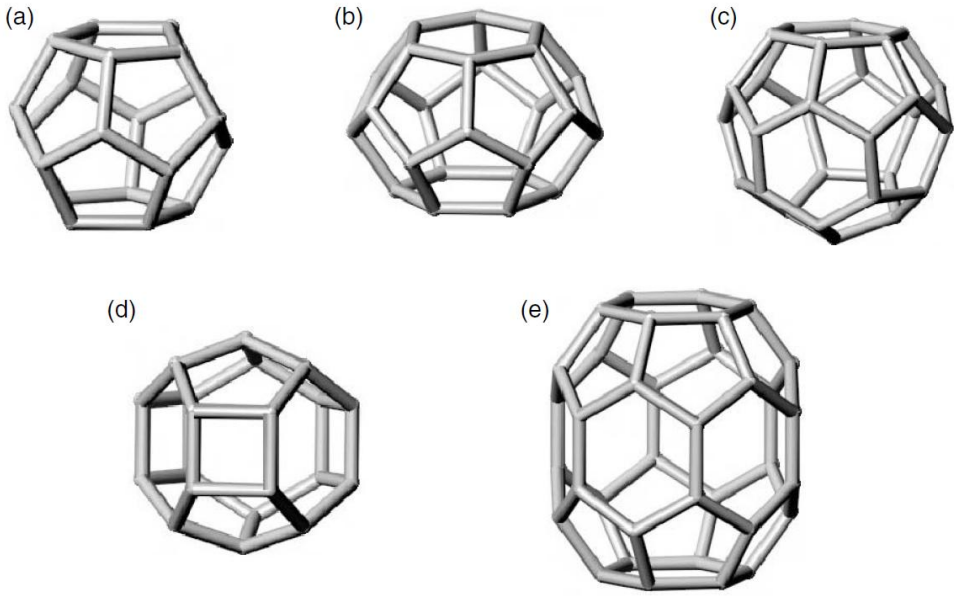

Figure 1.8 Cavities of clathrate gas hydrates: (a) pentagonal dodecahedron (5^{12}), (b) tetrakaidecahedron ($5^{12}6^2$), (c) hexakaidecahedron ($5^{12}6^4$), (d) irregular dodecahedron ($4^3 5^6 6^3$), and (e) icosahedron ($5^{12}6^8$) [14].

Depending on the guest molecule and/or the thermodynamic condition three clathrate gas hydrate structures can be formed (*Figure 1.9*): SI, SII and SH [14, 92].

The structure SI is formed by two small dodecahedral cavities (5^{12}) and six large tetrakaidecahedral cavities ($5^{12}6^2$). The crystal system has a cubic structure (space group Pm3n) with 12.03 Å edge and 46 water molecules. SI structure is able to encage small gas molecules, such as carbon dioxide, methane and hydrogen sulfide.

The Structure SII is composed by sixteen 5^{12} cavities and eight hexakaidecahedral cavities ($5^{12}6^4$). The structure contains 136 water molecules and the crystal has a cubic structure (space group Fd3m) with 17.3 Å edge. As example of SII formers we can cite propane and tetrahydrofuran (THF) [93-94]. In these cases, the large hydrate-forming molecule occupies the large $5^{12}6^4$ cages while the small 5^{12} cages remain empty. The enclathration of small molecules in these available cages is therefore possible. Indeed, mixed clathrate gas hydrates

of SII formers and gas molecules such as CO_2 and CH_4 are widely studied [83, 95-97]. In presence of some SII formers, CO_2 and CH_4 hydrates can be formed at lower pressures and higher temperatures compared to the single SI condition formation. These molecules having this behavior to form CO_2 and/or CH_4 hydrates at milder conditions will be called in this work thermodynamic promoters or additives.

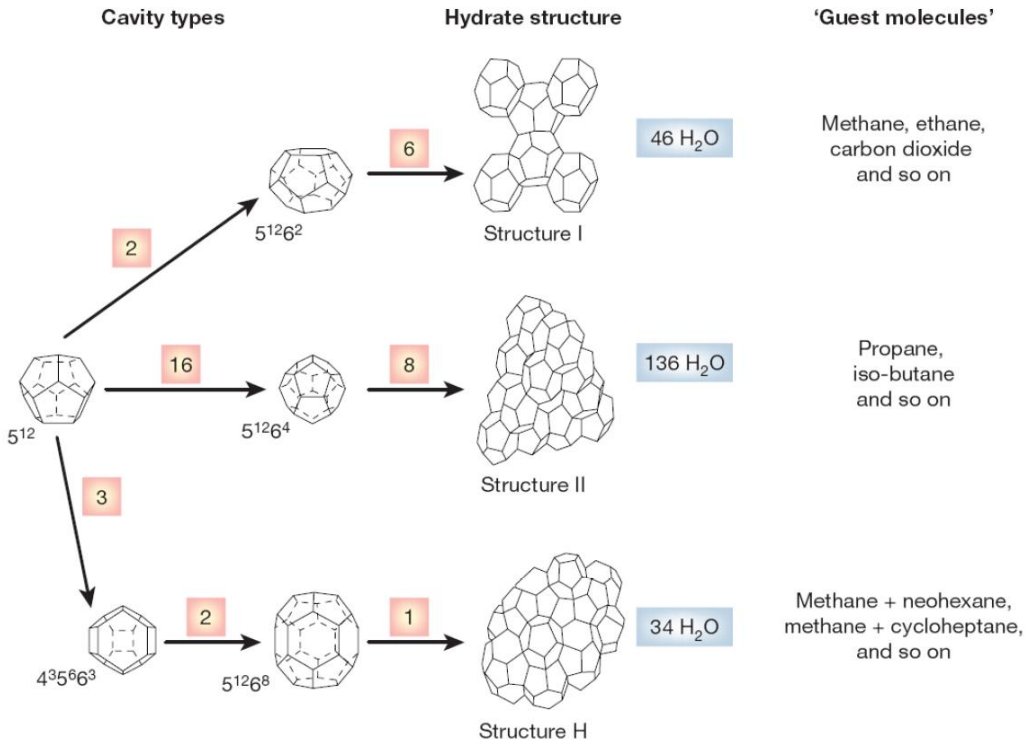

Figure 1.9 Structures of clathrate gas hydrates (adapted from Sloan and Koh [14]).

The structure SH is less common than SI and SII. Its unit crystal is made up of three 5^{12} cavities, two irregular dodecahedral cavities ($4^3 5^6 6^3$) and one icosahedral cavity ($5^{12}6^8$). The crystal framework is a hexagonal structure (space group P6/mmm) with 34 water molecules. In contrast to SI and SII structures that can be formed in presence of a single guest former, the structure SH requires two formers to be stabilized: one small molecule such as methane and a large SH former molecule, such as neohexane, cycloheptane or methylcyclohexane [92, 98].

For further information about the structures of clathrate gas hydrates the readers can refer to the book entitled "Clathrate Hydrates of Natural Gases" by Sloan and Koh [14].

Knowing the structure of formed hydrate allows determining the hydration number (υ). This property is defined as the ratio between the number of water molecules and guest molecules. For example, if methane occupies the eight cages (two small and six larges) of SI structure,

the hydration number will be 46 /8 = 5.75. This value can also be interpreted as the composition of hydrate phase. However, gas hydrates are non-stoichiometric compounds, which means that the full occupancy of cages is generally not reached. The real composition of hydrate can be calculated by knowing the occupancy rate of each cage and applying the *Equation 1.1*.

$$\upsilon = \frac{N_{water}}{\sum_i \sum_j C_i \theta_i^j} \tag{1.1}$$

where: N_{water} is the number of water molecules per unit cell; C_i is the number of cage type *i* per water molecule in unit cell; θ_i^j is the occupancy rate of cage type *i* by the guest molecule *j*.

Another important property of clathrate hydrates is their density (ρ) and like the hydration number it depends on the occupancy rate of each cage. The expression allowing to calculate the hydrate density is shown in *Equation 1.2* [14].

$$\rho = \frac{N_{water} MW_{water} + \sum_{j=1}^{C} \sum_{i=1}^{N} \theta_i^j C_i MW_j}{N_{Avo} V_{cell}} \tag{1.2}$$

where: MW_{water} is the molecular weight of water; MW_j is the molecular weight of guest *j*; N_{Avoa} is the Avogadro's number, 6.023 x 10^{23} molecules/mol; and V_{cell} is the volume of unit cell.

For semi-clathrate hydrates the formed structure will depend on the kind of former/promoter molecule and/or its concentration in the system. Unlike the clathrate gas hydrates, the semi-clathrates are stoichiometric compounds and their structures are related to the hydration number in the following general formula: promoter.n_{hyd}.H_2O. The tetra-*n*-butylammonium bromide (TBAB) semi-clathrate, for example, can form various structures with n_{hyd} varying from 2.3 to 38 [53, 55-57, 99-101]. Lipkowski *et al.* [99] reported a trigonal cell for TBAB.2.3H_2O semi-clathrate. Shimada *et al.* [56] and Oyama *et al.* [101] have reported details of two structures: TBAB.26H_2O (tetragonal cell) and TBAB.38H_2O (orthorhombic cell), also called TBAB semi-clathrates type A and B, respectively. They described that these structures contain some empty 5^{12} cages that are able to enclathrate small gas molecules such as CH_4, CO_2 and H_2S (*Figure 1.10*). Shimada *et al*. [56] and Kamata *et al*. [58] were the first

to propose that TBAB semi-clathrate can be used in a selective gas separation process. Since, other applications of TBAB semi-clathrate have been proposed, such as gas storage [102] and refrigeration [103-104]. Recently, Muromachi *et al.* [57] detailed the structure of TBAB.38H_2O formed with CO_2. They observed that, formed at mild CO_2 pressure, this structure is the most effective for CO_2 capture.

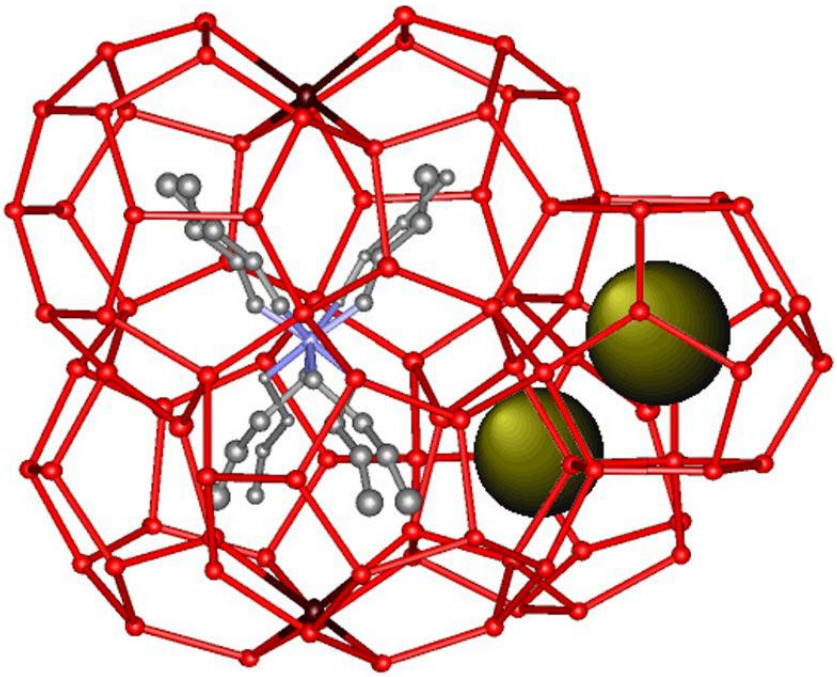

Figure 1.10 Structure of TBAB/Gas semi-clathrate hydrates (nhyd = 38) [56].

Other promoters, such as the tetra-n-butylphosphonium bromide (TBPB) for alkylphosphonium salts and the tributylphosphine oxide (TBPO) for trialkylphosphine oxides, have their hydrate structures detailed in literature [105-106]. Like TBAB semi-clathrates, these promoters can form many structures and they have some empty 5^{12} cages that can trap small gas molecules.

Some semi-clathrate densities found in literature are listed in *Table 1.5.*

Table 1.5 Density of semi-clathrates.

Semi-Clahtrate	Density /g/cm3	Ref.
TBAB.26H_2O	1.094	[51]
TBAB.38H_2O	1.045	[56]
CO_2.TBAB.38H_2O	1.132	[57]
TBPB.38H_2O	1.054	[105]
TBPO.34.5H_2O	0.97	[106]

1.2.2 Phase diagram

Phase diagram allows determining the existing phase regions of a system. These regions are delimited by the equilibrium phase transition curves. *Figure 1.11* presents a typical *Pressure-Temperature* diagram for methane + water system.

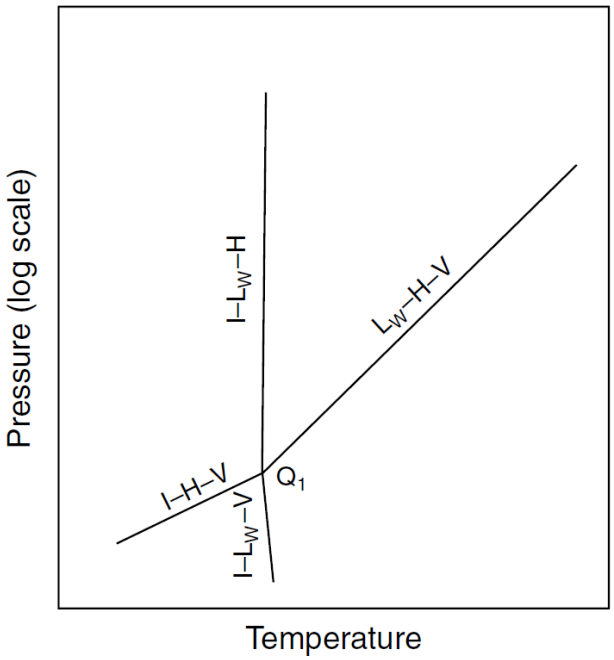

Figure 1.11 Typical phase diagram for methane + water system [14].

For clathrate gas hydrates systems these equilibrium curves are obtained by measuring the so called dissociation conditions. It corresponds, generally, to the *p-T* equilibrium points in which the hydrate-liquid-gas phases coexist. In literature it is possible to find several equilibrium data for systems involving hydrate phases [45, 48]. From here, due to the scope of this work, we are going to focus in hydrate systems from gas phases containing CO_2, CH_4 and CO_2+CH_4 mixture.

Figure 1.12 shows the equilibrium curves of CO_2 and CH_4 hydrates measured by Goel *et al.* [107]. Comparing the two systems it is possible to observe a zone where carbon dioxide can exist as hydrate while methane hydrate can dissociate into gas phase. This zone lies above the ice (or water)–hydrate–CO_2 gas (or liquid) phase line but below the ice (or water)–hydrate–CH_4 gas phase line (Regions A and B in the *Figure*). Here, the dissociation temperature of carbon dioxide hydrates is higher than that of methane hydrates at a given pressure, or the dissociation pressure of carbon dioxide hydrates is lower than that of methane hydrates at a

given temperature. For example, at 2.9 MPa, the dissociation temperature of methane hydrates is 274 K whereas that for carbon dioxide hydrates is 280 K. This difference indicates a possible selective capture in a gas separation process.

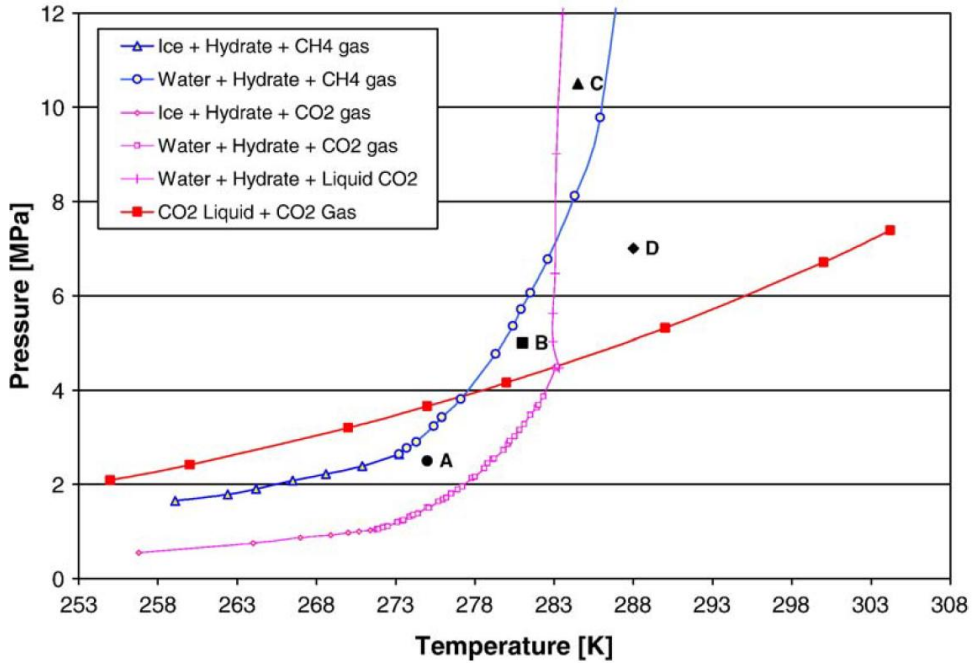

Figure 1.12 Hydrate forming conditions of carbon dioxide and methane [107].

It is possible to find in literature works that measured the phase equilibrium of CO_2+CH_4 mixed hydrates [97, 107-109]. These works showed that the equilibrium pressures of CO_2+CH_4 mixture hydrates are between that of pure CO_2 hydrates and CH_4 hydrates. Besides, the equilibrium pressure of CO_2+CH_4 mixed hydrates decreases with the increase of the composition of CO_2 in the mixture gas (*Figure 1.13)*. In other words, it is noted that the phase equilibrium conditions for the CO_2+CH_4 mixed hydrates approach those of CO_2 hydrates as CO_2 composition increases in the CO_2+CH_4 mixture.

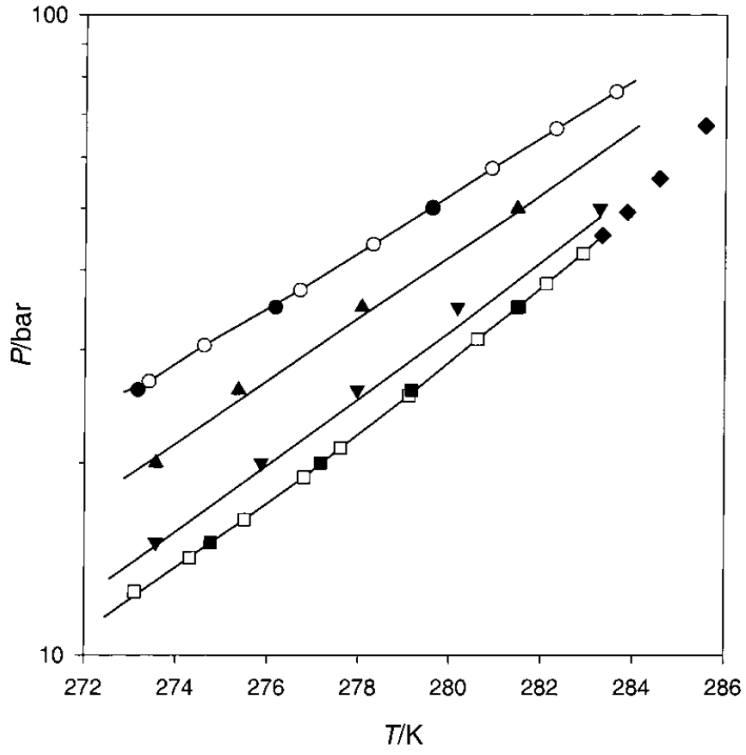

Figure 1.13 Equilibrium hydrate formation for CO_2, CH_4 and CO_2+CH_4 mixture: ○, CH_4 hydrate, data from Adisasmito et al. [108]; ●, CH_4 hydrate, data from Seo et al. [109]; □, CO_2 hydrate, data from Adisasmito et al. [108] ; ■, CO_2 hydrate, data from Seo et al. [109]; ▲, y = 20 mol% CO_2, data from Seo et al. [109]; ▼, y = 60 mol% CO_2, data from Seo et al. [109].

Figures 1.14a and *b* present the isobar *T-x* and isothermal *P-x* envelope phase diagrams for CO_2 + CH_4 + H_2O system, respectively. In *Figure 1.14a* hydrate phase formation is possible on and below the respective equilibrium lines. From an isothermal point of view in *Figure 1.14b*, the lower equilibrium pressure of CO_2 hydrate can be interpreted as a preferential enclathration of CO_2 molecules with respect to methane.

Lee *et al*. [97] provided a detailed study about hydrate structure and cage occupancy in CO_2 + CH_4 hydrates. They used X-ray diffraction measurements and showed that the CH_4 + CO_2 hydrates prepared from an equimolar gas mixture composition form structure SI. The cage occupancy of CH_4 and CO_2 molecules enclathrated in the hydrate frameworks was detailed using Raman spectroscopy technique. For the CH_4 + CO_2 hydrates, the concentrations of CO_2 in the hydrate phase were higher than those in the gas phase. The Raman measurements of the CH_4 + CO_2 hydrates also indicated that the population of CH_4 molecules in the small 5^{12} cages of the SI hydrate structure was higher than that in the large $5^{12}6^2$ cages, and the CO_2

molecules preferentially occupy the large $5^{12}6^2$ cages. Belandria *et al.* [110] also demonstrated that the hydrate phase from $CO_2 + CH_4$ mixture contains more enclathrated CO_2 than CH_4.

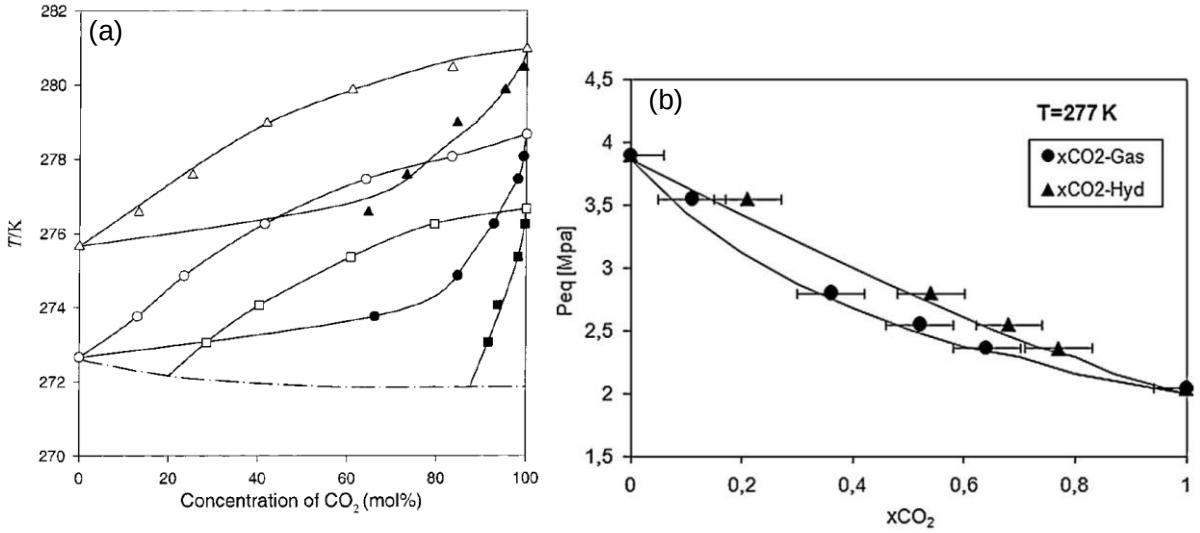

Figure 1.14 Envelope phase diagrams for $CO_2 + CH_4 + H_2O$ system; (a) Δ, gas phase at 35 bar; ▲, hydrate phase at 35 bar; ○, gas phase at 26 bar; ●, hydrate phase at 26 bar; □, gas phase at 20 bar; ■, hydrate phase at 20 bar , data from Seo et al. [109]; (b) ▲, hydrate phase at 277 K; ●, gas phase at 277 K, data from Herri et al. [111]

Semi-clathrates and hydrates formed from some SII structure promoters can be stable at ambient pressure. In other words, these compounds don't need to encage gas molecules to stabilize their crystal framework. As a result, the binary S*olid-Liquid* phase behavior can be established for these systems, making it possible to define the limit of existence of hydrate phase region [85, 101, 112]. These diagrams are useful for determining at a given temperature the solid fraction of a diphasic mixture. In *Figure 1.15* the *T-w* phase diagram (*w* being the mass fraction) of TBAB + water system obtained from experimental data in literature is presented. The equilibrium points set define the *liquidus* curve that delimit the existence region of hydrate phase (below) and the monophasic liquid phase (above). At stoichiometric composition of semi-clathrates the *liquids* curve is at the maximum value and the solid melts congruently.

The polymorphism of TBAB was reported by Gaponenko et al. [113] and Shimada et al. [114] from crystal structure analysis by X-ray diffraction measurements. Therefore, the deflection of the *T−w liquidus* curve in *Figure 1.15* is related to the different thermodynamic stabilities of the hydrates having different hydration numbers.

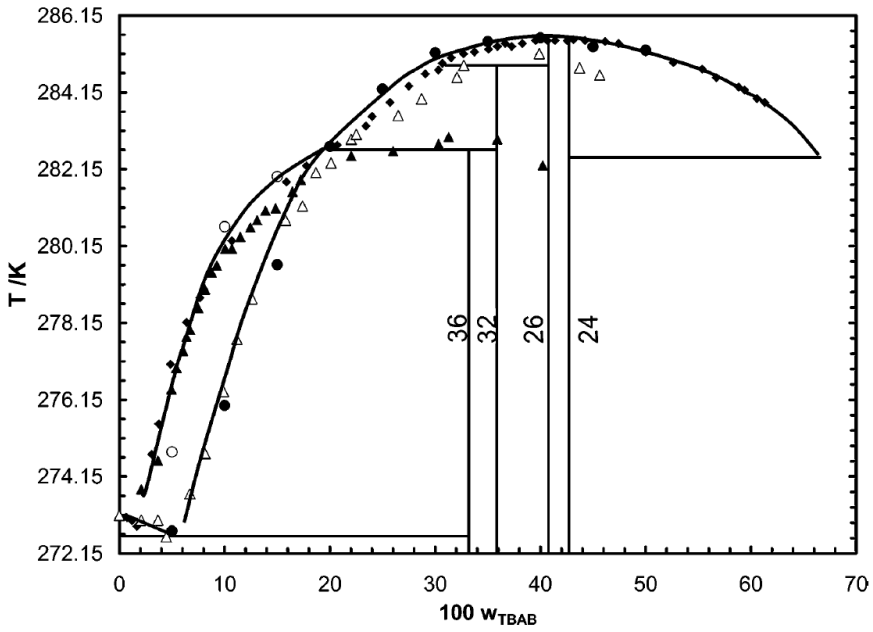

Figure 1.15 Experimental data in literature for phase behavior of TBAB + water binary system in existing region of TBAB hydrate; ♦, Lipkowski et al. [99]; Δ, Oyama et al. [101]; ▲, Oyama et al. [101], ●, Darbouret et al. [115]; ○, Darbouret et al. [115].

Figure 1.16 illustrates the effect of thermodynamic promoters. Taking CO_2 as an example, these molecules form hydrate at higher temperature and lower pressure compared to single CO_2 hydrate. The presence of even a small amount of TBAB can lower the pressure and raise the temperature for TBAB/CO_2 hydrate. For example, the equilibrium temperature increases from 278.9 K for CO_2 hydrate to 290.3 K for TBAB/CO_2 hydrate at 2.61 MPa and for mass fraction TBAB aqueous solution of 0.32.

Since the formed structures are different from traditional SI and SII, the promoters can represent not only a gain of stability but also improvements in kinetics aspects of hydrate formation and capture selectivity.

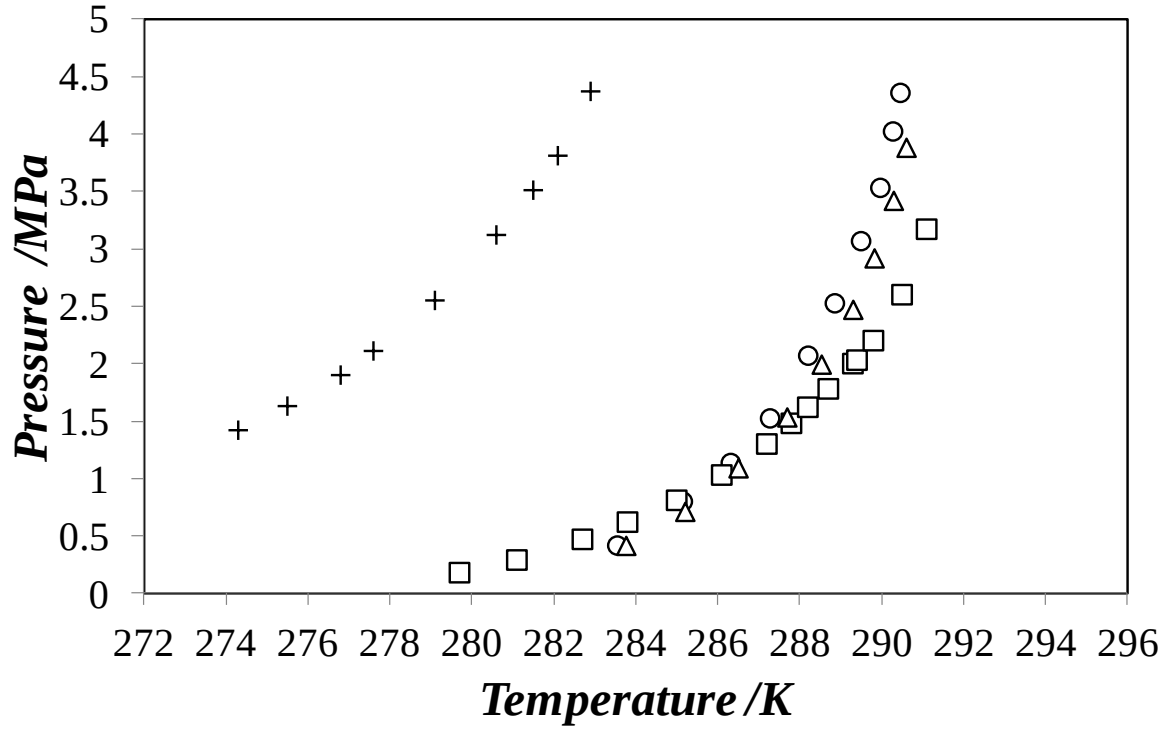

Figure 1.16 Hydrate equilibrium conditions for systems containing promoters; +, CO_2 + water system, data from Adisasmito et al. [108]; ○, TBAB + CO_2 + water system, w_{TBAB} = 0.19, data from Ye et al. [116]; Δ, TBPB + CO_2 + water system, w_{TBPB} = 0.20, data from Suginaka et al. [117]; □, THF + CO_2 + water system, w_{THF} = 0.19, data from Lee et al. [97].

Like in single CO_2 and CH_4 hydrates the semi-clathrates formed with promoters salts present higher stability with CO_2 compared to CH_4. However, some authors observed an inversion of stability when some SII structure formers, such as THF and tetrahydropyran (THP), were present in the system [97, 118-120]. Furthermore, some works with TBPO promoters evidenced the same inversion, where the hydrate phase containing CH_4 is more stable than with CO_2 [121-122].

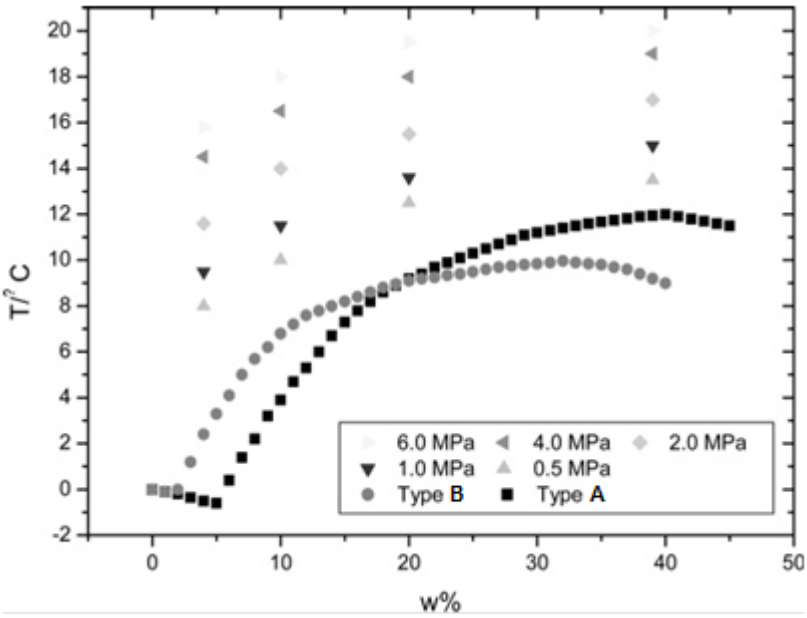

Figure 1.17 T−w diagram of the semiclathrate hydrates formed in the system of tetra-n-butylammonium bromide (TBAB) + water pressurized with methane (adapted from ref. [123]); w is the mass fraction of TBAB in aqueous solution.

Figure 1.17 presents the experimental data of TBAB/CH_4 semi-clathrate in a *w-T* phase diagram. This phase diagram show the limits of existence of hydrates in a range of promoter composition, which is an important information that must be taken into account for determining the operation conditions for hydrate based processes. Moreover, Li *et al.* [123] observed that the addition of TBAB causes the hydrate equilibrium pressure to be drastically lowered by 52 to 96 % at a specified temperature and, equivalently, the hydrate equilibrium temperature to be raised by about 4 to 17 K at a specified pressure, depending on the concentration of TBAB in water. Methane capture into semi-clathrates was confirmed by a shift of the clathrate stability when TBAB is present. Kobori *et al.* [124] measured the same kind of phase diagram for TBAB/CO_2 semi-clathrate.

In literature, several authors have measured the liquid-vapor-hydrate equilibrium data for systems containing promoters. Among these systems, there are tetra-n-butyl ammonium bromide (TBAB) + CO_2 + water [125-127], TBAB + CH_4 + water [125, 128-129], tetra-n-butyl ammonium chloride (TBAC) + CO_2 + water [127, 130], (TBAC) + CH_4 + water [131], tetra-n-butyl phosphonium chloride (TBPC) + CO_2 + water [132], (TBPC) + CH_4 + water [132]. Some works on modeling the phase behavior in presence of these compounds have also been done [47, 133-134].

Concerning the hydrate phase equilibrium data with promoters and CO_2 + CH_4 mixture we can cite the works of Deschamps & Dalmazzone [126], Acosta *et al.* [135], Xia *et al.* [136], Lee *et al.* [97], Fan *et al*. [137] and Long *et al.* [138].

In 2009, Deschamps & Dalmazzone [126] studied (CO_2 + CH_4) hydrate equilibrium with a 0.4 mass fraction of TBAB. The enthalpies and temperatures of dissociation of TBAB/($0.5CO_2$ + $0.5CH_4$) hydrates were measured by Differential scanning calorimetry (DSC) in a range of temperature from 290.9 to 292.4 K and pressure ranging from 1.14 to 3.20 MPa. The results showed that high concentrations of TBAB salts can enlarge the hydrate stability zone.

Later, Acosta *et al.* [135] used a isochoric equilibrium cell to measure the effect of TBAB concentration on the equilibrium conditions for semiclathrates formed from two compositions of CO_2+CH_4 mixtures (40 and 60 mol% of CO_2). The experiments were carried out with a TBAB mass fraction in aqueous solutions varying from 0.05 to 0.20. They noticed that, with both gas mixture compositions, the pressure required to form semiclathrates at a given temperature decreased as the TBAB concentration increased.

Xia *et al.* [136] studied the TBAB/(CO_2+CH_4) and THF/(CO_2+CH_4) hydrates. The gas mixture was composed of 45 mol% of CO_2. The mole fractions of TBAB and THF solutions were fixed at 0.0234 and 0.0556, respectively. The hydrate formation conditions were measured by *T-cycle* method in the temperature range of 274.15 to 294.95 K and the pressure ranges up to 6.72 MPa. They observed that both TBAB and THF can reduce the hydrate formation pressure of CO_2+CH_4 mixture, but the effect of THF is better than that of TBAB in the high temperature region.

Lee *et al.* [97] also worked with the promoter THF for investigating the phase equilibrium behavior of THF/(CO_2+CH_4) hydrates at the THF stoichiometric concentration of 5.56 mol %. They used X-ray diffraction (XRD) to confirm that the hydrate structure formed is the SII and by using Raman spectroscopy technique they observed that the CH_4 and CO_2 molecules were encaged only in the small 5^{12} cages of the SII hydrate framework, whereas the large $5^{12}6^4$ cages were fully occupied by THF molecules.

Fan *et al.* [137] used the tetrabutylammonium halide (bromide/TBAB, chloride/TBAC, and fluoride/TBAF) salts as thermodynamic promoters. The CO_2+CH_4 mixture gas phase was composed by 33 mol% of CO_2. The equilibrium hydrate formation conditions were measured

by an isochoric pressure-search method in a range of temperature from 280.2 K to 291.3 K and range of pressure from 0.61 MPa to 9.45 MPa with 0.00293 mole fraction of tetrabutylammonium halide. They concluded that TBAF provided the best stabilization of CO_2+CH_4 hydrates compared to the two other. However the high toxicity of this promoter prevents its application in hydrate-based process.

Finally, Long *et al.* [138] measured the equilibrium data for TBAB/(0.33CO_2+0.67CH_4) semi-clathrates for TBAB mass fraction ranging from 1.76 to 14.0 wt%. The tested temperature and pressure ranged from 273.6 to 294.2 K and from 0.54 to 14.57 MPa, respectively. They observed that at 1.76% in mass fraction TBAB solutions promote hydrate formation at low pressure (lower than 3 MPa) and have no significant promoting effect at high pressure. They concluded that phase equilibrium conditions for TBAB semiclathrate hydrates of CH_4+CO_2 mixture are mainly determined by the concentration of TBAB solution.

1.2.3 Kinetic aspects of crystallization phenomenon

The gas hydrate formation is a crystallization process, which is characterized by two distinct phenomena, namely, nucleation and growth [139]. Nucleation is perhaps the most challenging step in understanding the process of crystallization of gas hydrates. At the same time, its understanding could be the key to the kinetic inhibition or promotion of this process [140].

Hydrate nucleation is a microscopic phenomenon during which small clusters of water and gas (hydrate nuclei) grow and disperse in an attempt to achieve critical size for continued growth [14]. Hydrate nucleation in general is a complex and stochastic process that occurs when the solution is in a supercooled or supersaturated state, i.e., the system is in a metastable region [139, 141]. The induction time is therefore defined in practice as the time elapsed until the appearance of a detectable volume of hydrate phase or, equivalently, until the consumption of a detectable number of moles of hydrate former gas [14].

During the induction period, the temperature and pressure conditions are within the hydrate stable region. However, hydrate does not form within this period because of metastability (i.e., the ability of a non-equilibrium state to persist for a long period of time). During the growth period, gas is being concentrated in the cages of hydrate structures. As the water is consumed by hydrate formation, the slope of the gas consumption trace eventually decreases with time [141]. In other words, the sudden appearance of hydrates results in the consumption

of supersaturation leading to the dramatic pressure drop.

As said above the induction time depends on the degree of supersaturation. Very long induction periods are observed at low supersaturarions. On the other hand, short induction time is obtained in high supersaturation sate. The induction period duration exhibits random behavior at lower supersaturarions and becomes increasingly deterministic as the supersaturation is increased.

Another way to reduce the induction time in crystallization of clathrate hydrates is exploring the memory effect. It is known that the recrystallization of hydrates occurs under milder conditions (*i.e.* lower pressure or higher temperature) than the initial nucleation. In hydrate systems some authors have reported the memory effect observing the reduction of induction time [142-144].

In CO_2 + CH_4 hydrates formed with THF, Zhong *et al.* [145] found that the induction times obtained in memory solutions were shorter than those obtained in fresh solutions under the same pressure and temperature conditions. Recently, Oshima *et al.*[142] investigated the memory effect in TBAB semi-clathrates by using optical microscopy. The experiments were carried out at two different concentrations (stoichiometric mole fraction for TBAB hydrate formation and lower mole fraction than stoichiometric one). The recrystallization of TBAB hydrate has been observed under milder condition than that of the initial crystallization in both concentrations. In particular, solution of the lower concentration is easily recrystallized.

The growth of the hydrate particles is explained in a three step process. The first step corresponds to the diffusion of the dissolved gas from the bulk of the liquid phase to the hydrate-liquid interface through the laminar diffusion layer around a particle. The second step relates to the adsorption "reaction" process at hydrate-liquid interface. This step describes the enclathration phenomenon of the gas molecules into the cages and the subsequent stabilization of the framework of the structured water. The third step is the heat release due to the exothermic characteristic of crystallization phenomenon. Since no accumulation is allowed in the diffusion layer around the particle, the rates of the above two first processes are equal. Therefore, the rate of growth per particle (*dn/dt*) in terms of the overall driving force can be expressed in *Equation 1.3* [139, 141].

$$\left(\frac{dn}{dt}\right)_p = K^* A_P (f - f_{eq}) \qquad (1.3)$$

where,

$$\frac{1}{K^*} = \frac{1}{k_r} + \frac{1}{k_d} \qquad (1.4)$$

where: K^* is the combined rate constant for the diffusion (k_d) and adsorption processes (k_r); A_P is the surface area of each particle; f is the fugacity of the gas; and f_{eq} is the three phase equilibrium fugacity at the hydrate surface temperature.

The identification of the driving force is based on thermodynamic considerations and on the fact that the gas hydrate formation is a crystallization process [139]. Since the three phase equilibrium fugacity represents the minimum fugacity at which hydrates can exist, the driving force for the hydrate crystallization process is given by the difference in the fugacity of the dissolved gas in the liquid and the three phase equilibrium fugacity at the hydrate surface temperature. The driving force may be simplified as the difference between the pressure at a given instant and the equilibrium pressure [14, 139, 141].

For hydrate formation from a binary gas mixture, the rate of growth per particle can be calculated from *Equation 1.5.*

$$\left(\frac{dn}{dt}\right)_p = \sum_{j=1}^{2}\left(\frac{dn_j}{dt}\right)_p = K_j^* A_P (f - f_{eq})_j \qquad (1.5)$$

where K_j^* and $(f - f_{eq})_j$ are the individual rate constants and driving forces; f_j is the fugacity of the component j in the liquid solution and $f_{eq,j}$ is the fugacity of the component j in the gaseous mixture at the three phase equilibrium pressure. The gas phase composition is thus included indirectly into the above expression through the fugacities.

1.3 Gas separation by hydrate formation (GSHF) for CO_2+CH_4 mixture

In this *Section* we will present the last studies done on gas separation by hydrate formation (GSHF) for CO_2 + CH_4 mixture systems in presence or not of promoters. The studies of Golombok *et al*. [146] and Denderen *et al.* [147] were among the first testing the feasibility to separate CO_2 from CO_2 + CH_4 mixture using a hydrate based process. Golombok *et al*. [146] showed that for appropriately selected pressure and temperatures, the kinetics of CO_2 uptake proceed much more quickly than those of methane uptake. Therefore, despite the fact that the phase boundaries for the pure components are relatively close, it may be possible to separate kinetically CO_2 from CO_2 + CH_4 mixture. More recently, Horvat *et al* [148] showed that CO_2 is encaged faster than CH_4 during hydrate formation process from CO_2+CH_4 mixture gas phase. These researches indicated that kinetic separation can replace equilibrium-stage separation in CO_2 capture from biogas. But how to enhance the selective enclathration of CO_2 by kinetic was still a difficult problem.

Denderen *et al.* [147] studied CO_2 removal from contaminated natural gas by experiments. They employed two compositions of CO_2 + CH_4 mixtures, one with 50 mol% of CO_2 and another with 25 mol% of CO_2. Applying a set temperature of 275 K and an initial pressure of 8 MPa they observed that the gas phase containing 50 % of CO_2 reduced to 39 % after hydrate formation. For the second composition, after the hydrate formation the gas phase composition on CO_2 reduced from 25% to 16%. They also concluded that GSHF depend on the amount of water used. Excess water above the pseudostoichiometric ratio of ca. 6 will always be required in an industrial process to provide slurry transport of CO_2 hydrate out of the reactor, after which the acid gas stream is regenerated for sequestration. They also suggested that hydrate based process may be used as pre-treatment for H_2S removal in biogas, since this gas form hydrate phase much more easily than CO_2 and CH_4.

Dabroski *et al*. [13] simulated a GSHF process for separating CO_2 from CO_2 + CH_4 mixture. Simulation calculations were made with the gas mixture containing 50 mol% of CO_2, being exemplary for biogas (digester gas) and landfill gas. They proposed a separation process using a cascade of continuously stirred tank crystallizer vessels, which can also be regarded as an ideal crystallizer column resembling a gas-hydrate-based scrubbing process (*Figure 1.18*). The set temperature was 273 K and the operating pressure was 2.62 MPa. The theoretical number of crystallizer stages to achieve a CH_4 purity higher 0.98 was nine. Therefore, it was found that the purification of biogas using a hydrate based process is generally feasible but

requires high pressure levels. The main drawback of the hydration process lies in its high methane loss, because of inadequate selectivity of the enclathration with respect to the liquid-phase absorption process. They believed that the application of hydrate promoters could decrease working pressures. Furthermore, the formation of semi-clathrates with polar-promoting agents, such as TBAB, would possibly result in an increased CO_2 solubility inside the solid phase.

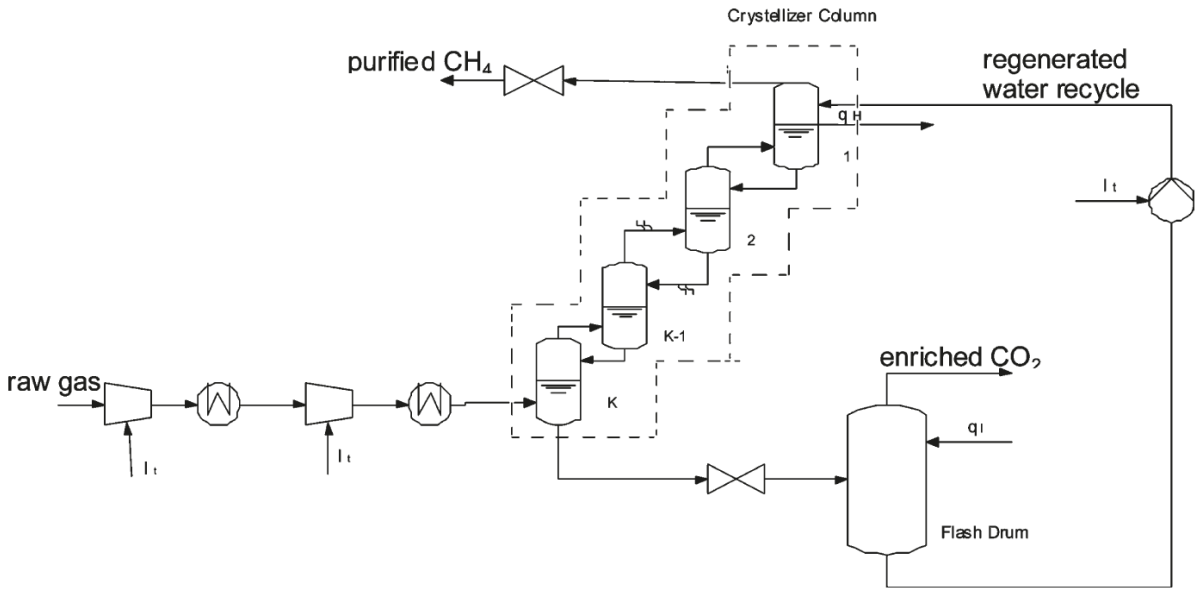

Figure 1.18 Proposed flowchart of GSHF process for CO_2 capture from CO_2+CH_4 mixture using a multi-staged crystallizer [13].

Unlike the other works that are mainly at a laboratory scale, Castellani *et al*. [88] carried out an experimental study on the application of gas hydrate technology to biogas upgrading with an up-scaled apparatus. In this equipment, hydrates are produced in a rapid manner, with hydrate formation times of few minutes. GSHF process was carried out at several operating pressures in the range from 4 to 7 MPa and two set temperatures, 275 and 277 K. Without the presence of H_2S, the highest value of the CO_2 capture selectivity was obtained at 6 MPa and 277 K in which the composition of CO_2 in vapor phase reduced from 0.39 to 0.29 after 30 minutes of hydrate formation. Theoretical energy evaluations show that hydrate based process is a viable technology, competitive with respect to other conventional separation methods. Improvements in the process can however be done.

Concerning thermodynamic promoters in GSHF for CO_2 + CH_4 mixture, we can cite the works of Ricaurte *et al.* [149-151], Zong *et al.*[90] and Xia *et al.* [87]. At first, Ricaurte *et al.* [151] investigated the use of water-soluble additives THF and/or sodium dodecyl sulfate

(SDS) at low concentrations in a GSFH process to capture CO_2 from a $0.75CO_2 + 0.25CH_4$ mixture. The influence of promoter concentration and process operating conditions on the gas consumption kinetics, the quantity of gas removed, and the selectivity of the separation were studied under quiescent hydrate-forming conditions in a batch reactor. The hydrate formation was observed in operating conditions of initial pressure ranging from 3 to 4 MPa and set temperature varying from 275 to 279 K. The concentration of promoters varied for THF from 0 to 4 wt% and for SDS from 0 to 4800 ppm. They observed that gas consumption and enclathration occur at high rates only when the two additives are used in combination. The enclathration rate is found to increase with increasing SDS concentration, with a maximum obtained in the range 1600−3000 ppm. However, this molecule had no effect on the quantity of gas removed and on the selectivity of the separation. Gas consumption rate increased with THF concentration. They obtained more gas removed and higher gas consumption rates with higher initial pressure and/or lower set temperatures.

Later, Recaurte *et al*. [149] studied the effects of several combinations of surfactants and organic compounds on the separation of CO_2 from a $0.75CO_2 + 0.25CH_4$ mixture by hydrate formation. Seven additives, three surfactants (SDS, Sodium dodecyl benzene sulfonate/SDBS and Dodecyl trimethyl ammonium chloride/DATCl) and four organic compounds (THF, 1,3-dioxolane/DIOX, 2-methyl-tetrahydrofuran/m-THF and cyclopentane/CP) were tested for various operating conditions and at different concentrations. Initial pressure varied from 3 to 4 MPa and the set temperature was fixed at 275 K. Their results showed that a suitable combination of a surfactant and an organic compound can, in some cases, strongly enhance the hydrate crystallization. The best results were obtained with a combination of the additives SDS and THF. Then, the authors suggested that the association of a kinetic and a thermodynamic promoter may be used to enhance hydrate kinetics and reduce induction times. However, further studies to understand the action mechanism of how this synergy works are necessary.

Zhong *et al.* [90] also used THF as thermodynamic promoter in a GSHF process for $0.4CO_2 + 0.6CH_4$ mixture. Experiments were carried out at a fixed temperature of 277.15 K and in the pressure range of 2.8 – 6.7 MPa. It was found that higher driving force resulted in a reduction of the final gas uptake as well as a significant decrease of the CO_2 recovery and separation factor. Moreover, the impact of the driving force on CO_2 separation from the CO_2+CH_4 mixture indicated that the competition between CO_2 and CH_4 for hydrate cage occupancy became stronger with the increase of driving force. As a result, a lower pressure at the given

temperature is preferred for CO_2 separation from the CO_2+CH_4 mixture by hydrate formation in the presence of THF.

More recently, Xia *et al.* [87] tested TBAB in GSHF process to separate CO_2 from $0.45CO_2$ + $0.55CH_4$ mixture. The experiments were carried out at initial pressure of approximately 3 MPa, set temperature of 285.9 K and concentration of TBAB in initial aqueous solution of 30 wt%. At final process the CO_2 mole fraction in gas phase was reduced to 0.29 and the hydrate phase was composed of 73 mol% of CO_2.

It is important to observe that the available works in literature report few tests of promoters and rarely show the contribution of hydrate phase in CO_2 selective capture. Moreover in practically all studies in literature the operation conditions were at relatively high pressure (>2.5 MPa) and/or low temperature (< 278 K) even in presence of thermodynamic promoters. If on the one hand applying a high driving force allows reducing the induction time leading to a kinetic gain, on the other hand it causes more energy consumption and reduction on the final CO_2 capture selectivity, as stated by Castellani *et al*. [88] and Zong *et al.*[90].

Therefore, select new promoters and measure new hydrate formation conditions with CO_2, CH_4 and CO_2+CH_4 mixtures as well as study the effect of these promoters in a GSHF process for biogas at milder conditions of pressure and temperature are the main motivations of this work.

Chapter 2

Process Simulation of Biogas Upgrading Using Gas Separation by Hydrate Formation*

Résumé

Le principal objectif de ce Chapitre est d'analyser les perspectives pour l'épuration du biogaz à partir d'un procédé de séparation de gaz par formation d'hydrates (GSHF). Dans la première partie, des diagrammes d'enveloppe de phases ont été construits en utilisant le logiciel CSMGem. Ces graphiques ont permis d'évaluer la sélectivité du couple méthane - dioxyde de carbone dans la phase hydrate à faible concentration de H_2S. Les résultats ont montré que la présence de ce dernier gaz diminue la pression nécessaire pour la formation de la phase hydrate, ce qui indique que ce gaz a une forte préférence pour cette phase. Dans la deuxième partie, une simulation de procédé GSFH a été réalisée en termes de bilan de matière et d'énergie. Le procédé est composé de quatre étapes de cristallisation à une température fixe de 3 °C. Chaque étape est associée à une pression spécifique. Les données d'équilibre de composition de phase pour chaque étape ont été obtenues en utilisant le logiciel CSMGem. Cette procédure a permis de calculer le bilan de matière du procédé simulé. Le bilan énergétique du procédé a été établi également. Les résultats ont montré la difficulté de séparer le couple de CH_4/CO_2 en présence de H_2S par la formation d'hydrates de gaz. En sortie du procédé, le biogaz traité présente une concentration en méthane de 87,7%. La perte de ce gaz durant le procédé est d'environ 29,8%. Le bilan énergétique a montré que le procédé GSHF nécessite une grande quantité d'énergie par rapport aux autres procédés bien connus. L'utilisation de promoteurs de la phase hydrate pourrait diminuer cette demande énergétique et améliorer l'efficacité de séparation du procédé. Enfin, une sélection de promoteurs thermodynamiques à étudier dans la partie expérimentale de cette thèse a été réalisée. Les promoteurs sélectionnés sont le TBAB, le TBPB, le TBPO et le THP.

* Content publish at 8th International Conference on Gas Hydrates (ICGH 2014) as proceedings entitled " Study of a hydrate-based process for purification of biogas constituents"

Abstract
The main purpose of this C*hapter* was to offer some perspectives for biogas upgrading using a design of gas separation by gas hydrate formation process (GSHF). In a first part, phases envelope diagrams in isothermal conditions were built using the software CSMGem. These graphics made it possible to assess the selectivity of the couple methane – carbon dioxide in the hydrate phase in different low concentrations of H_2S. Results showed that the presence of H_2S decreases the pressure required for the formation of the hydrate phase, indicating that this gas has a major preference for this phase. In the second part, a process simulation for GSFH was performed in terms of mass and energy balance. The process was composed of four stages of crystallization working at a temperature of 3 °C. Each stage was associated to a specific pressure. The phase composition equilibrium data for each stage was obtained using CSMGem software. This procedure allowed to calculate the mass balance of the simulated process. The energy balance was also calculated. The results show the difficulty to separate the couple CH_4/CO_2 in presence of H_2S via gas hydrate formation. At the end of the process, the treated biogas presents a methane concentration of 87.7 %. The methane loss in the process is of about 29.8 %. The energy balance showed that the GSHF process require a high amount of energy compared to the other well-established processes. The use of hydrate promoters could decrease this energetic demand and improve the separation rate of the process. Finally, a selection of thermodynamic promoters to be studied in the experiments in this thesis was carried out. The selected promoters were TBAB, TBPB, TBPO and THP.

2.1 Objectives

Since the biogas is composed manly by methane and carbon dioxide, it is important to know how these gases interfere in the conditions of hydrate phase formation and the selectivity of each compound in this phase. At the same time, since hydrogen sulfide forms very stable hydrate at low pressure [152], it is important to know how much its presence impacts the formation of the hydrate phase and the efficiency of separation. Some studies dealing with the simulation of gas hydrate processes for CH_4/CO_2 separation have been published [13, 153]. However they did not take into account the presence of H_2S.

The objectives of the work of this *Chapter* were: (i) to study the selectivity of the couple CH_4/CO_2 in hydrate phase by construction of phases envelope diagrams in different concentration of H_2S in order to evaluate the parameters of a possible process separation; and (ii) to evaluate the mass and energy balance for a possible GSHF (gas separation by gas hydrate formation) process for biogas upgrading using a mixture of methane, carbon dioxide and hydrogen sulfide as a model biogas.

2.2 Method

The results presented in this work were obtained using the software CSMGem as provided in the reference [154]. This software was designed for thermodynamics computations involving hydrate phase and it uses Gibbs energy minimization method for the calculations. It makes possible to calculate the equilibrium condition needed for the formation of the hydrate phase for a given system composition and pressure or temperature. The hydrate formation predictions given by this software was compared to several hydrate formation data, showing a good accuracy [155]. Its algorithm uses flash calculation in order to obtain multi-phase equilibrium data. It uses a re-derived statistical thermodynamic model for hydrate phase assuming a system at constant volume. This model is coupled with the most recent models for the other phases.

For the first part of this study which is the construction of phases envelope diagrams, three systems were tested. *Table 2.1* presents the mole fraction of each system. Note that the water mole fraction was fixed to 0.9, in order to always have a liquid phase in presence. In systems 2 and 3, the concentration of H_2S in the vapor phase was fixed at 1 and 2 %, respectively. Therefore, the equilibrium data at the moment of formation of the hydrate phase was obtained for each combination of CH_4/CO_2 concentration.

It was decided to study these systems in isothermal process at two different temperatures: 3 and 5 °C. As a result, the diagrams were done in function of equilibrium pressure calculated from the model and the normalized mole fraction of one gas (CO_2 for example) in vapor and hydrate phase.

Table 2.1. Mole fractions of different system studied in this work.

System	H_2O	CH_4	CO_2	H_2S
1	0.9	0 – 0.1	0 – 0.1	0
2	0.9	0 – 0.099	0 – 0.099	0.001
3	0.9	0 – 0.098	0 – 0.098	0.002

In order to make diagram analysis easier, the composition of CH_4/CO_2 in each phase was normalized eliminating water and H_2S.

The process simulation of GSHF in terms of mass and energy balance was carried out in order to estimate the potential of this separation technique for biogas upgrading. In this simulation

the biogas was considered as a gas mixture containing the following concentration in mole: 59.4% of CH_4; 39.6% of CO_2; 1% of H_2S.

The configuration of the process was defined on the basis of some results found in literature and our results from the phases envelope diagram. Herri *et al*. [111] measured the equilibrium pressure for hydrate formation for a system containing water, methane and carbon dioxide at 4 °C and presented a phase envelope diagram for this system. Their results showed that the CH_4/CO_2 envelope curve is narrow and the separation by hydrate formation process for upgrading biogas will not be achieved by one step of crystallization, but will require a multi-stage process as also suggested by Dabrowski *et al*. [13]. There are two possible configurations for this process: the first is a cascade of tank crystallizer vessels, the process being controlled by a single pressure [5]. The second is the same cascade of tank crystallizer vessels, but with individual pressure process for each vessel. The simulation presented in this work used the second configuration, because the use of different pressures among each stage makes it possible to improve the separation rate. Indeed, since the composition of vapor phase changes from one stage to another, the pressure of hydrate formation also changes. The whole process was simulated using a temperature of 3 °C in order to decrease the pressure requirement of the process. The pressure for each stage was chosen in order to provide the best gas separation with the smallest possible loss of methane in the hydrate and liquid phase. The criteria used for choosing each condition of the process at each stage will be discussed later in this *Chapter*. The software CSMGem was used to calculate the equilibrium data in each stage.

To make easier the understanding of the mass balance, two variables were introduced: ω_i^j is the mole fraction of compound i at stage j in the flow entering stage j; β_i^j is the mole fraction of compound i at stage j after the equilibrium.

For energy balance of the simulated GSHF biogas was considered as an ideal mixture, i.e., constituted by gases that behave as ideal gases. The whole extensive properties of the mixture were then calculated by the weighted average of the sum of each property of the pure compounds (see *Equation 1.1*). The thermodynamic data of each compound was obtained from the online data base of NIST web-book [156] and in the books of Sandley [157] and Sloan and Koh [14].

$$\lambda_{mixture} = \sum z_i \lambda_i \qquad (2.1)$$

Where: $\lambda_{mixture}$ - mixture extensive property; z_i - mole fraction of compound i in the mixture; λ_i - extensive property of the pure compound i.

The condition of the biogas entering into the process was 30 °C and 1 bar. Incoming water was considered at a temperature of 15 °C. The hydrate phase formation enthalpies for methane, carbon dioxide and hydrogen sulfide were respectively 56.84, 65.22 and 28.4 kJ/mole.

The energetic efficiency of all equipments was estimated to 0.75 (ratio between the energy estimated and the energy demanded). The compression stage was considered as an isentropic process with an efficiency of 0.75. The energy of pumping the liquid and the agitation in the crystallizer tank corresponded to 5 % for the total energy. The energy needed in order to carry out each stage/step of the process (compression, cooling and heating) was always expressed on the base of mole of input biogas (mol_{bg}).

2.3 Results and discussion

2.3.1 Phase envelope diagrams

Figures 2.1 and *2.2* present the phase envelope diagrams for the couple CH_4/CO_2 in an isothermal system containing a 0.9 water mole fraction and variable H_2S mole fractions. It can be observed that the increase of H_2S concentration decreases the equilibrium pressure for hydrate phase formation. This can be explained by the fact that H_2S is an acid polar gas, which allows a stronger interaction with the network of water molecules of the hydrate. These interactions facilitate the stabilization of hydrate structure requiring low pressure for its formation. This result also indicates that H_2S has a major preference for hydrate phase, which allows to conclude to the possibility to use hydrate processes as a preliminary step in order to eliminate the hydrogen sulfide from biogas or other similar gas mixture.

It can also be observed in *Figures 2.1* and *2.2* that the saturation lines of vapor and hydrate phases are close, regardless of the presence or not of H_2S. This result indicates that there is no major preference of one gas to the hydrate phase even in presence of hydrogen sulfide. Indeed, observing carefully the diagrams, it is possible to see that CO_2 forms gas hydrate in a lower pressure compared to methane. Besides, with a higher solubility in liquid water compared to methane, it is evidenced that carbon dioxide has a slight preference to the hydrate phase. In this case, the biogas separation using gas hydrate process could also be treated as a CO_2 gas storage process.

These results are in accordance to those presented by Herri et al. [111]. These authors experimentally measured the equilibrium pressure for hydrate formation for a system containing water, methane and carbon dioxide. Although they have used the fixed temperature at 4 °C, their results are very close to those presented in *Figures 2.1* and 2.*2*.

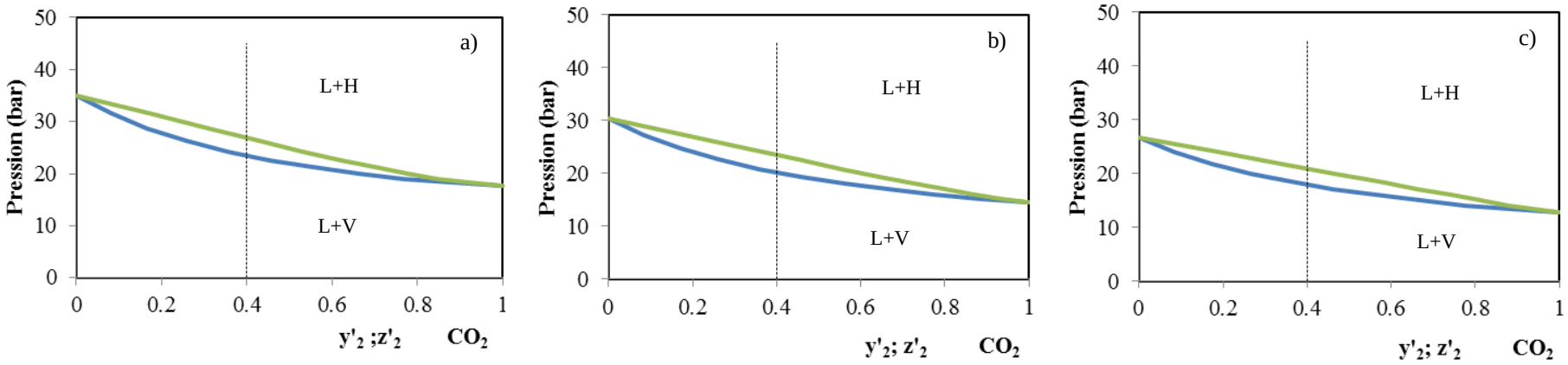

Figure 2.1. Phases envelope diagram for the couple CH_4/CO_2 in isothermal system at 3 °C containing 0.9 water mole fraction: a) system 1 without H_2S; b) system 2 with 0.001 H_2S mole fraction; c) system 3 with 0.002 H_2S mole fraction; green line, saturation line of hydrate phase; blue line, saturation line of vapor phase; y'_2 – normalized mole fraction of CO_2 in vapor phase; z'_2 – normalized mole fraction of fraction of CO_2 in hydrate phase.

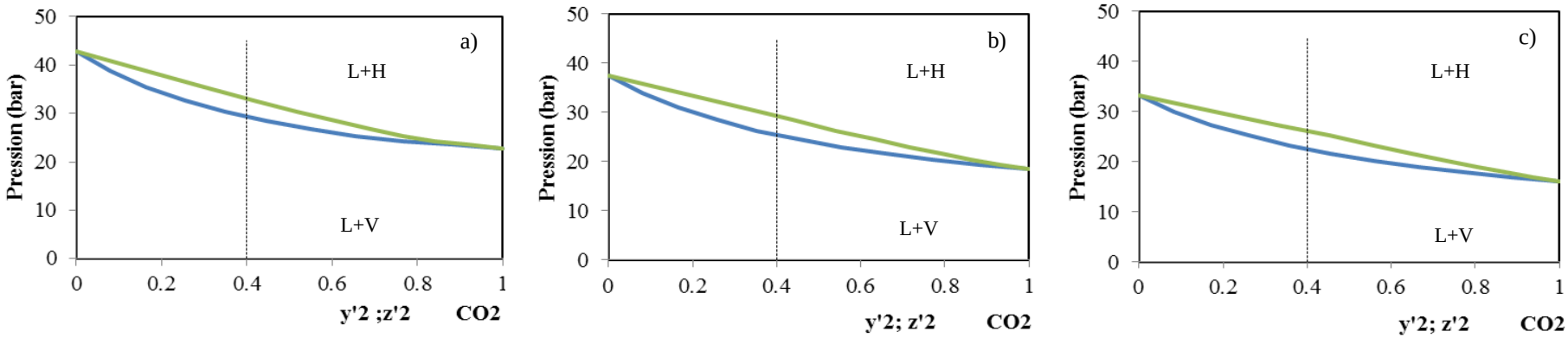

Figure 2.2. Phases envelope diagram for the couple CH_4/CO_2 in isothermal system at 5 °C containing 0.9 water mole fraction: a) system 1 without H_2S; b) system 2 with 0.001 H_2S mole fraction; c) system 3 with 0.002 H_2S mole fraction; green line, saturation line of hydrate phase; blue line, saturation line of vapor phase; y'2 – normalized mole fraction of CO_2 in vapor phase; z'2 – normalized mole fraction of fraction of CO_2 in hydrate phase.

The results presented in this study show that the separation by hydrates formation process for upgrading biogas may not be achieved by one step of crystallization but requires a multi-stage process as also suggested by Dabrowski et al [13].

2.3.2 Simulation of gas separation process

2.3.2.1 Mass balance

The *Figure 2.3* presents a simplified process flow diagram for the SGHF process that was simulated during this work. The whole process is composed by four stages, each one having different process conditions. The mass balance analysis has been made assuming a fixed number of moles of biogas (5000 moles) entering at stage 1.

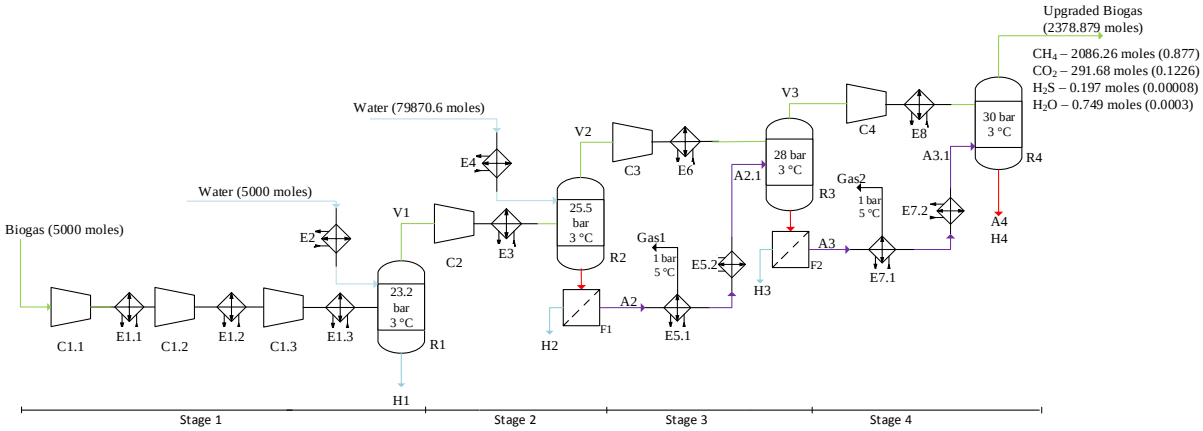

Figure 2.3. Simplified process flow diagram of GSHF process for upgrading biogas using a multi-stage crystallizer. In the figure: C – compressor; E – heat exchanger; R – crystallizer tank; F – filter; V – vapor phase; L – liquid phase; H – hydrate phase.

During the first stage, the objective was to maximize the amount of H_2S in the hydrate phase. As mentioned above, this gas forms very stable gas hydrates at low pressure and its removing is essential. Moreover, it has been noted that the higher pressure is, more gas hydrates are formed and more H_2S is trapped in the cavities. To form more gas hydrates, it was decided to convert all liquid water in hydrate, which means working in an hydrate-vapor biphasic system. The problem was to fix the pressure and water mole fraction to be used. Tests performed using the software CSMGem showed that, the higher mole fraction of water is ($\omega^1_{H_2O}$), the stronger the pressure is and more H_2S is eliminated in the hydrate phase (see *Figure 2.4*). However, the consequence was that more methane was also trapped in this phase, causing a higher methane loss in the process. *Figure 2.4* shows that more than 90 % of H_2S

can be enclathrated in the hydrate phase using a mole fraction of water of 0.7, but it will cause a methane loss of about 30%. The best combination, providing a good removal of H_2S without losing much methane, was a mole fraction of water about 0.5 and a pressure of 23.2 bars. These conditions made it possible to trap about 78 % of H_2S in the hydrate phase, as shown in *Table 2.2* and *Figure 2.4*. On the other hand, methane loss was about 11 % in this stage.

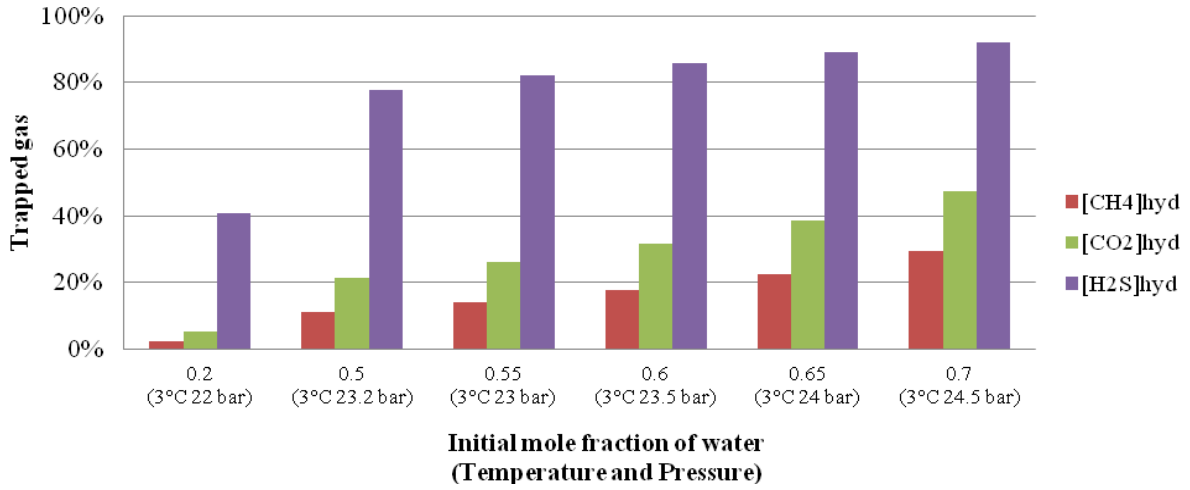

Figure 2.4. Percentage of trapped gas in the hydrate phase with respect to initial mole fraction of water ($\omega^1_{H_2O}$) in an hydrate-vapor biphasic equilibrium.

In stages 2, 3 and 4, the objective was to perform the separation of the CH_4 + CO_2 gas mixture. An addition of water was made at stage 2 (reminding that all water at stage 1 was converted in hydrate). Obviously the water added in the next stages will come from water recycling (from the following stages). This procedure allowed to save the energy from cooling system. After several tests using the CSMGem software, the amount of water needed at the second step is fixed to 79871 moles, providing a mole fraction about 0.95 ($\omega^2_{H_2O}$). This composition offers a good separation of the couple CH_4/CO_2. From calculations of equilibrium in the presence of high quantities of water showed an enhancement of the separation process due to the higher solubility of CO_2 in water compared to the methane.

The pressure used in stages 2, 3 and 4 was chosen in order to offer the best separation with gas hydrate formation with the smallest possible methane loss. Pressures slightly above the formation pressure of hydrate phase provided a good separation with a small methane loss.

At the end of stage 2 and 3 the liquid phase is depressurized and slightly heated in order to eliminate the dissolved gases (Gaz1 and Gaz2 in *Figure 2.3*). This procedure makes it possible to avoid that the CO_2 (major dissolved gas) returns to the process.

Table 2.2. Results in terms of mass for each stage of the simulated GSHF process.

Phase composition	Inlet		stage 1		stage 2[(1)]		stage 3		stage 4	
	mole	mole fraction	mole	β_i^1	mole	β_i^2	mole	β_i^3	mole	β_i^4
Vapor phase	5000	0.5	4205.5	0.421	3320.7	0.04	2718.74	0.033	2378.9	0.03
CH_4	2970	0.594	2636.4	0.627	2416.5	0.728	2215.1	0.815	2086.3	0.877
CO_2	1980	0.396	1556.4	0.37	900.4	0.271	502.2	0.184	291.7	0.122
H_2S	50	0.01	11.1	0.003	2.48	8×10^{-4}	0.601	2×10^{-4}	0.2	8×10^{-5}
H_2O	0	0	1.7	0.0004	1.2	4×10^{-4}	0.92	3×10^{-4}	0.8	3×10^{-4}
Liquid phase	5000	0.5	0	0	78515	0.93	77015	0.947	76332.6	0.962
CH_4	-	-	0	0	53	7×10^{-4}	63.31	8×10^{-4}	71.83	9×10^{-4}
CO_2	-	-	0	0	519.9	7×10^{-3}	377	5×10^{-3}	263.4	3×10^{-3}
H_2S	-	-	0	0	3.9	5×10^{-5}	1.2	2×10^{-5}	0.5	6×10^{-6}
H_2O	5000	0.5	0	0	77938.3	0.993	76573.6	0.997	75996.8	0.997
Hydrate phase			5794.5	0.579	2240.3	0.03	1582.8	0.02	669.3	0.008
CH_4	-	-	333.6	0.0576	166.8	0.075	143.5	0.091	66.7	0.104
CO_2	-	-	423.6	0.0731	136.2	0.061	73.3	0.046	22.5	0.034
H_2S	-	-	38.9	0.0067	4.7	0.002	1.0	2×10^{-4}	0.2	8×10^{-5}
H_2O	-	-	4998.3	0.8626	1932.6	0.863	1364.9	0.8623	576.96	0.8621

(1) input of 79871 moles of water in the system

As it can be observed in *Table 2.3*, at the end of the four stage separation process the methane mole fraction in the upgraded biogas is 0.877. To obtain a higher concentration more stages are needed, but at the expense of additional methane loss. The recovery was about 70.2 %, i.e., from 2970 moles of methane that entered the process 2086 moles was recovered in the upgraded biogas. Methane loss was essentially in the hydrate phase (711 moles, about 23.9 % of all methane). A useful solution to minimize this problem is to recover this methane in hydrate phase at the end of each step of crystallization by dissociation of the formed gas hydrates. However this will imply that CH_4 could be polluted by H_2S, for instance. This will obviously greatly depend on the kinetics of formation and dissociation of CH_4/CO_2 gas hydrates in presence of H_2S. This point will be essential to investigate the performances of the global process.

Several works have notified these negative points in gas separation using gas hydrates and proposed the application of hydrate promoters to improve the process parameters [91, 147, 158]. The use of thermodynamic and kinetic promoters can reduce the formation pressure of hydrate phase, improve the selectivity of the enclathration of one gas and accelerate the formation rate of hydrate phase. But they can have also some drawbacks, such as the decrease of enclathration capacities [13] which would raise the amount of water used in the process.

2.3.2.2 Energy balance

The *Table 2.3* presents the electrical energy set that must be provided for carrying out the compression steps in the SGHF process presented in this work. It may be observed that stage 1 represents the highest energy requirement. This is caused by the high pressure increase (from 1 to 23.2 bar) at the process entrance.

Table 2.3. Electrical energy set demanded for performing the compression steps in the SGHF process.

Stage 1 (kWh/mol_{bg})	Stage 2 (kWh/mol_{bg})	Stage 3 (kWh/mol_{bg})	Stage 4 (kWh/mol_{bg})	Total (kWh/mol_{bg})
4.997×10^{-3}	0.082×10^{-3}	0.0645×10^{-3}	0.0386×10^{-3}	4.848×10^{-3}

The energy needed for cooling purpose in the crystallizer tanks (energy required to compensate the thermal effect of hydrate phase formation) and the vapor and liquid phase is presented in *Table 2.4*. The cooling step for vapor phase consisted basically in dropping the temperature of the gas coming out from the compressor down to the target value, i.e., at 3 °C. It must be said that in the stage 1 it was only taken into account the cooling of the gas leaving the third compressor step. For the first and second compression steps it was considered that the gas was cooled (normally down to 20 °C) using water utility at 15 °C. This procedure allowed reducing the energy requirement of the cooling system at the stage 1. The higher energetic requirement in the cooling system for the stage 1 is justified by the highest compression ratio submitted to the gas in this stage which causes a higher temperature at the compressor outlet.

Table 2.4. Electrical energy set demanded for performing the cooling steps in the SGHF process.

	Stage 1 (kWh/ mol_{bg})	Stage 2 (kWh/ mol_{bg})	Stage 3 (kWh/ mol_{bg})	Stage 4 (kWh/ mol_{bg})	Total (kWh/ mol_{bg})
Vapor phase	1.954×10^{-3}	0.105×10^{-3}	0.0833×10^{-3}	0.051×10^{-3}	2.193×10^{-3}
Liquid phase	0.335×10^{-3}	5.356×10^{-3}	0.871×10^{-3}	0.844×10^{-3}	7.407×10^{-3}
Crystallizer tanks	3.513×10^{-3}	1.369×10^{-3}	0.946×10^{-3}	0.390×10^{-3}	6.217×10^{-3}

In the line of liquid phase are presented the energies required to reduce the water temperature down to 3 °C. In this process, the stage 2 needed the highest amount of energy, which is explained by the fact that in this stage the mole fraction of water is about 0.95 ($\omega^2_{H_2O}$), i.e., for each vapor phase mole entering inside the crystallizer tanks R2 there were 19 moles of water that should be cooled from 15 °C to 3 °C. In other words, this stage is characterized by the cooling of a high amount of water leading to a high energetic demand. On the other hand, in stage 1 the mole ratio of the incoming gas and water was about 1 requiring a small amount of energy for cooling the whole incoming water. For stages 3 and 4 the liquid phase was at a temperature close to 3 °C which explains the small energy requirement.

The last line of *Table 2.4* refers to the energy that the cooling system must provide to maintain the crystallizers at constant temperature during the gas hydrate formation. From the results, it can be observed that stage 1 requires more energy. In this stage, the whole amount of water is converted to gas hydrate. In other stages only small amounts of gas hydrate were formed, requiring therefore less energy from the cooling system.

Table 2.5. Parameters of different biogas upgrading techniques.

	Electricity demand [kWh/ mol_{bg}] x 10^3	Thermal demand [kWh/ mol_{bg}] x 10^3	Separation efficiency [% CH_4]	Methane loss [vol. %]	Pressure process [bar]	References
Pressurized scrubbing water (PSW)	4,5 – 6,1	0	98 – 99,5	0,5 – 2	5 – 10	[159-160]
Chemical absorption	1,4 – 3,4	6,8	99.9	0,1	0,1 – 0,4	[159-160]
Pressure swing adsorption (PSA)	4,5 – 5,7	0	90 – 98,5	1 – 5	4 – 7	[159-160]
Membrane	4,1 – 7,5	0	85 – 99	2 – 8	5 – 8	[159-160]
GSHF	21	0	87,7	29.75	23 - 30	This work

The parameters obtained in the simulated GSFH for biogas upgrading in this work were compared to well-established techniques in *Table 2.5*. The electricity demand was higher compared to other techniques and can be explained by the high pressure and by the constant use of cooling power. The methane loss was very high and as discussed above it can be solved by recovering the methane in a possible selective dissociation of the gas hydrates. It must be borne in mind that the simulation was a first approach, but it provides possibilities of improvements not only from the viewpoint of the separation efficiency, but also in energy consumption, for example by recovering the cold produced by hydrates dissociation.

Another important parameters of the process are the kinetics aspects, such as induction time and growth crystalline rate. Nevertheless, it couldn't be taken into account in the simulated process.

The use of thermodynamic promoters could reduce the number of stages, rise the separation efficiency, reduce the methane losses and reduce the operations cost. This is a field that was explored in this thesis. A selection of these compounds was therefore carried out and the results are shown in the next *Section.*

2.4 Selection of additives

The results obtained in this *Chapter* lead us to seek through results from literature some thermodynamic promoters that could improve the separation process for the couple CH_4/CO_2. Therefore, we carried out a selection of promoters using the following criteria: the ability of the additive to promote the formation of the hydrate phase by decreasing the pressure formation and increasing the temperature; low volatility; low toxicity; low impact to the environment.

The thermodynamic promoters participate in the structure of hydrate and can be divided in two groups [48]: those that do not change the classical structures of clathrates formed with water, such as tetrahydrofuran (THF), tetrahydropyran (THP), cyclopentane etc [91, 119, 161-162]; and those that change the water cages in the traditional clathrates structures, such as the tetra-n-butyl ammonium bromide (TBAB), tetra-n-butyl ammonium fluoride (TBAF), tetra-n-butyl phosphonium bromide (TBPB), tetra-n-butyl phosphonium chloride (TBPC) etc [51, 56, 101, 163-164].

Concerning the selection of thermodynamic additives, it was interesting to separate those which favor the formation of hydrate containing essentially CO_2, such as the peralkyl-ammonium salts (TBAB and TBAF) [125, 128-129, 137] and the peralkyl-phosphonium salts (TBPB and TBPC) [117, 132], from those that seem to favor the preferential insertion of CH_4: the tetrahydrofuran (THF) [97], the tetrahydropyran (THP) [119] and the tributylphosphine oxide (TBPO) [121, 165]. The TBAF, having a high toxicity was excluded as well as the TBPC because it wasn't found commercially available. THF being considered as air pollutant was also excluded. Therefore, the selected promoters were TBAB, TBPB, TBPO and THP.

However, we can note that supposed selectivity effect are often deduced from (*p*,T) phase equilibrium data measured in the presence of pure gases. Data concerning phase composition in presence of these same additives with mixtures of gases $CO_2 + CH_4$ are hardly found in literature, which makes efficiency evaluation of a possible separation process impossible in the present state of knowledge.

As far as we know at the moment of writing this work, there is no study on $CO_2 + CH_4$ gas separation by hydrate formation using TBAB, TBPB, TBPO or THP with phase composition measurements in all phases (hydrate, gas and liquid). With gas phase composition we can cite the studies provided by Xia *et al.*[136] and Acosta *et al* [135]. However, their works only

supplied gas phase composition at equilibrium point of hydrate formation. The other data available are only for phase diagrams [126, 137].

Chapter 3

Experimental Methods

Résumé

Dans ce Chapitre nous allons décrire les équipements et les procédures expérimentales utilisées pendant ce projet de recherche. La Calorimétrie différentielle à balayage a été utilisé pour mesurer les températures de dissociation et les enthalpies de dissociation des hydrates simples (promoteur + eau) et d'hydrates de gaz avec les promoteurs. L'étude du procédé de séparation de gaz par la formation des hydrates de gaz (GSHF) ainsi que la mesure de la capacité de stockage de gaz par les hydrates de THP/CO_2 et THP/CH_4 ont été réalisés dans un réacteur instrumenté à haut pression. Les critères pour ces études sont expliqués. Les procédures expérimentales sont également décrites. Un ensemble d'équations basé sur les bilans de matière sont proposés pour caractériser la composition des phases à l'équilibre. Les incertitudes ont été déterminées en appliquant la méthode de propagation d'incertitude.

Abstract

In this *Chapter* we describe the equipments and the experimental procedures used during this research project. Differential scanning calorimetry (DSC) was used to measure the dissociation temperatures and dissociation enthalpies for simple promoter hydrate at ambient pressure and for mixed promoter/gas hydrates. The study of gas separation by hydrate formation (GSHF) as well as the estimation of gas storage capacity for THP/CO_2 and THP/CH_4 gas hydrates were performed in an instrumented high pressure cell. The criteria for these studies are explained. The experimental procedures are also described. A set of equation based on mass balance are proposed for characterizing the equilibrium phase composition. The expanded uncertainties are determined using the uncertainty propagation method.

3.1 Materials

The chemical compounds were purchased from Alfa Aesar and Sigma Aldrich while the gases were purchased from Air Liquide. *Table 3.1* summarizes all materials used during the experiments. All solutions were prepared using gravimetric method in an analytical balance (Metler Toledo AW205) with precision of 10^{-5} g. Deionized water (Millipore Elix S) was used to prepare the solutions. The promoters tetrabutylammonium bromide (TBAB), tetrabutylphosphonium bromide (TBPB) and tributylphosphine oxide (TBPO) are in solid phase at 20 °C while the tetrahydropyran (THP) is in liquid phase having a boiling point of 88 °C. *Table 3.2* shows more properties of these compounds.

Table 3.1.Materials used in the experiments.

Material	Supplier	Purity*
Carbon dioxide	Air liquide	$x_{CO_2} > 0.9995$
Methane	Air Liquide	$x_{CH_4} > 0.9999$
Helium	Air liquide	$x_{He} > 0.999$
TBAB	Alfa Aesar	$w_{TBAB} > 0.99$
TBPB	Alfa Aesar	$w_{TBPB} > 0.98$
TBPO	Sigma Aldrich	$w_{TBPO} > 0.95$
THP	Sigma Aldrich	$w_{THP} > 0.99$
LiCl	Sigma Aldrich	$w_{LiCl} > 0.98$

*x: mole fraction; w: mass fraction

Table 3.2. Properties of thermodynamic hydrate promoters.

	TBAB	TBPB	TBPO	THP
Formula	$(CH_3CH_2CH_2CH_2)_4N(Br)$	$(CH_3CH_2CH_2CH_2)_4P(Br)$	$[CH_3(CH_2)_3]_3P(O)$	$C_5H_{10}O$
Molecular weight (g/mol)	322.27	339.33	218.32	86.13
Chemical structure	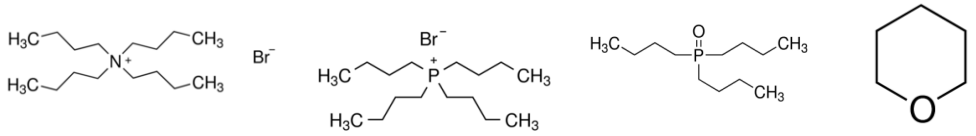			

3.2 Differential scanning calorimetry analysis

3.2.1 Overview

Differential scanning calorimetry (DSC) consists in measuring continuously the heat flow exchanged between a sample and a thermostat submitted to a thermal program. In order to eliminate the instabilities causes by other factors than the physical transition of the studied samples, the reference signal obtained from an empty cell is subtracted from the signal of the sample cell submitted to the same temperature variations. The temperature difference between sample and reference sample cell is recorded as a direct measure of the difference in the heat flow rates to the sample and the reference sample cell [166].

The differential signal is the essential characteristic of Differential Scanning Calorimeter. The capacity to operate in dynamic mode is another characteristic and for that, it is distinguished from most classic calorimeters. Experiments using DSC can be carried out by applying various "modes of operation": constant temperature constant rate cooling or warming, modulated rate cooling or warming [167], and stepwise cooling or warming. This technique allows to determine the heat capacity of the sample during a heating program and, if phase transition takes places, DSC thermogram provides the measurement of latent heat (for hydrate systems we will call dissociation enthalpy). The phase transition temperature can also be established.

DSC is also a rapid and sensitive technique, widely used for characterization of phase transition. The Department of Chemical and Chemical Engineering at Ensta ParisTech have developed and validated over the years protocols for studying hydrates, mainly regarding measurements of dissociation temperatures and enthalpies [85-86, 168-171]. Dalmazzone *et al*. [170] validated this technique by measuring the dissociation temperature of methane clathrate in different sodium chloride aqueous solutions. They showed that it is possible to measure hydrate phase transition not only at atmospheric pressure but also at high pressure for gas hydrate formation. Their results were compared to the literature showing a good agreement.

This method is faster than the PVT method and has the advantage of using very small amount of sample. The main limitation of this technique is the lack of agitation, which makes quantitative measurements difficult.

It must be borne in mind that in DSC apparatus what is measured is the heat flow that the differential system changes with the furnace during the thermal program (warming, cooling or isothermal steps). The temperature probe is not in contact with the sample, but it is located in the furnace and monitors the experimental temperature. Therefore, the measurement of the exact temperature in the sample cell is made indirectly. For that, a calibration temperature protocol must be carried out in order to compensate the temperature lag between programmed temperature (T_P) and the temperature of sample. This protocol consists in using pure compounds (also called calorimetric standards) for which the solid to liquid phase transition temperature is very well known. The difference between the measured temperature (T_M) and the known melting temperature of the calorimetric standards (T_S) is used to determine the correction function (*Equation 3.1*). The calibration protocol must be performed at various scanning rates ($\alpha = dT_P/dt$) because this parameter has to be accounted for:

$$T_S - T_M = A + BT_M + C\alpha + D\alpha^2 \qquad (3.1)$$

The parameters *A*, *B*, *C* and *D* of *Equation 3.1* are adjusted to fit with the calibration results. The parameters *B* and *C* being dependents of the heat capacity and conductivity of the sample cell, it is strongly advised to repeat the calibration protocol every time that the cell is changed.

3.2.2 Equipment

For the measurements of dissociation temperatures of gas hydrates, the equipment HP-µ DSC VII (SETARAM), which was specially developed for this purpose, was used. *Figure 3.1* presents a scheme of this equipment.

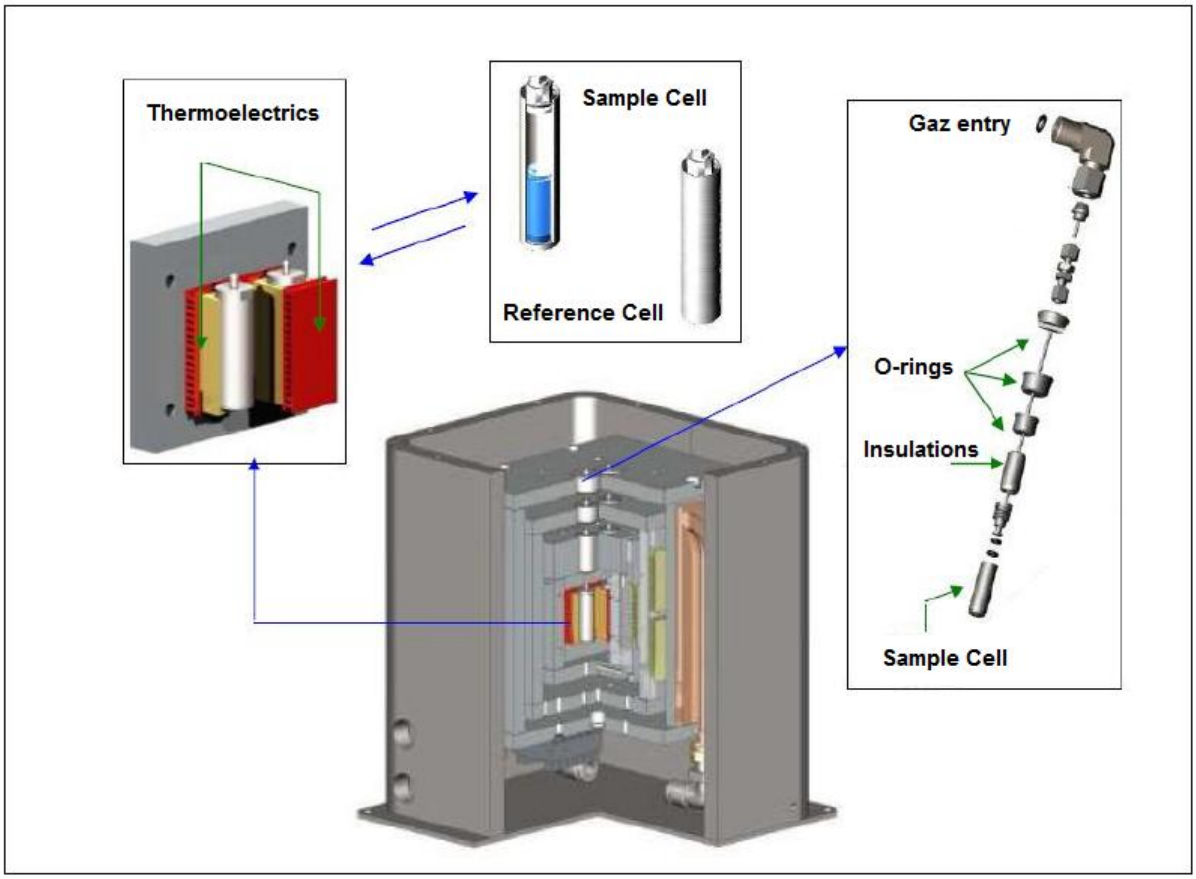

Figure 3.1. Schematic presentation of HP-μ DSC VII (SETARAM).

Two high pressure Hastelloy cells (a sample cell containing the liquid solution and a reference cell that was left empty) were placed in the temperature-controlled DSC furnace. For experiments involving gases, the sample cell was connected to a gas cylinder (*Figure 3.2*). The pressure inside the sample cell was controlled by a pressure-regulating valve and measured using a pressure transducer GE DRUCK (PTX-7800) with a resolution of 0.05 MPa in a 0.1 to 70 MPa pressure range. A cooling bath was used to remove heat from the equipment during the experiments.

The equipment was temperature calibrated in the range of interest for hydrate studies (from 234 to 353 K) using the melting of high purity mercury and naphthalene samples at heating rates α of 0.2, 0.5, and 1.0 $K \cdot min^{-1}$. Ice melting was used to determine the uncertainty of the measured phase change temperatures and enthalpies, which were found to be ± 0.04 K and ± 3 %, respectively.

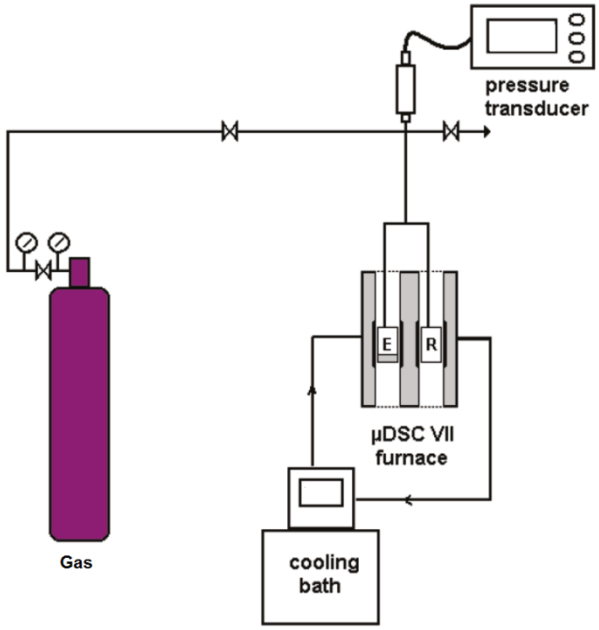

Figure 3.2. DSC experimental dispositive. E: sample cell; R: reference cell [172].

3.2.3 Experimental protocols

In all experiments, the cleaned and dried sample cell was filled with 30-60 mg of promoter solution in water at the desired concentration. Then the cell was inserted into the DSC furnace, connected to the gas line and purged several times to eliminate the remaining air. The set pressure was achieved using the pressure-regulating valve. For experiments without gas (atmospheric pressure), the gas cylinder was closed and the purge valves were kept open.

The dynamic and stepwise methods were used to measure the dissociation temperatures. In both methods the first step consisted in crystallizing all sample into the cell. For that, the system was cooled down from 293.1 K to 248.1 K at a rate α of 1 K.min^{-1} and kept at 248.1 K during 20 minutes to ensure the complete freezing of the liquid. In dynamic method, the temperature of the sample was increased from 248.1 to 298.1 K at a constant heating rate α of 0.2 or 0.5 K.min^{-1}. For stepwise method, the temperature of sample was raised at 1 K min^{-1} from 248.1 K to a temperature which is at most 0.6 K lower than the dissociation temperature. The temperature was then increased by steps of 0.1 K with isothermal intervals of 3-5 h between each step. The typical heat-flow profiles obtained in this work by using these methods are presented in *Figures 3.3* and *3.4*.

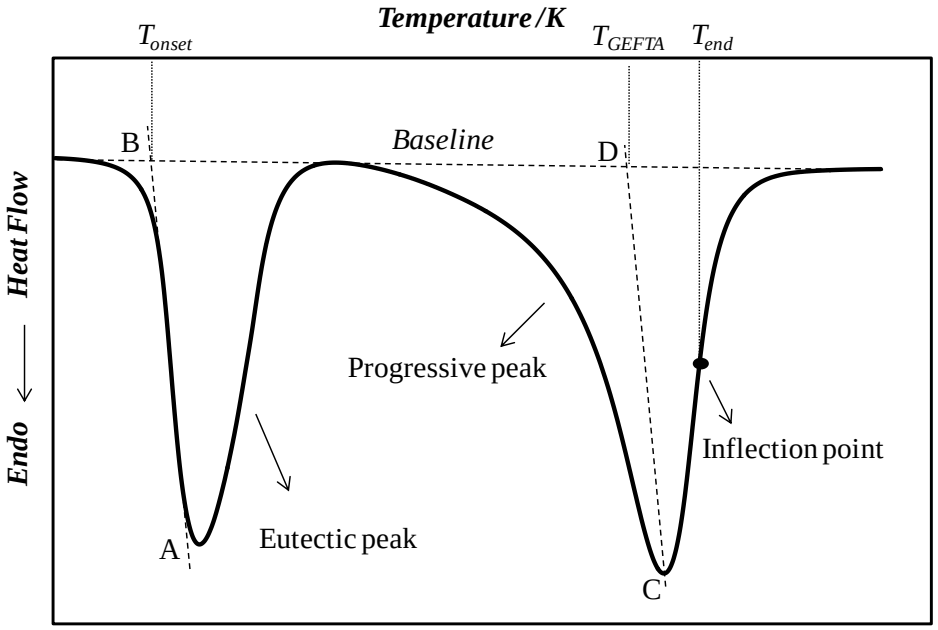

Figure 3.3. Determination of phase change temperatures from heat flow peaks obtained by DSC in dynamic method.

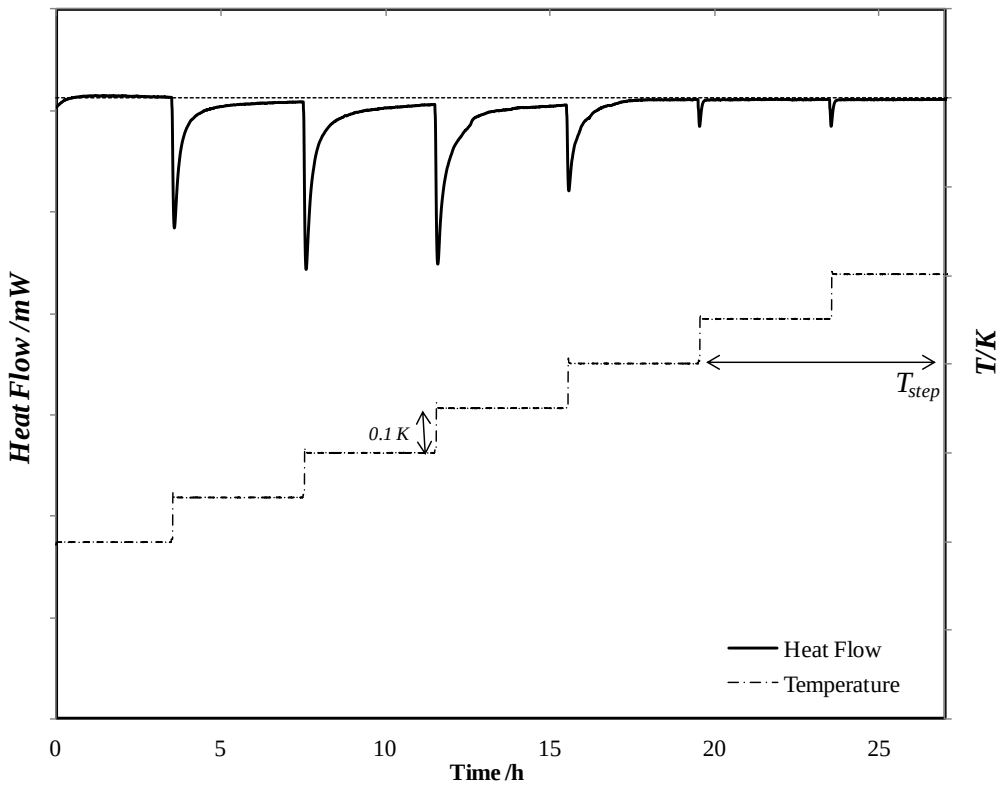

Figure 3.4. Determination of melting temperature from DSC stepwise method.

For dissociation enthalpy measurements (ΔH_{Diss}^{DSC}) the total conversion of aqueous solution into solid phase is necessary. However, this is difficult to achieve in the case of gas hydrates, due to specificities of DSC. In addition to the lack of stirring inside the cell, the first drawback is the weak solubility of gas in the liquid phase, which limits the interfacial mass transfer required to form the gas hydrate phase. The second aspect is due to the higher degree of super cooling needed to form the gas hydrate phase which favors the formation of metastable gas-free solids, such as ice or simple promoter hydrate. As a result in order to maximize the hydrate production and eliminate the metastable phases, the multiple cooling-heating cycles protocol described by Martinez *et al.* [83] was tracked.

For each cycle the sample was cooled down to 248.1 K (T_L) at cooling rate of 1 K min^{-1} and kept at this temperature for 20 minutes. Then the sample was heated at scanning rate of 2 K min^{-1} to a temperature T_H lower than the dissociation temperature of the most stable hydrate. The temperature of the sample was then maintained at T_H during 20 minutes and a new cycle was started (see *Figure 3.5*). The disappearance of the free water results in a reduction of the size of the peaks of crystallization and melting of the ice and/or metastable phases cycle after cycle. In the meanwhile, the stable hydrate accumulates during the global process. After the last cycle, the sample was heated to 298.1 K at heating rate α of 0.2 K min^{-1} and the dissociation enthalpy was measured. The number of cycles required to obtain a good peak resolution allowing measurement of the dissociation enthalpy was determined experimentally. When necessary we also used the multi-cycle protocol in order to eliminate the metastable phases and improve the resolution the melting peak allowing us to establish more precisely the dissociation temperatures. In literature other authors have used multi-cycle protocol in order to measure enthalpy or obtain a better peak resolution for phase transition temperature measurements [73, 83, 126, 173].

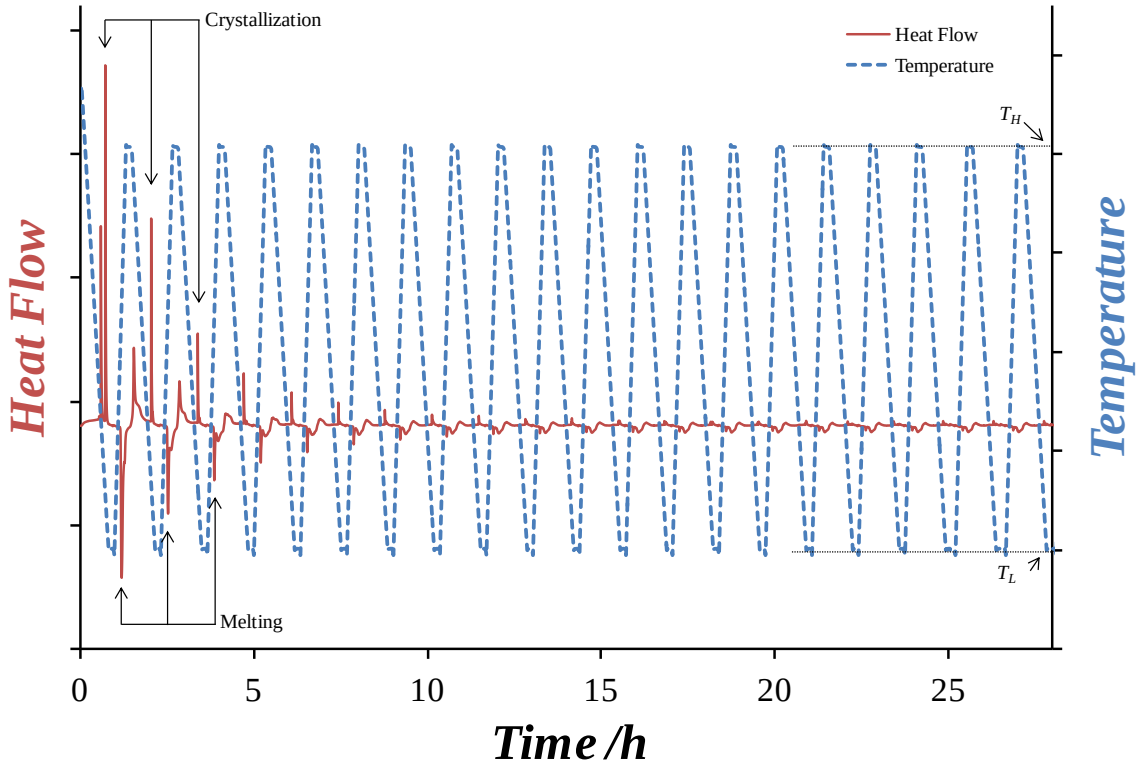

Figure 3.5. Multiple cooling-heating cycles protocol.

Figure 3.6 represents a typical DSC thermogram used to measure the dissociation enthalpy (ΔH_{Diss}^{DSC}). It corresponds to the value of the area obtained from the integration of the heat flow signal between the beginning and the ending of melting peak.

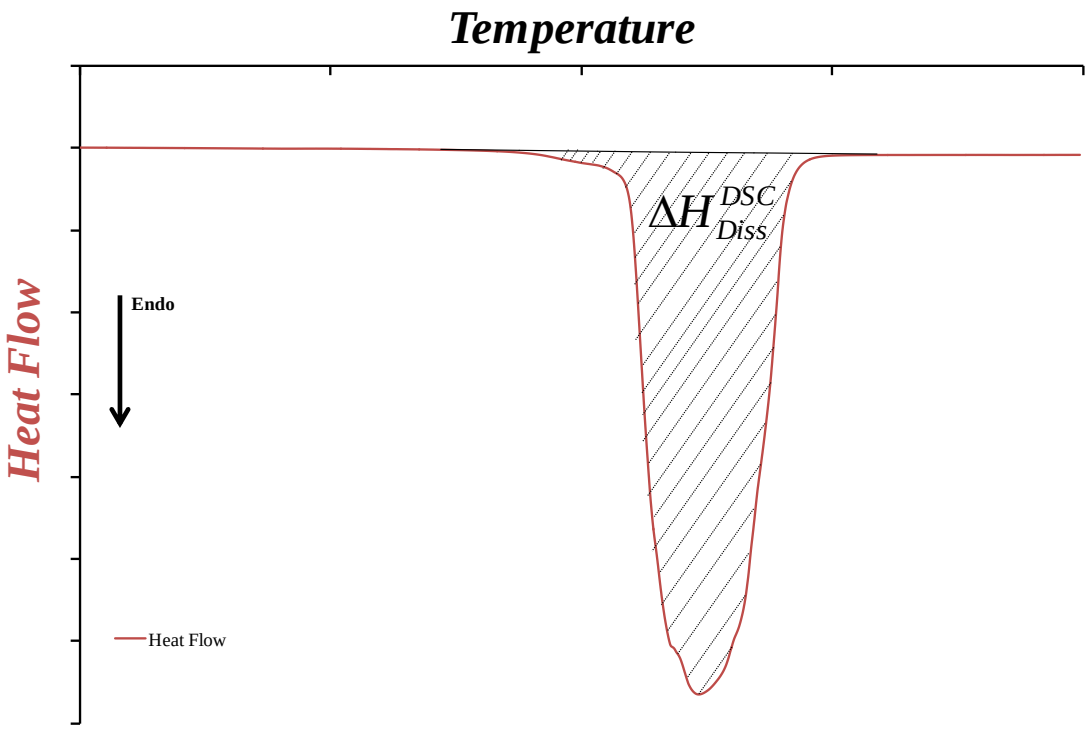

Figure 3.6. Determination of dissociation enthalpy ΔH_{Diss}^{DSC} from a DSC thermogram.

3.2.2.1 Dissociation temperatures measurement

The analysis of the thermograms obtained from the dynamic and stepwise methods (*Figures 3.3* and *3.4*, respectively) allowed us to measure the temperatures of phase transition of the studied systems.

For pure, eutectic or stoichiometric compositions the phase transition occurs in isothermal condition and the T_{onset} was used to determine the melting temperature. This temperature corresponds to the intersection of the auxiliary line through the descending peak slope (dashed line AB in the *Figure 3.3)* and the baseline. This auxiliary line tangents the inflection point in the descending peak slope.

The simple promoter hydrate and the mixed promoter/gas hydrate present essentially incongruent melting at all studied conditions (promoter composition and gas pressure). As a result, the thermograms from dynamic method present a progressive peak and the measured melting point represents the temperature at which the last solid vanishes. In such case, there remain some controversy on which method should be used to measure the dissociation temperature. Three methods were proposed:

T_{GEFTA}*:* corrected peak temperature proposed by the German Society for Thermal Analysis (GEFTA) [174]. It corresponds to the intersection point between the baseline and the dashed line CD which is parallel to the dashed line AB (see *Figure 3.3*). Using this method, it is assumed that the end dissociation occurs at *extremum* peak temperature taken into account the delay response of heat flow signal.

$T_{end}(\alpha = 0)$*:* inflection point extrapolated at null heating rate. Kousksou *et al.* [175] proposed that after scanning the sample at various heating rate, the extrapolation of the inflection point T_{end} (*Figure 3.3*) at null heating rate should provide the end melting temperature. In our work, we repeated the measurements at heating rate α of 0.2 and 0.5 K.min^{-1}, then extrapolated T_{end} to $\alpha \rightarrow 0$ (See *Figure 3.7*).

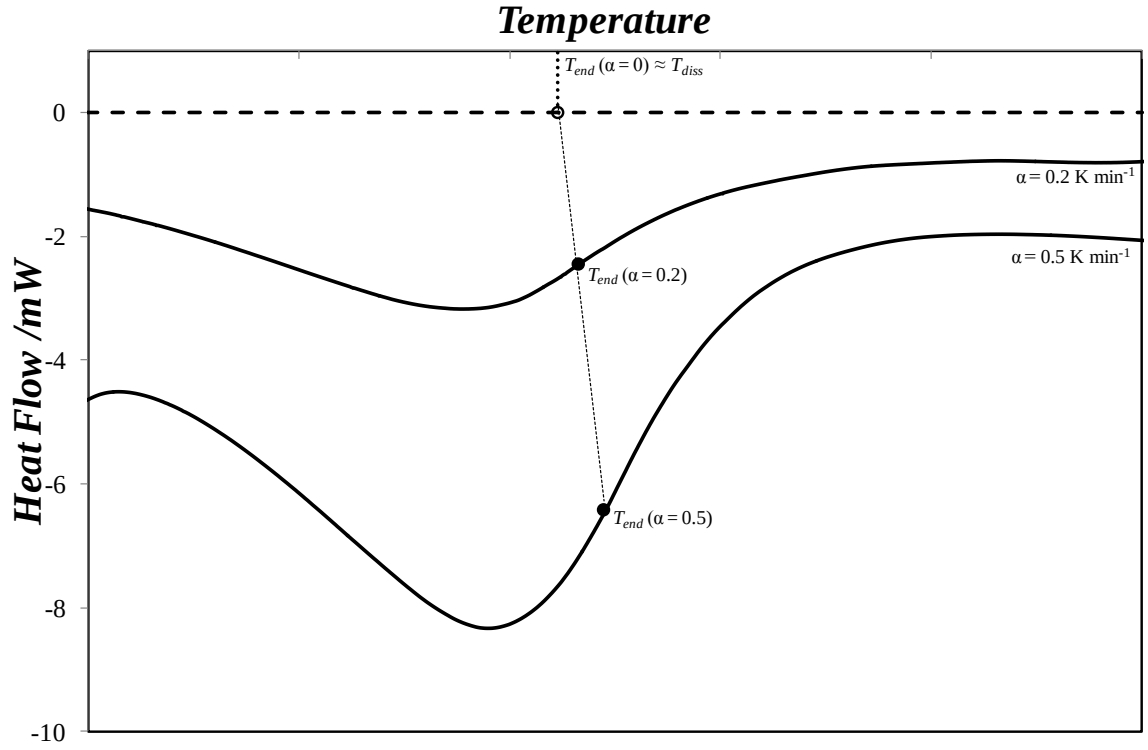

Figure 3.7. Determination of dissociation temperature (T_{diss}) by using T_{end} characteristic temperature; α is heating rate.

T_{step}: final step temperature [171, 173, 176-177]. This characteristic temperature is obtained using stepwise method, in which the sample is heated by steps of 0.1 K until complete melting. The dissociation temperature is associated to the last step temperature showing endothermic melting signal (see *Figure 3.4*). This method is more precise and robust compared to the other two. Nevertheless, the main drawback is that one experiment takes several tens of hours. In our experiments, at least 3 hours of isothermal plateau were required

to achieve the equilibrium at each step (the increment temperature being very small, the driving force for melting the solid is equally weak).

A study involving semiclathrates using DSC technique was done by Lin *et al.* [171]. They evaluated the accuracy of each characteristic temperature (T_{GEFTA}, $T_{end}(\alpha = 0)$ and T_{setp}) by measuring the dissociation temperatures of tetra-n-butyl phosphonium bromide (TBPB) semi-clathrates and the melting point of ice in presence of sodium chloride (NaCl). They showed that the T_{step} has the highest accuracy followed by $T_{end}(\alpha = 0)$ and T_{GEFTA}.

The choice of the method for equilibrium temperature determinations was made depending on the complexity of each system. *Table 3.3* summarizes the methods applied for all the cases encountered.

The TBPB systems were relatively the simplest, because the thermograms obtained from dynamic method made it possible to explore $T_{end}(\alpha = 0)$ or T_{GEFTA}. In these systems we prioritized $T_{end}(\alpha = 0)$ for being more accurate than T_{GEFTA}. In TBPO systems, we also prioritized $T_{end}(\alpha = 0)$. However, in cases where the inflection point was hard to distinguish due to the possible presence of metastable phases [173], multiple cooling-heating cycles were applied and T_{GEFTA} and T_{step} were used to define the dissociation temperature. Finally, THP systems were the most complex, the hydrate dissociation occurring in a liquid-liquid demixtion region. Therefore we decided to apply the stepwise method in all conditions.

Table 3.3. Characteristic Temperatures used to establish the dissociation point for each system.

System		Characteristic Temperatures			
Promoter		T_{onset}	T_{GEFTA}	$T_{end}(\alpha = 0)$	T_{step}
TBPB	+ H_2O	O		O	
	+ H_2O + Gas		O	O	
TBPO	+ H_2O	O		O	O
	+ H_2O + Gas		O	O	O
THP	+ H_2O	O			O
	+ H_2O + Gas				O

The uncertainty of T_{step} was considered equal to the increment temperature at each step, i.e., 0.1 K. For $T_{\mathrm{end}}(\alpha = 0)$ and T_{GEFTA}, the uncertainties of 0.4 K and 0.5 K, respectively, were defined taken into account the study of Lin *et al.* [171]. Besides, the results obtained in our

work by these two methods showed no more than 0.4 K deviation compared to the highest accurate method *Tstep* (see *Table 4.10*). The relative uncertainty of dissociation enthalpy was estimated based on the calibration of the equipment, i.e., 3 %.

3.3 Measurements in instrumented reactor

In this section we describe the equipments and the experimental procedures that were used to evaluate the selected promoters in GSHF process.

3.3.1 Equipment

The equipment that was used for the study of gas separation and gas storage capacity (*Figure 3.8*) is a high pressure reactor developed by ARMINES/CTP (France). It is composed of a cylindrical equilibrium cell having two sapphire windows, which allow visualizing the phase behavior. This cell is made of stainless steel (Type X6NiCrTiMoVB25152 / Alloy 286) to withstand hydrogen embrittlement and can be operated at a pressure up to 40 MPa and temperature range of 233-373 K. Its inner volume was found to be equal to 206.0 ± 1.5 mL. The cell contains a strong agitation system, gas and liquid inlet and outlet connections, as well as temperature and pressure probes. Temperature inside the reactor was measured by a platinum probe (PT 100) with an uncertainty of 0.02 K. The measurement of pressure was made by two calibrated pressure transducers (GE DRUCK, PTX 611), one for low pressure (LPT) range (5 MPa ± 0.15 % full scale) and the other for high pressure (HPT) range (40 MPa ± 0.15 % full scale). A data acquisition unit (AIOP, PC10) connected to a personal computer assures the recording of pressure and temperature data. The continuous recording of pressure and temperature makes it possible to detect any phase transition as well as the equilibrium conditions. The temperature of the cell was controlled by a thermostatic bath (Tamson Instruments, TV4000 LT) equipped with glass windows to allow observing the interior of the reactor during experiments.

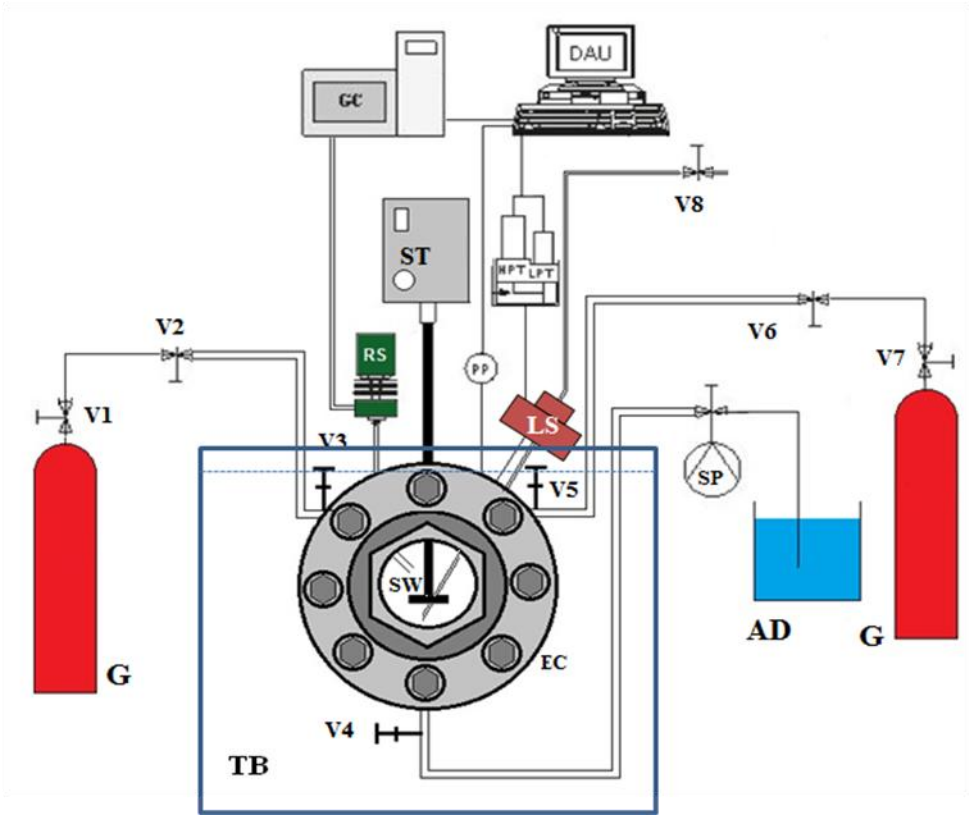

Figure 3.8. Scheme of the high pressure reactor for hydrates studies. AD - additive solution; DAU - data acquisition unit; EC - equilibrium cell; G - gas cylinder; GC - gas chromatograph; HPT - high pressure transducer; LPT - Low pressure transducer; LS - Liquid sampling; PP - platinum probe; RS - gas sampling Rolsi™ system; SP - syringe pump; ST - stirring system; SW - sapphire window; TB - thermostatic bath; V1-V7 - feeding valves;V8 - mircovalve.

The reactor has an automatic gas sampling system and a manual liquid sampling system. The system allowing sampling in gas phase consists of an electromagnetic online micro sampler (rapid on-line sampler-injector: ROLSI™) developed at ARMINES/CTP [178-179]. It is connected to a gas chromatographer (Perichrom PR2100) allowing the instantaneous analysis of the sample. *Figure 3.9* shows the schematic representation of this gas sampling system. The transfer line is heated to a temperature above that of the equilibrium cell to avoid the condensation of the components in the gas sampled. A continuous stream of carrier gas drives the sample into the GC. A ROLSI controller unit sets the temperature of the sampling valve and the transfer lines. This controller makes it possible to actuate the ROLSI controlling the valve's opening time with a resolution of 0.01s.

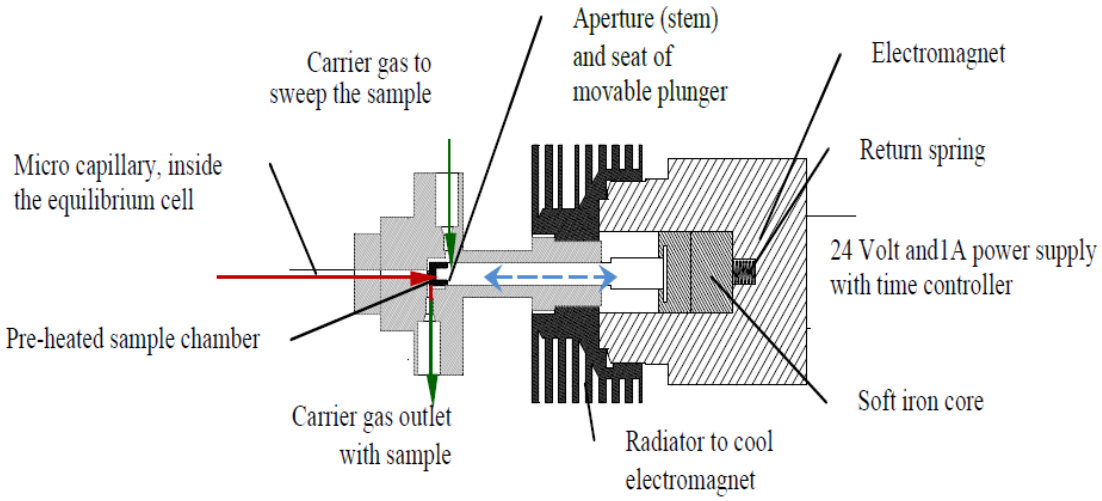

Figure 3.9. Schematic representation of the gas sampling ROLSI system [180].

Liquid sampling is performed through a tube installed inside the equilibrium cell. Sampling is carried out by the difference between the pressure inside the reactor and exterior, which allows the ascension of the liquid. A mircovalve ensures that a very tiny amount of liquid is taken. The liquid entrance of this tube contains of sintered metal to filter the liquid avoiding that crystals of hydrate are also taken. For proper liquid sampling a minimum volume of 60 mL of liquid phase in the reactor was necessary. Smaller volumes could not be in contact with the liquid sampler and gas phase could be lost at the moment of sampling.

3.3.2 Procedures for gas separation by gas hydrate formation study

3.3.2.1 Defining the overall protocol for clathrate formation

Before starting the reactor experiments, it was necessary to define the operation conditions of pressure, temperature and the initial promoter mass fraction. For that reason, information about phase equilibrium is needed. Since our objective was to form only promoter/gas hydrate, we need to know the stability regions limits for each system. Let's take the example of the systems CO_2+TBAB+H_2O and TBAB+H_2O which experimental data of phase transition are shown in the *Figure 3.10.* From these data, if we decided to use as operation condition the mass fraction of 0.25 and CO_2 pressure of 2 MPa, our set temperature (T_{set}) has to be higher than 284 K and less than 289.9 K to form only TBAB/CO_2 hydrate. In *Chapter 4* we will present more information about the stability limits of hydrates for the studied promoters.

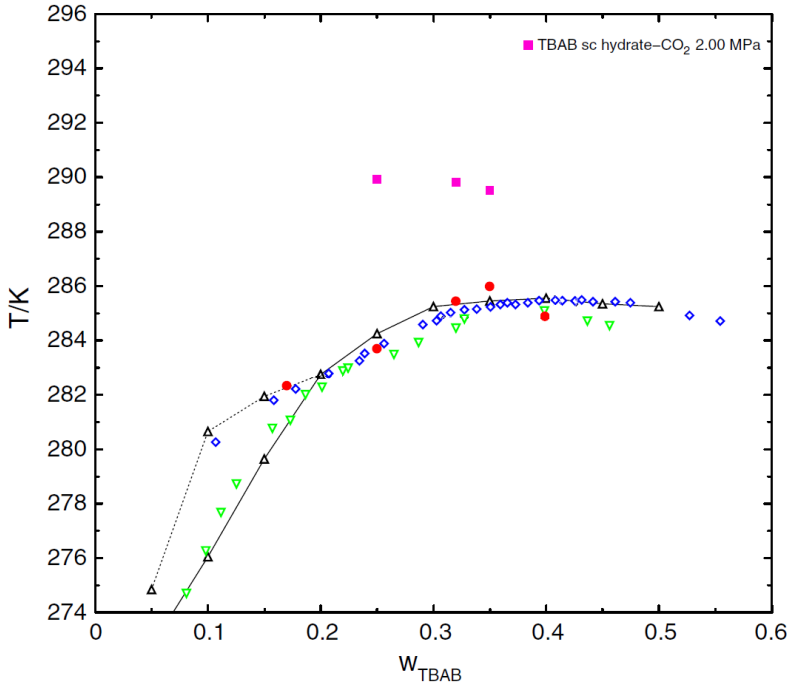

Figure 3.10. Phase diagram for TBAB semi-clathrate and CO_2/TBAB semi-clathrate. experimental data: black triangles [115]; green triangles [101]; blue lozenges [99]; red circles [126]; rose squares [126]. According to Darbouret [115] the solid line refers to TBAB semi-clathrate type A and the dashed line refers to the type B. (adapted from Deschamps & Dalmazzone [126]).

It must be borne in mind that in hydrate-based process it is recommend forming liquid-hydrate slurries in order to facilitate the transfer of the fluid using a liquid pump. A high initial mass fraction of promoter may provide a high solid content in the slurry and increase the viscosity, thus impeding the transfer [181]. Based on this constraint, we decided to use as reference an aqueous solution of TBAB at w_{TBAB} = 0.10. In this composition, the maximum solid content is 31.20 % of TBAB.38H_2O + gas hydrates [57]. By fixing this maximum solid content, we established the initial mass fraction for the other promoters taking into account their respective hydrate composition. *Table 3.4* summarizes the used initial promoter composition in the experiments.

Table 3.4. Initial aqueous promoter composition used in the experiments; υ is the hydration number.

Promoter	wt %	mol %	Max. solid content	υ
TBAB	10.00	0.617	31.20%	38 [57]
TBPB	10.35	0.793	31.20%	38 [105]
TBPO	8.12	0.724	31.20%	34.5 [106]
THP	6.86	1.516	31.20%	17 [119]

Once fixed the initial promoter composition, we had to define the operating gas pressure. The mild conditions pressure (2.2 MPa) and temperature (T_{set} = 281.1 K) were chosen in order to enhance the applicability of the GSHF process. Other authors studying the CO_2 separation from CO_2 + CH_4 mixture by gas hydrate formation used more severe experimental pressures (above 2.2 MPa) and temperatures (below 281.1 K) [87-91, 161].

Following these criteria and respecting the constraints we carried out some tests in order to define the more appropriate experimental protocol. The previously cleaned and dried equilibrium cell was first evacuated with a vacuum pump to eliminate the remaining air inside. The thermostatic bath was programmed to maintain a constant initial temperature of 291.6 K in the cell. The gas phase was then inserted from the corresponding cylinders through a pressure-regulating valve and suitable time was left for pressure stabilization. In the case of two gases (CO_2 and CH_4), the gas mixture was prepared directly in the cell, starting with CO_2 until a determined pressure (p_{CO2}) was reached. After temperature stabilization CH_4 was fed in until the pressure set for the experiment was reached. The CO_2 + CH_4 mixture inside the cell had a composition of 39.0 ± 0.8 mol% of CO_2 simulating a typical biogas from agricultural wastes [8-10]. This composition was checked using a gas chromatograph GC (Perichrom, PR2100) coupled to the gas sampling ROLSI^{TM} system. A volume of 60 ± 0.5 ml of additive aqueous solutions at desired concentration was inserted into the cell using an ISCO syringe pump. The agitation was then turned on at 600 rpm, provoking a slight pressure decrease due to the dissolution of the gases in the liquid phase. The system was at kept constant conditions during at least 120 minutes for complete dissolution of the gas.

From this point we tested 3 protocols, which profiles of temperature and pressure are presented in *Figures 3.11* and *3.12.* After the gas dissolution, the protocol 1 (*Figure 3.11a*) consisted in decreasing directly the temperature down to T_{set}. The crystallization was confirmed by a sudden temperature increase followed by the pressure drop due to the gas

consumption. The main drawback of this protocol is that the chosen operation conditions ($p \approx$ 2.2 MPa and T_{set} = 281.1 K) provide a small driving force resulting in a high induction time (more than 12 h). Having such high induction time, the crystallization takes place generally during the night. Therefore, monitoring of gas phase evolution during the hydrate formation is difficult because the gas sampling must be actuated only during the hydrates formation in order to limit the perturbation of equilibrium due to multiple sampling. In the protocol 2 (*Figure 3.11b)*, after waiting at least 2 h at T_{set}, we forced a first crystallization by decreasing the temperature down to 275.1 K (T_{FC}). Once the crystallization started the temperature was heated back to T_{set}. Although in this protocol we can control the crystallization, the kinetic evaluation is disturbed by the variation of temperature up to T_{set}.

Finally, the third protocol (*Figure 3.12*) was proposed in order to explore the "memory effect" of gas hydrate crystallization. This phenomenon consists in a recrystallization under milder conditions than the initial nucleation. In hydrate systems some authors have reported the memory effect observing the reduction of induction time [142-144]. Moreover, exploring this phenomenon is also important because in hydrate-based process the recycle of liquid phase is conceivable, thus it is expected that the memory effect will have an influence on the crystallization.

The third protocol is composed by two steps of crystallization: First crystallization (FC) and Main crystallization (MC). FC is represented in *Figure 3.12a*. After the gas solubilization (period **AB**) the temperature of the cell was decreased down to 275.1 K (T_{FC}) and the crystallization was observed (period **BC**). During hydrate formation some gas phase samples were taken and analyzed by GC to observe the evolution of their composition with time. The hydrate formation took place during 50 minutes (period **CD**) and then the temperature was increased up to the 291.6 K (period **DE**) and kept constant for 30 minutes (period **EF**). These durations of periods **CD** and **EF** were determined after several tests. A high **CD** period with a small **EF** period means a high memory effect, thus disturbing the kinetic evaluation at the main crystallization step.

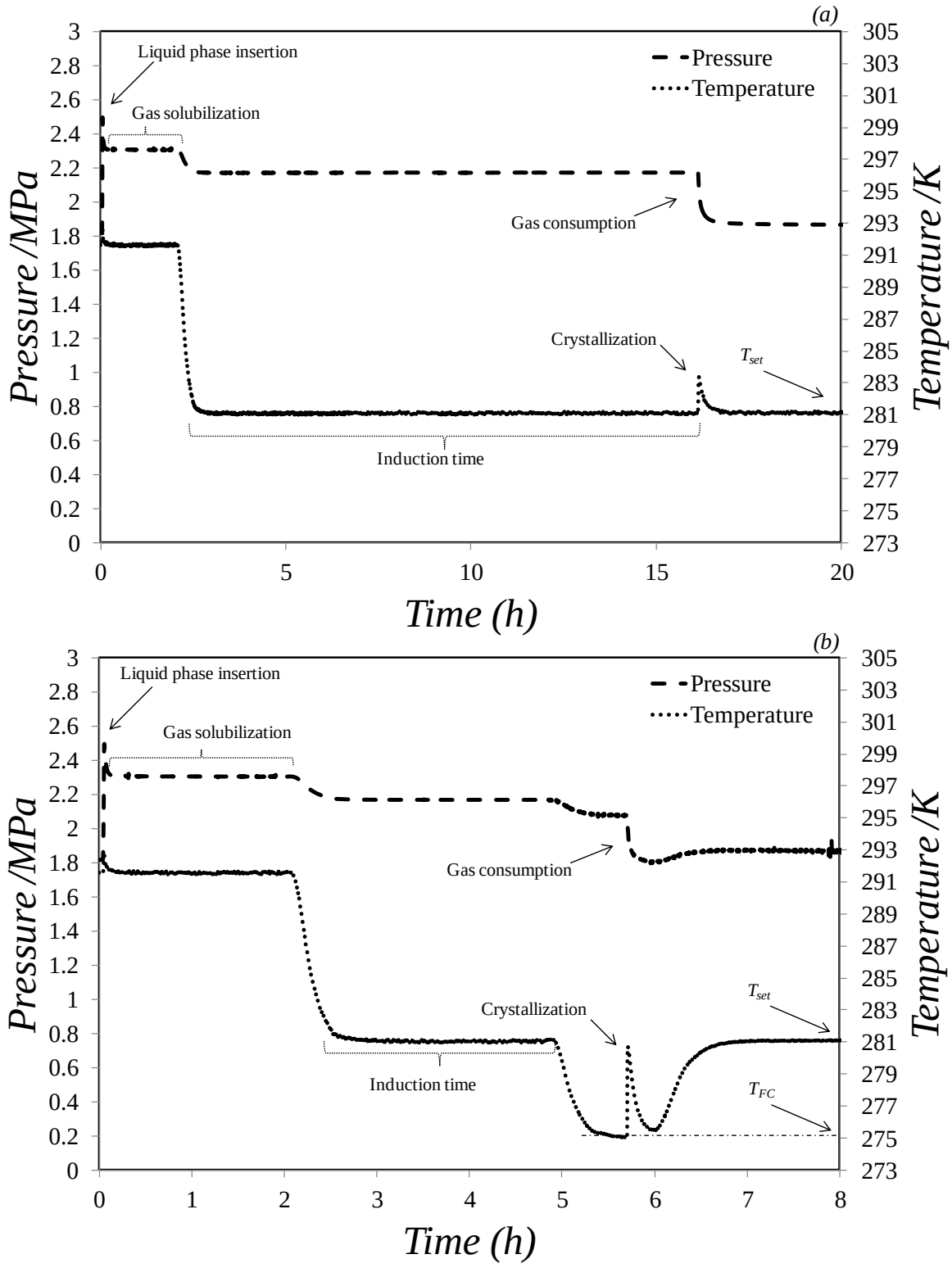

Figure 3.11. Pressure and temperature profiles during gas separation by hydrate formation protocols; (a) protocol 1; (b) protocol 2.

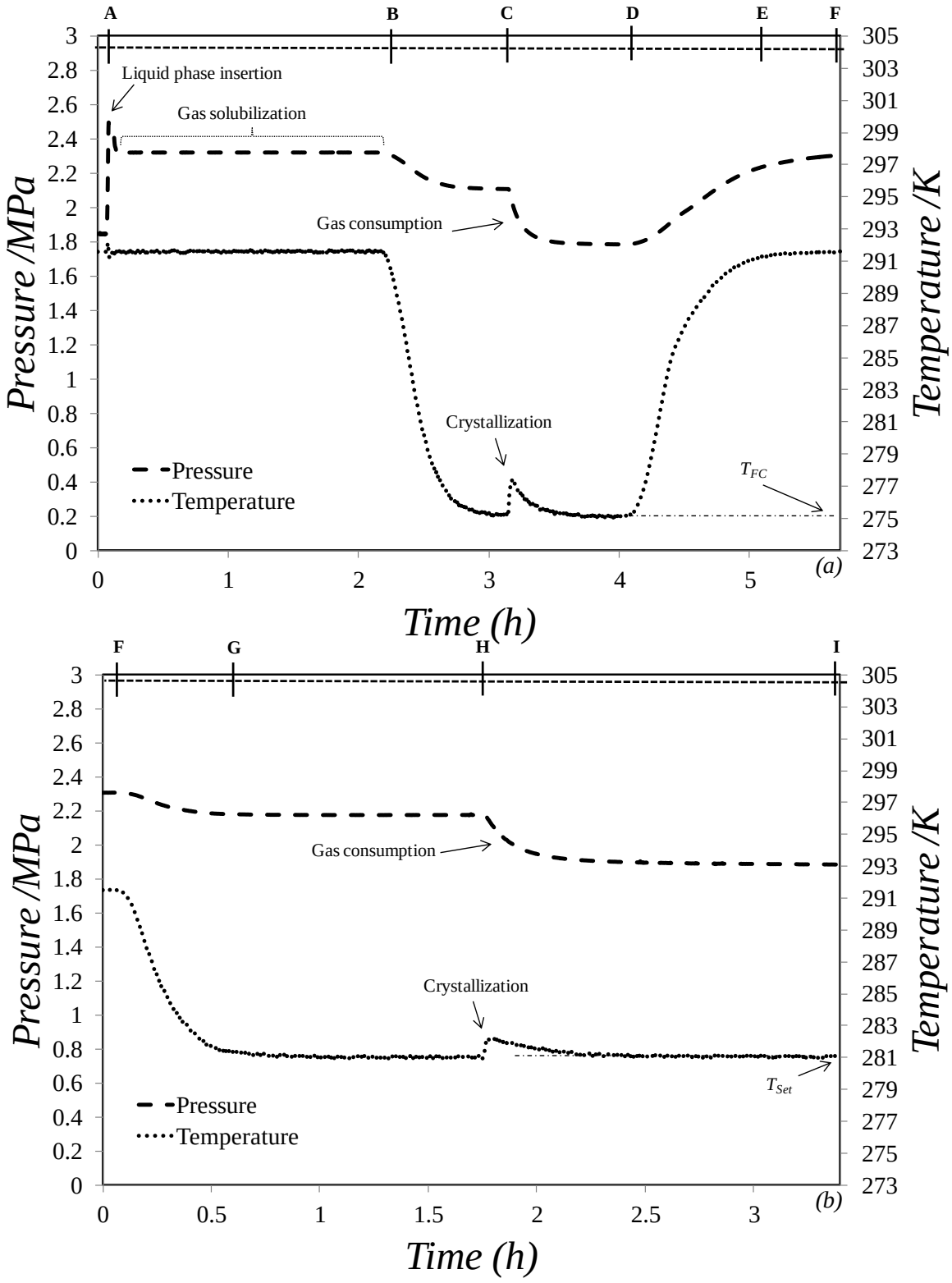

Figure 3.12. Pressure and temperature profiles during gas separation by hydrate formation final protocol; (a) First crystallization (FC); (b) Main Crystallization (MC).

The main crystallization step observed in *Figure 3.12b* started at the end of the period **EF** of the previous step. The temperature was then decreased down to the set temperature 281.1 K.

Once T_{set} reached, the period **GH** before crystallization was treated as the relative induction time. Gas samplings were performed during the hydrate formation and the evolution of gas phase composition was measured. The main crystallization takes place for 1.5 hours (period **HI**). After that, the system was heated to the initial temperature and kept constant for at least 15 hours. Then, the protocol starting from point **B** and ending at point **I**, was repeated at least two times in order to check the reproducibility of the results. In the last repetition the experimental protocol for equilibrium and dissociation steps was performed (*Figure 3.13*). This protocol consists in waiting the equilibrium state 24 hours after the crystallization. We have considered that this time was sufficient to reach the equilibrium. The temperature was then heated to 283.1 K and kept constant for 24 more hours. Finally, the experiment was concluded by returning the system to the initial temperature.

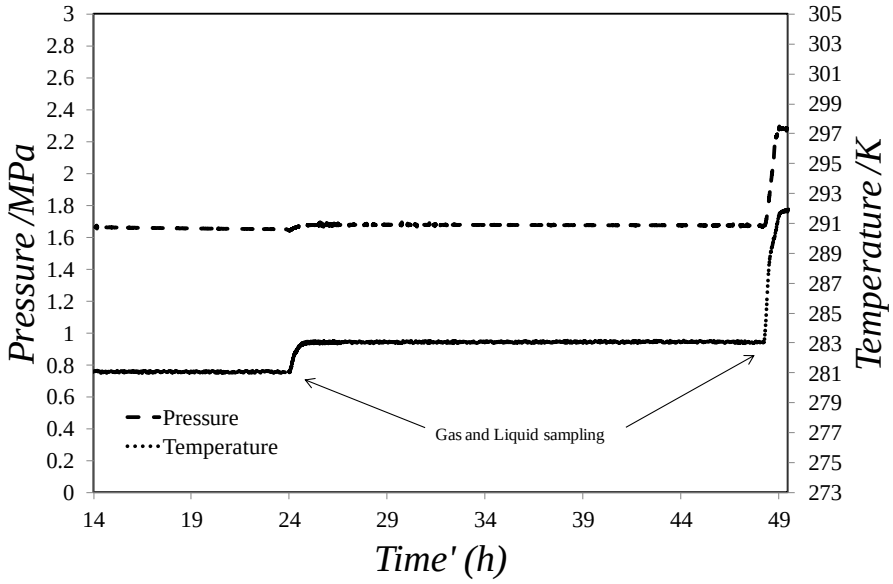

Figure 3.13. Pressure and temperature profiles during gas separation by hydrate formation final protocol: equilibrium and dissociation steps; Time' is the time taking as origin the crystallization.

In each equilibrium step, samples of gas and liquid phases were taken to analysis by GC and refractometry method, respectively. The composition of existing phases was therefore estimated. The whole process starting before point **A** was carried out twice for each promoter in order to check the reproducibility of the results.

The protocols for gas and liquid phase analysis, as well as the calculations of the composition of each phase, will be described in forth coming sections.

Evaluation of kinetics aspects

The kinetic effects of each promoter in GSHF process were evaluated by three main parameters:

- Relative induction time: the period of time starting when the system reaches the isothermal state till the apparition of hydrate phase
- Gas consumption rate: the pressure drop rate (*-dp/dt*) after the crystallization. This parameter was calculated at 10, 20 and 30 minutes after the nucleation.
- CO_2 capture rate: the evolution rate of CO_2 gas phase composition ($-dy_{CO2}/dt$) after the crystallization. This parameter was also calculated at 10, 20 and 30 minutes after the nucleation.

Evaluation of thermodynamic aspects

In terms of thermodynamic effects of each promoter in GSHF process, the evaluation was made from the results of equilibrium phase composition. Once characterized the equilibrium state, two main parameters were calculated for each promoter and compared between them: the selectivity of hydrate phase and the CO_2 capture percent by the hydrate phase. These parameters are defined in the *Section 3.3.2.4.*

3.3.2.2 Gas phase analyze

The gas phase was analyzed using a GC gas chromatographer (Perichrom PR2100) coupled to the gas sampling ROLSI system installed in the cell. For our experiments the GC device dispositive was equipped with a Thermal Conductivity Detector (TCD) and a packed column Restek Rt-XLSulfur (length, 2 m; o.d., 1/8 in., 100/120 mesh). This column guaranties under suitable operation conditions a good separation of CO_2+CH_4 gas mixture with a small retention time. *Table 3.5* shows the best operation conditions that provide a good separation with a small retention time. These conditions were determined after several tests with CO_2 + CH_4 gas mixtures. Helium was used as carrier gas because it has a different enough thermal conductivity compared to the CO_2 and CH_4.

Table 3.5. Operations conditions for the CG gas chromatograph.

Carrier gas	Helium
Detector	TCD
Pressure carrier gas (KPa)	150
Oven temperature (K)	353
Detector temperature (K)	393

The GC was calibrated for CO_2 and CH_4. The direct injection calibration method [182] was applied to ensure the accuracy required for our tests. Using accurate syringes (Extreme micro syringe MS GFN100) known volumes of gas (10, 20, 30, 40 and 50 µl) were injected into to CG and the corresponding area under the peak was measured. The calibration curves were fitted to a second-order polynomial equation relating the peak area to the number of moles calculated from Soave-Redlich-Kwong (SRK) Equation of State (EoS) [183] (See Appendix). *Figure 3.14* and *Table 3.6* show the obtained calibrations curves and the fitted values of the parameter equations. The general calibration equation is $n_{gasGC} = aS^2 + bS$, where n_{gasGC} is the calculated number of gas moles in the sample, *S* is the corresponding peak area, and *a* and *b* are the fitted parameters.

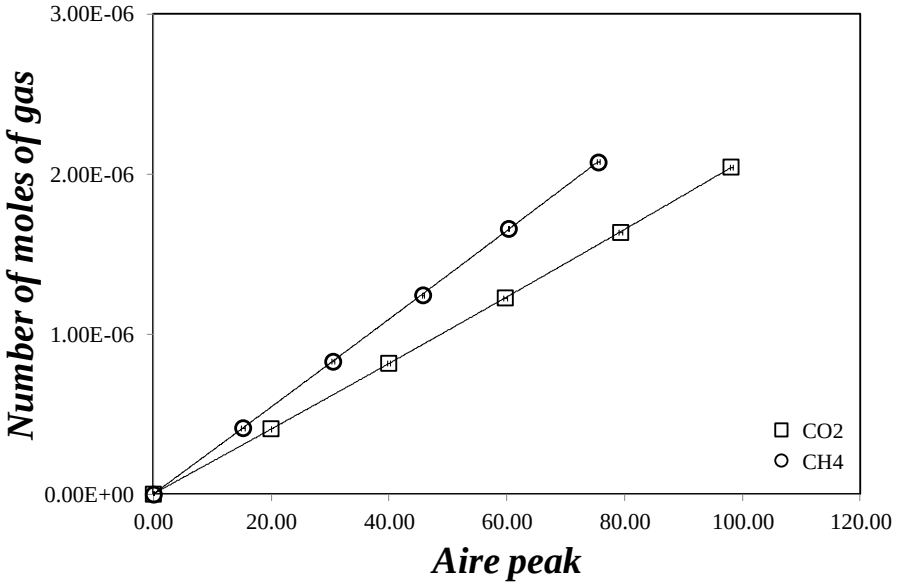

*Figure 3.14. Calibration curves for GC from CO_2 and CH_4; solid lines are the fitted second-*order equations.

The relative deviations between the experimental number of moles and the value calculated from the calibrations equations was always less 1%, the higher value being about 0.68 %. Therefore we considered an relative uncertainty of 1 % for this analysis.

Table 3.6. Fitted parameters from the calibration curves of gas chromatography.

Gas	**Fitted polynomial equation parameters**	
	a	*b*
CO_2	7.460×10^{-12}	2.006×10^{-8}
CH_4	5.596×10^{-12}	2.709×10^{-8}

To validate the experimental procedure for gas phase analysis from the ROLSI sampler we carried out an experiment in the reactor. The evacuated, cleaned and dried cell was filled with 2.45 MPa of CO_2 at 293.4 K. Then CH_4 was introduced until the pressure of 6 MPa and the temperature of 293.4 K. We waited about 4 hours to ensure the homogeneity of this gas mixture. We analyzed four gas samples at intervals of 3 minutes. The resulting chromatogram from this test is shown in the *Figure 3.15*.

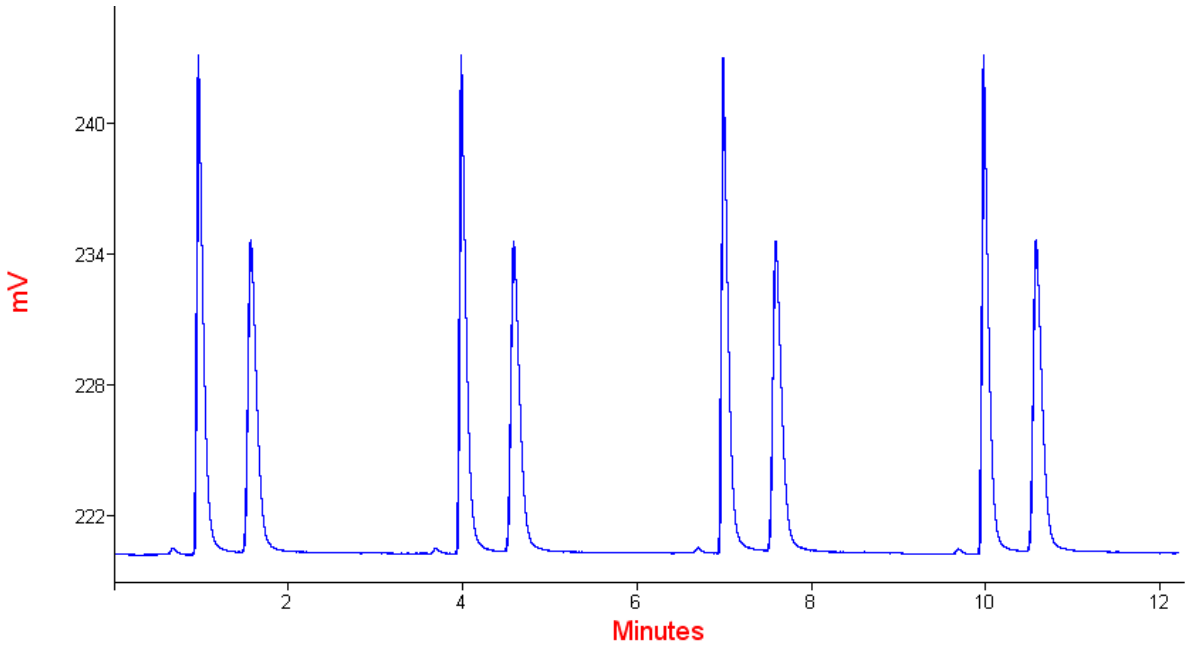

Figure 3.15. Chromatogram of sample of gas mixture CO_2-CH_4 taken from ROLSI system.

As we can see, there is almost no difference between the samples showing the accuracy of the sampling system. The gas composition measured the CG in mole fraction was 0.385 for the CO_2 and 0.615 for the CH_4. These values are very close to those obtained from SRK EoS for

which the calculated gas composition for CO_2 and CH_4 was 0.381 and 0.619, respectively. These results validate our experimental procedure for gas phase with a relative uncertainty of 1%.

3.3.2.3 Liquid phase analyze

Works available in literature for GSHF normally give the difference from the initial and final composition of gas phase and the number of moles removed. The composition of hydrate phase is rarely taken into account. This information is important to evaluate more precisely the gas separation process. For that reason, analysis of the liquid phase is necessary so that the composition of hydrate phase can be estimated by mass balance equations. The mass balance calculation applied to our system in order to estimate the gas content of the hydrate phase will be detailed in the next section.

We performed a series of test with different techniques that could be used to analyze the liquid phase of our systems. The idea was to determine the most accurate technique and most adapted to our experiments in the reactor. The sample of liquid phase was taken directly from the reactor using the device described in the previous section. Given the small volume of the reactor, it was important to use a method that requires a small amount of liquid sample for the analysis. This way, the equilibrium state would not be perturbed.

We tested four methods to analyze the liquid phase: analysis by atomic absorption of a salt tracer; electric conductivity measurements, analysis by infrared spectroscopy and refraction index measurements. The procedure and the obtained results as well as the selected method are exposed below.

Analysis by atomic absorption of a salt trace

It is known that the presence in a very low concentration of lithium ions (a few ppm) does not interfere in the hydrate formation and its structure [184]. It can therefore be used as a salt tracer for the liquid phase analysis. In other words, we can say that after the formation of hydrate phase, the mass of lithium is conserved. Therefore, since we know the initial ($w_{Li_i^+}$) concentration of Li^+ and the concentration of Li^+ after the hydrate formation ($w_{Li_f^+}$), we can calculate the mass of solution that was converted into hydrate. *Equations 3.2* and *3.3* are applied:

$$w_{Li_i^+} m^{sol}{}_i = w_{Li_f^+} m^{sol}{}_f \qquad (3.2)$$

Then:

$$m^{sol}{}_f = \frac{w_{Li_i^+} m^{sol}{}_i}{w_{Li_f^+}} \qquad (3.3)$$

Where: $m^{sol}{}_i$ is the initial mass of solution inserted in the reactor at the beginning of the experiment; $m^{sol}{}_f$ is the mass of solution non converted in hydrate phase.

To analyze the concentration of lithium ions we used the atomic absorption spectroscopy (AAS). This technique makes it possible to quantify chemical elements by measuring the absorbed radiation (light) when these elements are excited by a specific radiation. To test the accuracy of this technique we carried out an analysis of lithium chloride (LiCl) aqueous solution at 14 ppm. We decided to use this concentration because in usual experiments involving hydrate formation the concentration used is between 4 and 10 ppm. In the case of hydrate formation, an increase of Li^+ concentration is expected.

The equipment used was a Solaar AA series spectrometer from Thermo Electrom corporation. For each analysis a calibration curve must be done. In our tests, we used a range of concentration of standard solutions from 2 to 40 ppM. A minimum volume of sample of 2 ml is required to obtain an accurate result. *Figure 3.16* shows the results for an analysis of a test solution of LiCl at 14 ppm.

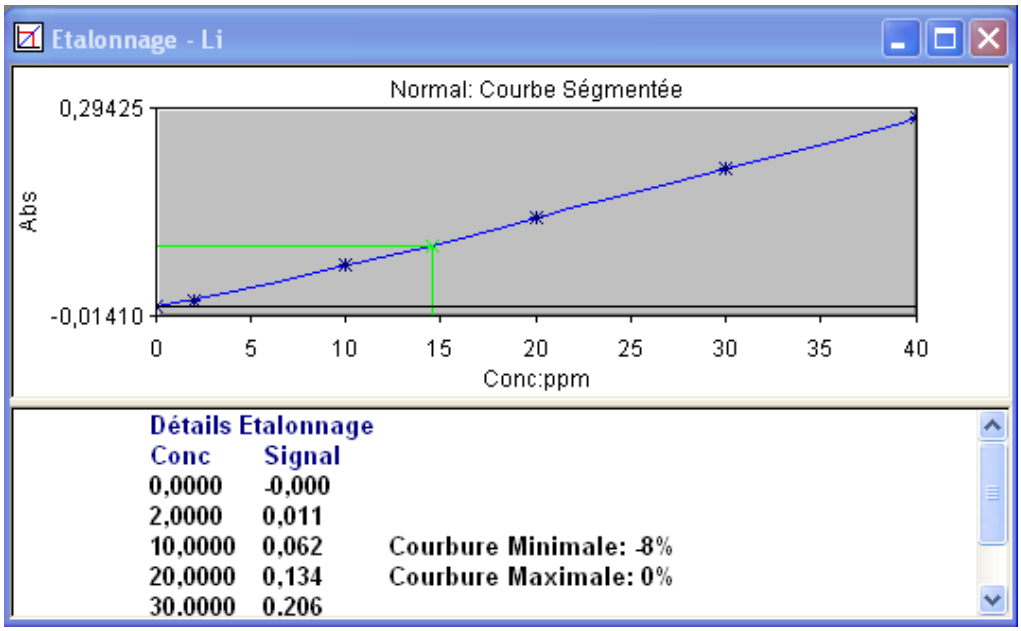

Figure 3.16. Calibration curve of Li; the green line indicates the sample test concentration.

The value obtained, 14.69 ppm, represents a relative deviation about 5 %, which can be considered acceptable given the very low concentration.

The main drawback of this technique is the necessity to take at least 2 ml of liquid sample. Regarding the reactor volume (206 ml), it is clear that this sampling will strongly perturb the system. Besides, this constraint would limit the number of experiment points that could be made.

Conductivity Measurement

The equipment used was composed of a 4 electrode cell (Knick, model ZU 6985) and a conductimeter (Knick Konduktometer 702, Germany). The measurement procedure was carried out as follows: the cleaned and dried electrode was immersed in the sample and the conductivity displayed by the meter was noted. For each concentration the conductivity was measured four times to ensure the reproducibly. The results are shown in *Figure 3.17.*

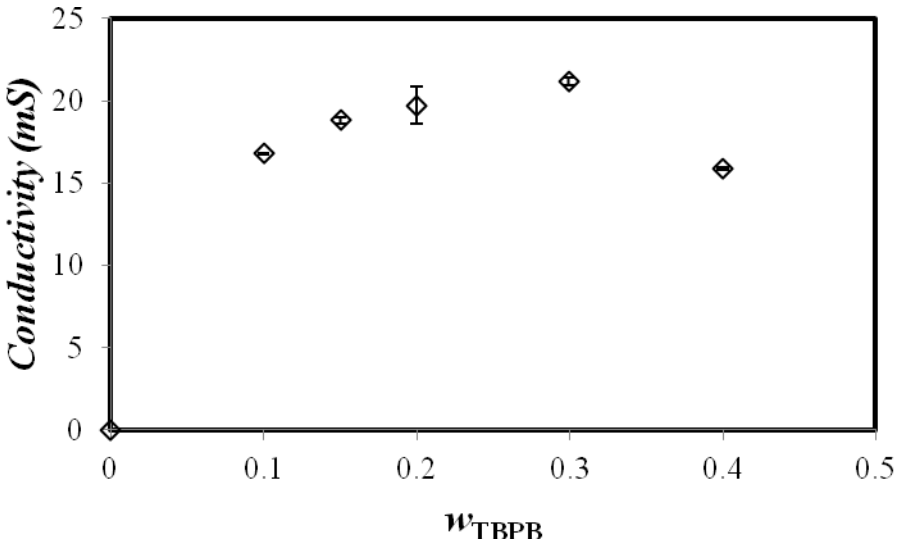

Figure 3.17. Measured conductivity of aqueous solutions of TBPB at different mass fraction (w_{TBPB}).

As we can see in the *Figure 3.17*, no accurate results were obtained since the conductivity increased up to a certain concentration and then decreased. This phenomenon may be related to the large size of the cations of TBPB salt used in the test or to the increase of the viscosity of the solution with the concentration, thus reducing the mobility of the ions [115].

Analysis by Fourier Transform InfraRed spectroscopy

Another technique tested was the Fourier Transform InfraRed spectroscopy (FTIR). The idea was to measure the additive concentration *in situ* using a fiber optic ATR-probe (Attenuated Total Reflection). It was thus necessary to ensure that FTIR is appropriate for measuring the additive concentration in liquid phase.

A Bruker Tensor 27 spectrometer with a ATR system was used for the measurements. Three mass fractions of TBAB in aqueous solutions were tested (0.05, 0.1 and 0.2). The results are shown in the *Figure 3.18.*

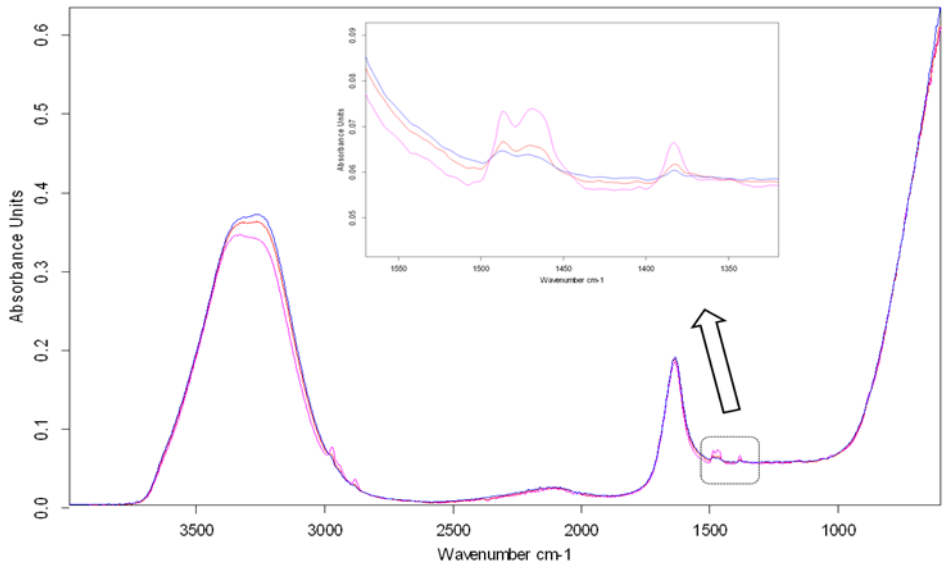

Figure 3.18. Infrared spectra from TBAB aqueous solutions; mass fraction: blue line 0.05; red line 0.1; rose line 0.2.

Even though the peaks are showing a rising trend with the additive concentration, the sensitivity was found very small, specially for the mass fraction of 0.05. A test using the fiber optic ATR-probe was carried out but no successful results were obtained.

Index of refraction

For liquid analysis in TBAB and TPBP solutions, some researchers suggested the measurement of refractive index [158, 185-186], which makes it possible to obtain the mass/mole concentration of salt in aqueous solution with high precision (uncertainty less than 1 %). Another advantage is that a small sample volume is required.

For our measurements an O.P.L. (France) refractive index instrument was used. The additive concentration was determined from a calibration curve made with several values of mass fraction for the specific additive. *Figure 3.19* shows the calibration curves carried out at fixed temperatures of 293.15 K for TBAB and TBPB and of 288.15 K for TBPO and THP. To ensure these set temperatures the refractive index device was coupled with a thermostatic bath (Julabo F25-ED, Germany).

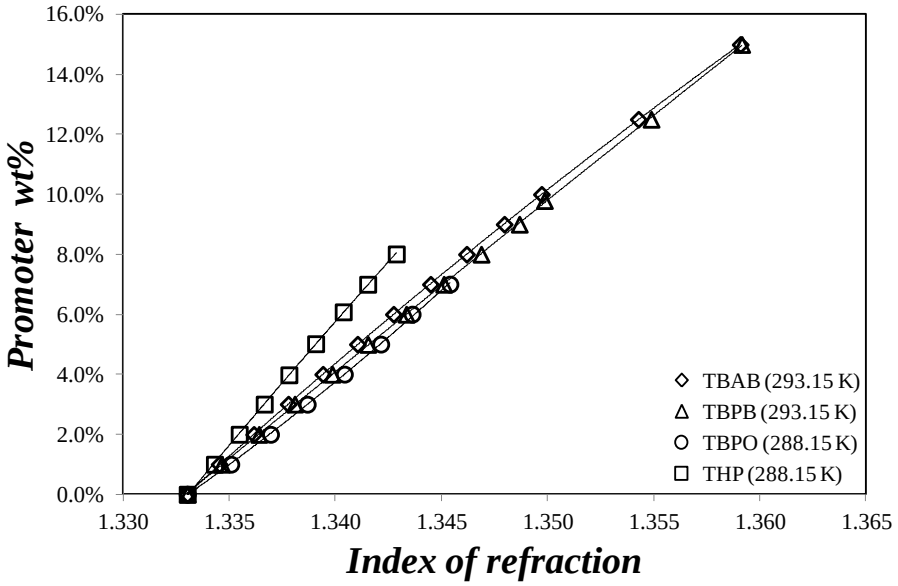

Figure 3.19. Calibration curves for the studied salts in different concentrations in aqueous solutions at fixed temperature.

The experimental data from *Figure 3.19* was fitted to a polynomial equation with general form of $w_{promoter} = aIR^2 + bIR + c$; where IR is the index of refraction, $w_{promoter}$ is the mass fraction of the specific promoter, *a*, *b* and *c* are the parameters of the model, which fitted values are given in *Table 3.7.*

Table 3.7. Fitted parameters from the calibration curves of index of refraction.

Additives	Fitted polynomial equation parameters		
	a	*b*	*c*
TBAB	-24.5895	71.9450	-52.2098
TBPB	-4.4314	17.6411	-15.6413
TBPO	56.8362	-146.5116	94.3080
THP	-35.2738	102.6041	-74.0944

The relative deviation between the values measured and the calculated was less than 0.5 %, which confirms the high precision of this technique. The liquid phase analysis were thus performed using refraction index measurements for all subsequent experiments of hydrates formation.

To take liquid samples from the reactor during an hydrate formation experiment, it was first necessary to turn off briefly the stirrer in order to avoid that the vortex let some gas escape by the collection line. Then the microvalve was slightly opened to extract a droplet of liquid,

which was analyzed using the IR device thermostated at the desired temperature. The additive concentration was then determined.

3.3.2.4 Mass balance equations

In this section we establish the mass balance equations to calculate the composition of each phase (hydrate, liquid and gas) in our experiments. Firstly, we need to calculate the total number of moles for each component at the beginning of the experiment. We consider a gas phase composed of two gases (*A* and *B*). Water and additive have the index *W* and *D*, respectively.

The experiment preparation starts with the reactor at the initial temperature T_0 being filled with the gas *A* at the pressure p_A. Knowing that the volume of gas ($V_0^{g_A}$) is equal to the known volume of the reactor (V_r) we can use the SRK EoS to calculate the compressibility factor of gas A (Z_A) and then the total number of moles of gas *A* (n_{g_A}), as follow in *Equation 3.4.* A detailed description of SRK EoS is shown in the *Appendix*.

$$Z_A = \frac{p_A V_0^{g_A}}{n_{g_A} R T_0} \Rightarrow n_{g_A} \qquad (3.4)$$

The gas B is then injected at temperature T_0 and pressure $p_B > p_A$. A gas mixture sample taken from ROLSI is analyzed in the GC and the composition of the gas mixture is measured. The EoS with gas mixture rules is used and the total number of gas (n_0^G) and the total number of gas B (n_{g_B}) are calculated (*Equation 3.5*).

$$Z_0^G = \frac{p_B V_r}{n_0^G R T} \Rightarrow n_0^G ; n_{g_B} \qquad (3.5)$$

The liquid phase composed of aqueous additive solutions (TBAB, TPBP, TBPO or THP) is introduced with a known volume (V_0^L) and mass fraction of additive (w_0). For aqueous solutions of TBAB and TBPB, the density was calculated using a correlation from Belandria *et al.* [185] which relative uncertainty is supposed to be less than 0.5 %. For TBPB solutions, we considered a higher relative uncertainty of 1 % since the correlation of Belandria *et al.* [185] was proposed for TBAB solutions. For TBPO aqueous solutions, we used the measured data of density from Higgins and Baldwin [187]. The relative uncertainty here was considered

to be less than 1 %. Finally for THP aqueous solution, we considered a density similar to the THF aqueous solutions. Furthermore, the density of liquid phase (ρ^L) was calculated using the correlation proposed by Ricaurte *et al.* [188], which relative uncertainty is supposed to be less than 2 %.

Therefore the initial mass of liquid phase (m_0^L) and the total number of water (n_W) and additive (n_D) can be calculated using *Equations 3.6 - 3.8*.

$$m_0^L = \rho_0^L V_0^L \qquad (3.6)$$

$$n_D = \frac{w_0 m_0^L}{MW_D} \qquad (3.7)$$

$$n_W = \frac{(1-w_0) m_0^L}{MW_W} \qquad (3.8)$$

After forming the hydrates, an equilibrium is reached at time *t*, characterized by a pressure p_t and a temperature T_t. Gas and liquid sampling are realized and the mole fraction of gas A and gas B in vapor phase (y_{g_A} and y_{g_B}) are measured as well as the mole fraction of additive (x) and water $(1-x)$ in liquid phase. Firstly we analyze the condensed phases (hydrate and liquid). For that we define some variables:

- n_W^L : number of moles of water in liquid phase
- n_W^H : number of moles of water in hydrate phase
- n_D^L : number of moles of additive in liquid phase
- n_D^H : number of moles of additive in hydrate phase
- $D.\upsilon.n_H$: hydrate composition
- υ : hydration number
- n_H : number of moles of hydrate

A mass balance of water and additive is therefore made:

$$n_W = n_W^L + n_W^H \qquad (3.9)$$

$$n_D = n_D^L + n_D^H \qquad (3.10)$$

Knowing that the number of moles of water in hydrate phase is the product of the hydration number by the number of moles of hydrate, and that in each mole of hydrate we have one mole of additive, *Equations 3.9* and *3.10* become:

$$n_W = n_W^L + \upsilon n_H \qquad (3.11)$$

$$n_D = n_D^L + n_H \qquad (3.12)$$

In a first step we are going to use the assumption that only one structure of hydrate is formed (see *Table 3.4*). In this case, the hydration number is a known and fixed value. We also neglect the number of moles of water and additive in gas phase.

The number of moles of water and additive in liquid phase is defined by:

$$n_W^L = (1-x)(n_W^L + n_D^L) \qquad (3.13)$$

$$n_D^L = x(n_W^L + n_D^L) \qquad (3.14)$$

We can divide *Equation 3.14* by *Equation 3.13:*

$$n_D^L = \frac{x}{(1-x)} n_W^L \qquad (3.15)$$

And multiply *Equation 3.11* by *x/(1-x):*

$$\frac{x}{(1-x)} n_W = \frac{x}{(1-x)} n_W^L + \frac{x\upsilon}{(1-x)} n_H \qquad (3.16)$$

Using the *Equation 3.15* in the *Equation 3.12:*

$$n_D = \frac{x}{(1-x)} n_W^L + n_H \qquad (3.17)$$

And finally subtracting *Equation 3.16* to *Equation 3.17* leads to *Equation 3.18* that allow calculating the number of moles of hydrate, all other variables being known.

$$\left(\frac{\upsilon x}{1-x} - 1\right) n_H = \frac{x}{1-x} n_W - n_D \qquad (3.18)$$

Now we calculate the content of gases A and B in each phase. For that we also define some variables:

$n_{g_A}^{L}$: number of moles of gas A in liquid phase

$n_{g_A}^{H}$: number of moles of gas A in hydrate phase

$n_{g_A}^{G}$: number of moles of gas A in gas phase

$n_{g_B}^{L}$: number of moles of gas B in liquid phase

$n_{g_B}^{H}$: number of moles of gas B in hydrate phase

$n_{g_B}^{G}$: number of moles of gas B in gas phase

$x_{g_A}^{*}$: solubility of gas A in liquid phase at p_t et T_t condition.

$x_{g_B}^{*}$: solubility of gas A in liquid phase at p_t et T_t condition.

The mass balance for each gas is:

$$n_{g_A} = n_{g_A}^{L} + n_{g_A}^{H} + n_{g_A}^{G} \qquad (3.19)$$

$$n_{g_B} = n_{g_B}^{L} + n_{g_B}^{H} + n_{g_B}^{G} \qquad (3.20)$$

The number of moles of gases A and B in liquid phase is calculated by *Equations 3.21* and 3.*22*.

$$n_{g_A}^{L} = x_{g_A}^{*} n_W^{L} \qquad (3.21)$$

$$n_{g_B}^{L} = x_{g_B}^{*} n_W^{L} \qquad (3.22)$$

where: x_g^{*} is the solubility of gas in liquid phase at p_t et T_t condition. Here, the solubility was calculated considering the liquid phase as pure water. Others authors [158, 186, 189-190] have made the same assumption. Indeed, some works in the literature have showed that the presence of thermodynamic promoters in low concentration (less than 10 wt%) have practically no effect on the solubility of the gas in the liquid phase [80, 188, 191-192]. For CO_2 the solubility was calculated using the model of Diamond and Akinfiev [193] and for CH_4 we used the equation of Krichevsky-Kasarnovsky [194] (*Equation 3.23*). The Henry's constant was calculated using the correlation proposed by Holder *et al*. [195].

$$x_g^* = \frac{f_g(p,T)}{H \exp\left[v_g^\infty \left(P - P_{H_2O}^{sat}\right) / RT \right]} \qquad (3.23)$$

where: $f_g\ (p,T)$ is the fugacity of the gas which will be calculated using SRK EoS; v_g^∞ is the partial molar volume of the gas at infinite dilution and we will use the average value of 32 $cm^3.mol^{-1}$ proposed by Holder *et al*. [196]; $P_{H_2O}^{sat}$ is the vapor pressure of pure water and its value will be obtained using NIST database; the expression in brackets corresponds to the Poynting correction; *H* is the Henry's constant and can be calculated using the *Equation 3.24.*

$$H = \exp(A + B/T) \qquad (3.24)$$

H is in MPa and *T* in K. The parameters of *Equation 3.24* can be found in the literature and *Table 3.8* report the values for CO_2 and CH_4.

Table 3.8. Parameters for Equation 3.24 [195].

Gas	A	B
CO_2	14.283146	-2050.3269
CH_4	15.826277	-1559.0631

To calculate the number of moles of each gas in gas phase it is necessary to calculate the volume of gas:

$$V^G = V_r - V^L - V^H \qquad (3.25)$$

The volume of liquid phase was calculated from its density, which was determined using the same assumptions discussed previously. For the volume of hydrate phase it was also calculated from its density. The density used for each promoter hydrate was calculated considering half occupancy of gas in the available cages in the hydrate structure. The uncertainties varied from the value of density of simple promoter hydrate (found in literature) and full cage occupancy of promoter/gas hydrate (found in literature or estimated from the formula proposed by Sloan and Koh [14]). The maximum variation being 10 %. For example for TBAB and TBAB/CO_2 hydrates (both with hydration number of 38), the densities are 1.07 g/cm^3 and 1.13 g/cm^3, respectively [57, 101], thus we used as density the value of 1.10 g/cm^3.

With the volume of gas phase and its composition, we calculate the number of moles of gas and then the number of moles of gas A and B.

$$Z^G = \frac{p_t V^G}{n^G R T_t} \Rightarrow n^G \qquad (3.26)$$

$$n_{g_A}^V = y_{g_A} n^G \qquad (3.27)$$

$$n_{g_B}^V = y_{g_B} n^G \qquad (3.28)$$

Finally we can calculate the number of moles of gas in the hydrate phase, which is an important parameter to evaluate more precisely the gas separation by hydrate formation process.

$$n_{g_A}^H = n_{g_A}^T - n_{g_A}^L - n_{g_A}^V \qquad (3.29)$$

$$n_{g_B}^H = n_{g_B}^T - n_{g_B}^L - n_{g_B}^V \qquad (3.30)$$

In order to evaluate the effect each promoter in the gas separation process, the selectivity (*S*) and the capacity of CO_2 removal in hydrate phase ($\%CO_2{}^H$) were calculated by the *Equations 3.31* and *3.32*, respectively.

$$S = \frac{\frac{n_{CO_2}^H}{n_{CO_2}^T}}{\frac{n_{CH_4}^H}{n_{CH_4}^T}} \qquad (3.31)$$

$$\%CO_2{}^H = \left(\frac{n_{CO_2}^H}{n_{CO_2}^T} \right) \cdot \left(n_H \right)^{-1} \qquad (3.32)$$

In order to validate the mass balance equations we used the data from the Ph.D of Brantuas [186]. He used a similar experimental procedure that we proposed to calculate the equilibrium phase composition of TBAB+CO_2+H_2O. The initial conditions from his work are summarized in the *Table 3.8*.

Table 3.8. Initial conditions from Brantuas's work [186] involving hydrate formation.

Set temperature (K)	285.1

Initial pressure (MPa)	1.86
V_r (cm^3)	1350
n_w (mol)	33.19
n_D (mol)	0.655
n_g (mol)	0.870

The hydration number was measured experimentally and the number of 36.9 was found. For the density of hydrate phase he used the value of 1.028 g/cm^3 which is the reported density by Gaponenko *et al*. [113] for a TBAB semi-clathrate having a number of hydration of 36. He considered that the presence of TBAB doesn't change the solubility of CO_2 in liquid phase and he calculated it using Diamond & Akinfiev's model [193]. For our calculations we made the same assumptions, except for hydration number. For this parameter we used 38 which the hydration number suggested by Muromachi [57] for TBAB/CO_2 semi-clathrates. The results in number of moles of CO_2 in each phase from Brantuas's work and our calculation as well as the relative deviation are presented in the *Table 3.9.*

Table 3.9. Comparison of number of moles of CO_2 in each phase in Brantuas's work [186] and our calculations.

Phase	Brantuas	Our calculations	RD (%)
Liquid (mol)	0.116	0.115	-0.91%
gas (mol)	0.215	0.211	-1.89%
hydrate (mol)	0.539	0.544	0.93%

As we can see the results are very close. The observed differences can be due to the way of calculations.

However, we made some assumptions that may have a direct impact on the final result. To assess how much they really impact the results we decided to perform an uncertainty propagation analysis on our set of equations.

3.3.2.5 Uncertainties

In order to evaluate the precision of our calculations based in the mass balance equations, we carried out an estimation of the expanded uncertainties (*U*) using the principle of uncertainty propagation from GUM [197]. Given a property (*y*) that is function of other measured

properties (x_1, x_2,..x_k) with their uncertainties ($u(x_1)$,$u(x_2)$,..$u(x_k)$), the uncertainty $u(y)$ can be calculated analytically using the expressions below:

$$y = f(x_1 \pm u(x_1), x_2 \pm u(x_2), ..., x_k \pm u(x_k)) \quad (3.33)$$

$$u^2(y) = \left(\frac{\partial f}{\partial x_1}\right)^2 u^2(x_1) + \left(\frac{\partial f}{\partial x_2}\right)^2 u^2(x_2) + ... + \left(\frac{\partial f}{\partial x_k}\right)^2 u^2(x_k) \quad (3.34)$$

Another way to estimate $u(y)$ is using Monte Carlo method [198-201]. For applying this method it is necessary to define what kind of probability density function (PDF) the uncertainty of the property x_k has. For our calculations we considered all parameters having a PDF of a uniform distribution.

We estimated the expanded uncertainty with 95% level of confidence (coverage factor of 2) in the number of moles of gas hydrate (n_H) and in the number of moles of gas in gas hydrate phase (n_g^H). Therefore, we considered two sources of uncertainties: experimental and hypothetical. For experimental uncertainties, it was taken into account the mole fraction of additive (x) at equilibrium condition, the initial volume of liquid phase (V_i^L) and the gas composition (y_g). The first variable was measured by refractometry using a calibration curve with less than 1 % of average absolute relative deviation (AARD); the second measured directly by the ISCO syringe pump (the uncertainty here corresponds to the precision of the apparatus); the third was measured by Gas Chromatography using a calibration curve with less than 1 % of average absolute relative deviation (AARD). Other experimental variables, such as temperature, pressure, and initial mass fraction of additive had their uncertainties neglected (normally less than 0.5 %). For hypothetical uncertainties, we have made four assumptions:

- The hydration number was considered as a fixed value corresponding to the stoichiometric composition (see *Table 3.4*). The others possible structures were taken into account as uncertainties.

- The small concentration of promoters in aqueous phase doesn't change the solubility of CO_2 and CH_4. Moreover, we considered an uncertainty of ± 5 % taking account the works of Lin *et al.* [191], Muromachi *et al.* [192] and Ricaurte *et al.* [188].

- The density of gas hydrate phase doesn't change in the range of pressure used in the experiments and corresponds to a hydrate having half occupancy of gas in the

available cages in the structure. The uncertainty was considered as the variation from none to full gas occupancy.

- The density of liquid phase doesn't chance in the range of pressure used in the experiments. The uncertainty of at most 2 % was considered taking account the literature [185, 187-188].

Table 3.10 summarizes the source of uncertainties used in the calculations. The expanded uncertainties were calculated for each equilibrium condition in all experiments and the results are presented in *Tables 5.5* and *5.6* in *Chapter 5*.

Table 3.10. Properties and their uncertainties used for uncertainty propagation calculations.

Properties	Type	Uncertainty	PDF
Additive mole fraction	Experimental	± 2 %	uniform
Liquid phase volume	Experimental	± 0.5 mL	uniform
Gas phase composition	Experimental	± 2 %	uniform
Hydration number	Hypothetical	– 31.5 %*	uniform
Solubility	Hypothetical	± 5 %	uniform
Gas hydrate density	Hypothetical	± 5 and 10 %**	uniform
Liquid phase density	Hypothetical	± 2 %	uniform

*Maximum value corresponding the variation of n_{Hyd} of 38 to 26 for TBAB and TBPB
** ± 5 % for promoter/CH_4 and ± 10 % for promoter/CO_2 system

A global sensitive analysis was also carried out and for the calculations involving CO_2. The solubility and the gas composition were the most sensitive parameters and its contribute to more than 80 % of the global uncertainty.

3.3.3 Protocol for gas storage capacity estimation

Experiments for determining the gas storage capacity of THP/CO_2 and THP/CH_4 gas hydrates were carried out using the instrumented reactor described in *Section 3.3.1*. The main criteria for comparing the two systems was using the same initial number of mol for each compound. *Table 3.11* presents the initial conditions for each system studied.

Table 3.11. Initial conditions for gas storage experiments involving THP promoter.

	CO_2	CH_4
p /MPa	2.34	2.58
T_0 /K	291.6	291.6
n^{gaz} /mol	0.2300 ± 0.001	0.2300 ± 0.001
w_{THP}	0.050 ± 0.001	0.050 ± 0.001

V_{liq}/cm^3	60 ± 0.5	60 ± 0.5

The applied experimental protocol for hydrate formation and equilibrium state characterization was the protocol 1 (*Figures 3.11a* and *3.13*) described in *Section 3.3.2.1.* The experiments were carried out twice for each system in order to check the reproducibility of the results. The gas content in the hydrate phase was estimated measuring w_{THP} at equilibrium (protocol in *Section 3.3.2.3*) and using the mass balance equations from *Section 3.3.2.4.* The expanded uncertainties were calculated for each equilibrium condition using the same criteria and assumptions described in *Section 3.3.2.5.* The results are presented in the *Tables 4.12* and *4.13* in *Chapter 4*.

Chapter 4

Phase Equilibria Study of Thermodynamic Hydrate Promoters*

Résumé

Ce chapitre présente les résultats expérimentaux de l'étude d'équilibre des phases concernant les promoteurs thermodynamiques sélectionnés TBPB, TBPO et THP. Le diagramme de phase type température versus composition pour les systèmes binaires promoteurs + eau ont été déterminé pour chacun des trois additifs. Les conditions de dissociation des hydrates de gaz en présence de promoteurs ont été également mesurées sous différentes pressions et compositions de la phase aqueuse. Les gaz étudiés comprennent le CO_2 pur, le CH_4 pur et un mélange de gaz CO_2 + CH_4 contenant 40 mol% de CO_2 afin de simuler la composition typique d'un biogaz obtenu à partir de déches agricoles. Les températures de transition de phase ont été déterminées en utilisant les méthodes de DSC dont les protocoles expérimentaux ont été décrits dans le Chapitre 3. Le réacteur instrumenté a été utilisé pour estimer la capacité de stockage de gaz dans les hydrates de THP/CO_2 et THP/CH_4. Les résultats des mesures d'équilibre de phases ont montré que la présence des promoteurs décale les courbes d'équilibre de phase V-L-H vers des valeurs plus basses de pression et des valeurs plus hautes en température. Les résultats ont été comparés à ceux de la littérature et un bon accord a été généralement observé. La comparaison entre les promoteurs en termes de gain de stabilité est présentée. L'étude de capacité de stockage de gaz a montré que THP est plus indiqué pour capturer le CH_4 que le CO_2. Les nouvelles données présentées ici représentent un point de départ pour les analyses de conception des procédés basés sur les hydrates des gaz.

Abstract

This chapter presents the experimental results of phase equilibria study involving the selected thermodynamic hydrates promoters TBPB, TBPO and THP. The phase diagrams temperature versus composition of the binary system (promoter + water) were determined for each additive. The dissociation conditions of promoters/gas hydrates were also measured under different pressures and compositions of aqueous liquid phase solutions. The gas studied were comprised of pure CO_2, pure CH_4 and CO_2 + CH_4 gas mixture containing 40 mol% of CO_2. This composition was chosen in order to simulate a typical biogas obtained from agricultural waste. The phase transition temperatures were determined using DSC experimental protocols that were described in Chapter 3. Using the instrumented reactor we also estimated the gas storage capacity of THP/CO_2 and THP/CH_4 hydrates. The results from phase equilibria measurements showed that the presence of promoters shifted the V-L-H three-phase equilibrium curves towards lower pressures and higher temperatures. The results were compared to the literature data, showing generally a good agreement. The comparison between the promoters with regards to stability gains is presented. The gas storage capacity study showed that THP is more indicated to capture CH_4 than CO_2. The new data presented here represents the starting point for the analyses of conceptual design of gas hydrate based processes involving the studied promoters with the different gas phases.

* Content published in *Fluid Phase Equilibria 2016,* 413, 28-35; *The Journal of Chemical Thermodynamics*, 2016, 102, 293-302; submitted as "Study of tetrahydropyran (THP) promoter in hydrate based process involving CO_2, CH_4 and CO_2+CH_4 gas mixture: phase equilibrium measurements and estimation of gas storage capacity."

4.1 Introduction

In binary systems (gas + water), CO_2 and CH_4 form SI structure and CO_2 gas hydrate is more stable than CH_4 gas hydrate [108, 111], which is interesting aspect for a possible selective CO_2 capture in a gas separation by gas hydrate formation process (GSHF). However, the high pressure and low temperature needed to form these gas hydrates demand high energy consumption [202], which limits its application in an industrial process. In order to reduce the gas hydrate formation pressure, thermodynamic promoters can be used. These molecules change the structure of the crystal and the phase equilibrium conditions of gas hydrates. Promoters, such as tetrahydrofuran (THF) and tetrahydropyran (THP) form the structure SII by occupying the large cages of this structure. The tetra-alkylammonium/alkylphosphonium salts form the so called semi-clathrate hydrates and have been extensively studied in the literature. The structure of these compounds contains empty dodecahedral cages that are able to trap some small gas molecules, such as CO_2 and CH_4.

The phase behavior of hydrates formed in the presence of CO_2, CH_4 or even gas mixture of CO_2 + CH_4, with some of these promoters has been published: tetra-n-butyl ammonium bromide (TBAB; CAS number 1643-19-2) [125-127, 137], tetra-n-butyl ammonium chloride (TBAC; CAS number 1112-67-0) [130-131, 137], tetra-n-butyl phosphonium bromide (TBPB; CAS number 3115-68-2) [117, 203-204]; THF (CAS number 109-99-9) [95-97, 136]. Some works on modeling the phase behavior in presence of these compounds have also been done [47, 133-134].

Some works have shown that the Tetra-n-butyl phosphonium bromide (TBPB) is interesting for some processes involving semi-clathrates, such as CO_2 storage or cold storage [81, 173, 205]. However, the study provided by Suginaka *et al.* [117] is the only one available in the literature concerning TBPB/CH_4 mixed semi-clathrates. Their work consisted of determining the phase equilibrium of this system only in stoichiometric composition. No data about hydrate-liquid-gas phase equilibria are available for TBPB/(CO_2+CH_4) semi-clathrate, information which is needed to design a process of gas separation via hydrate formation. In literature some works have already been done with CO_2+CH_4 gas mixture, but the majority consider only TBAB additive [126, 135-137].

Another molecule that forms semi-clathrates gas hydrate is the tributylphosphine oxide (TBPO; CAS number 814-29-9). The study of Alekseev *et al.* [106] showed that, in aqueous

solutions, this molecule forms a hydrate phase which structure contains some available dodecahedral cages that can encage gas molecules, such as CH_4 or CO_2. Such promoter can be interesting in GSHF process. However, knowledge about the three phase equilibria is important in order to demonstrate the feasibility of the process as well as its design. As far as we know, for TBPO/gas semi-clathrates, the studies provided by Du *et al.* [122] and Cha *et al.* [121] are the only available in the literature. In these works the hydrate- liquid- vapour phase equilibria were determined at two compositions, i.e. 26 wt.% and 30 wt.%.

Tetrahydropyran (THP Cas number 142-68-7) forms SII hydrate structure and some works showed that this promoter can form more gas hydrate phase with CH_4 than CO_2 [94, 119-120]. This inversion of stability can be explored for selective gas separation of $CO_2 + CH_4$ by trapping CH_4 in the solid phase. However, the lack of data about phase behavior, specially as regards the THP concentration dependence makes difficult the evaluation about the potentially to use this promoter in the GSHF process. Here we propose a larger study of this promoter.

Many studies have been published recently on $CO_2 + CH_4$ separation using gas hydrate formation with and without hydrate promoters [87-89, 206] . However, TBPB, TBPO and THP have not been tested yet and could be interesting to improve the gas separation process.

The composition of the gas mixture containing 40 mol.% of CO_2 and 60 mol.% of CH_4 is representative of most biogases, especially those resulting from the digestion of agricultural wastes [8-10]. It is known that other compounds, such as hydrogen sulfide (H_2S) and volatile organic compounds (VOC) are present in a real biogas, but in small quantities. Because these compounds must be removed from the gas prior to any other treatment, we did not consider them in this work.

The objective of the work presented in this C*hapter* was to determine the binary (promoter + water) phase behavior and the hydrate – liquid – gas equilibrium conditions for promoters in presence of CO_2, CH_4 and $CO_2 + CH_4$ gas mixture in a composition close to biogas. The promoters studied were TBPB, TBPO and THP. TBPB/CO_2 semi-clathrate have already been studied in the literature, thus it was not concerned by this study.

The measurements of dissociation conditions were performed normally at pressures below 3 MPa. The objective was the provide equilibrium data at low pressures enhancing the industrial applicability of the promoters in gas hydrate based process (higher pressures

implies higher energy consumption).

The phase transition temperatures were measured using the DSC techniques that was described in the *Chapter 3*. The gas storage capacity was estimated applying the experimental protocol described in the *Section 3.3.3* at the *Chapter 3*.

The S*ections* in this *Chapter* will explore the results obtained for each promoter. In the *Section 4.2* we present the results on the hydrate – liquid equilibrium conditions for TBPB + H_2O system and the hydrate – liquid – gas equilibrium conditions for TBPB + CH_4 and ($0.4CO_2$ + $0.6CH_4$) + TBPB + H_2O systems in a range of mass fractions of TBPB in aqueous solutions varying from 0.05 to 0.35. The pressure ranges used in the experiments were 1 to 8 MPa for CH_4 and 1 to 2 MPa for CO_2+CH_4 gas mixture. *Section 4.3* presents the phase behavior of TBPO semi-clathrate at atmospheric pressure determined in TBPO mass fraction in water ranging from 0.05 to 0.40. In presence of CO_2, CH_4 and $0.4CO_2$ + $0.6CH_4$ gas mixture, the measurements of phase transition temperatures were carried out in a 0.05 - 0.30 range of mass fraction of TBPO and gas pressure ranging from 1 to 3 MPa. The study involving THP promoter is presented in *Section 4.4.* The binary phase behavior temperature versus composition was determined at THP mass fraction ranging from 0.025 to 0.500. THP/gas hydrates stability conditions were determined under pressure varying from 1 to 3 MPa and THP mass fraction from 0.050 to 0.030. The gas storage capacity of THP/CO_2 and THP/CH_4 gas hydrates was estimated. Finally, *Section 4.5* provides a comparison between the promoters examined in this thesis.

The studies concerning the promoters TBPB and TBPO were published in [204, 207].

4.2 Systems involving TBPB promoter

Dissociation temperature of TBPB single semi-clathrate and TBPB/CH_4 semi-clathrate were measured using TBPB mass fraction ranging from 0.05 to 0.35 and a range of CH_4 and CO_2+CH_4 mixture pressure from 1 to 8 MPa and 1 to 2 MPa, respectively.

4.2.1 TBPB + H_2O system

Figure 4.1 shows the DSC thermograms obtained by the dynamic method for measuring the dissociation temperature of single TBPB semi-clathrate at a mass fraction interval of 0.05 to 0.35. In the first endothermic peak starting at 272 K the T_{onset} is almost independent of TBPB mass fraction. Then, it is attributed to the melting of eutectic mixtures of ice and the single TBPB semi-clathrate. The subsequent peak is due to the progressive melting of excess single TBPB semi-clathrate with T_{end} increasing with the increase of TBPB mass fraction (w_{TBPB}).

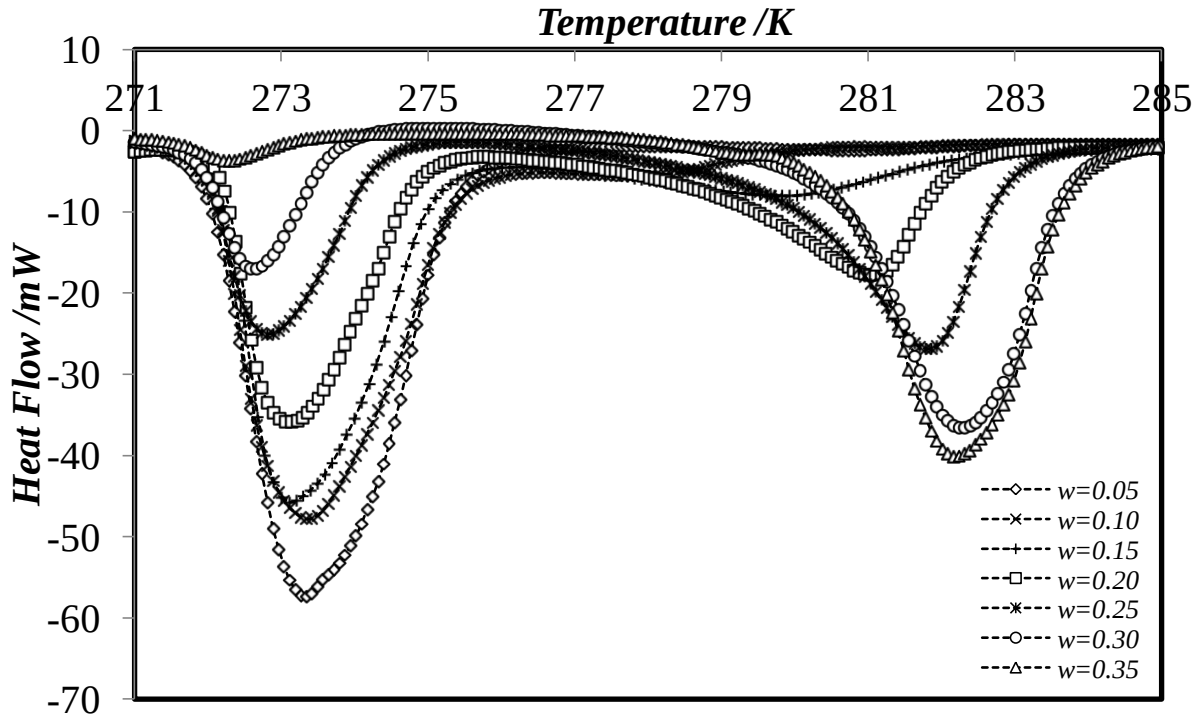

Figure 4.1. DSC thermograms of the melting of single TBPB semi-clathrate at variable additive composition recorded at 0.5 K min^{-1}; w is the value of TBPB mass fraction.

We observed that the increase of the TBPB mass fraction reduces the area of the eutectic peaks. At w_{TBPB} = 0.35 the eutectic peak is very small, which indicates that there is a small amount of free water and the system is near to the stoichiometric composition of TBPB

hydrate. Lin *et al.* [171] using DSC dynamic method also obtained a small eutectic peak at w_{TBPB} = 0.35 and a total absence of this peak at w_{TBPB} = 0.37. They observed that at w_{TBPB} = 0.37 the shape of the peak differ from what is observed in the case of typical isothermal melting process. They attributed this behavior to the existence of metastable TBPB semi-clathrate having incongruent melting, such as the TBPB.36H_2O proposed by Dyadin & Udachin [51]. However, no peritectic peak was observed in our results. This kind of peak could correspond to a structure transition and then confirm the presence of another semi-clathrate structure. Indeed, Dyadin & Udachin [51] reported that stable single TBPB semi-clathrates have a formula of TBPB.32H_2O, which corresponds to a stoichiometric composition at w_{TBPB} = 0.371. Comparing to our results, we can then conclude that the stoichiometric composition is slightly higher than w_{TBPB} = 0.35.

The measured phase transition temperatures for TBPB+H_2O using DSC dynamic method are presented in *Table 4.1*. Firstly we observed that the temperatures of eutectic melting, which were measured using T_{onset}, do not vary, considering the associated uncertainty, with the additive concentration. The maximum variation was of 0.3 K. These obtained values are very close to those available in literature, i.e. 272.3 K from Mayoufi *et al.* [205] and 272.5 K from Lin *et al.* [171]. For the temperatures of the progressive melting of TBPB semi-clathrates, we observed that the increase of TBPB mass fraction increase the stability of hydrate phase, the highest value being 282.0 K for w_{TBPB} = 0.35. The obtained dissociation temperatures values were plotted in *Figure 4.2* and compared to those found in the literature.

Table 4.1. Measured phase transition temperatures of TBPB+H_2O system at different TBPB mass fractions.

w_{TBPB}	Eutectic[a] T_{onset}/K	T_{end}[b]/ K
0.05	272.1	273.8
0.1	272.2	278.2
0.15	272.2	280.5
0.2	272.4	281.2
0.25	272.4	281.6
0.3	272.1	281.8
0.35		282.0

Standard uncertainties *u* are: [a] $u(T_{onset})$ = 0.2K; [b] $u(T_{end}(\alpha = 0))$ = 0.4 K

We observed that our measurements are in good agreement with published data. From w_{TBPB} = 0.05 to w_{TBPB} = 0.15 the *liquidus* curve rose by 6.7 K, from 273.8 K to 280.5 K . For the mass fraction going from 0.25 to 0.35, this variation was only of 0.9 K with a trend to

stabilize around 282.0 K. This fact emphasizes that, at w_{TBPB} = 0.35 we are close to the stoichiometric composition. Besides, the flattening of *liquidus* curves near the stoichiometric composition is also observed in many others semi-clathrates [164]. Our maximum value was for w_{TBPB} =0.35, i.e. 282.0 K which is slightly lower than 282.1 K, 282.4 K and 282.6 K obtained by Lin *et al. [171],* Suginaka *et al*. [112] and Zhang *et al*. [203], respectively. This variation can be related to the different measurement methods applied by authors, with their respective uncertainties. Suginaka *et al*. [112] used thermomicroscopy method while Zhang *et al*. [203] and Lin *et al*. [171] used DSC method. However, Zhang *et al*. [203] used dynamic method and considered as the dissociation point the *extremum* temperature peak. Lin *et al*. [171] used the stepwise method to measure the dissociation temperature. This method consists of increasing the sample temperature stepwise with long isothermal intervals between steps until the complete melting of the solid [176, 208-209]. They showed that it is the most accurate method, though it is very much time-consuming, since the uncertainty is the increment temperature, i.e. 0.1 K. On the other hand, a high discrepancy of 2.8 K was found between our results and that from Suginaka *et al*. [112] at w_{TBPB} = 0.1. The results from Mayoufi *et al.* [205] were generally lower than our measurements, especially for TBPB mass fraction ranging from 0.15 to 0.35. According to Lin *et al*. [171] the reason for these lower values from Mayoufi *et al.* [205] is that they considered the corrected peak temperature (T_{GEFTA}) as phase transition point, which is normally lower than the T_{end} temperature.

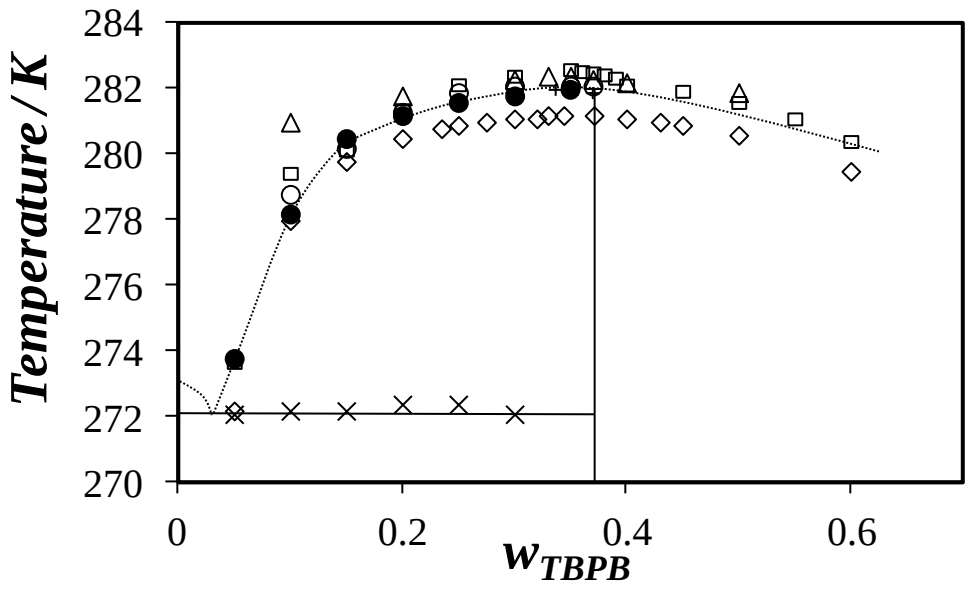

Figure 4.2. Temperature phase boundaries, T versus TBPB mass fraction, w_{TBPB}, in a binary system of TBPB + H_2O phase diagram: ● This study; □ data from Zhang et al. [203]; ◊ data from Mayoufi et al. [205]; ○ data from Lin et al. [171]; ∆ data from Suginaka et al. [112]; + data from Dyadin and Udachin [51]; × This work, eutectic points; dotted line is a proposition of liquidus curve behavior.

4.2.2 TBPB + H_2O + Gases system

To the best of our knowledge, only one data set is available in the literature for TBPB+CH_4+H_2O *[117]*. However, they only include the hydrate formation points for a TBPB mass fraction of 0.35, considered to be the stoichiometric composition of TBPB hydrate. In *Figure 4.3* our measurements using DSC dynamic method at w_{TBPB} = 0.35 are compared with those from Suginaka *et al. [117]*.

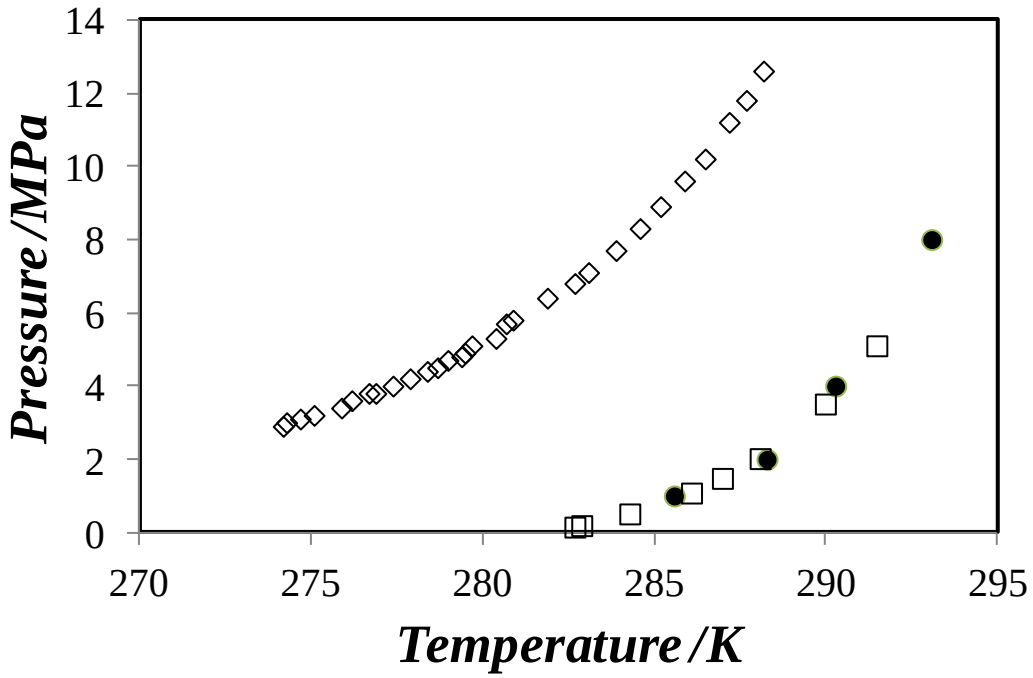

Figure 4.3. Equilibrium hydrate formation for CH_4 in pure water and for CH_4 in TBPB solution at w_{TBPB} = 0.35; ● CH_4 in TBPB solution at w_{TBPB} = 0.35, this study ;◊ CH_4 in pure water [210] ;□ CH_4 in TBPB solution at w_{TBPB} = 0.35 [117]

It may be clearly observerd in *Figure 4.3* that our results are in good agreement with the only available data in the literature, which confirms the reliability of our measurements using DSC dynamic method. Moreover, compared to pure CH_4 clathrate, which experimental data are from Maekawa *et al*. [210], we can also observe a high stabilization of TBPB semi-clathrates in presence of CH_4, which confirms that this gas has a good affinity with the empty cages of the semi-clathrates structure [105].

Figure 4.4 presents the heat flow curves for TBPB aqueous solutions in presence of CH_4 using the DSC dynamic method. We observed that at intermediate concentrations (*Figure 4.4a*), a series of eutectic peaks appear near 272 K regardless the CH_4 pressure. For higher concentration (*Figure 4.4b*) these eutectic peaks practically disappear.

In *Figures 4.4a* and *4.4b* we observed endothermic peaks between 280 and 285 K regardless the pressure of CH_4. These peaks may be related to the incomplete conversion of metastable single TBPB semi-clathrate to stable TBPB/CH_4 semi-clathrate caused by the lack of agitation in the DSC cells. For a complete conversion, a very long multicycles thermal program is necessary [83].

The melting peaks observed above 285 K are due to the dissociation of the TBPB/CH_4 semi-clathrate. We observed that the increase of TBPB mass fraction and CH_4 pressure shifted the hydrate melting peak towards higher temperatures, showing a better stabilization of TBPB/CH_4 semi-clathrate in these conditions.

The absence of eutectic peak at w_{TBPB} =0.35 in *Figure 4.4b* could be related to the stabilization of a different TBPB semi-clathrate structure. In available literature we found three possible structures mentioned by some authors. Dyadin & Udachin [51] proposed two structures, one with hydration number of 32 (w_{TBPB}=0.371) and another with 36 (w_{TBPB}=0.35), the first one being the most stable in the absence of gas pressure. Recently Muromachi *et al*. [105] provided a crystal structure analysis of TBPB semi-clathrate and found a hydration number of 38 (w_{TBPB}=0.331). However, they did not give the melting point of this structure. Another conclusion from the work of Muromachi *et al*. [105] is that one of the three available empty dodecahedral cages is not identical to the two other and according to the authors this characteristic indicates that not only the size of the guest molecule is important to the enclathration but also its shape.

In *Figure 4.4a* a second peak appears at the end of the melting peak at 4 and 8 MPa. This is could be due to a mass transfer resistance of CH_4 at the liquid-vapor interface after the hydrate dissociation.

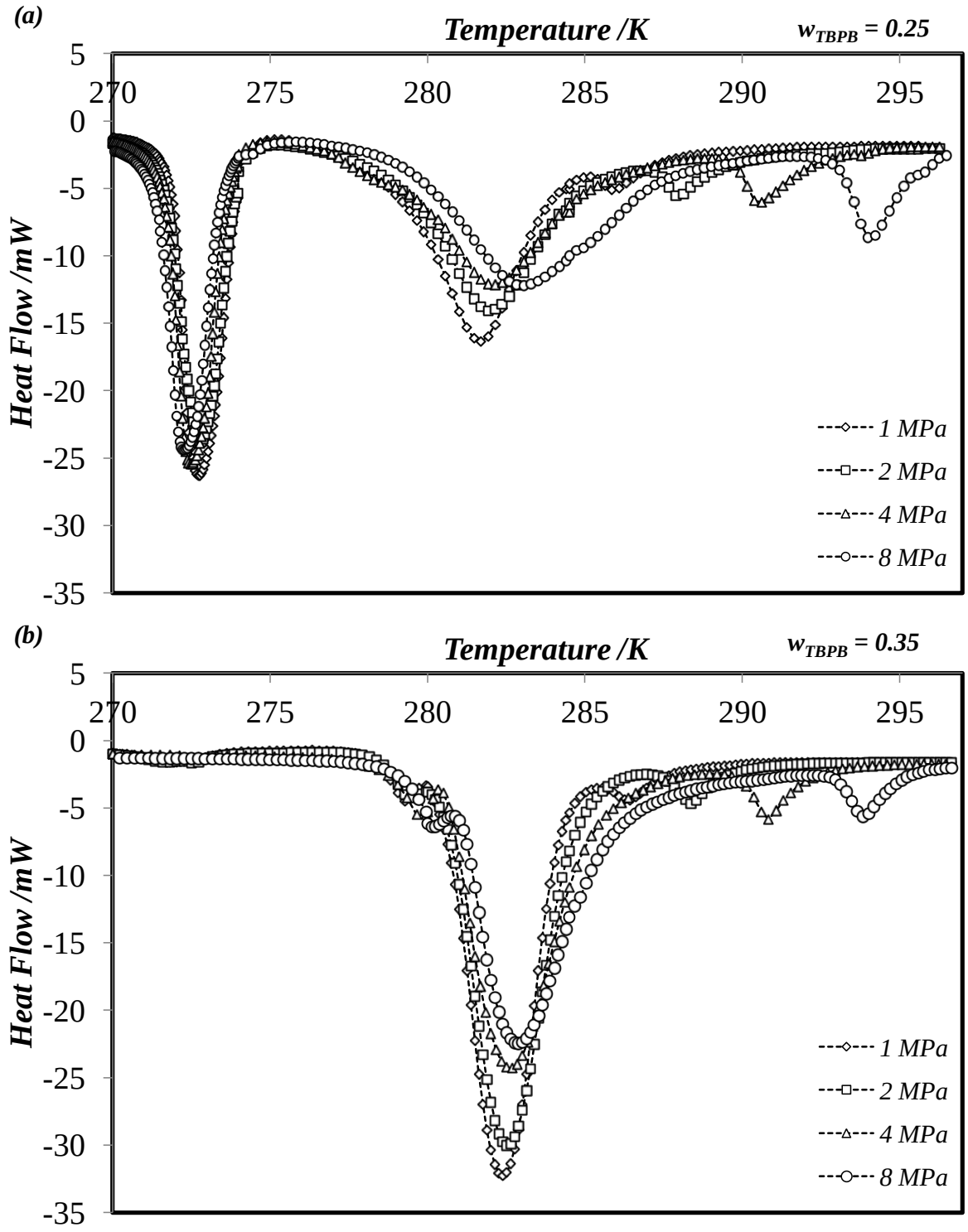

Figure 4.4. DSC curves from TBPB aqueous solutions in presence of CH_4 at heating rate of 0.5 K min^{-1}: (a) w_{TBPB} = 0.25; (b) w_{TBPB} = 0.35.

The measured dissociation temperatures for TBPB/CH_4 semi-clathrate are gathered in *Table 4.3* and plotted in *Figure 4.5.* The stability of TBPB/CH_4 semi-clathrate increases with CH_4 pressure and TBPB mass fraction, in a rangeof w_{TBPB} = *0* to 0.35. Compared to the single TBPB semi-clathrate, the dissociation temperatures for TBPB/CH_4 semi-clathrate are

increased by 6.6 to 14.5 K at w_{TBPB} = 0.05 depending on CH_4 pressure. On the other hand, at w_{TBPB} = 0.35 the gain of stability for TBPB/CH_4 semi-clathrate was smaller, i.e., from 3.6 to 11.1 K. The reason for higher temperature stability is the insertion of CH_4 gas molecules in the available empty cages of the semi-clathrate structure. Once inside the cavities the gas molecules interact with the aqueous structure by van der Waals forces increasing the thermodynamic stability of the whole structure.

Table 4.3. Dissociation temperatures of TBPB/CH_4 Semi-clathrate at CH_4 pressure from 1 to 8 MPa and TBPB mass fraction (w_{TBPB}) from 0.05 to 0.35.

w_{TBPB}	T_{diss} /K[a]			
	1.0 MPa	2.0 MPa	4.0 MPa	8.0 MPa
0.05	280.8	-	287.3	288.8
0.10	284.3	286.0	288.9[b]	291.5[b]
0.15	285.3	286.9	289.9[b]	292.7
0.20	285.6	287.6	290.3[b]	292.9
0.25	285.9	287.7	290.3	292.9
0.30	285.9	288.0	290.5	293.1[b]
0.35	285.6	288.3	290.3	293.1

Standard uncertainties *u* are: [a] $u(T_{end}(\alpha = 0)) = 0.4$ K; [b] $u(T_{GEFTA}) = 0.5$ K; $u(p) = 0.05$ MPa.

Figure 4.6 presents the temperature phase boundaries of semi-clathrate hydrates at various CH_4 pressures. This diagram allows the evaluation of the stability limits for the CH_4/TBPB semi-clathrate for a fixed pressure at variable TBPB mass fraction. For example, considering a system containing initially CH_4 at 2 MPa and aqueous solution of TBPB at w_{TBPB} = 0.15, in order to form only CH_4/TBPB semi-clathrate, the temperature should be set between 280.5 K (dissociation temperature of single TBPB semi-clathrate) and 286.7 K (dissociation temperature of CH_4/TBPB semi-clathrate). This information is also important to define the operating conditions for gas storage and gas separation processes based on hydrate formation.

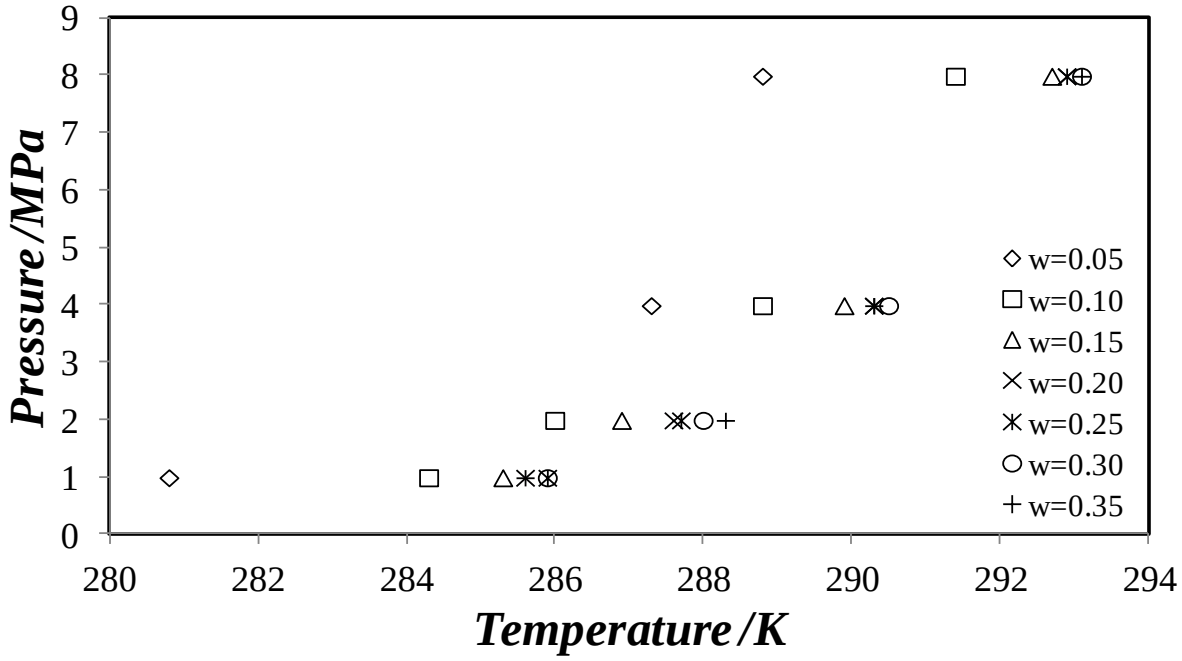

Figure 4.5. Experimental hydrate equilibrium date for TBPB/CH_4 semi-clathrate; w is the value of TBPB mass fraction.

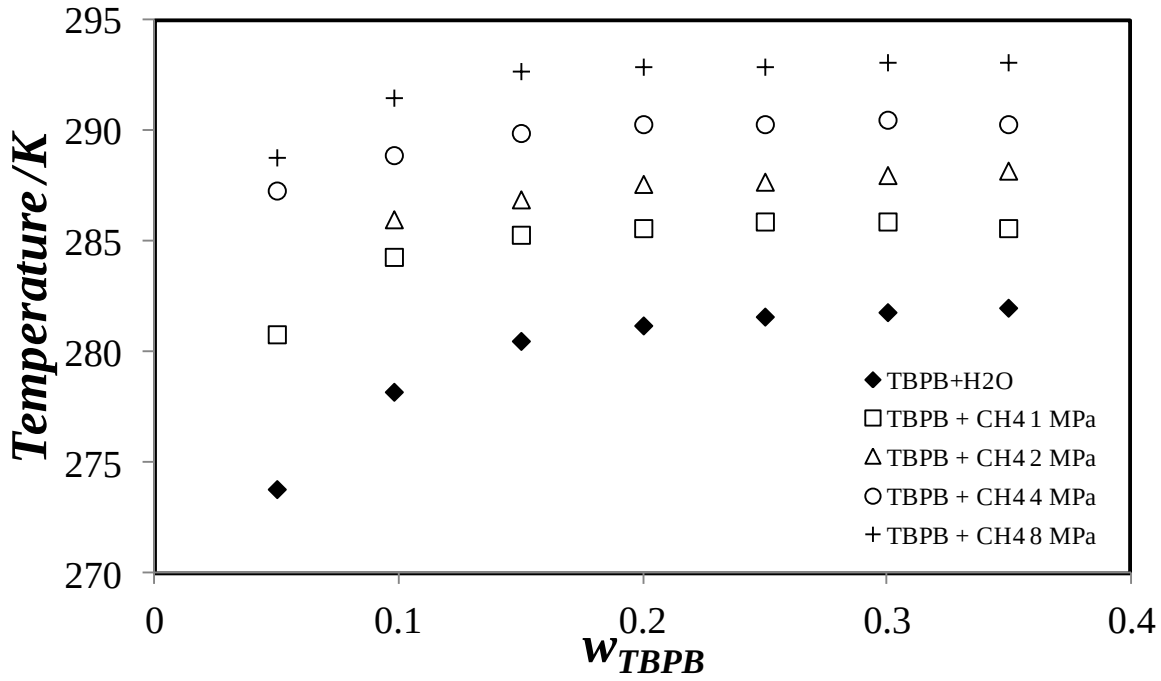

Figure 4.6. Temperature phase boundaries for single TBPB semi-clathrate and TBPB/CH_4 semi-clathrate; w_{TBPB} is the TBPB mass fraction.

In order to evaluate a possible selectivity of TBPB semi-clathrates with CO_2 or CH_4 we have plotted in *Figure 4.7* available data in literature for TBPB/CO_2 and our results for TBPB/CH_4 semi-clathrate. We notice that TBPB semi-clathrate seems to have a higher affinity for CO_2 compared to CH_4 at pressure below 4 MPa. If we observe the tendency of the set points, we can note that at a given pressure the selectivity changes, i.e., TBPB forms more stable hydrates with CH_4. This is observed at w_{TBPB} = 0.1 and pressure of 4 MPa.

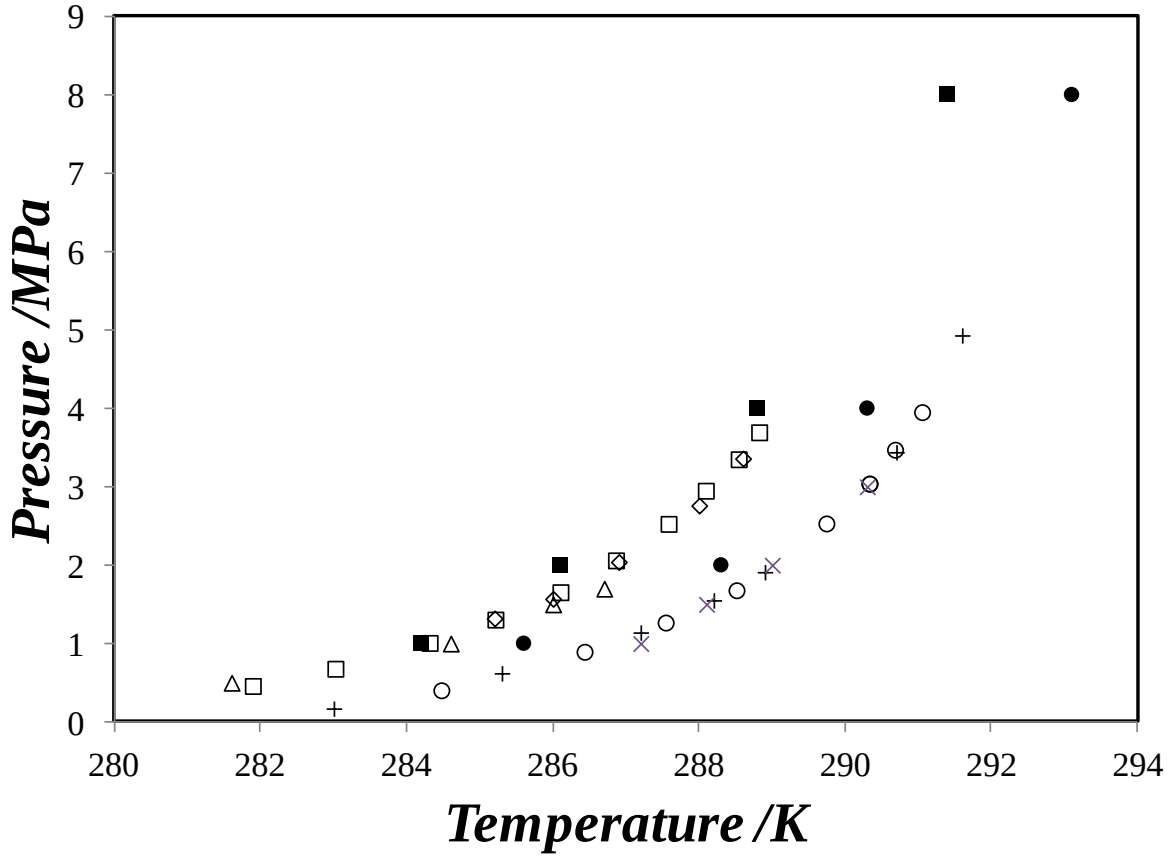

Figure 4.7. Experimental three phase equilibrium data for TBPB+CO_2+ H_2O and TBPB+CH_4+ H_2O systems; ■ TBPB+CH_4+ H_2O at w_{TBPB} = 0.1, this study; ● TBPB+CH_4+ H_2O at w_{TBPB} = 0.35, this study; □ TBPB+CO_2+ H_2O at w_{TBPB} = 0.1; data from Zhang et al. [203]; ◊ TBPB+CO_2+ H_2O at w_{TBPB} = 0.1, data from Shi et al. [211]; ⊿ TBPB+CO_2+ H_2O at w_{TBPB} = 0.1, data from Mayoufi et al. [205] ; ○ TBPB+CO_2+ H_2O at w_{TBPB} = 0.35, data from Zhang et al. [203]; + TBPB+CO_2+ H_2O at w_{TBPB} = 0.35, data from Suginaka et al. [112].

Thinking of a possible gas separation by hydrate formation process for the gas mixture of CO_2+CH_4, the difference between the thermodynamic stabilities of TBPB/CO_2 semi-clathrate and TBPB/CH_4 semi-clathrate indicates that CO_2 has a slight preference to the hydrate phase. However, thermodynamic stability is not the only parameter that must be taken into account

in this kind of process. It is also necessary to know the amount of gas stored in the hydrate phase. In this case, compared to other promoters, TBPB seems to have a higher CO_2 gas storage capacity [172]. In any cases, quantitative measurements of phase composition (especially in hydrate phase) are required to evaluate precisely the gas separation process.

From (*p,T*) phase equilibrium data it is possible to estimate the dissociation enthalpy of TBPB/CH_4 semi-clathrate (ΔH) per mole of CH_4 at w_{TBPB} = 0.35 using Clapeyron equation [93, 212-213]:

$$\frac{dP}{dT} = \frac{\Delta H}{T\Delta V} \tag{4.1}$$

where, , T is temperature, ΔV is the volume change caused by the dissociation of hydrate phase into water and gas.

For a rigorous calculation, knowledge about CH_4 solubility in TBPB aqueous solutions and densities of solid hydrate and TBPB aqueous solutions is necessary but no data about these properties were found in literature. We thus used Clausius-Clapeyron approximation, which consists in neglecting the contribution of condensed phases to the volume change:

$$\frac{d\ln P}{d(1/T)} = -\frac{\Delta H}{ZR} \tag{4.2}$$

where R is the ideal gas constant and Z is the compressibility factor of gas phase, which was calculated using Soave-Redlich-Kwong equation of state.

To apply this equation two assumptions were made:

(*i*) ΔV only depends on the volume of gas phase and therefore the molar volume of liquid phase is equal to that of the hydrate;

(*ii*) the CH_4 solubility in liquid phase is neglected, i.e., it is assumed that all CH_4 presented in condensate phase pass to gas phase after the hydrate dissociation.

Furthermore, the use of Clausius-Clapeyron equation is more accurate for low pressures [93, 214] because the errors caused by the above assumptions are reduced. Therefore, we used the data below 4 MPa. The estimated values of dissociation enthalpies for TBPB/CH_4 are presented in *Table 4.4*.

Table 4.4. Dissociation enthalpies of TBPB/CH_4 semi-clathrate at w_{TBPB} = 0.35 estimate from Clausius-Clapeyron equation.

P / MPa	T / K	ΔH $\left(kJ \cdot mol_{CH_4}^{-1}\right)$
1.0	285.7	203.5
2.0	288.1	199.3
4.0	290.3	193.1

The straight line obtained by plotting ln(*p*) vs. 1/T (correlation factor = 0.999, see *Figure 4.8*) validates the assumptions related to Clausius-Clapeyron equation. Using the (*p,T*) phase equilibrium data of TBPB/CH_4 semi-clathrate at w_{TBPB}<0.35 the values of the slopes are almost independent of composition. This observation may indicate that in the range of pressure from 1 to 4 MPa, CH_4 stabilizes the same structure of TBPB semi-clathrate regardless the TBPB mass fraction. In other words, in these thermodynamic conditions we can suppose that there is no structure transition. The value of $d\ln P/d(1/T)$ was found to be about 25.0 K.

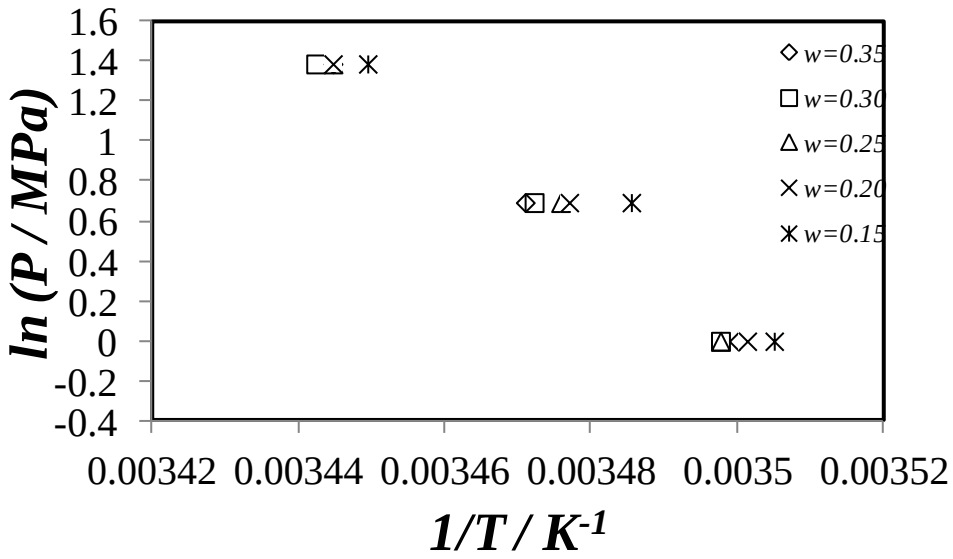

Figure 4.8. Clapeyron p-T phase diagram for TBPB+CH_4+ H_2O system; w is the value of TBPB mass fraction.

Mauyoufi *et al.* [172] used the Clausius-Clapeyron equation to estimate the dissociation enthalpy of TBPB/CO_2 semi-clathrates. They found a value of 144 $kJ \cdot mol_{CO_2}^{-1}$ which is lower than the values found in this work for TBPB/CH_4 semi-clathrate. This difference supports the hypothesis discussed above that CO_2 forms TBPB semi-clathrate more easily than CH_4 and

reinforces the possibility to use the TBPB in process of CO_2 capture from gas mixture of CO_2+CH_4.

From here, we will discuss the results involving the CO_2 + CH_4 gas mixture. For this study, the pressure range of 40 mol. % CO_2 + 60 mol. % CH_4 gas mixture used was from 1 to 2 MPa,. The aim was to provide a detailed phase diagram in a range of pressures compatible with a possible gas separation process. At higher pressures the process would not be viable from an energetic point of view. The measured dissociation temperatures are presented in *Table 4.5.*

Table 4.5. Dissociation temperatures of TBPB/CO_2+CH_4 semi-clathrates at gas phase pressure from 1 to 2 MPa and TBPB mass fraction (w_{TBPB}) from 0.05 to 0.35 (Gas mixture containing 40 %mol of CO_2) .

w_{TBPB}	T_{diss} /K[a]		
	1.0 MPa	1.5 MPa	2.0 MPa
0.05	281.4	282.5	283.3
0.10	284.2	285.4	286.7
0.15	285.0	286.7	287.5
0.20	285.9	287.2	288.3[b]
0.25	286.0	287.6[b]	288.6
0.30	286.2		288.6
0.35	286.1		288.4

Standard uncertainties *u* are: [a] $u(T_{end}(\alpha = 0)) = 0.4$ K; [b] $u(T_{GEFTA}) = 0.5$ K; $u(p) = 0.05$ MPa.

From w_{TBPB} = 0.05 at 1 MPa to w_{TBPB} = 0.35 at 2 MPa the temperature varied from 281.4 to 288.3, i.e., a gain of 6.9 K. The stabilization gain happens specially from 0.05 to 0.20, i.e., 4.5, 4.7 and 5 for 1, 1.5 and 2 MPa, respectively. From w_{TBPB} =0.2 to 0.35 the gain is around 0.2, 0.4 and 0.1 K for 1, 1.5 and 2 MPa, respectively. This evidences the possibility to design a process working at lower concentrations without losing hydrate stability. Besides, in these conditions the condensed phases (liquid-hydrate) will be in form of gas hydrate slurry. The advantages of gas hydrate slurries are well discussed in available literature [81-82, 104].

As observed in the study with only CH_4, the dissociation temperature increase with the pressure and the TBPB mass fraction. The stability of mixed TBPB/CO_2+CH_4 semi-clathrate was higher compared to the single TBPB semi-clathrate. This result indicates that the gases are incorporated into the empty cages of the semi-clathrate structure. Moreover, the dissociation temperatures were slightly higher than those from TBPB/CH_4 semi-clathrate. This is probably due to the presence of CO_2, which forms TBPB semi-clathrates that are more

stable than with CH_4 (see *Figure 4.7*). Acosta *et al.* [135] have noted the same behavior in their study with CO_2+CH_4 gas mixture in presence of TBAB aqueous solutions.

However, our results do not enable to define the distribution of each gas in semi-clathrate structures, In particular, it is not possible to determine the selectivity of the separation process since the composition of phases may not be determined in DSC experiments. To answer this question more experiments will be necessary to enable characterizing the hydrate phase.

For gas separation using semi-clathrate gas hydrates it is important to know the stability region where the hydrate phase will be formed. To increase separation efficiency it is suitable to form only gas-containing semi-clathrate. The temperature phase boundary diagram (*Figure 4.9*) helps selecting the best operation conditions to be used to achieve this goal.

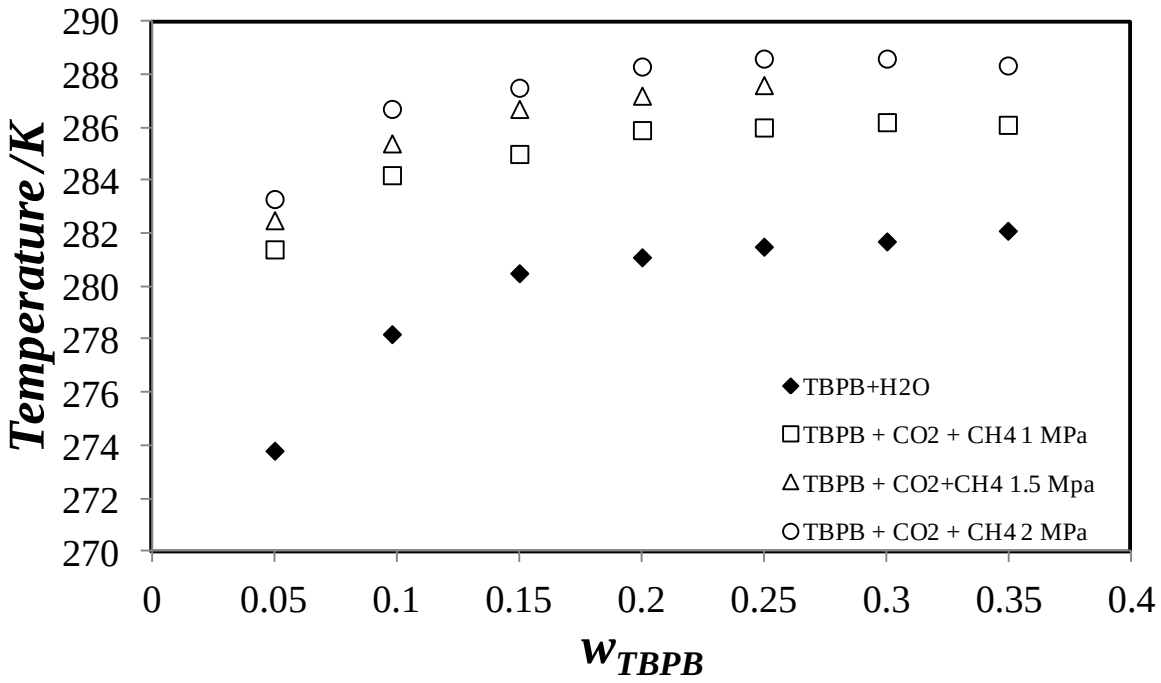

Figure 4.9. Temperature phase boundaries for single TBPB semi-clathrate and TBPB/CH_4+CO_2 (Gas mixture containing 40 %mol of CO_2).

4.3 Systems involving TBPO promoter

Dissociation temperatures of TBPO single semi-clathrate were measured in a range of TBPO mass fraction from 0.05 to 0.40. For TBPO/gas (CH_4, CO_2 and CO_2+CH_4) semi-clathrates, the equilibrium temperatures were determined in a range of TBPO mass fraction from 0.05 to 0.30 and a range of gas pressures from 1 to 3 MPa.

4.3.1 TBPO + H_2O system

Figure 4.10 presents DSC thermograms obtained from dynamic method during the melting of TBPO semi-clathrate at various additive mass fractions. We observe a first peak starting at around 272 K regardless the TBPO concentration. This peak is attributed to the melting of the eutectic mixture composed largely of ice and in minority of TBPO semi-clathrate. The second peak corresponds to the progressive melting of excess TBPO semi-clathrate. It seems that the *extremum* temperature peak increases only from w_{TBPO}= 0.05 to 0.10 and then remains almost constant around 280 K. This indicates a flattening of *liquidus* curves, which was already observed for other semi-clathrates [164].

The reduction of the size of eutectic peak with the increase of w_{TBPO} is due to the decreasing of free water available after semi-clathrate crystallization. Nevertheless, it was expected to see an absence of the eutectic peak at higher concentrations indicating that the system is equal or above the stoichiometric composition. In literature we found a first structure of TBPO.28H_2O which corresponds to w_{TBPO} = 0.30 [51, 106, 215]. Alekseev *et al.* [106] carried out a study of a crystal of TBPO semi-clathrate formed from TBPO aqueous solutions with w_{TBPO} = 0.10 - 0.15. They isolated one structure and characterized it with the formula of TBPO.34.5H_2O (w_{TBPO}=0.26). However, the thermograms from 26 wt.% still presented eutectic peaks, which may indicate a difficulty to convert all water into hydrate. This difficulty could be related to the fact that TBPO and H_2O can become partially immiscible at room temperature over a given concentration range [187]. As a result, it is possible that during the cooling phase, the system was not homogeneous and then the water was not completely converted to hydrate. Therefore, metastable phases could be formed. In order to eliminate any metastable phase and to ensure a complete conversion of water into hydrate, we used the multiple cooling-heating cycles. The dissociation phenomenon was carried out using DSC dynamic and stepwise methods. Some thermograms from these approaches are shown in *Figures 4.11* and *4.12.*

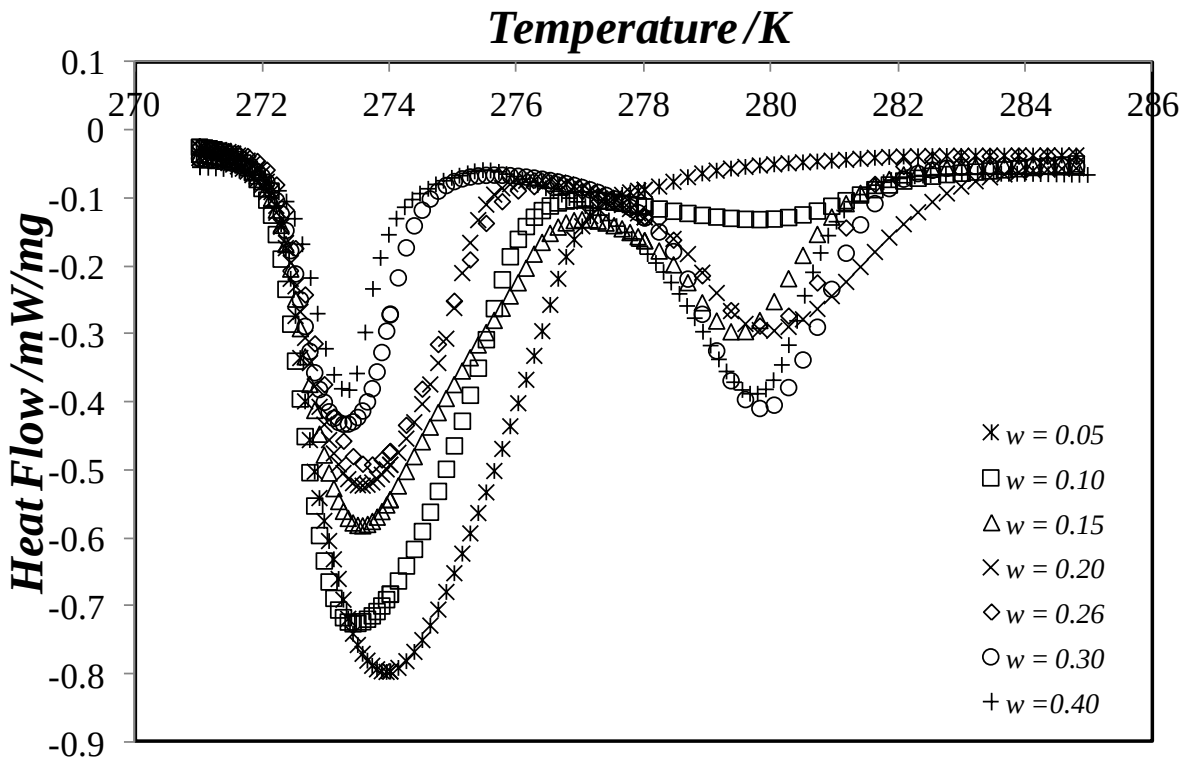

Figure 4.10. DSC thermograms of the melting of single TBPO semi-clathrate at variable additive composition recorded at 0.5 K min^{-1}; w is the value of TBPO mass fraction.

From *Figure 4.11*, we observe that at w_{TBPO} = 0.26 a small eutectic peak is still present, while for w_{TBPO} = 0.30 and 0.40 it completely disappeared. These results lead us to conclude that stoichiometric composition of TBPO + H_2O system is between w_{TBPO} = 0.26 and 0.30. We also observe from *Figure 4.11* that the progressive peaks corresponding to the melting of the TBPO semi-clathrate are at least 1 K higher than the peaks obtained using one cooling-heating step. We attribute these higher temperatures to the removal of metastable phases having incongruent melting that could be present. Indeed, Alekseev *et al.* [106] and Dyadin and Udachin [51] explain that several polyhydrates are formed from TBPO + H_2O system and the hydration number of 28 was, in fact, an averaged value for all these structures.

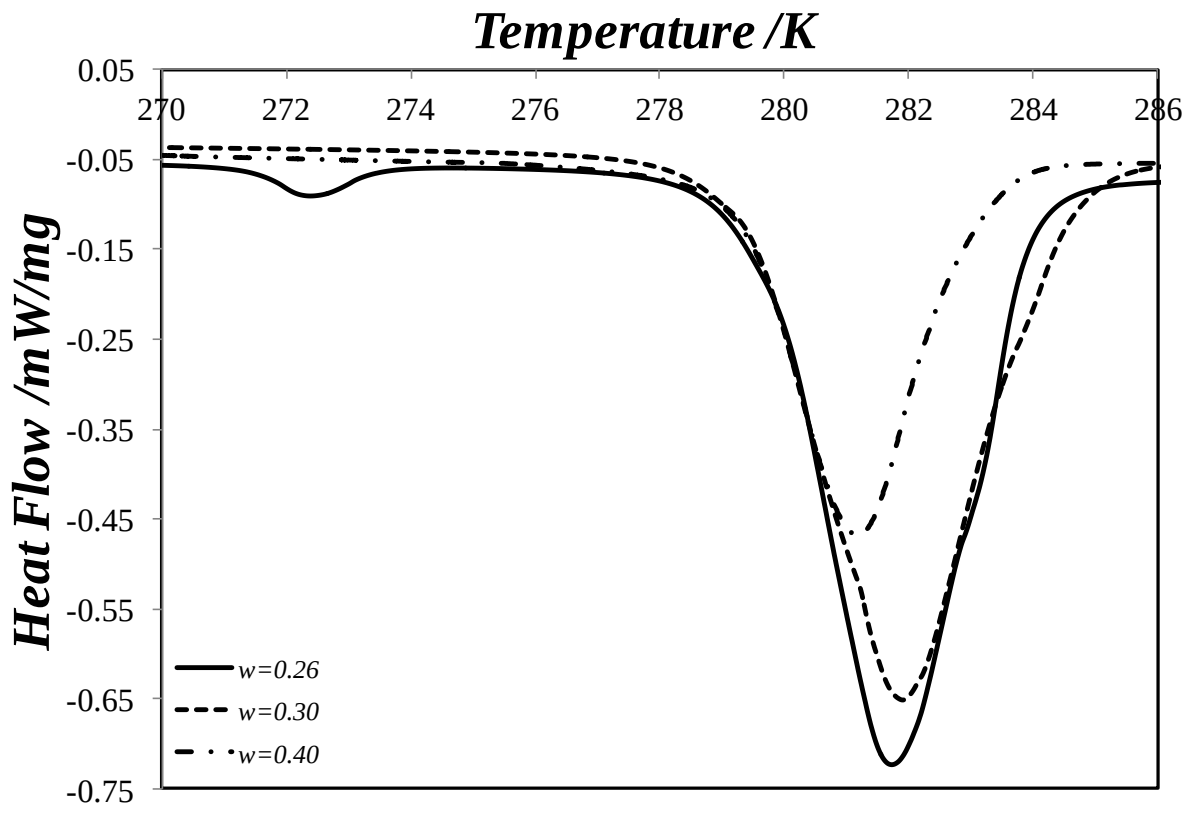

Figure 4.11. DSC thermograms of the melting of single TBPO semi-clathrate obtained using multiple cooling-heating cycles at variable additive composition recorded at 0.5 K min^{-1}; w is the value of TBPO mass fraction.

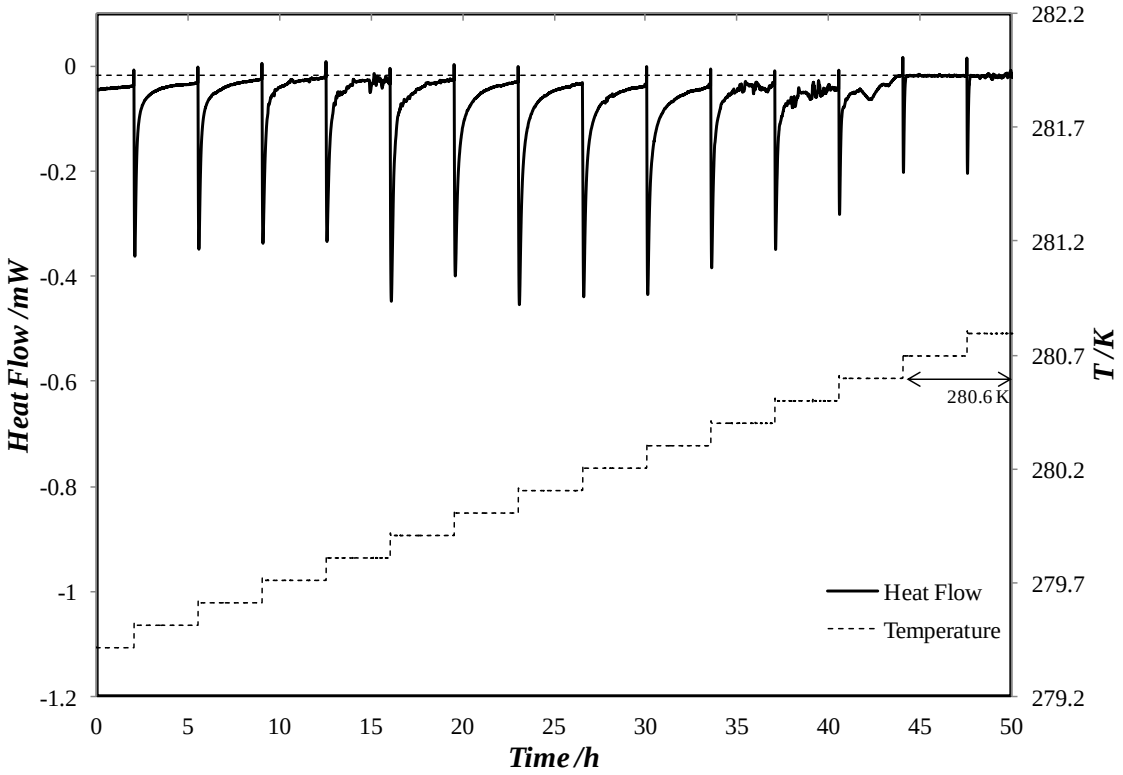

Figure 4.12. Heat Flow and temperature profiles during DSC stepwise method of TBPO semi-clathrate formed from a solution at w_{TBPO} = 0.20.

We can observe in *Figure 4.12* the final step temperature of TBPO semi-clathrate formed from a solution at w_{TBPO} = 0.20 being around 280.6 K. The measured phase transition temperatures using DSC method for TBPO semi-clathrates formed from different additive concentrations are presented in *Table 4.6*. We observe that the increase of TBPO mass fraction increases the stability of hydrate phase from 0.05 to 0.30, then the dissociation temperature decreased at w_{TBPO} = 0.40. The highest value being 281.0 K for w_{TBPO} = 0.30. The measured dissociation temperatures values are plotted in *Figure 4.13*.

Table 4.6. Measured phase transition temperatures of TBPO+H_2O system at different TBPO mass fractions.

w_{TBPO}	*Tdiss*/ K[a]
0.05	278.1[b]
0.10	280.3
0.15	280.5
0.20	280.6
0.26	280.9
0.30	281.0
0.40	280.5

Standard uncertainties *u* are: [a] $u(T_{step})$ = 0.1 K; [b] $u(T_{end}(\alpha = 0))$ = 0.4 K

From *Figure 4.13* we observe that the *liquidus* curve and the liquid-liquid solubility curve measured by Higgins and Baldwin [187] stay almost constant and symmetrical from w_{TBPO} = 0.10 to 0.40. As regards the TBPO semi-clathrate, from w_{TBPO} = 0.05 to 0.10 the *liquidus* curve rises by 2.2 K, i.e., from 278.1 to 280.3 K. Then, from w_{TBPO} = 0.15 to 0.30, the difference is only 0.5 K. At w_{TBPO} = 0.40 the curve seems to decrease, indicating that system is, indeed, beyond the stoichiometric composition which is supposed to be near w_{TBPO} = 0.30.

The dissociation temperature measured at w_{TBPO} = 0.30 using one cooling-heating cycle was around 280.2 K, which is very close to 280.3 K, the melting point mentioned by Dyadin *et al*. [51] for a hydrate having a composition of TBPO.28H_2O. However, after using cooling-heating cycles in order to eliminate any metastable phases and convert all TBPO into semi-clathrate, the dissociation temperature rose almost 1 K, being 281.0 K. As written above, the hydration number of the compound TBPO.28H_2O is an averaged value from several polyhydrates. Probably, most of these structures were metastable phases having melting temperatures lower than stable hydrate, which could explain the discrepancy of the melting point mentioned by Dyadin *et al*. [51] and our results. A similar behavior was also observed by Lin *et al*. [173] measuring the melting point of semi-clathrates formed from TBAB+TBPB+H_2O system. Although the very detailed study carried out by Alekseev *et al*. [106] for the compound TBPO.34.5H_2O no information about the melting point was provided.

The dissociation enthalpy measured at w_{TBPO} = 0.30, which is very close to the stoichiometric composition, was about 219.4 J g^{-1}. This value is lower than the dissociation enthalpy of ice (333 J g^{-1}), but higher than the other well know semi-clathrates, such as the TBAB (~200 J g^{-1}) [101] and TBPB (~200 J g^{-1}) [112, 173]. As far as we know, there is no available data about

dissociation enthalpy of TBPO semi-clathrate in literature that we could compare to our results.

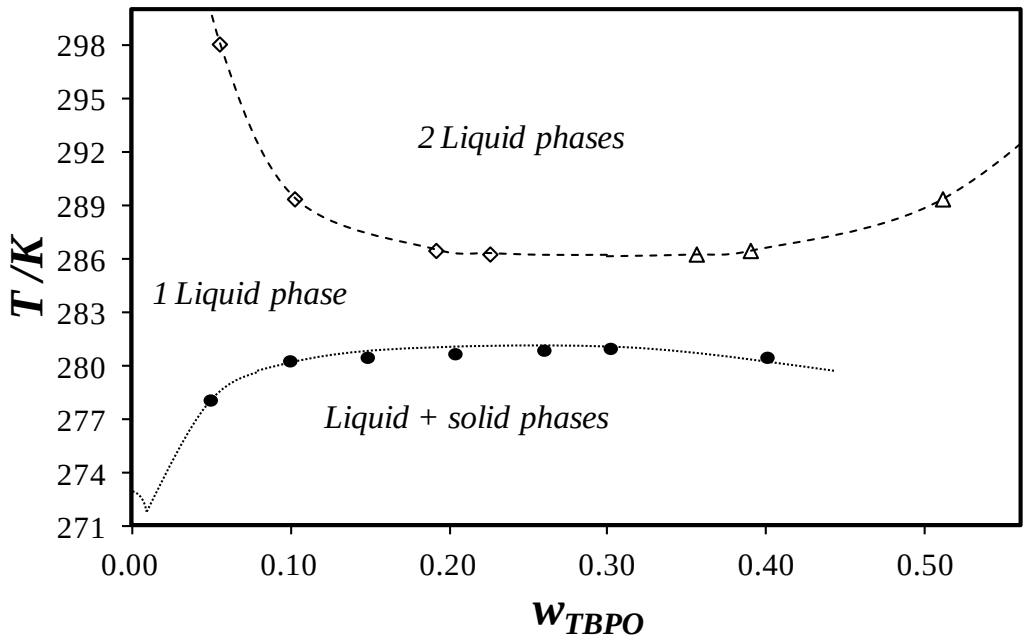

Figure 4.13. Temperature phase boundaries, Temperature versus TBPO mass fraction (w_{TBPO}): ● dissociation point of TBPO semi-clathrate, this work; Δ solubility point of water in TBPO, (Higgins and Baldwin [187]); ◊ solubility point of TBPO in water (Higgins and Baldwin [187]); dotted line is a proposition of liquidus curve behavior; dashed line is a proposition of liquid-liquid solubility curve behavior.

4.3.2. TBPO + H_2O + Gases system

We measured the hydrate-liquid-vapor equilibrium conditions for TBPO/CO_2, TBPO/CH_4 and TBPO/(CO_2+CH_4) semi-clathrates at TBPO mass fraction ranging from 0.05 to 0.30 and gas pressure varying between 1 and 3 MPa. The measured values are listed in *Table 4.7*. The subscripts "*b*" and "*c*" denote that the dissociation temperature was determined by T_{GEFTA} and T_{step} methods, respectively, while the remaining data were obtained by T_{end} ($\alpha = 0$) method. As said in the Section 2.2.1, T_{GEFTA} and T_{step} were used to estimate the dissociation temperatures when it was not possible to determine the inflection point. For some cases, having used T_{GEFTA} or T_{end} ($\alpha = 0$), we also measured the dissociation temperature by the stepwise method in order to compare the results to the most accurate method. Then, we can note from the Table 3 that the results from dynamic method (T_{end} ($\alpha = 0$) and T_{GEFTA}) have shown a good agreement with those of stepwise method. In these cases having two temperatures for the same condition, the

reader should consider those from the stepwise method as the equilibrium point. These equilibrium data are plotted in *Figures 4.14 - 4.18*.

Table 4.7. Dissociation temperatures of TBPO/CO_2, TBPO/CH_4 and TBPO/(CO_2+CH_4) semi-clathrates at gas phase pressure ranging from 1 to 3 MPa and TBPO mass fraction (w_{TBPO}) from 0.05 to 0.30 (Gas mixture containing 40 ± 1 mol.% of CO_2).

w_{TBPO}	T_{diss} /K[a]			
	CO_2			
	1.0 MPa	1.5 MPa	2.0 MPa	3.0 MPa
0.05	284.4[b]	285.6	286.7	288.0
0.10	285.7	286.6	287.5	288.6
0.15	286.4 (286.0[c])	287.3 (287.0 [c])	288.0	289.2
0.20	286.1	287.1	288.1 (288.0[c])	289.2[b]
0.26	285.7	286.7	287.5	288.7
0.30	285.8[c]	286.7[b] (286.8[c])	287.8[c]	289.3 (289.0[c])
	CH_4			
	1.0 MPa	1.5 MPa	2.0 MPa	3.0 MPa
0.05	285.2[b]	287.2[b]	288.8[b]	291.2[b]
0.10	287.1	289.0	290.6	292.3
0.15	287.4[c]	289.2[c]	290.8[c]	292.4[c]
0.20	287.7	289.4	291.0 (290.9[c])	292.5
0.26	287.4[b]	289.0	290.4[b]	292.2[b]
0.30	287.4[c]	289.1[c]	290.5[c]	292.4[b]
	$0.40CO_2 + 0.60CH_4$			
	1.0 MPa	1.5 MPa	2.0 MPa	3.0 MPa
0.05	284.6[b]	286.6[b]	288.1	290
0.10	286.1	287.6	288.9	290.5
0.15	287.2 (286.9[c])	288.4[c]	289.8 (289.7[c])	291.3[c]
0.20	286.8	288.1	289.4	291.1
0.26	286.9[b]	288.5[b]	289.8[b]	291.4[b]
0.30	287.0[c]	288.6[b]	290.1[c]	291.5[c]

Standard uncertainties: [a] $u(T_{end}(\alpha = 0)) = 0.4$ K; [b] $u(T_{GEFTA})$=0.5 K ; [c] $u(T_{STEP})$=0.1 K ; $u(p) = 0.05$ MPa.

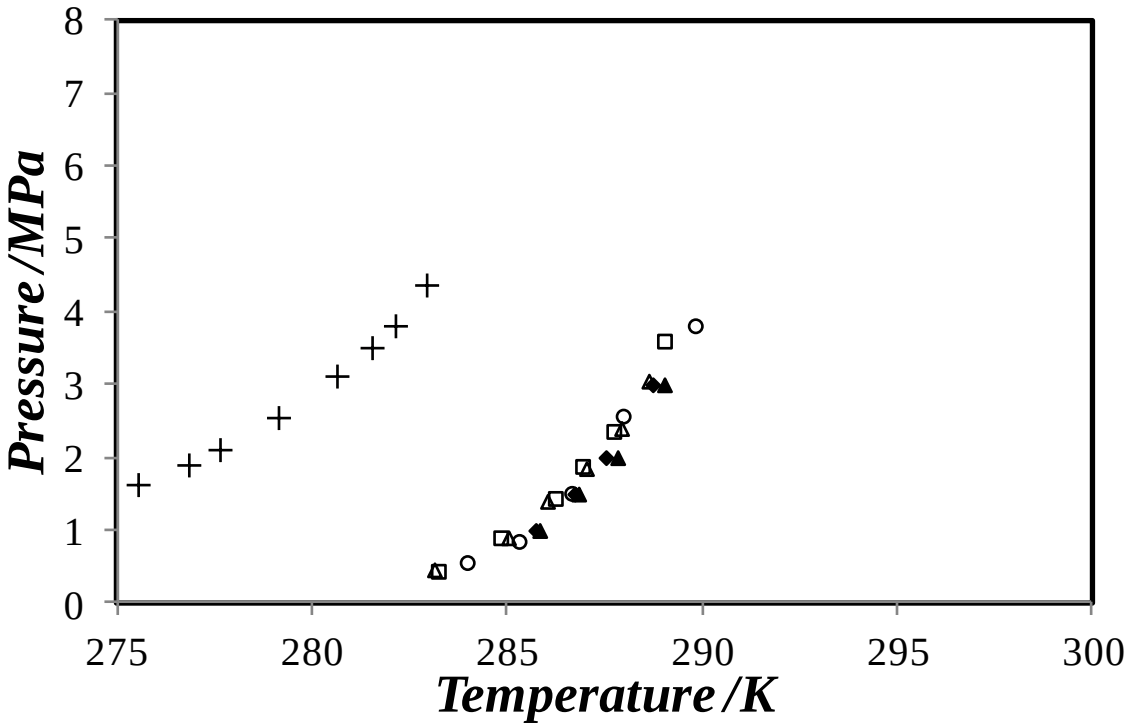

Figure 4.14. Equilibrium hydrate formation for CO_2 in pure water and for CO_2 in TBPO solution at w_{TBPO}=0.26 and 0.30; ♦, TBPO+CO_2+ H_2O at w_{TBPO} = 0.26, this study; ▲, TBPO+CO_2+ H_2O at w_{TBPO} = 0.30, this study; □, TBPO+CO_2+ H_2O at w_{TBPO} = 0.26, data from Cha et al. [121]; ◭, TBPO+CO_2+ H_2O at w_{TBPO} = 0.30, data from Cha et al. [121] ; ○, TBPO+CO_2+ H_2O at w_{TBPO} = 0.26, data from Du et al. [122]; +, CO_2+ H_2O, data from Adisasmito et al. [108].

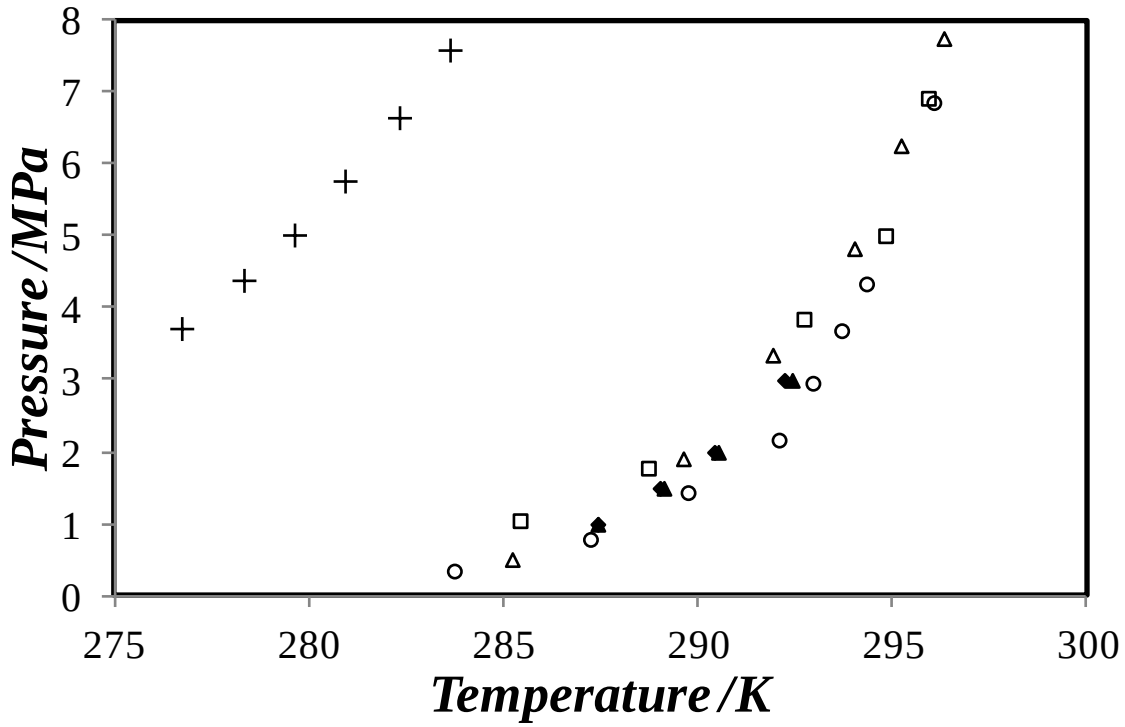

Figure 4.15. Equilibrium hydrate formation for CH_4 in pure water and for CH_4 in TBPO solution at w_{TBPO}=0.26 and 0.30; ♦, TBPO+CH_4+ H_2O at w_{TBPO} = 0.26, this study; ▲, TBPO+CH_4+ H_2O at w_{TBPO} = 0.30, this study; □, TBPO+CH_4+ H_2O at w_{TBPO} = 0.26, data from Cha et al. [121]; ∆, TBPO+CH_4+ H_2O at w_{TBPO} = 0.30, data from Cha et al. [121] ; ○ TBPO+CH_4+ H_2O at w_{TBPO} = 0.26, data from Du et al. [122]; +, CH_4+ H_2O, data from Adisasmito et al. [108].

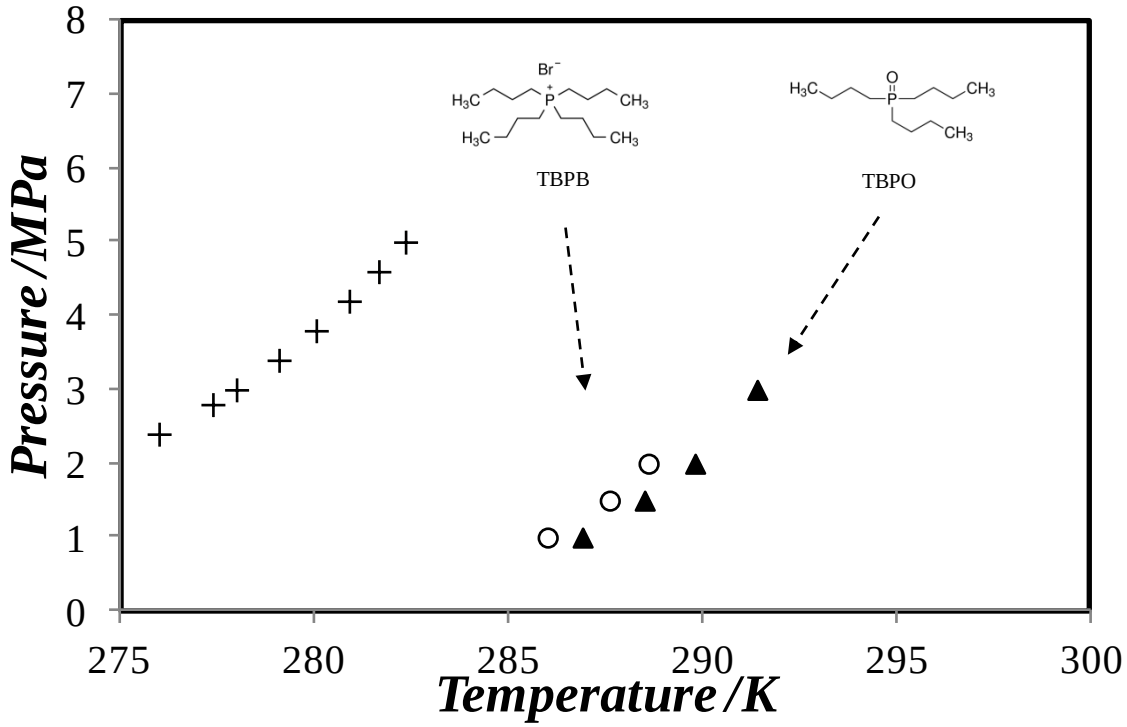

Figure 4.16. Equilibrium hydrate formation for CO_2 + CH_4 in pure water and for CO_2 + CH_4 in TBPO solution at w_{TBPO}=0.26; ▲, TBPO+CO_2+CH_4+H_2O at w_{TBPO} = 0.26, this study; ○ TBPB+CO_2+CH_4+H_2O at w_{TBPB} = 0.25, data from Sales Silva et al.[216]; +, CO_2 + CH_4+ H_2O calculated data from CSMGem [154]; gas mixture containing 40 ± 1 mol.% of CO_2.

Figures *4.14*, *4.15* and *4.16* show the gas hydrate equilibrium curves for TBPO/gas semi-clathrate measured at w_{TBPO} = 0.26 and 0.30. The available data from literature are also plotted in order to compare with our results. In general, compared to the respective pure gas clathrate, the TBPO/gas semi-clathrates are more stable, which confirms the inclusion of gas molecules into the available empty cages in the TBPO semi-clathrate structure. Indeed, Alekseev *et al.* [106] proposed that the compound having the formula TBPO.34.5H_2O contains some empty dodecahedral cages that are able to encage small molecules, such as CO_2 and CH_4. These kinds of cages are also present in TBAB.38H_2O semi-clathrate, which is known for its ability to trap CO_2 molecule [57].

In *Figure 4.14* we observe that our results are in good agreement with literature. Moreover, the curves of TBPO/CO_2 semi-clathrates at w_{TBPO} = 0.26 and 0.30 are very close to each other. Such behavior, which was also observed by Cha *et al*. [121], obeys to the same trend observed for single TBPO semi-clathrate (practically no variation of dissociation temperature between w_{TBPO} = 0.26 and 0.30).

For TBPO/CH_4 semi-clathrates in *Figure 4.15*, our results are located between those from Du *et al.* [122] and Cha *et al.* [121]. Note that, although these authors used the same method to determine the equilibrium conditions (step-heating pressure-search method in a isochoric cell), there is a high discrepancy between their data. It is probably due to the complexity of the system that forms several polyhydrates, among which may exist some metastable phases.

This problem was not observed for TBPO/CO_2 semi-clathrates, since all data seem to be in agreement. This different behavior might be related to higher solubility of CO_2 compared to CH_4. During hydrate phase formation, the interfacial mass transfer is limited by the solubility of gas in liquid phase. Thus, CO_2 is more easily transferred to the liquid phase and encaged into the semi-clathrate structure thanks to its higher solubility. As a result, less metastable phases are formed.

We compare in *Figure 4.16* the equilibrium curve of TBPO/(CO_2+CH_4) semi-clathrate at w_{TBPO} = 0.26 to the equilibrium curve of TBPB/CO_2+CH_4 semi-clathrate at w_{TBPB} = 0.25 obtained from the Section 4.2.2. We observe that TBPO additive forms more stable hydrate phase with CO_2+CH_4 gas mixture than the TBPB additive. This could be related to the different kind of molecular structure of semi-clathrate that these additives form, as well as the different molecular interactions that the guest molecules have with the water framework. While for TBPB additive cation/anion couple form ionic bonding with the semi-clathrate structure, TBPO additive with the high electronegative oxygen may form hydrogen bonds with the water framework and/or the encaged gas molecule [105-106].

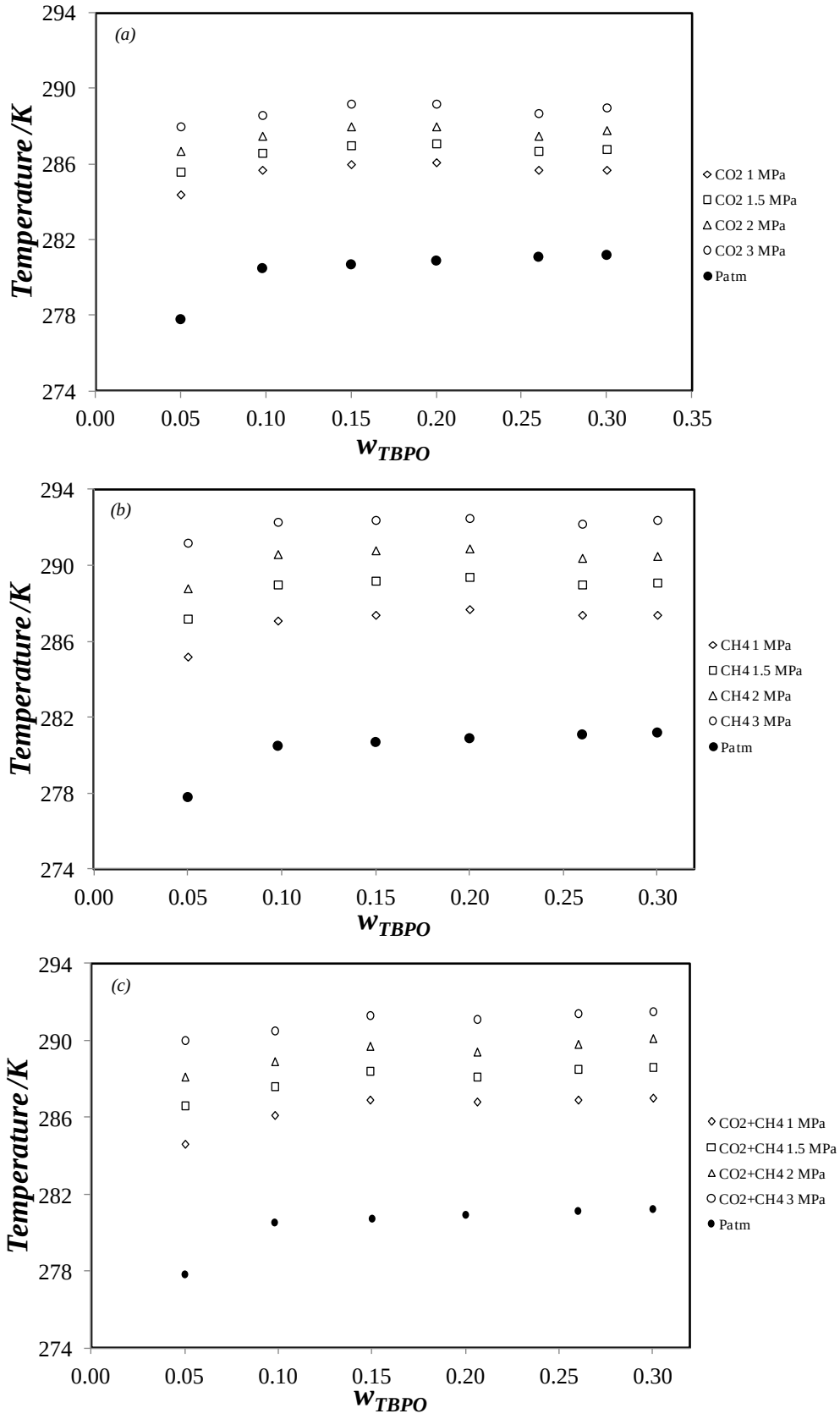

Figure 4.17. Temperature phase boundaries for single TBPO semi-clathrate and TBPO/Gas semi-clathrate: (a) CO_2; (b) CH_4; (c) CO_2+CH_4 (Gas mixture containing 40 ± 1 mol.% of CO_2).

The temperature phase boundaries for TBPO/gas semi-clathrates are presented in *Figure 4.17*. We observe a high stabilization of TBPO/gas semi-clathrate compared to the single TBPO semi-clathrate. Depending on the pressure, at w_{TBPO} = 0.05 the gain of stability is from 6.6 to 10.2 K for TBPO/CO_2 semi-clathrate. For the same mass fraction this gain is higher for TBPO/CH_4 semi-clathrate, i.e, from 7.4 to 13.4 K. These higher dissociation temperatures are due to the insertion of the gas molecules (in our case, CO_2, CH_4 and CO_2+CH_4) in the available empty cages of the semi-clathrate structure.

In general, at fixed TBPO mass fraction, the stability of TBPO/gas semi-clathrate increase with gas pressure. For a fixed pressure, the stability increases from w_{TBPO} = 0.05 to 0.10. Taken into account the experimental uncertainties, in *Figures 4.17(a)* and *4.17(b)*, from w_{TBPO} = 0.10 to 0.20 the *liquidus* curve is practically constant, having a tendency to decrease at w_{TBPO} = 0.26. Then, at w_{TBPO} = 0.30, the dissociation temperature is slightly higher, following the same behavior observed by Cha *et al*. [121]. For the TBPO/(CO_2+CH_4) semi-clathrate in *Figure 4.17(c)*, at a fixed pressure the dissociation temperature increases from w_{TBPO} = 0.05 to 0.15 and then tends to stabilize.

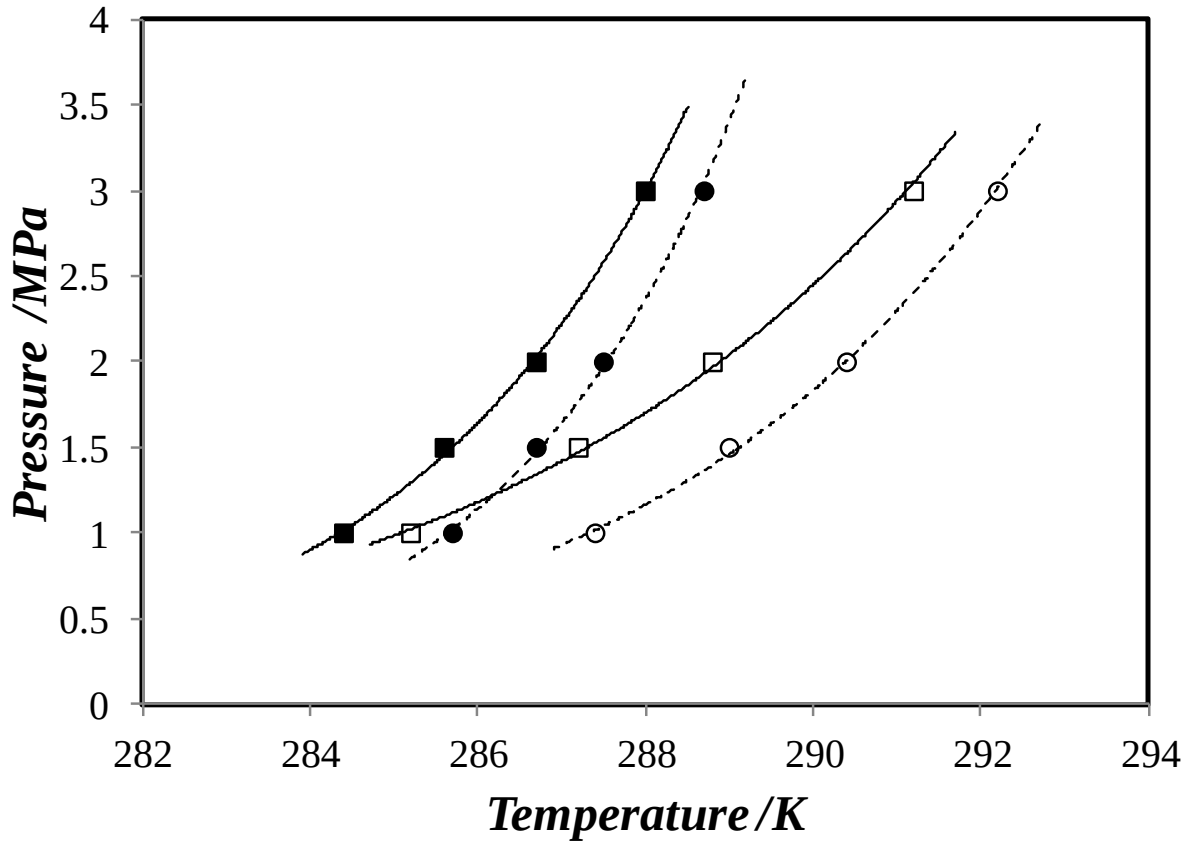

Figure 4.18. Experimental three phase equilibrium data for TBPO+CO_2+ H_2O and TBPO+CH_4+ H_2O systems; ■ TBPO+ CO_2+ H_2O at w_{TBPO} = 0.05; ● TBPO+ CO_2+ H_2O at w_{TBPO} = 0.26; □ TBPO+ CH_4+ H_2O at w_{TBPO} = 0.05; ○ TBPO+CH_4+ H_2O at w_{TBPO} = 0.26; solid and dashed lines are the exponential curve fitted from the data.

The tendency observed by Cha *et al.* [121] and Du *et al.* [122] that TBPO forms more stable semi-clathrate with CH_4 was also confirmed by our study (see *Figure 4.18*). This result represents an inversion of stability because, normally, the CO_2 hydrates are more stable [111], even with other additives [125, 132, 217]. This inversion of stability could be related to the stabilization of different semi-clathrate structures for each gas and/or to the intermolecular interaction that the additive could have with the gas molecule.

We also observe that the equilibrium curves are more distant compared to the other additives, such as TBAB [217] and TBPB [204]. This observation may indicate that TBPO could be more efficient in a possible gas separation by hydrate formation process involving CO_2+CH_4.

The dissociation enthalpy (ΔH) of TBPO/CO_2 semi-clathrate per mole of water was measured using DSC. The results are presented in *Table 4.8*. We couldn't measure the

dissociation enthalpy for TBPO/CH_4 semi-clathrates due to the low resolution peaks obtained. However we can estimate its value per mole of gas from the (*p*,*T*) phase equilibrium data by using Clapeyron equation [93, 212-213]. For an accurate estimation it would be necessary to know the solubility of CO_2 and CH_4 in TBPO aqueous solutions, as well as the densities of the liquid and solid phase. However, no data about these parameters are available in literature. We thus used Clausius-Clapeyron approximation (see *Equation 4.2*), which consists in neglecting the contribution of condensed phases to the volume change. To apply this equation, we also made the same assumptions as mentioned in *Section 4.2.2*.Moreover, we only used this equation for one component gas phase. For gas mixture, another assumption that gas composition does not change should be done, which increases the inaccuracy of the approximation. The results are listed in *Table 4.8.*

Table 4.8. Dissociation enthalpies of TBPO/CO_2 and TBPO/CH_4 semi-clathrate at w_{TBPO}=0.30; ΔH^{DSC} measured from DSC apparatus; ΔH estimated from Clausius-Clapeyron equation.

		CO_2	
P / MPa	T / K	$\Delta H^{DSC\ a}$ $\left(kJ \cdot mol_{H_2O}^{-1}\right)$	ΔH $\left(kJ \cdot mol_{CO_2}^{-1}\right)$
1.0	285.8	6.85	212
1.5	286.8	6.89	205
2.0	287.8	7.35	198
3.0	289.0	7.43	182
		CH_4	
P / MPa	T / K	ΔH^{DSC} $\left(kJ \cdot mol_{H_2O}^{-1}\right)$	ΔH $\left(kJ \cdot mol_{CH_4}^{-1}\right)$
1.0	287.4	-	149
1.5	289.1	-	148
2.0	290.5	-	147
3.0	292.4	-	144

[a] *Standard relative uncertainty ur is: ur(ΔH^{DSC}) = 3%.*

In *Figure 4.19,* we plotted ln(*p*) vs. 1/*T* and observed that the obtained straight lines fitted from experimental point had a correlation factor higher than 0.995, which validates the assumptions related to Clausius-Clapeyron equation. We also observed that, for a same system, the curves slopes were almost equal regardless the additive mass fraction. Indeed, the values of $d\ln p/d(1/T)$ were found to be about 28.9 ± 1.1 K for TBPO + CO_2 + H_2O system and 19.0 ± 0.6 K for TBPO + CH_4 + H_2O system. These almost constants values may indicate

that in the investigated range of pressure (1 to 3 MPa), there is no semi-clathrate structure transition.

For TBPO/CO_2 semi-clathrate the dissociation enthalpy per mole of water increases with pressure following the same behavior for others semi-clathrates gas hydrates, such as TBAB/CO_2 [126] and TBPB/CO_2 [172]. In the work of Deschamps & Dalmazzone [126] the dissociation enthalpy of TBAB/CO_2 semi-clathrate varied from 6.23 $kJ \cdot mol_{H_2O}^{-1}$ to 7.13 $kJ \cdot mol_{H_2O}^{-1}$ for pressure raging from 0.83 MPa to 2.25 MPa. For TBPB/CO_2 semi-clathrate, the dissociation enthalpy measured by Mayoufi *et al.* [172] varied from 6.65 $kJ \cdot mol_{H_2O}^{-1}$ to 7.67 $kJ \cdot mol_{H_2O}^{-1}$ for pressure ranging from 1.0 MPa to 1.7 MPa. Note that these discussed values are closed to the results presented in the *Table 4.8*.

On the other hand, the ΔH per mole of CO_2 decreases with pressure, which is explaines by the deviation from the ideality of CO_2 observed by the diminution of the compressibility factor. At a pressure of 3 MPa, *z* changes rapidly, which explains low value of ΔH. An averaged value taking into account the pressure range from 1 to 2 MPa was about 205 ± 6 $kJ \cdot mol_{CO_2}^{-1}$, which is close to values found by Cha *et al.* [121], i.e., 211.6 $kJ \cdot mol_{CO_2}^{-1}$. Using the data from w_{TBPO} = 0.26, we found the value of 228 ± 7 $kJ \cdot mol_{CO_2}^{-1}$, which remains close to the value proposed by Cha *et al.* [121], i.e., 219.5 $kJ \cdot mol_{CO_2}^{-1}$ and relatively higher compared to the value proposed by Du *et al.* [122], i.e., 206.3 $kJ \cdot mol_{CO_2}^{-1}$. For TBPO/CH_4 semi-clathrate the averaged values of the dissociation enthalpy is about 147 ± 3 $kJ \cdot mol_{CH_4}^{-1}$ for w_{TBPO} = 0.30. This value is in good agreement with that from Cha *et al.* [121], i.e, 158.8 $kJ \cdot mol_{CH_4}^{-1}$.

An estimation of CO_2 storage capacity of TBPO semi-clathrate was calculated from the ratio of the dissociation enthalpy estimated by *Equation 4.2* and dissociation enthalpy measured using DSC apparatus. The result is a H_2O/CO_2 mole ratio that allows to roughly estimate gas storage capacity of the TBPO semi-clathrate, which was found to be 5.8 ± 0.3 wt. %. This is lower than the CO_2 storage capacity calculated by Lin *et al.* [104] for the TBAB semi-clathrate, ie., ~9.4 wt.%. Further details about the uncertainties of this approach can be found in [172].

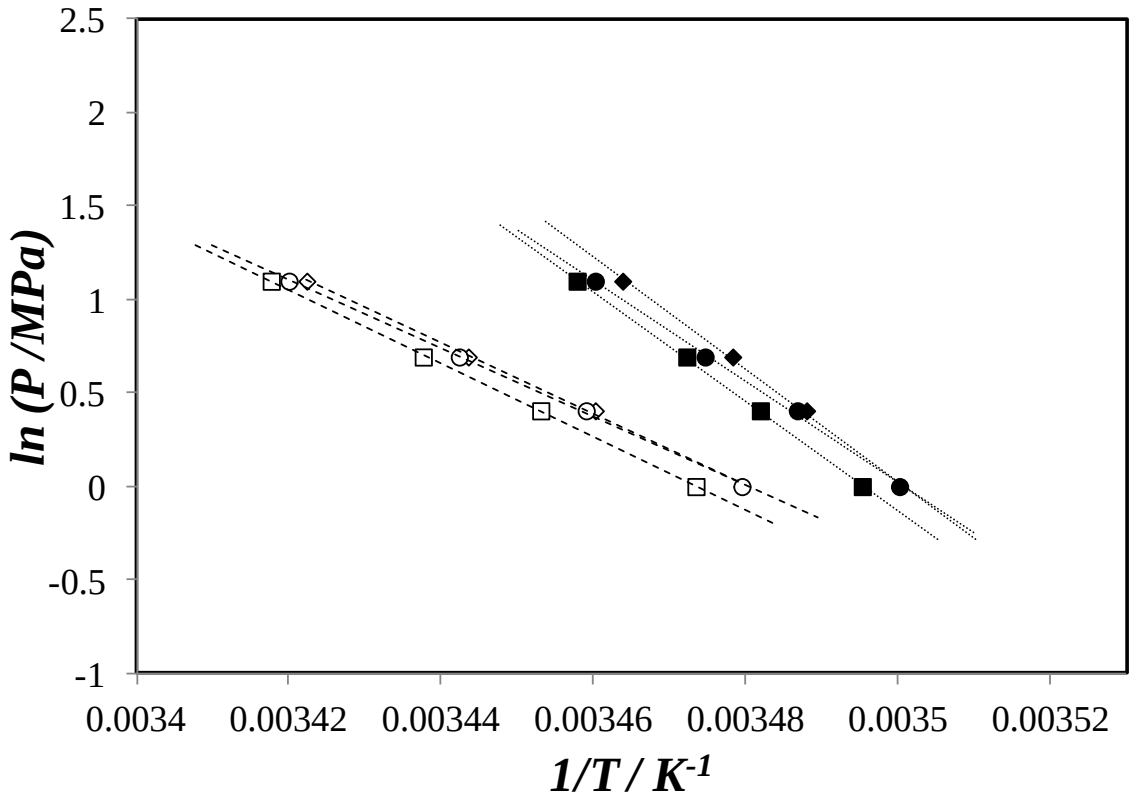

Figure 4.19. Clapeyron p-T phase diagram for TBPO + CO_2 + H_2O and TBPO + CH_4 + H_2O system; for TBPO/CO_2 semi-clathrate: ■ is w_{TBPO} = 0.20, ♦ is w_{TBPO} = 0.26 and ● is w_{TBPO} = 0.30; for TBPO/CH_4 semi-clathrate: □ is w_{TBPO} = 0.20, ◊ is w_{TBPO} = 0.26 and ○ is w_{TBPO} = 0.30; w is the value of TBPO mass fraction; dashed and dotted lines are the linear fitted curves.

4.4 Systems involving THP promoter

This section is composed by two parts. In the first one we will present and discuss the results from phase equilibria measurements of systems containing the promoter THP. The phase behavior of THP + H_2O was determined in a range of THP mass fraction from 0.025 to 0.500. In presence of gas phase (CH_4, CO_2 and CO_2+CH_4), the THP/gas hydrate conditions were measured in a range of THP mass fraction from 0.0500 to 0.300 and a range of gas pressure from 1 to 3 MPa. In the second part the estimated gas storage capacity of THP/CO_2 and THP/CH_4 gas hydrates will be evaluated.

4.4.1 Phase equilibrium measurements

In *Figure 4.20* we present the melting thermograms of solid phases present in the THP + H_2O system at additive mass fraction interval of 0.025 to 0.15. The thermograms shown in *Figure 4.20* were obtained by the dynamic method at constant heating rate. We observe a first peak starting at around 271 K regardless the additive mass fraction. This peak is related to the melting of the eutectic mixture composed by ice and THP hydrate. At w_{THP} = 0.025 the eutectic peak is followed by the ice melting peak. The two peaks appear with about 1.5 K of temperature difference. On the other hand, from w_{THP} = 0.05 to w_{THP} = 0.101 the eutectic and ice-melting peaks are merged due to the decreasing melting temperature of ice. From w_{THP} = 0.125 the eutectic peak is followed by the melting of THP hydrate phase. The shape and the peak resolution obtained by the dynamic method in the cases presented couldn't provide an accurate measurement of the phase transition temperatures. Therefore stepwise method was applied. Some thermograms are presented in *Figure 4.21*.

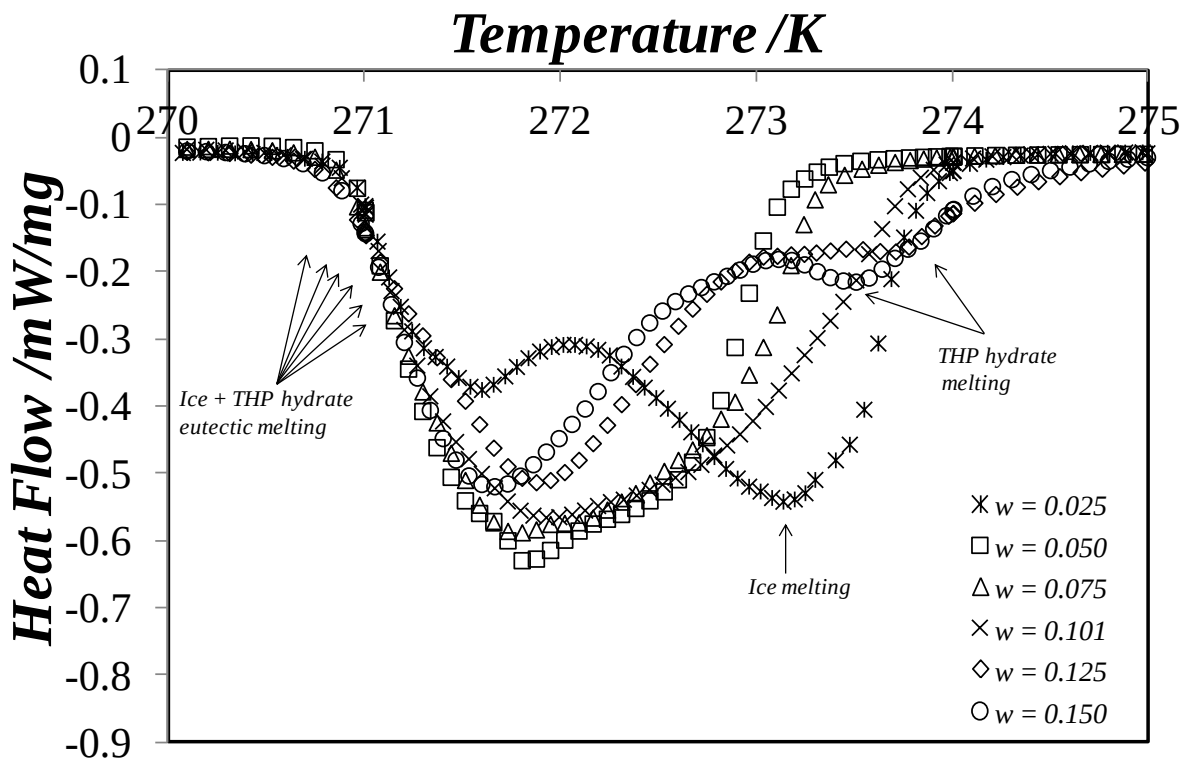

Figure 4.20. DSC thermograms of the melting of solid phases in THP + H_2O system at atmosphere pressure recorded at 0.5 K min^{-1}; w is the value of THP mass fraction.

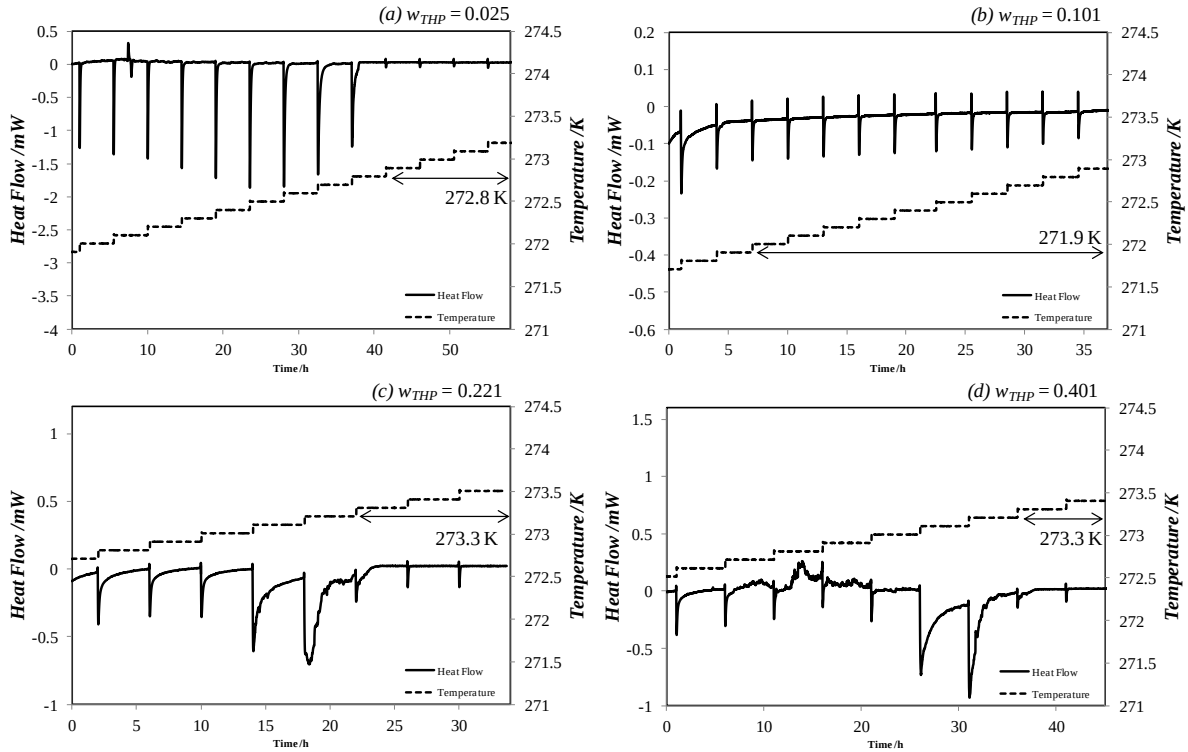

Figure 4.21. Heat Flow and temperature profiles during DSC stepwise method of THP + H_2O system at atmosphere pressure.

Following the trend observed in *Figure* 4.20 the dissociation temperature of the solid phase decrease from w_{THP} = 0.025 to w_{THP} = 0.100 (*Figures 4.21a* and *4.21b*). Then at w_{THP} = 0.221 (*Figure 4.21c*) and w_{THP} = 0.401 (*Figure 4.21d*) the transition temperature shows that the systems has reached an invariant. The measured values obtained by stepwise method are presented in *Table 4.9* and plotted in *Figure 4.22.*

Table 4.9. Measured phase transition temperatures of THP+H_2O system at different THP mass fractions.

w_{THP}	T_{onset} [a] /K (Eutectic)	T_{step} [b] /K (Ice)	T_{step} [b] /K (THP hydrate)
0.025	271.2	272.8	
0.050	271.3	272.5	
0.075	271.3	272.2	
0.101	271.3	271.9	
0.125	271.2		272.8
0.150	271.2		273.2
0.220			273.3
0.300			273.3
0.401			273.3
0.500			273.3

Standard uncertainties *u* are: [a] $u(T_{onset})$ = 0.2 K [b] $u(T_{step})$ = 0.1 K.

The eutectic melting temperatures are practically constant around 271.2 K. No more eutectic is observed above w_{THP} = 0.220, which was expected since this composition represents the hydrate stoichiometry (w_{THP} = 0.2195 for THP.17H_2O), Thus for compositions w_{THP} > 0.220, THP is in excess and no more ice is formed.

The values of ice melting temperature decrease from 272.8 K to 271.9 K for w_{THP} increasing from 0.025 to 0.101. Above w_{THP} = 0.125, THP hydrate becomes more stable and its dissociation temperature increases from 272.8 K to 273.3 K for w_{THP} ranging from 0.125 to 0.500. It is interesting to observe that above w_{THP} = 0.150 the dissociation temperatures are practically constant, indicating that the system is invariant over the concentration interval.

In *Figure 4.22* we present the measured values of phase transition temperatures and we define the domain of existence of phases for the THP + H_2O binary. This system is known to exhibit liquid-liquid demixtion in a composition region, which limits were measured by Stephenson et al. [218]. Their liquid-liquid solubility curve for THP in water ends at w_{THP} = 0.129 and 273.15 K. From w_{THP} = 0.025 to w_{THP} = 0.101 the ice-liquid curve decreases by 0.9 K, i.e.,

from 272.8 K to 271.9 K. Then, *liquidus* curves reach the eutectic composition, which is probably between w_{THP} = 0.101 and w_{THP} = 0.125. From w_{THP} = 0.125 to w_{THP} = 0.500 the *liquidus* curve, delimiting now the domain of existence of THP hydrate, rises only 0.5 K. The invariant interval observed above w_{THP} = 0.150 obeys the Gibbs phase rule (F = C - P + 2; F: degree of freedom; C: number of compounds; P: number of existing phases), in which the degree of freedom is equal to zero.

Comparing to THF hydrate, which phase behavior was determined by Delahaye *et al*. [85], the dissociation temperatures of THP hydrate are lower. At stoichiometric composition for THF hydrate (w_{THF} = 0.1907), the phase transition temperature is 277.87 K, while for THP hydrate at stoichiometric composition, the value is 273.3 K. This difference is probably due the existence of the invariant interval in THP + H_2O system.

In the presence of gas (CO_2, CH_4 and CO_2 + CH_4), the measurements of dissociation temperatures of THP/gas hydrates were carried in the range of pressure from 1 to 3 MPa and THP mass fraction ranging from 0.050 to 0.300. Stepwise method was applied and the results are presented in *Table 4.10* and plotted in *Figures 4.23 - 4.27.*

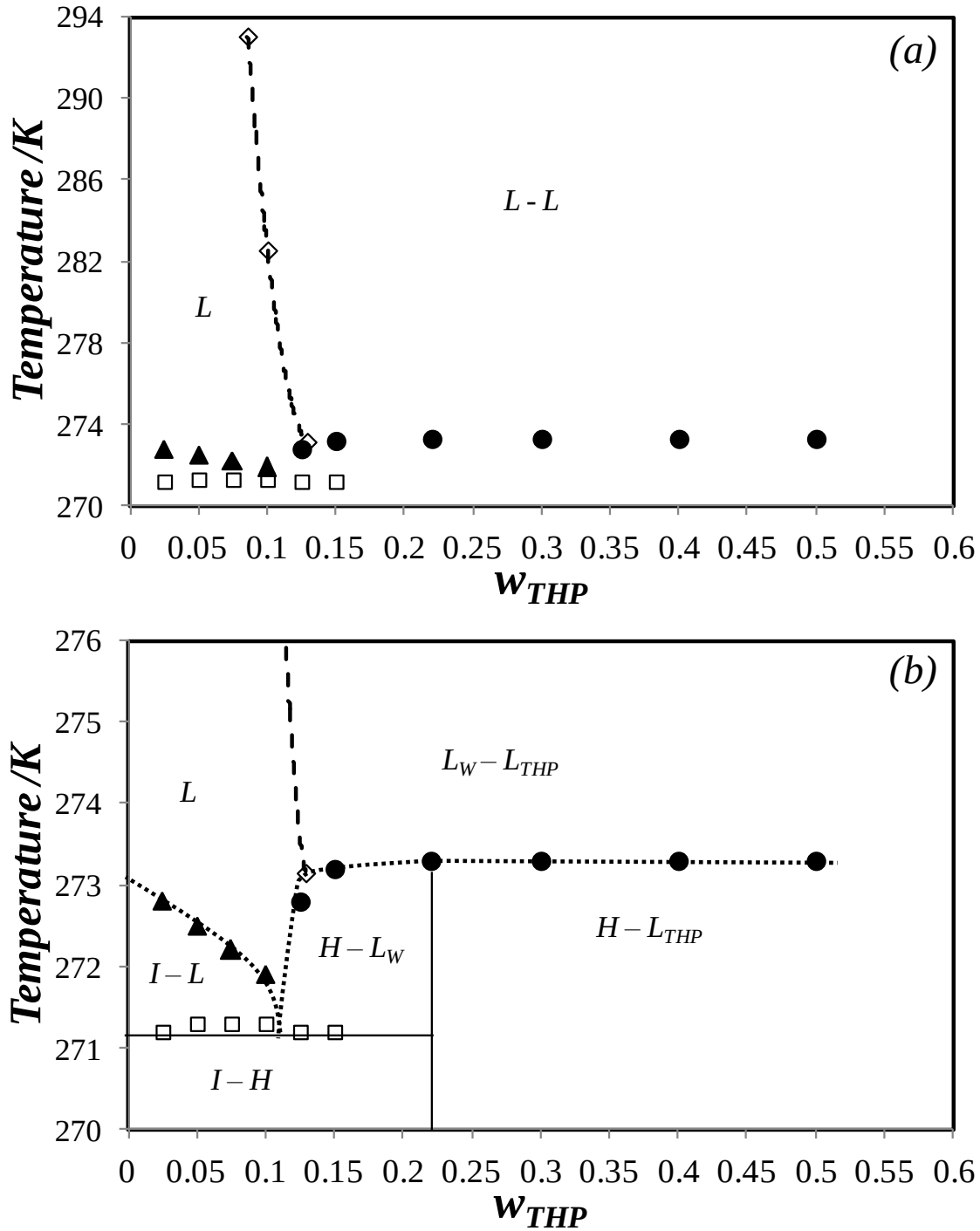

Figure 4.22. Temperature phase boundaries, Temperature versus THP mass fraction (w_{THP}): □ dissociation point of eutectic mixture, this work; ▲ dissociation point of ice solid phase (I), this work; ● dissociation point of THP hydrate phase (H), this work; ◊ solubility point of THP in water, Stephenson et al. [218];(a) large scale of temperature axis; (b) small scale of temperature axis; dotted line is a proposition of liquidus curve behavior; dashed line is a proposition of liquid-liquid solubility curve behavior.

Table 4.10. Dissociation temperatures of THP/CO_2, THP/CH_4 and THP/(CO_2+CH_4) hydrates at gas phase pressure ranging from 1 to 3 MPa and THP mass fraction (w_{THP}) from 0.050 to 0.300 (Gas mixture containing 40 ± 1 mol.% of CO_2).

w_{THP}	T_{diss} /K[a]			
	CO_2			
	1.0 MPa	1.5 MPa	2.0 MPa	3.0 MPa
0.050	281.6	283.7	285.1	286.7
0.101	283.2	284.6	285.9	286.9
0.150	283.8	285.1	286.2	287.0
0.220	283.9	285.2	286.7	287.1
0.300	283.5	285.1	286.0	287.0
	CH_4			
	1.0 MPa	1.5 MPa	2.0 MPa	3.0 MPa
0.050	283.8	286.4	288.6	291.6
0.101	286.0	288.3	290.3	292.7
0.150	286.2	288.7	290.6	293.1
0.220	286.5	288.8	290.6	293.6
0.300	286.0	288.2	289.7	292.6
	$0.40CO_2 + 0.60CH_4$			
	1.0 MPa	1.5 MPa	2.0 MPa	3.0 MPa
0.050	283.1	285.8	287.6	290.3
0.101	285.3	287.3	288.7	291.4
0.150	285.4	287.5	288.9	291.6
0.220	285.3	287.5	289.0	291.7
0.300	285.0	287.3	288.9	291.5

Standard uncertainty *u* is: [a] $u(T_{step})$ = 0.1 K.

In *Figures 4.23 - 4.25* we present the equilibrium curves for THP/gas hydrates measured at stoichiometric composition (w_{THP} = 0.220). The equilibrium conditions of THP/CO_2, THP/CH_4 and THP/(CO_2+CH_4) gas hydrate were shifted towards lower pressures and higher temperature compared to CO_2, CH_4 and CO_2+CH_4 gas hydrate, respectively. This behavior confirms the capacity of THP hydrate to trap small molecules in the empty dodecahedral (5^{12}) cages presents in the structure SII. It was confirmed that the hexakaidecahedral cages ($5^{12}6^4$) from this structure is filled by the THP [119, 219].

Compared to data available in the literature presented in the same figures, our results are in good agreement, which confirms the good accuracy of the experimental method used. THP/CO_2 and THP/CH_4 gas hydrates equilibrium curves are also compared to THF/CO_2 and THF/CH_4 gas hydrates equilibrium curves. These systems are compared in their respective stoichiometric composition (w_{THF} = 0.1907 for THF). THF/gas hydrates seem to form more stable hydrates, specially at higher pressures. This behavior can be related due to the different size and shape between the two promoters as well as the interactions with the water framework from the larges cages ($5^{12}6^4$) [219]. *Figure 4.26* provide further more comparisons between these four systems.

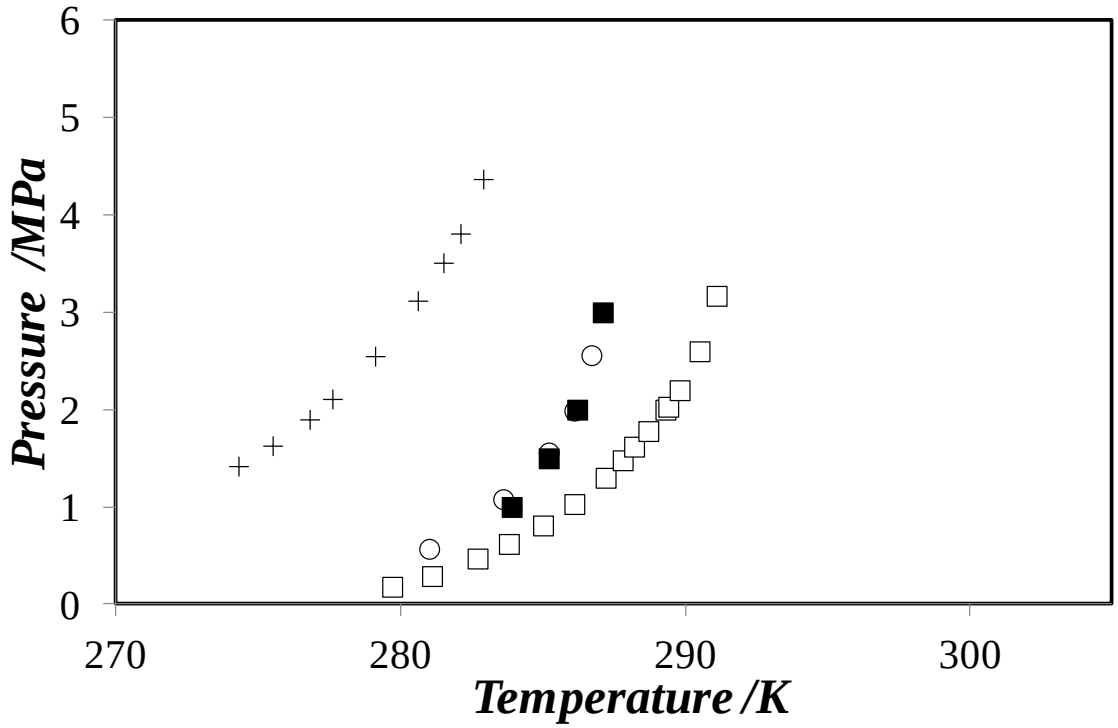

Figure 4.23. Equilibrium hydrate formation for CO_2 in pure water and for CO_2 in THP and THF solution; ■, THP + CO_2 + H_2O at w_{THP} = 0.220, this study; ○, THP + CO_2 + H_2O at w_{THP} = 0.24, data from Iino et al. [119]; □, THF + CO_2 + H_2O at w_{THF} = 0.1907, data from Lee et al. [97]; +, CO_2 + H_2O, data from Adisasmito et al. [108].

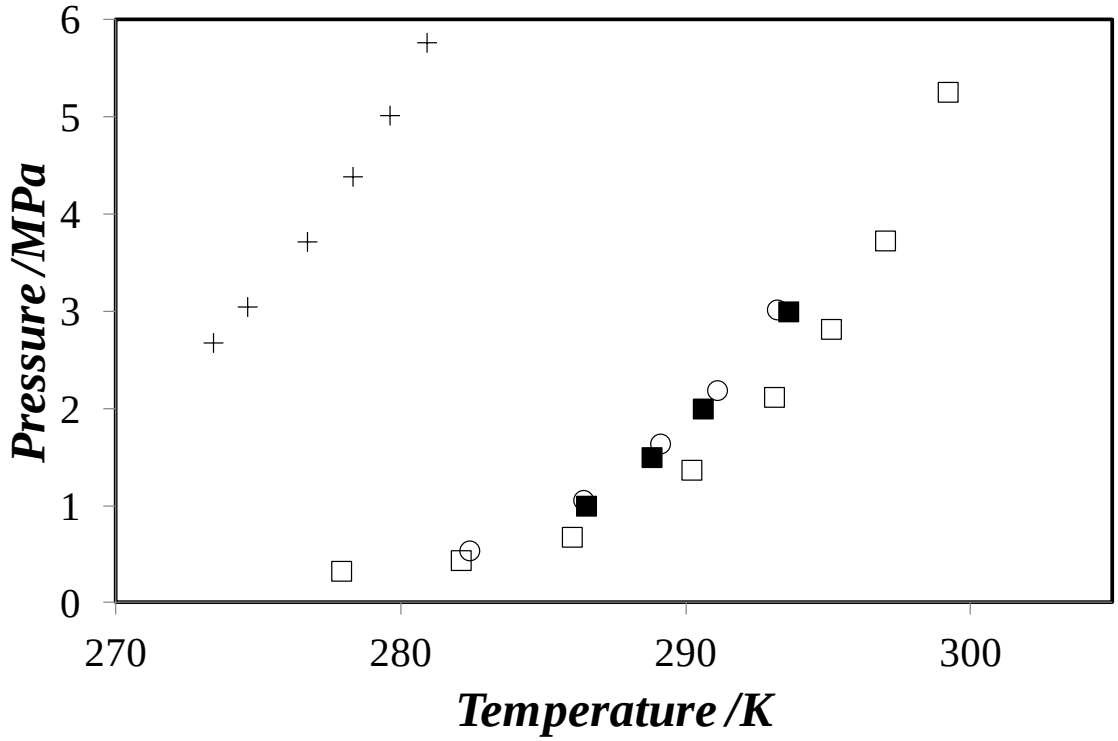

Figure 4.24. Equilibrium hydrate formation for CH_4 in pure water and for CH_4 in THP and THF solution; ■, THP + CH_4+ H_2O at w_{THP} = 0.22, this study; ○, THP + CH_4 + H_2O at w_{THP} = 0.24, data from Iino et al. [119]; □, THF + CH_4 + H_2O at w_{THF} = 0.1907, data from Lee et al. [97]; +, CH_4 + H_2O, data from Adisasmito et al. [108].

In *Figure 4.25* we compare the THP/(CO_2+CH_4) gas hydrate equilibrium curve to systems containing other promoters at their respective stoichiometric composition. The composition of (CO_2+CH_4) gas mixture was practically similar. Small differences are observed between tetrabutylphosphonium bromide (TBPB) and tributylphosphine oxide (TBPO), while higher differences are obtained with THF, which maintains the same trend observed in *Figures 4.23* and *4.24*. The differences among these systems can be related to the hydrate crystal structure as well as the kind of interactions between the guest and host molecules. TBPO, THF and THP seem to have the same kind of interactions (hydrogen bonds, specially between the oxygen atom from these molecules and water framework) but different structures. TBPO hydrate corresponds to the formula TBPO34.5H_2O with three available dodecahedral cages [106], while THP and THF form the known clathrate structure SII. For TBPB.38H_2O, the bond length of Br–O is longer than that of O–O from the water framework [105].

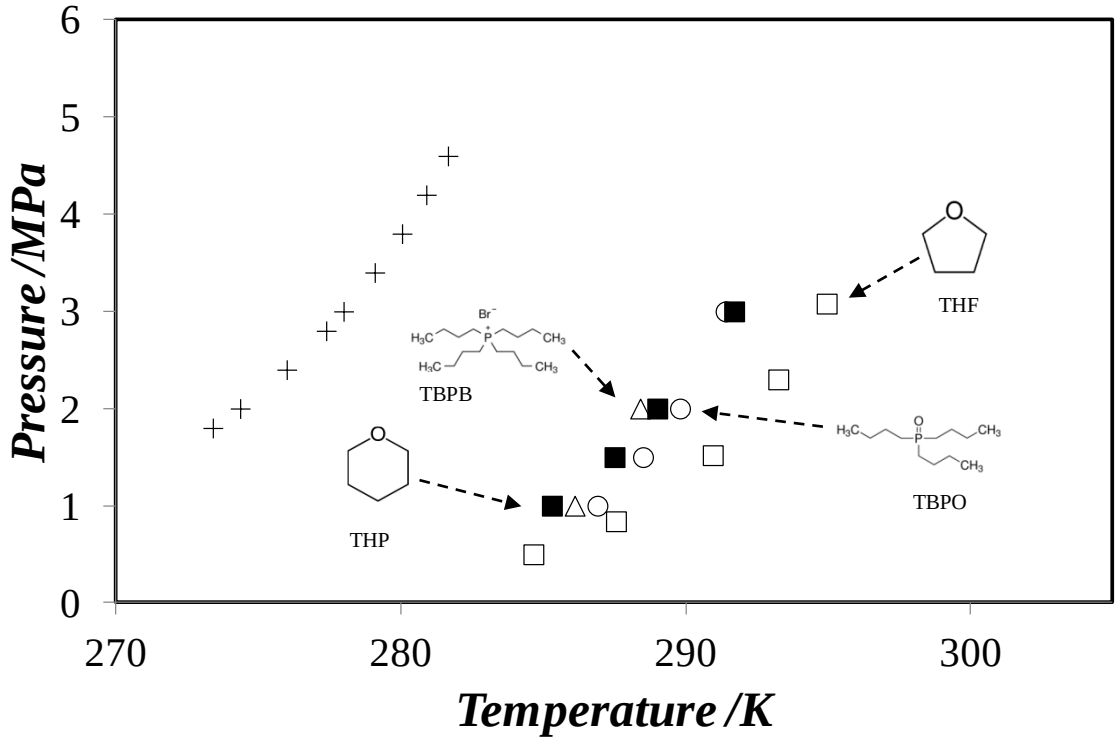

Figure 4.25. Equilibrium hydrate formation for CO_2 + CH_4 in pure water and for CO_2 + CH_4 in THP and THF solution; ■, THP + CO_2 + CH_4 + H_2O at w_{THP} = 0.22, this study, gas mixture containing 40 ± 1 mol.% of CO_2 ; ○, TPBO + CO_2 + CH_4 + H_2O at w_{TBPO} = 0.26, data from Sales Silva et al. [207], gas mixture containing 40 ± 1 mol.% of CO_2; Δ, TBPB + CO_2 + CH_4 + H_2O at w_{TBPB} = 0.35, data from Sales Silva et al. [204] , gas mixture containing 40 ± 1 mol.% of CO_2; □, THF+ CO_2 + CH_4 + H_2O at w_{THF} = 0.1907, data from Xia et al. [136], gas mixture containing 38.5 mol.% of CO_2 ; +, CO_2 + CH_4+ H_2O calculated data from CSMGem [154]; gas mixture containing 40 mol.% of CO_2.

In *Figure 4.26* we compare hydrate equilibrium curves for THP/CO_2 and THP/CH_4 gas hydrate at w_{THP} = 0.050 and w_{THP} = 0.220. We confirm that the THP hydrate stabilizes more stable gas hydrate phase with CH_4 than with CO_2. This inversion in the phase equilibrium conditions (CO_2 gas hydrates is more stable than CH_4 gas hydrate) was also observed by other authors [119-120, 220]. The high difference on equilibrium temperatures at fixed pressure indicates the possibility of capturing CH_4 in hydrate phase from CO_2 + CH_4 gas mixtures

The inversion of stability observed in *Figure 4.26* can be explained by two hypothesis: occupancy of gas guest molecule in the small cage [97, 119] and different guest-host molecular interactions in the structure [219]. Lee *et al.* [97] observed that in CO_2 + CH_4 gas hydrate phase, the large tetradecanhedral ($5^{12}6^2$) cages of structure SI were mostly occupied

by CO_2 molecules while the small dodecahedral (5^{12}) cages were mainly filled by CH_4. Therefore, they suggested that CH_4 have more affinity toward 5^{12} cages and, since in structure SII formed with THP and THF molecules these are the only available cages, it is expected that they will be more filled with CH_4 than with CO_2. This difference in cage affinity could explain the disparity of stability. For Narayanan *et al*. [219] that carried molecular dynamics simulation for THP/CO_2 and THP/CH_4 gas hydrates, the steric repulsions between CO_2 and the dodecahedral (5^{12}) cages limits its motion and promotes interactions between THP guest molecule and the water framework. This phenomenon is less intense with CH_4.

In *Figure 4.26*, we also observe that THF can be used to capture CH_4 in a gas separation by gas hydration formation process (GSHF). But another criterion that must be evaluated is the gas storage capacity. It is not only an important parameter for GSHF process, but also for other processes based on hydrate formation, such as gas storage for transportation and refrigeration. In Section *4.4.2* the results about estimation of THP/CO_2 and THP/CH_4 gas hydrate gas storage capacity will be presented and discussed.

In spite of a higher stabilization compared to THP, industrial application of THF is undesirable due the fact that it is a harmful air pollutant. On the other hand, THP is not reported to be an air pollutant, in addition to being less volatile than THF.

In *Figure 4.27* the temperature phase boundaries of THP/gas hydrate are presented. Compared to THP hydrate at ambient pressure, the presence of gas further stabilizes the hydrate phase. This gain of stability starts from 9.1 K (THP/CO_2 gas hydrate w_{THP} = 0.050 and 1.0 MPa) and can reach 20.3 K (THP/CH_4 gas hydrate at w_{THP} = 0.220 and 3.0 MPa).

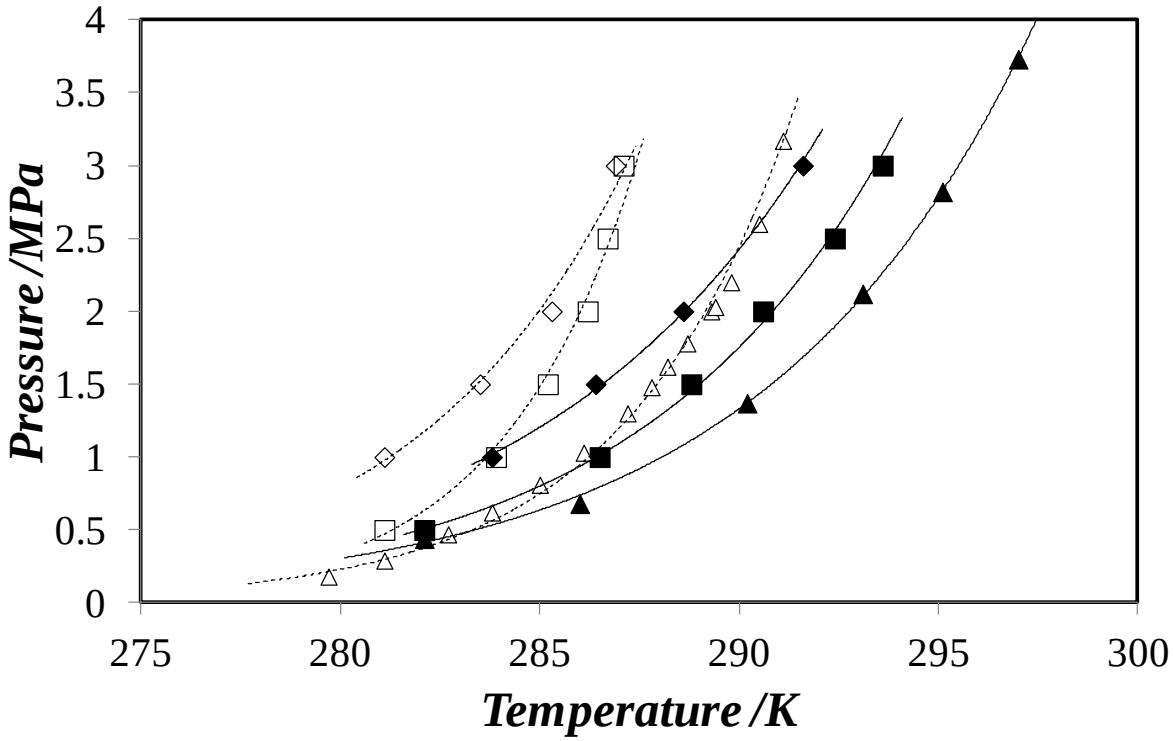

Figure 4.26. Experimental V-L-H three phase equilibrium data for THP + CO_2 + H_2O, THP + CH_4+ H_2O, THF + CO_2 + H_2O and THF + CH_4+ H_2O systems; ◊, THP + CO_2 + H_2O at w_{THP} = 0.050, this work; □, THP + CO_2 + H_2O at w_{THP} = 0.220, this work; Δ, THF + CO_2 + H_2O at w_{THF} = 0.1907, data from Iino et al. [119]; ♦, THP + CH_4 + H_2O at w_{THP} = 0.050, this work; ■, THP + CH_4 + H_2O at w_{THP} = 0.220, this work; ▲, THF + CH_4 + H_2O at w_{THF} = 0.1907, data from Iino et al. [119]; solid and dashed lines are the exponential curve fitted from the data.

It is interesting to notice in *Figure 4.27a* that for THP/CO_2 increasing the pressure reduces the effect of THP mass fraction on the *liquidus* curve. At 3.0 MPa the phase transition temperatures are almost constant regardless w_{THP}. This same behavior was also observed by Delahaye *et al.* [85] for THF/CO_2 gas hydrates. For THP/CH_4 and THP/(CO_2+CH_4) gas hydrates (*Figures 4.27b* and *4.27c*, respectively) we observed dependence with THP composition at fixed pressure. In general, the *liquidus* curves rises from w_{THP} = 0.050 to w_{THP} = 0.220 and then have a slight tendency to fall from w_{THP} = 0.300.

These phase diagrams show the limits of existence of hydrates, which is an important information that must be taken into account for determining the operation conditions for hydrate based processes.

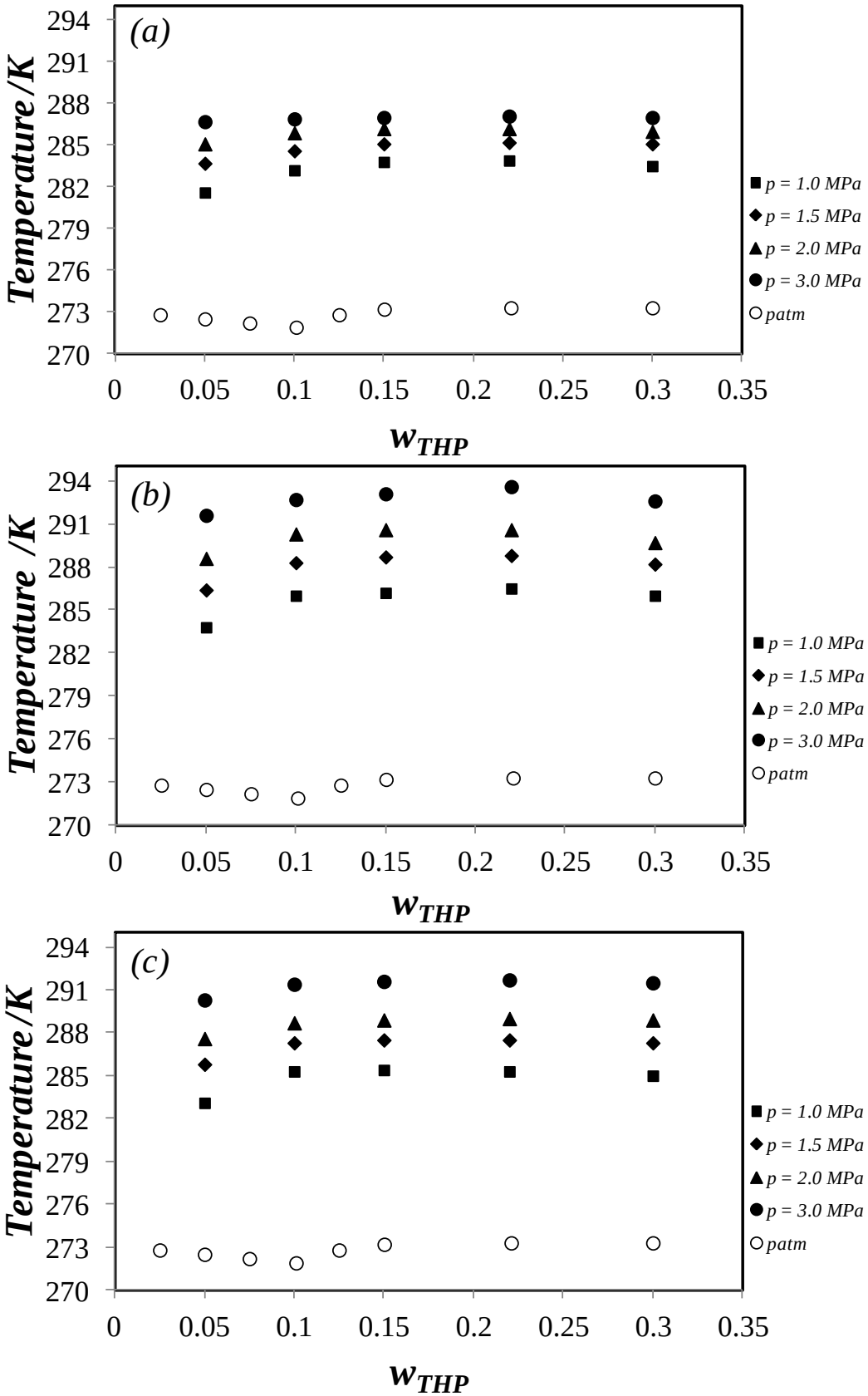

Figure 4.27. Temperature phase boundaries for single THP hydrate and THP/Gas gas hydrate: (a) CO_2; (b) CH_4; (c) CO_2+CH_4 (Gas mixture containing 40 ± 1 mol.% of CO_2).

From *p-T* data of THP/CO_2 and THP/CH_4 gas hydrates, we obtain an estimation of dissociation enthalpies per mole of gas using Clausius-Clapeyron approach (See *Equation 4.2*). The assumptions for applying this equation were the same than in *Sections 4.2.2* and *4.3.2.* The values are presented in the *Table 4.11*.

Figure 4.28 shows the Clapeyron ln*p*-1/*T* phase diagram for THP/CO_2 and THP/CH_4 gas hydrates at different w_{HTP}. Note that for all conditions the equilibrium curves form almost perfect straight lines, with correlation factors higher than 0.985. This validates the assumptions related to Clausius-Clapeyron equation. In each system, the slope of the curve $-d\ln P/d(1/T))$ was almost the same regardless the promoter concentration. For THP/CO_2 gas hydrate the value was -27.1 ± 0.2 K, being higher than the value for THP/CH_4, i.e. -13.5 ± 0.6 K. From Clapeyron equation, this lower value can indicate that larger amounts of CH_4 are incorporated into to the THP hydrate than CO_2, which was confirmed by the works of Iino *et al.* [119] and Narayanan *et al.* [219].

Table 4.11. Dissociation enthalpies of THP/CO_2 and THP/CH_4 gas hydrates at w_{THP}=0.22; ΔH estimated from Clausius-Clapeyron equation.

CO_2		
P / MPa	T / K	ΔH $\left(kJ \cdot mol_{CO_2}^{-1}\right)$
1.0	283.9	214
1.5	285.2	207
2.0	286.2	199
3.0	287.1	183
CH_4		
P / MPa	T / K	ΔH $\left(kJ \cdot mol_{CH_4}^{-1}\right)$
1.0	286.5	105
1.5	288.8	104
2.0	290.6	103
3.0	293.6	101

As observed for TBPO/CO_2 semi-clathrate in *Section 4.3.2,* the dissociation enthalpy of THP/CO_2 gas hydrate also decrease with increasing pressure. This can be related to the deviation from the ideality of CO_2 evidenced by the diminution of the compressibility factor as well as by an increase of gas inclusion into the hydrate upon increasing the pressure. On

the other hand, for THP/CH_4 gas hydrate this reduction of dissociation enthalpy is less apparent.

We calculated the dissociation enthalpy of THF/CO_2 and THF/CH_4 gas hydrates from data of Lee et al. [97]. At 2 MPa, for THF/CO_2 the value was 135 $kJ \cdot mol_{CO_2}^{-1}$, which is lower than for THP/CO_2. Nevertheless, at 2.12 MPa the value of dissociation enthalpy for THF/CH_4 was 103 $kJ \cdot mol_{CH_4}^{-1}$ which is the same for THP/CH_4.

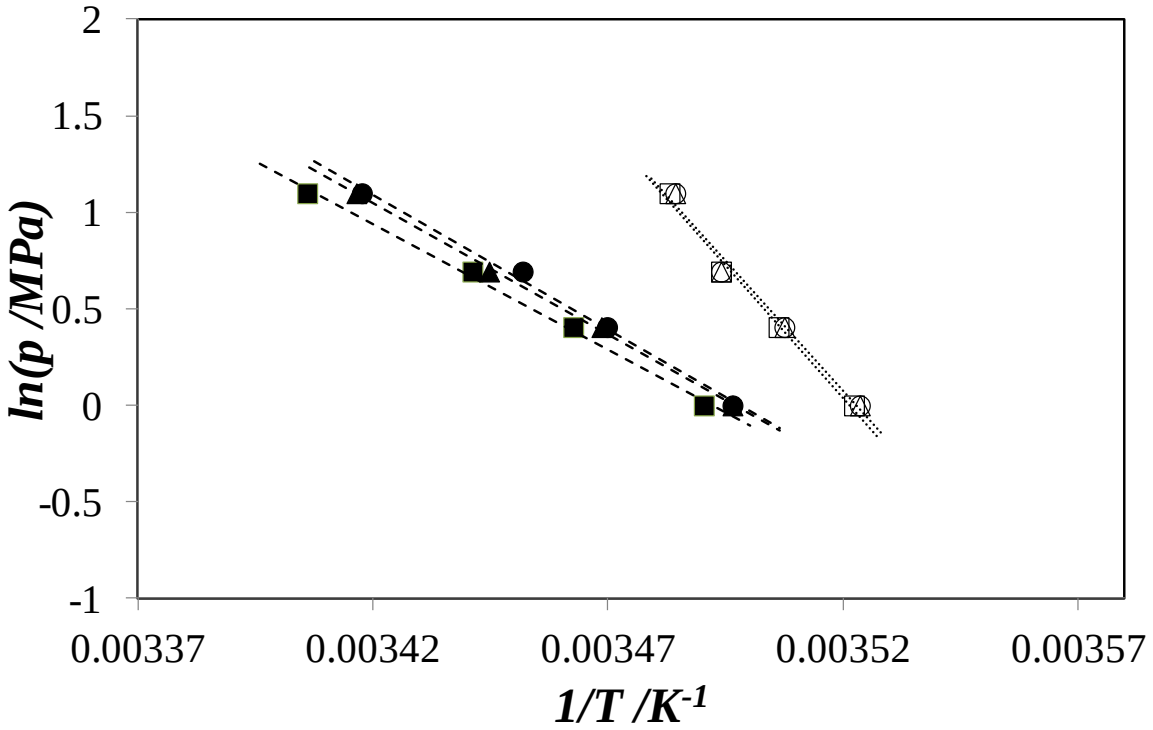

Figure 4.28. Clapeyron p-T phase diagram for THP+ CO_2 + H_2O and THP + CH_4 + H_2O system; for THP/CO_2 gas hydrate: Δ is w_{THP} = 0.101, □ is w_{THP} = 0.22 and ○ is w_{THP} = 0.30; for THP/CH_4 gas hydrate: ▲ is w_{THP} = 0.101, ■ is w_{THP} = 0.22 and ● is w_{THP} = 0.30; w is the value of THP mass fraction; dashed and dotted lines are the linear fitted curves.

4.4.2 Gas storage capacity of THP/CO_2 and THP/CH_4 gas hydrate

We experimentally measured the gas content of THP/CO_2 and THP/CH_4 gas hydrates in a high pressure cell. For each system, the experiments were carried out twice (run 1 and run 2) in order to check the reproducibility of the results. The experiments were carried out at different initial pressure for each system, because as said previously in the *Section 3.3.3*, the goal here was to compare the results obtained with a same initial number of moles for each compound. Besides, the different initial pressures are also due to the different solubilities of the two gases in the liquid phase. We inserted into to reactor 0.2300 ± 0.0012 mol of gas and 0.0348 ± 0.0007 mol of THP, which corresponds to 60 ml of aqueous solution at w_{THP} = 0.050. *Figure 4.29* presents the pressure and temperature profiles obtained in each experiment. The characterization of equilibrium phase composition is presented in *Tables 4.12* and *4.13.* Here the gas storage capacity is evaluated by the dodecahedral cage occupancy of gas (θ) in the SII structure formed with THP. Considering the hypothesis of full occupancy of THP in the eight hexakaidecahedral cages, there remain sixteen available dodecahedral cages. Therefore, for each mol of stoichiometric THP.17H_2O hydrate at most 2 moles of gas may be trapped.

In *Figure 4.29a* we notice that the crystallization of gas hydrate starts at different times. Gas hydrate formation is confirmed by a sudden temperature increase (crystallization being an exothermic phenomenon) followed by a pressure drop due to gas consummation. These two steps in the crystallization process are explained by the induction time, during which the hydrate formation is delayed although the systems has entered into the hydrate phase existence region [141, 221-222]. When the over saturation is suddenly broken the heat release causes the quick temperature increase while the excess gas is rapidly consumed. When the supersaturation ends, the hydrate phase growth requires further gas transfer, from the gas phase toward the hydrate – liquid interface. The all phenomenon is controlled by the driving force, which can be expressed as the difference between the pressure at a given instant and the equilibrium pressure. The higher this difference, the higher the driving force and the smaller the induction time, thus reducing the stochastic nature of the crystallization phenomenon.

In *Figure 4.29b*, the crystallization starts before the system reaches the set temperature. The THP/CH_4 gas hydrate being more stable (equilibrium conditions at higher temperatures and lower pressures) and the higher pressure in the reactor leaded to a higher driving force and consequently a smaller induction time compared to THP + H_2O + CO_2.

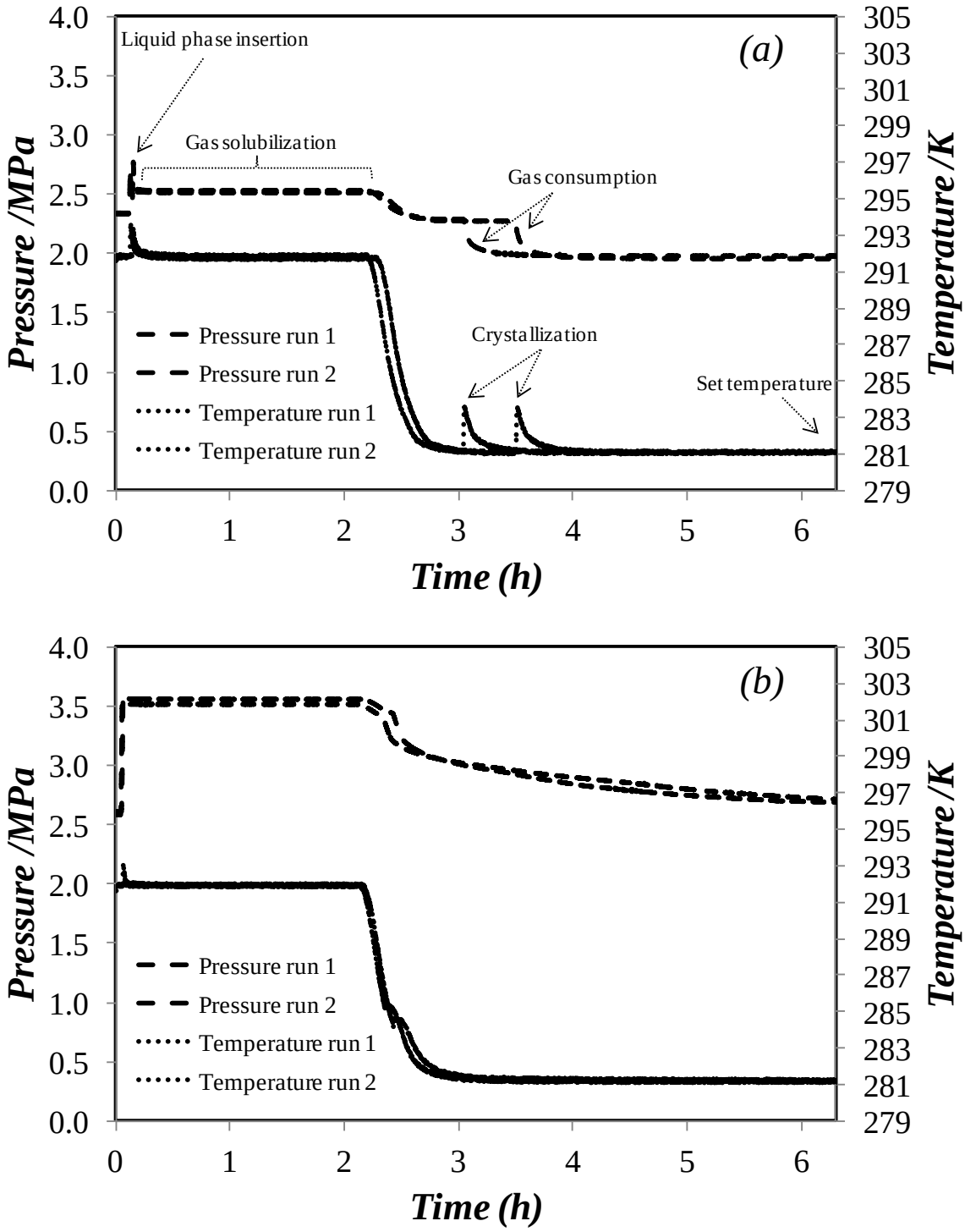

Figure 4.29.Pressure and temperature profiles during gas storage capacity experiment: (a) THP + H_2O + CO_2 system; (b) THP + H_2O + CH_4 system

Comparing the two systems during the gas consumption phase after the first hydrate formation, we notice that for THP + H_2O + CO_2 system the equilibrium pressure is reached more quickly than for THP + H_2O + CH_4. This behavior is probably due to the different solubilities. The CO_2 having higher solubility, the interfacial mass transfer toward the solid

phase is faster compared to CH_4.

In *Tables 4.12* and *4.13* we observe a good reproducibility between the experimental runs. The increase of equilibrium temperature from 281.1 to 283.1 K promoted a dissociation of an amount of gas hydrate which is observed by the increase of w_{THP} and the reduction of n^H.

Table 4.12. Characterization of equilibrium in terms of phase composition for THP + CO_2 + H_2O; n^H: amount of THP hydrate formed; $n_{CO2}{}^H$: amount of CO_2 in hydrate phase; $n_{CO2}{}^L$: amount of CO_2 in liquid phase; $n_{CO2}{}^G$: amount of CO_2 in gas phase; θ: 5^{12} cage occupancy of CO_2.

	Equilibrium conditions							
Run	Pressure / MPa	Temperature /K	THP /wt.%	n^H x 10^3 /mol[a]	$n_{CO2}{}^H$ x 10^3 /mol[a]	$n_{CO2}{}^L$ x 10^3 /mol	$n_{CO2}{}^G$ x 10^3 /mol	θ /%
1	1.98	281.1	1.130	27.1 ± 0.6	35.3 ± 2.6	46.8	147.7	65.13
	2.08	283.1	1.650	24.9 ± 0.6	28.2 ± 2.5	46.3	155.2	56.62
2	1.97	281.1	1.212	27.6 ± 0.6	36.1 ± 2.6	46.3	147.1	65.40
	2.07	283.1	1.730	24.4 ± 0.6	28.7 ± 2.5	46.2	154.3	58.81

[a] calculated values ± expanded uncertainty calculated from uncertainty propagation method with 95 % coverage

For THP + H_2O + CO_2 system in *Table 4.12* we note that the amount of gas in the hydrate phase ($n_{CO2}{}^H$) is slightly smaller than in liquid phase ($n_{CO2}{}^L$). The high amount of free water and the relatively high solubility of CO_2 result in this behavior. However it is important to note that the gas hydrate phase fraction is smaller (z^H = 0.153) than liquid phase (z^L = 0.804), therefore, we can notice the high gas storage capacity of the hydrate phase.

In *Table 4.13*, the amount of CH_4 in gas hydrate phase is higher than that of CO_2. On the other hand, the amount of CH_4 in liquid phase is very small.

Examining 5^{12} cage occupancy (θ), it can be observed that CO_2 occupies around 65 % of the available cages at 281.1 K and 57 % at 283.1 K. In contrast, the cage occupancy of CH_4 reached practically 100% regardless the temperature. Our results are in good agreement with the work of Iino *et al.* [119]. These authors estimated the gas storage capacity by powder X-ray diffraction (PXRD) measurements and they found 59 % and 100 % of 5^{12} cage occupancy for THP/CO_2 and THP/CH_4 gas hydrate, respectively, at 281 K and 2.3 MPa.

Table 4.13. Characterization of equilibrium in terms of phase composition for THP + CH_4 + H_2O; n^H: amount of THP hydrate formed; $n_{CH4}{}^H$: amount of CH_4 in hydrate phase; $n_{CH4}{}^L$: amount of CH_4 in liquid phase; $n_{CH4}{}^G$: amount of CH_4 in gas phase; θ : 5^{12} cage occupancy of CH_4.

	Equilibrium conditions							
Run	Pressure / MPa	Temperature /K	THP /wt.%	n^H x 10^3 /mol[a]	$n_{CH4}{}^H$ x 10^3 /mol[a]	$n_{CH4}{}^L$ x 10^3 /mol	n_{CH4} x 10^3 /mol	θ /%
1	2.53	281.1	0.958	29.2 ± 0.4	59.8 ± 1.2	2.11	168.1	100.00
	2.59	283.1	1.302	27.2 ± 0.4	57.0 ± 1.3	2.10	171.0	100.00
2	2.55	281.1	0.873	29.9 ± 0.4	57.6 ± 1.3	2.12	169.0	96.40
	2.60	283.1	1.265	27.5 ± 0.4	55.5 ± 1.3	2.11	171.0	100.00

[a] calculated values ± expanded uncertainty calculated from uncertainty propagation method with 95 % coverage

The higher amount of CH_4 trapped into the hydrate phase and the weak solubility of this gas in liquid phase are in contrast with CO_2. We can then imagine a gas separation process involving only the condensed phases (liquid and hydrate) in which CH_4 would be separated from CO_2 by being trapped in the hydrate phase while CO_2 would be dissolved in the liquid phase.

4.5 Comparison between the promoters

Figures 4.30 to *4.32* provide a comparison between the selected promoters TBAB, TBPB, TBPO and THP in terms of H – L – V equilibrium curves at compositions of the aqueous solutions equal or close to the respective stoichiometries of hydrates.

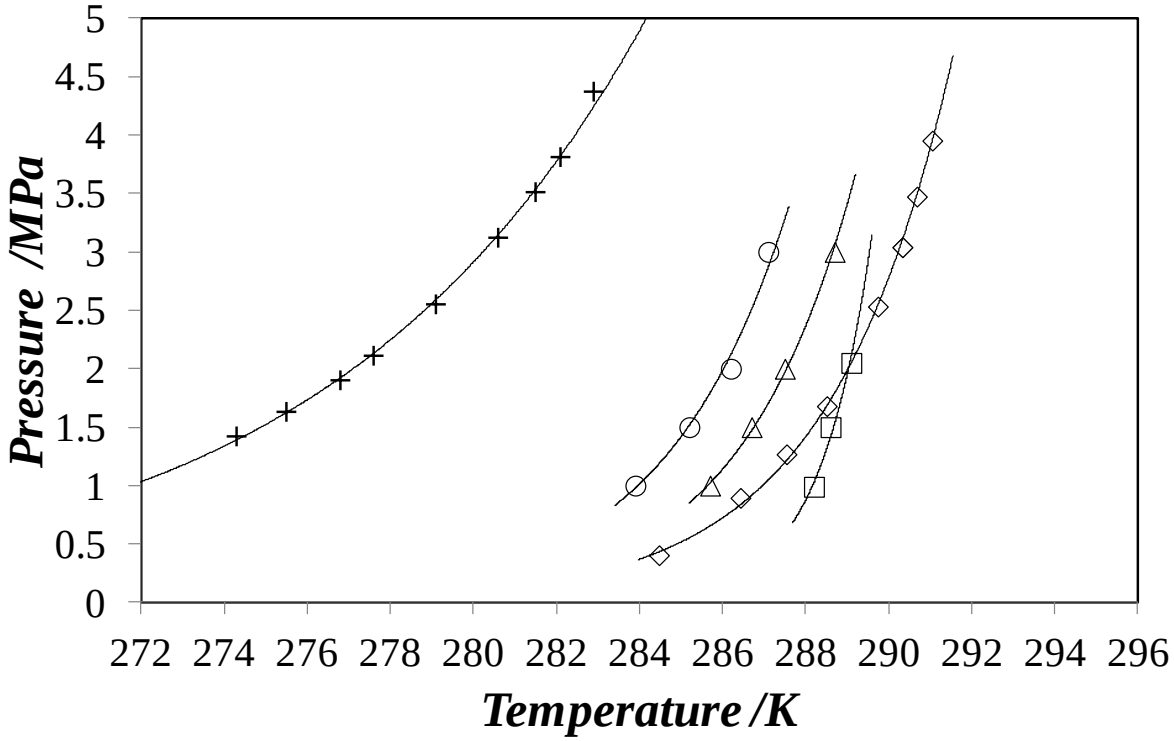

Figure 4.30. Equilibrium hydrate formation for CO_2 in pure water and for CO_2 in TBAB, TBPB, TBPO and THP solution; □, TBAB + H_2O + CO_2 at w_{TBAB} =0.32, data from Najibi et al. [223]; ◊, TBPB + H_2O + CO_2 at w_{TBPB} =0.35, data from Zhang et al. [203]; Δ, TBPO + H_2O + CO_2 at w_{TBPO} =0.26, this work; ○, THP + H_2O + CO_2 at w_{THP} =0.22, this work; +, CO_2 + H_2O, data from Adisasmito et al.[108]; solid lines are the exponential curve fitted from the data.

F*igures 4.30 - 4.32* confirme the capacity of all promoters to shift the equilibrium curves of gas hydrates towards lower pressures and higher temperatures. In *Figure 4.30*, for promoters involving CO_2 gas phase, THP exhibits the lowest stabilization effect, followed by TBPO. Them, at pressures lower than 2 MPa TBAB seems to be more stable while to for higher pressures TBPB/CO_2 becomes more stable.

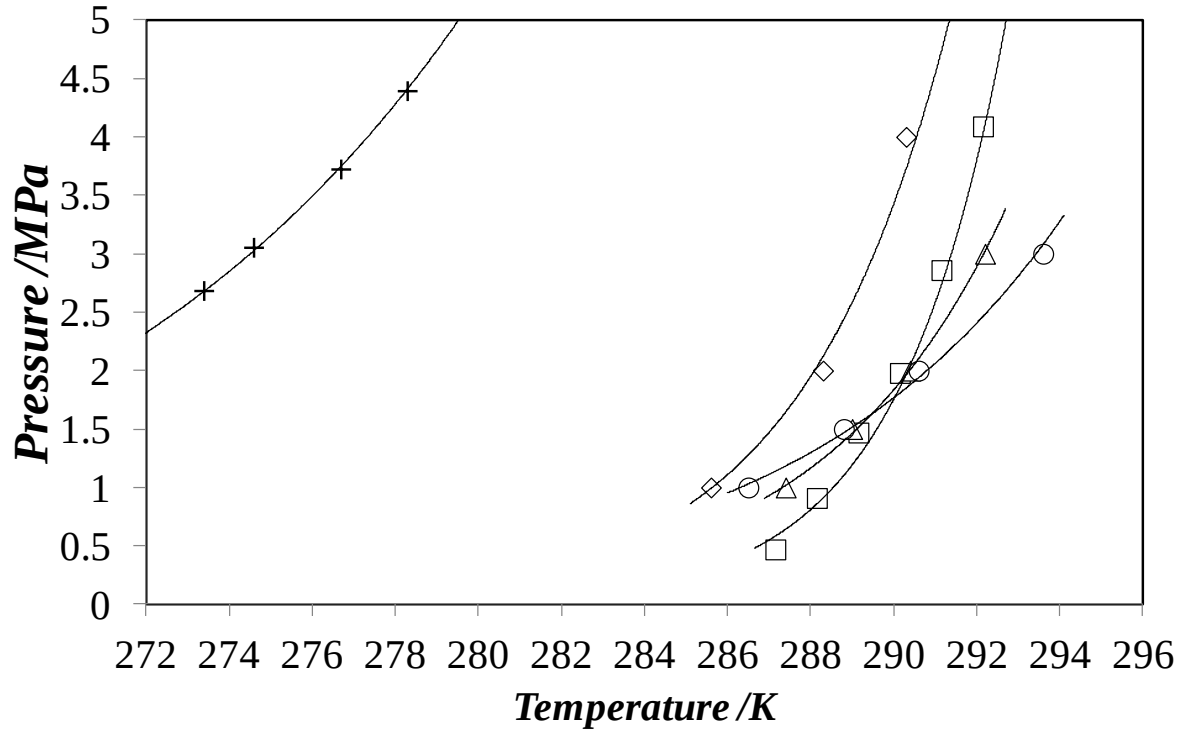

Figure 4.31. Equilibrium hydrate formation for CH_4 in pure water and for CH_4 in TBAB, TBPB, TBPO and THP; □, TBAB + H_2O + CH_4 at w_{TBAB} =0.38, data from Li et al. [123]; ◊, TBPB + H_2O + CH_4 at w_{TBPB} =0.35, this work; Δ, TBPO + H_2O + CH_4 at w_{TBPO} =0.26, this work; ○, THP + H_2O + CH_4 at w_{THP} =0.38, this work; +, CH_4 + H_2O, data from Adisasmito et al. [108]; solid lines are the exponential curve fitted from the data.

In *Figure 4.31* TBPB forms the less stable gas hydrate phase in presence of CH_4. At pressure equal to 2 MPa, there is practically no difference between the three promoters TBAB, TBPO and THP. For smaller pressures TBAB seems to be the more efficient for trapping CH_4 . At higher pressures THP is the more efficient. Furthermore, the results presented in the previous *Section* show a maximum storage capacity of THP/CH_4 gas hydrate due to the full occupancy of cages, increasing the potential interest of this promote.

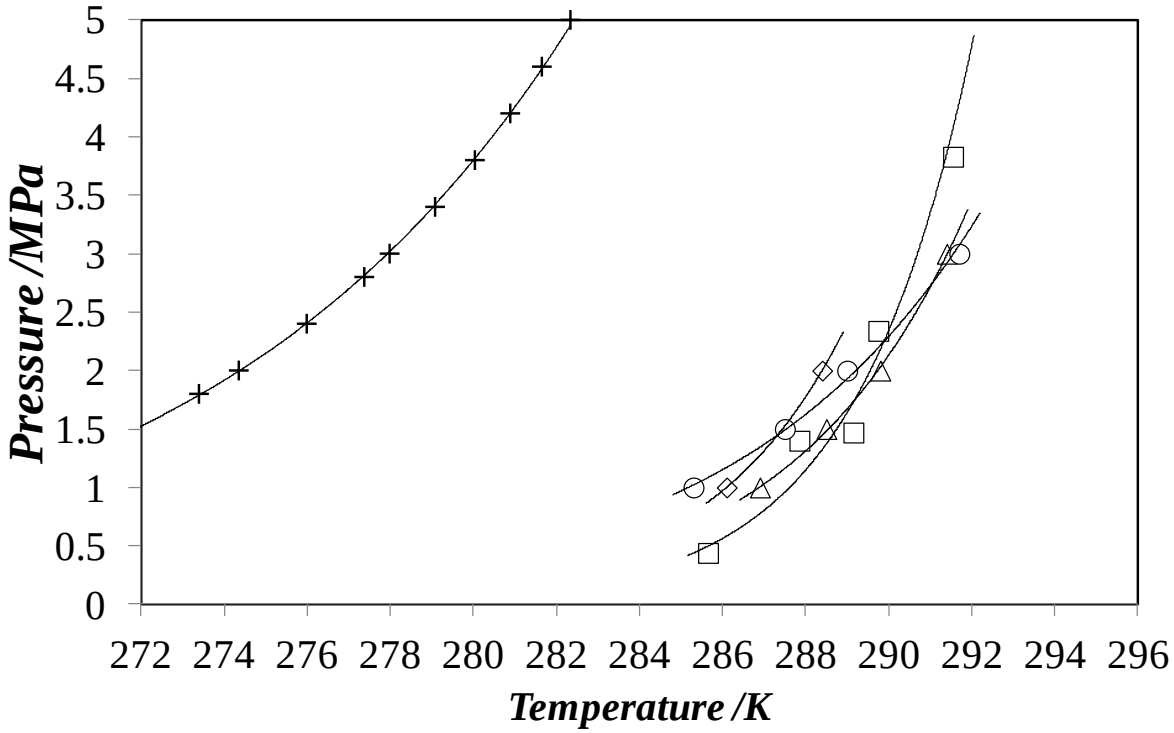

Figure 4.32. Equilibrium hydrate formation for CO_2 + CH_4 in pure water and for CO_2 + CH_4 in TBAB, TBPB, TBPO and THP solution; □ TBAB + CO_2 + CH_4 + H_2O at w_{TBAB} = 0.30, data from Xia et al. [136], gas mixture containing 39 mol.% of CO_2; ◊, TBPB + CO_2 + CH_4 + H_2O at w_{TBPB} = 0.35, this study, gas mixture containing 40 ± 1 mol.% of CO_2; ○, TBPO + CO_2 + CH_4 + H_2O at w_{TBPO} = 0.26, this study, gas mixture containing 40 ± 1 mol.% of CO_2; ○, THP + CO_2 + CH_4 + H_2O at w_{THP} = 0.22, this study, gas mixture containing 40 ± 1 mol.% of CO_2; +, CO_2 + CH_4+ H_2O calculated data from CSMGem [154]; gas mixture containing 40 mol.% of CO_2; ; solid lines are the exponential curve fitted from the data.

For the systems containing CO_2 + CH_4 gas mixture in a composition near to biogas, TBAB seems to provide the better stability gain at lower pressures (*Figure 4.32*) while for higher pressures THP seems to give better results. The information presented in this Chapter is important to define operating conditions and consequently the driving force which have impacts on the efficiency of a hydrate-based process. Other parameters with regard to thermodynamic and kinetic nature of gas separation process, such as separation factor and crystalline growth rate, will be treated in the next *Chapter*.

Chapter 5

Study of biogas upgrading by hydrate formation in presence of promoters: kinetics and thermodynamics measurements

Résumé

Ce chapitre présentera et discutera les résultats des mesures quantitatives effectuées en réacteur instrumenté pour l'épuration du biogaz par le procédé de séparation par formation d'hydrates (GSHF). Un mélange CO_2 + CH_4 contenant 39.0 mol% de CO_2 a été utilisé comme biogaz simulé. Un nouveau protocole explorant l'effet mémoire a été appliqué afin vérifier la réduction du temps d'induction sous condition de faible force motrice. Les promoteurs sélectionnés TBAB, TBPB, TBPO et THP ont été testés et évalués tant du point de vue de la cinétique (temps d'induction, taux de consommation de gaz et taux de capture de CO_2) que de celui de la thermodynamique (quantité de gaz piégé, sélectivité). L'impact des hypothèses faites pour les calculs de composition de phases a été pris en compte en appliquant la méthode de propagation des incertitudes.

Abstract

In this chapter we will present and discuss the results obtained from the experiments in instrumented reactor for biogas upgrading using the gas separation by hydrate formation (GSHF) process. A CO_2 + CH_4 gas mixture containing 39.0 mol% of CO_2 was used as simulated biogas. A new protocol exploring the memory effect was performed in order to verify the reduction of induction time under small driving force condition. The selected promoters TBAB, TBPB, TBPO and THP were tested and evaluated in kinetics and thermodynamics aspects, such as gas consumption rate, amount of gas trapped into the hydrate phase and selectivity. The impact of the assumptions made for the phase composition calculations was taken into account by using the uncertainty propagation method.

5.1 Introduction

Biogas can be valorized by separating CO_2 from CO_2 + CH_4 mixture. Gas separation processes such as Pressure Water Scrubbing (PWS), Pressure Swing Adsorption (PSA), Chemical Absorption and Membrane are well documented techniques, which have their advantages and drawbacks. However, we are always looking for other alternatives. In recent years, the gas separation process based on hydrate formation (GSHF) has taken special attention in academic community. This process is based on a phase transition in which gases from a mixture could be selectively captured into a solid phase formed from an aqueous solution. The advantages of GSHF process over the conventional processes such as amine-based chemical absorption is that the GSHF process is the most environmentally friendly since it uses water as a solvent to capture CO_2 and the regenerative or dissociation step is less energy intensive [158, 224].

However, the results presented in *Chapter 2* and literature [202] showed that GSHF process using only water requires a high amount of energy. The use of thermodynamic promoters can reduce the energetic exigency, as well as improve the kinetic and thermodynamic conditions of the process. These molecules moderate the formation conditions (higher temperature and lower pressure) of hydrate phases. In literature the tetrabutylphosphonium bromide (TBAB) and tetrahydrofuran (THF), also known to form semi-clathrate and SII clathrate structures, respectively, were extensively tested as promoters for the GSHF processes [42-44, 66, 69, 87, 90-91, 149, 225].

According to Babu et al. [226], although the liquid phase promoters (both sII and semiclathrates promoters) employed so far reduce the operating pressure significantly, they also result in low rate of hydrate formation and low separation factor and gas consumption. Hence, there are still ongoing efforts to search for new promoters.

In literature [69, 149, 225], GSHF process is normally evaluated by measuring the gas uptake, which is expressed by the ratio of mol of gas removed from gas phase by mol of water. Obviously, many assumptions are made. For example, authors usually don't take into account the density variation of the liquid and hydrate phases. The uncertainties for such assumptions can lead to high global uncertainty. Besides, the approach of gas uptake does not allow evaluating precisely the contribution of hydrate phase in the gas separation process.

Moreover, we can cite the recent works of Xia *et al.* [87], Zhong *et al*. [90] and Ricaurte *et al.*

[91, 149] that studied GSHF process using promoters involving CO_2 and CH_4. They used the promoters TBAB and THF to study the CO_2 capture from CO_2 + CH_4 mixture in a composition close to biogas. It is interesting to notice that although they used thermodynamic promoters, the operating pressure on their experiments were relatively high (> 2.5 MPa) and/or set temperature were relatively low (< 275 K).

Here we report a different point of view of the process. The contribution of hydrate phase was evaluated individually by estimating its composition. Moreover, the impact of the assumptions were taken into account by using the uncertainty propagation method [197, 201].

Therefore, we proposed a new study of GSHF process for biogas upgrading using thermodynamic promoters. The selected promoters, TBAB, tetrabutylphosphonium bromide (TBPB), tributylphosphine oxide (TBPO) and tetrahyropyran (THP), were used during the experiments. TBPB, TBPO and THP were tested for the first time. A new protocol exploring the memory effect of hydrate crystallization was performed and the kinetic aspects of the process were evaluated as well. Conditions of small driving force were applied in order to enhance the applicability of promoter in hydrate-based process.

For the experiments a gas mixture of CO_2 + CH_4 containing (39.0 ± 0.8) mol% of CO_2 was prepared directly into the reactor. This composition corresponds to a typical biogas produced by the digestion of agricultural wastes [8-10]. The initial promoter composition was chosen for a same maximum solid content (see *Table 3.4* in *Chapter 3*). The experimental protocols were described in *Chapter 3, Section 3.2.2.*

In *Sections 5.2* and *5.3* we will discuss and compare the kinetics of GSHF process for each promoter. The equilibrium *P, T* conditions and corresponding phase composition will be presented in S*ection 5.4*.

5.2 First Crystallization

The focus here is to evaluate the influence of each promoter on the hydrates formation kinetics. The protocol consisted in forcing a first crystallization by applying a high driving force, which is represented by a low temperature of 275.1 K, followed, after dissociating the hydrates formed, by a second crystallization at lower driving force (higher temperature). In this *Section* we will discuss the results obtained in the First Crystallization (FC) step. *Figure 5.1* shows some pressure and temperature profiles obtained during the experiments.

In *Figure 5.1a* the hydrate crystallization is confirmed by a sudden temperature increase followed by a pressure drop due to the gas consumption (*Figure 5.1b*). This quick temperature increase is due to the heat released when the supersaturated metastable state is suddenly broken. Furthermore, in *Figure 5.1a* it is possible to notice that the beginning of hydrate formation occurs at different times for each promoter. For the condition studied, THP seems to promote the hydrate formation faster than the other promoters by presenting the smallest induction time. This tendency is followed by TBPB, TBAB and TBPO.

The pressure drop rate observed in *Figure 5.1b* may be related to the rate of hydrates crystallization. TBPO exhibits the highest crystallization rate, consuming more gas in the same period compared to the other promoters. After 30 minutes of crystallization the pressure dropped from approximately 2.1 MPa to less than 1.8 MPa. In contrast, with the system containing TBPB the pressure dropped from approximately 2.1 MPa to just below 2.0 MPa during the same period of time.

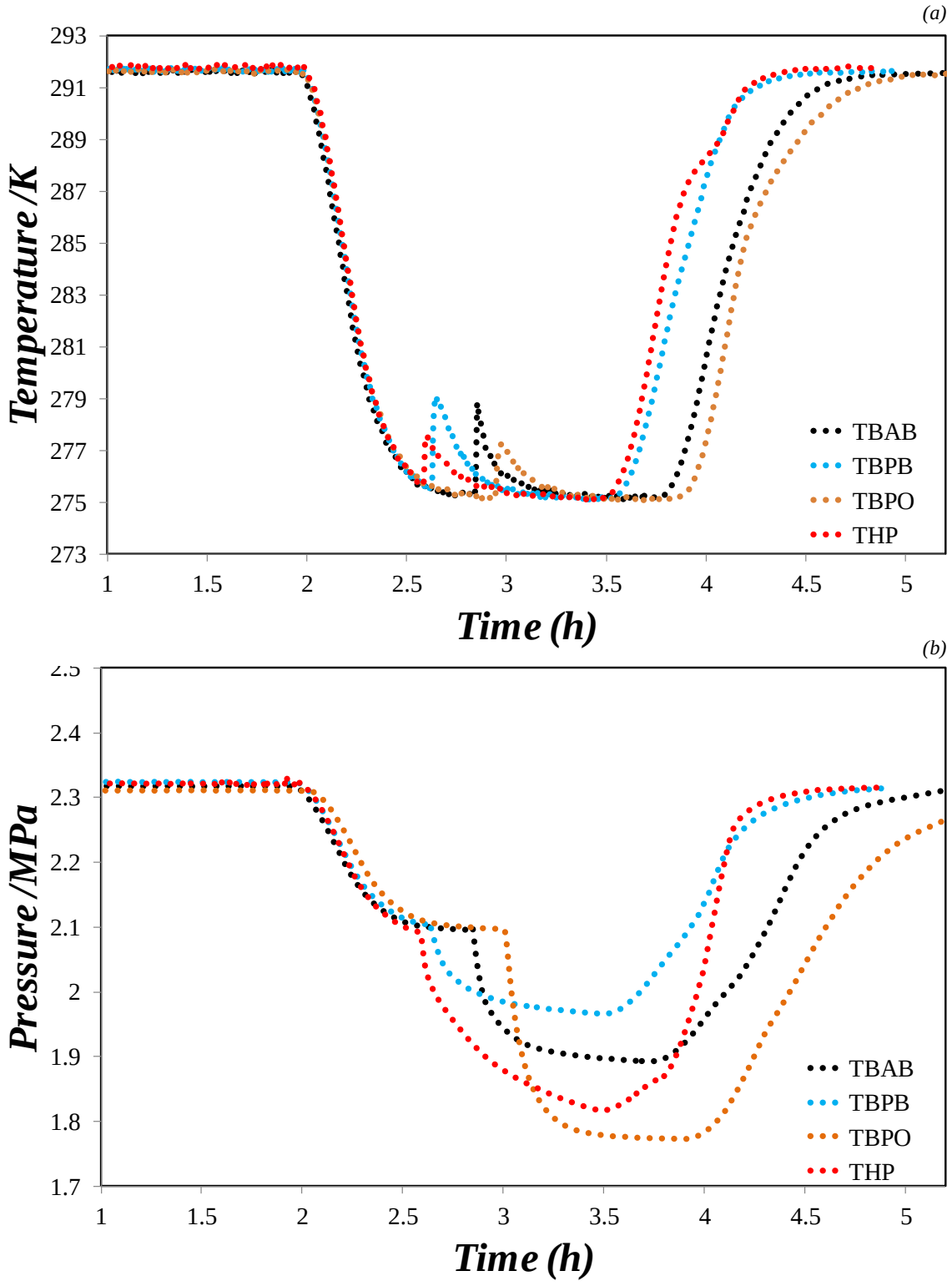

Figure 5.1. First Crystallization results: (a) temperature profiles; (b) pressure profiles.

The average values of induction time and gas consumption rate are listed in *Table 5.1*. For easier comprehension we plotted the values of gas consumption rate in *Figure 5.2*.

Table 5.1. Induction times and gas consumption rates for FC experiments.

	Induction Time (min)	*- dp/dt x 10^3 (MPa/min) t=10 min*	*- dp/dt x 10^3 (MPa/min) t=20 min*	*- dp/dt x 10^3 (MPa/min) t=30 min*
TBAB	6.15 ± 5.18^{a}	163 ± 7^{a}	96 ± 4^{a}	68 ± 3^{a}
TBPB	$1.99 \pm 1.67^{a,b}$	105 ± 21^{b}	66 ± 13^{b}	48 ± 9^{b}
TBPO	$17.13 \pm 14.45^{a,c}$	262 ± 8^{c}	157 ± 6^{c}	108 ± 5^{c}
THP	$0.58 \pm 0.74^{a,b,d}$	$154 \pm 4^{a,d}$	$101 \pm 4^{a,d}$	78 ± 3^{d}

[a], [b], [c] and [d] Tukey-test with $p < 0.05$.

The values presented in *Table 5.1* are the average from six measurements followed by the standard deviation. The induction time is normally related to the delay of hydrate formation from the moment when the system has entered into the hydrate phase existence region [141, 221-222].

Since the cooling rate of the reactor is limited, we measured the time elapsed from the moment when the system reached the set temperature till the moment when the crystallization started. In other words, we took the isothermal period before the crystallization as the induction time. Considering the values in *Table 5.1,* it can be concluded that THP presented the smallest induction time, followed by TBPB, TBAB and TBPO. The magnitude of the standard deviation can be considered as normal, based on the stochastic nature of hydrates nucleation [69, 141, 221-222, 227].

Analyses of variance (ANOVA) were performed in order to verify if the means are different from each other. The F calculated were higher than F statistic for all tests, which rejects the null hypothesis that the means are equal. Tukey-test was then carried out in order to define which means differ to each other. In induction time, TBAB has no significant difference ($p < 0.05$) from the other promoters. TBPB and THP are statistically equal and TBPO is different from these two.

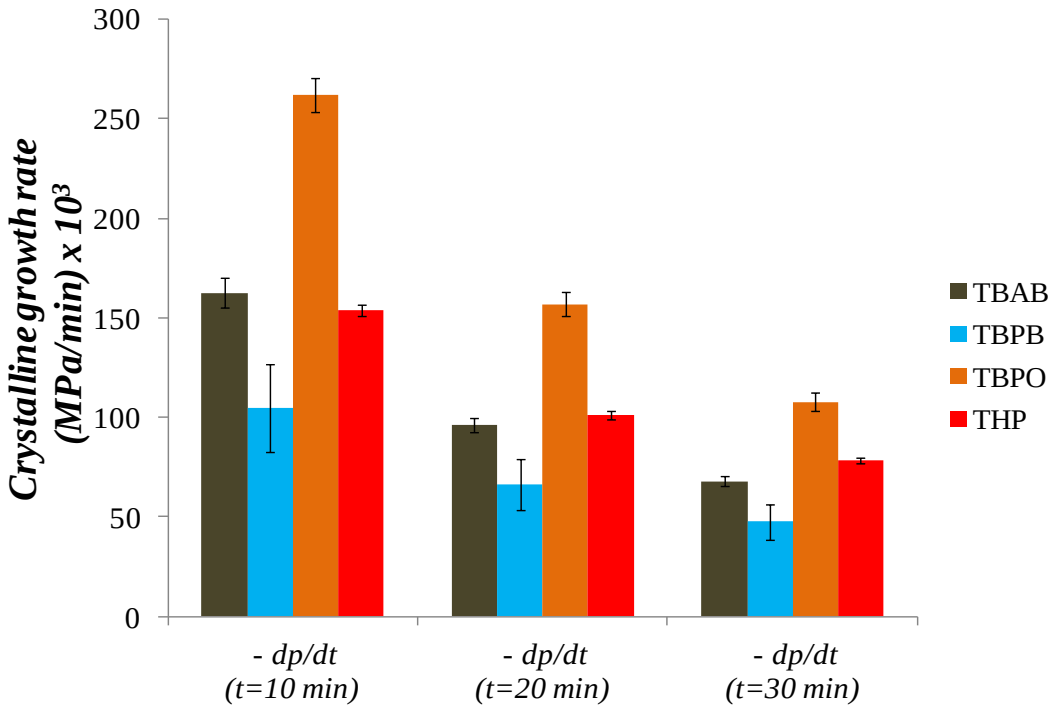

Figure 5.2. Gas consumption rate results for First Crystallization.

The gas consumption rate, represented by the pressure drop rate (*dp/dt*) after starting the crystallization, may be related to the rate of crystal growth of the hydrates. From the values in *Table 5.1* and *Figure 5.2* TBPO presented the highest effect on this parameter. This result can be related to the relatively high induction time presented by this promoter in the experiments. During this period more gas is dissolved in the super saturated liquid. Then, when this metastable state is broken, the excess gas is rapidly consumed, causing the fast decrease of pressure. On the other hand, TBPB presented a small induction time and the smallest gas consumption rate. We also attributed this behavior to the possibility of single TBPB hydrates being formed because, for these conditions of pressure and temperature, this metastable phase can appear (see *Section 4.2* at *Chapter 4*). During the 10 and 20 first minutes of crystallization TBAB hydrates rate of formation has no significant difference compared to THP hydrates. Then, after 30 minutes all promoters were different from each other.

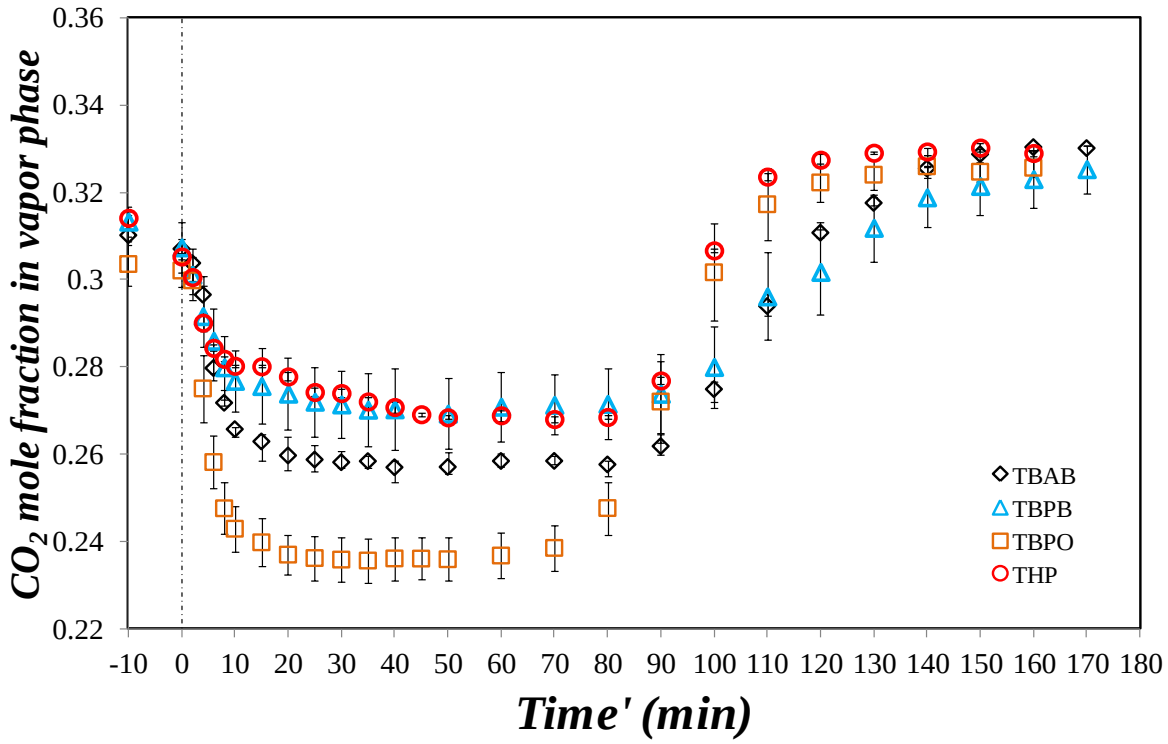

Figure 5.3. First Crystallization results: evolution of CO_2 composition in gas phase after the crystallization (time' = 0).

Figure 5.3 shows the evolution of CO_2 concentration in the gas during the crystallization. For all promoters the mole fraction of CO_2 decreased in the first minutes of crystallization. This observation indicates that in this period CO_2 was preferentially consumed to form the hydrate phase. The promoter TBPO presented the highest CO_2 capture power, decreasing the vapor concentration of CO_2 from almost 0.31 to less than 0.24 in the first 20 minutes of crystallization. On the other hand, THP hydrate formation only decreased the CO_2 vapor concentration from almost 0.31 to just under 0.28 in the same period.

The measured parameter of CO_2 capture rate for each promoter is presented in *Table 5.2* and plotted in *Figure 5.4.* The values presented are an average of six measurements, followed by the standard deviation.

Table 5.2. CO_2 capture rate during FC experiments; results expressed as mole fraction unit per minute.

	$-dy_{CO2}/dt \times 10^3$ (t = 10 min)	$-dy_{CO2}/dt \times 10^3$ (t = 20 min)	$-dy_{CO2}/dt \times 10^3$ (t = 30 min)
TBAB	4.13 ± 0.28^{a}	2.37 ± 0.29^{a}	1.63 ± 0.16^{a}
TBPB	$3.06 \pm 0.78^{a,b}$	$1.68 \pm 0.46^{a,b}$	$1.20 \pm 0.28^{a,b}$
TBPO	5.92 ± 0.25^{c}	3.26 ± 0.08^{c}	2.21 ± 0.06^{c}
THP	2.50 ± 0.08^{d}	1.37 ± 0.09^{d}	1.04 ± 0.05^{d}

^{a}, ^{b}, ^{c} and ^{d} Tukey-test with $p < 0.05$.

The highest value of CO_2 capture rate was for TBPO promoter after 10, 20 and 30 minutes of crystallization. This is probably related to the high gas consumption rate observed in the presence of this promoter, as shown in *Table 5.1*. On the other hand, the smallest CO_2 capture rate was observed for THP.

Comparing the values in *Table 5.2*, TBAB have no significant statistical difference with TBPB during the 10, 20 and 30 first minutes of crystallization. For the same periods, TBPB, TBPO and THP are significantly different.

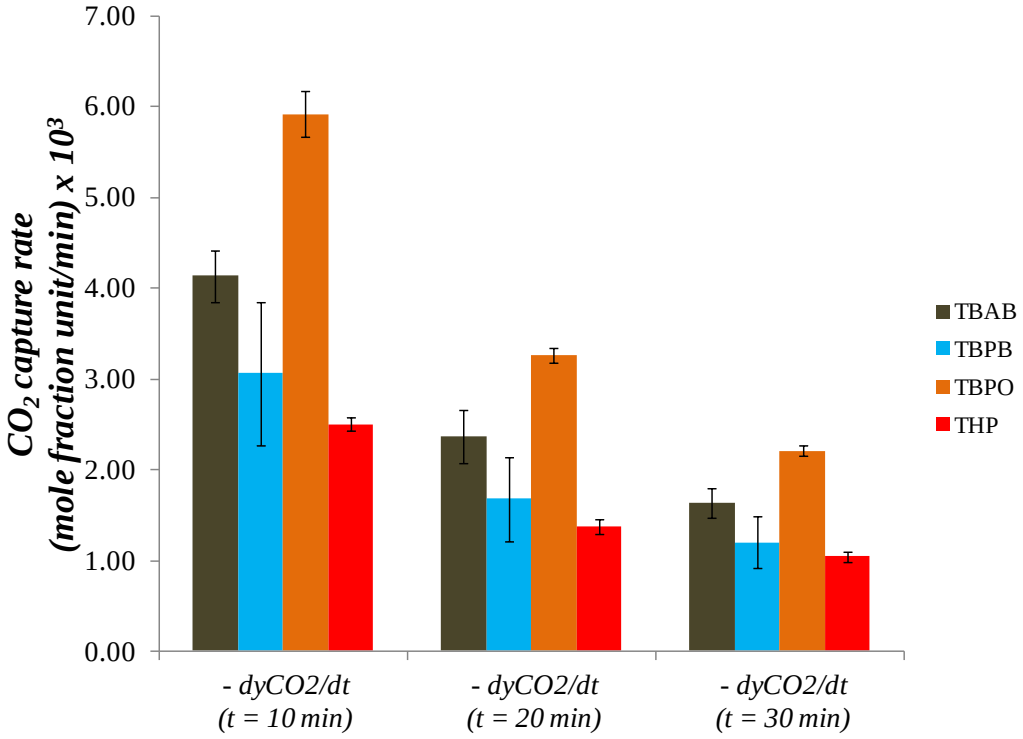

Figure 5.4. CO_2 capture rate for First Crystallization.

5.3 Main Crystallization

After the First Crystallization and subsequent dissociation steps, we carried out the protocol to study the hydrate formation at smaller driving force, thus at higher set temperature. We called this next step the Main Crystallization because the set temperature corresponds to a suitable value in a possible GSHF process. The protocol consisted in decreasing the temperature of the cell down to a set value of 281.1 K right after the dissociation that followed the First Crystallization. *Figure 5.5* shows some temperature and pressure profiles obtained using this protocol.

Figure 5.5a presents the recorded temperature signal for each promoter during the experiments. As explained in previous *Section*, hydrate formation is confirmed by a sudden temperature increase. Therefore, we observed that the system containing TBPB quickly formed the hydrate phase (crystallization starting before reaching the set temperature). THP also formed hydrate phase with small induction time; a few minutes at set temperature was necessary to start the nucleation. On the other hand, for TBAB and TBPO a longer isothermal period was necessary to start the nucleation.

In *Figure 5.5b* the profiles of pressure correspond to gas consumption after the crystallization. The shape of the signal can be interpreted as three stages. At the first stage, in the first minutes of hydrate formation, the pressure signal is practically a straight line characterizing constant gas consumption (CGC). During this period the excess gas in the over saturated liquid phase is consumed. The driving force is at a maximum value. For TBPB this stage is almost inexistent since the nucleation started practically without over saturation period (no induction time). The second stage starts when the supersaturation ends and the hydrate crystal growth requires further gas transfer from the gas phase toward the hydrate – liquid interface. This period is characterized by falling gas consumption (FGC) and is controlled by the mass transfer resistances as well as the decreasing driving force. When the driving force is null, no further gas is consumed (constant pressure) and the hydrate formation process is considered complete. At this moment, the system is near to equilibrium state (Eq).

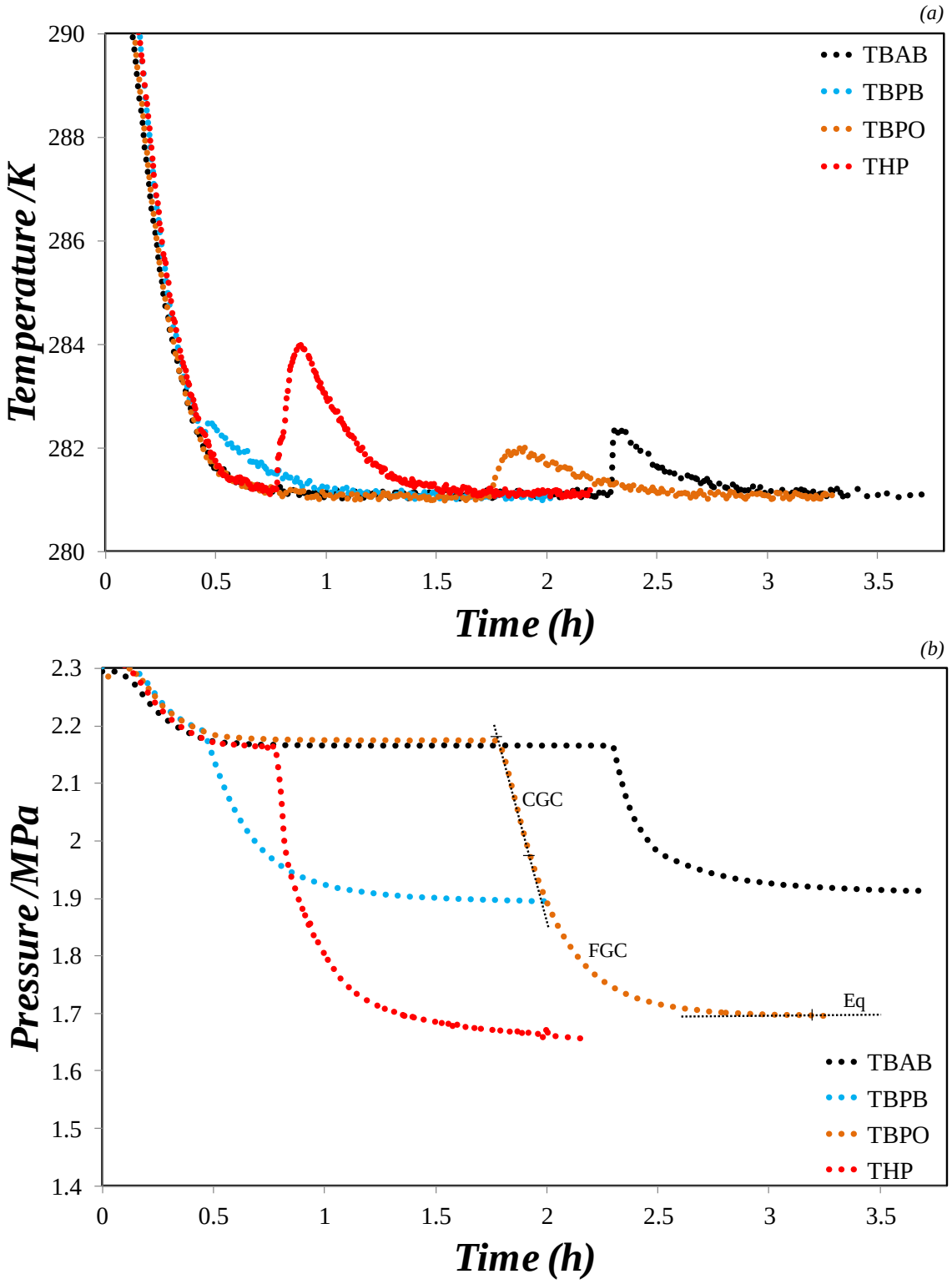

Figure 5.5. Main Crystallization results: (a) temperature profiles; (b) pressure profiles.

The measured kinetic parameters for the main crystallization step, such as induction time and gas consumption rate are listed in *Table 5.3.* Gas consumption rates for each promoter are also plotted in *Figure 5.6*, allowing easier visualization.

Table 5.3. Induction time and gas consumption rate for MC experiments.

	Induction Time (min)	*- dp/dt x 10^3 (MPa/min) t=10 min*	*- dp/dt x 10^3 (MPa/min) t=20 min*	*- dp/dt x 10^3 (MPa/min) t=30 min*
TBAB	113.74 ± 39.26^{a}	162 ± 7^{a}	103 ± 2^{a}	75 ± 2^{a}
TBPB*	- ^{b}	$158 \pm 5^{a,b}$	117 ± 3^{b}	89 ± 2^{b}
TBPO	$69.28 \pm 46.77^{a,c}$	211 ± 14^{c}	177 ± 8^{c}	140 ± 4^{c}
THP	9.53 ± 9.04^{d}	336 ± 7^{d}	208 ± 3^{d}	153 ± 3^{d}

* No induction time observed (Hydrate phase always started before reaching the set temperature)
^{a}, ^{b}, ^{c} and ^{d} Tukey-test with $p < 0.05$.

It is important to notice in *Table 5.3* that the system containing TBPB promoter did not present induction time, since for this promoter the crystallization started before reaching the set temperature. In other words, in all experiments, TBPB presented a very high memory effect, allowing much easier (or faster) recrystallization under milder conditions than the initial crystallization. Such reduction of the induction time after a first cycle of crystallization/melting was already observed in hydrate systems [142-144].

Observing the other values of induction times, we note that the randon nature of this phenomenon is still present and marked by a high standard deviation. However, the memory effect was confirmed by considerably reducing the period necessary for the nucleation. Tests without the First Crystallization (see *Protocol 1* in *Section 3.3.2.1*) leaded to very high induction times; several days were sometimes necessary to form hydrates. Beyond that, the difference of memory effect between each promoter could be related to the number of residual structures that each system maintains after the First Crystallization. These residual structures may be cage-like structures [228] or conformations of guest molecules [142].

Furthermore, comparing to the First Crystallization (*Table 5.1*), the induction time values of Main Crystallization were higher (except with TBPB), which is expected since the set temperature of this last one provides a smaller driving force.

The nucleation phenomenon of hydrate phase and its stochastic nature is often cited as a drawback for industrial application of hydrate based process. The exploration of memory effect could offer a solution to this problem since the liquid phase is supposed to be recycled at each new crystallization step.

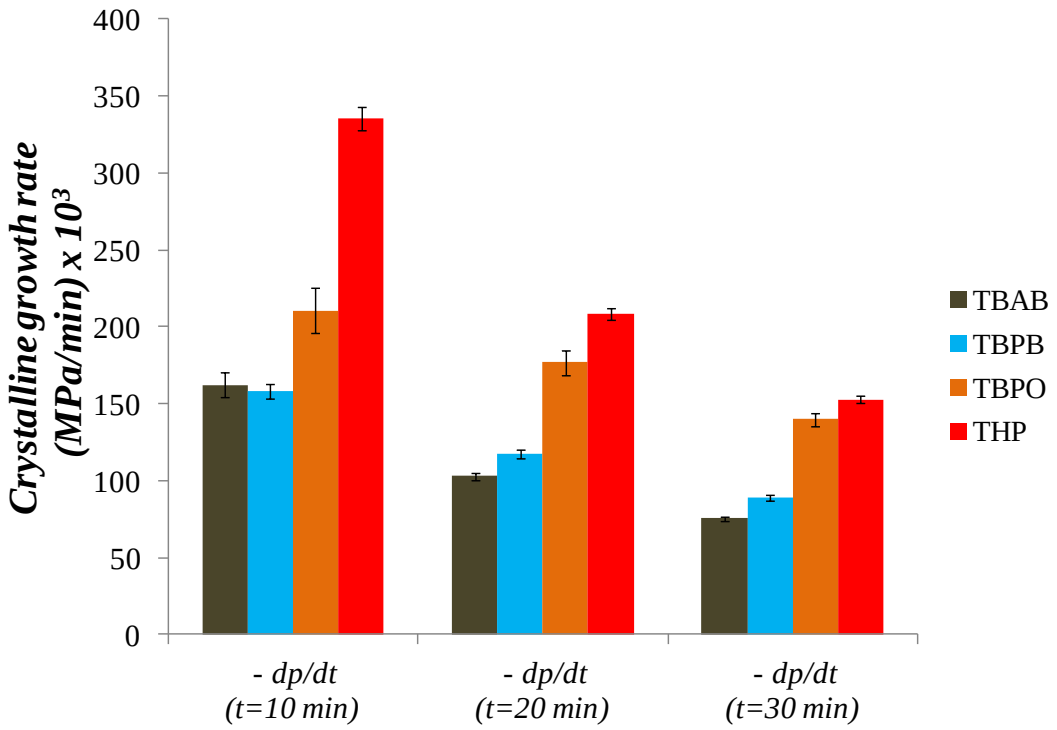

Figure 5.6. Gas consumption rate results for Main Crystallization.

In *Table 5.3* and *Figure 5.6* we can observe the impressive enhancement of gas consumption rate for the system containing the promoter THP. It is even higher than those from the First Crystallization. This result is unexpected since the set temperature of Main Crystallization is higher which provide smaller gas solubility and theoretically smaller crystal growth rate. We attribute this behavior to various aspects. The first relates to the driving force, which was the highest for THP among all promoters, since the equilibrium pressure was the smallest (see *Table 5.5*). The second could be a higher vapor-hydrate interface area which would reduce the gas path into the cages, as stated by [146-147]. In this case, one part of the gas could be directly transferred to the hydrate phase, thus eliminating the gas transfer path in bulk liquid phase. The third aspect that could explain this higher gas consumption would be a simultaneous enclathration of CO_2 and CH_4 at similar rates. For the other promoters CO_2 seemed to be encaged first (see *Figures 5.3* and *5.6*). In *Figure 5.7* we observe the evolution of CO_2 gas phase composition (y_{CO2}) after the crystallization. For THP y_{CO2} is almost constant, which seems to confirm the hypothesis of simultaneous enclathration.

For the promoters TBAB and TBPO the gas consumption rate of Main Crystallization were almost equal to those from First Crystallization. TBPB presented a substantial increase, which can be related to the fact that only mixed promoter/gas hydrate was formed, while at First Crystallization the set temperature allowed the formation of metastable single promoter

hydrate.

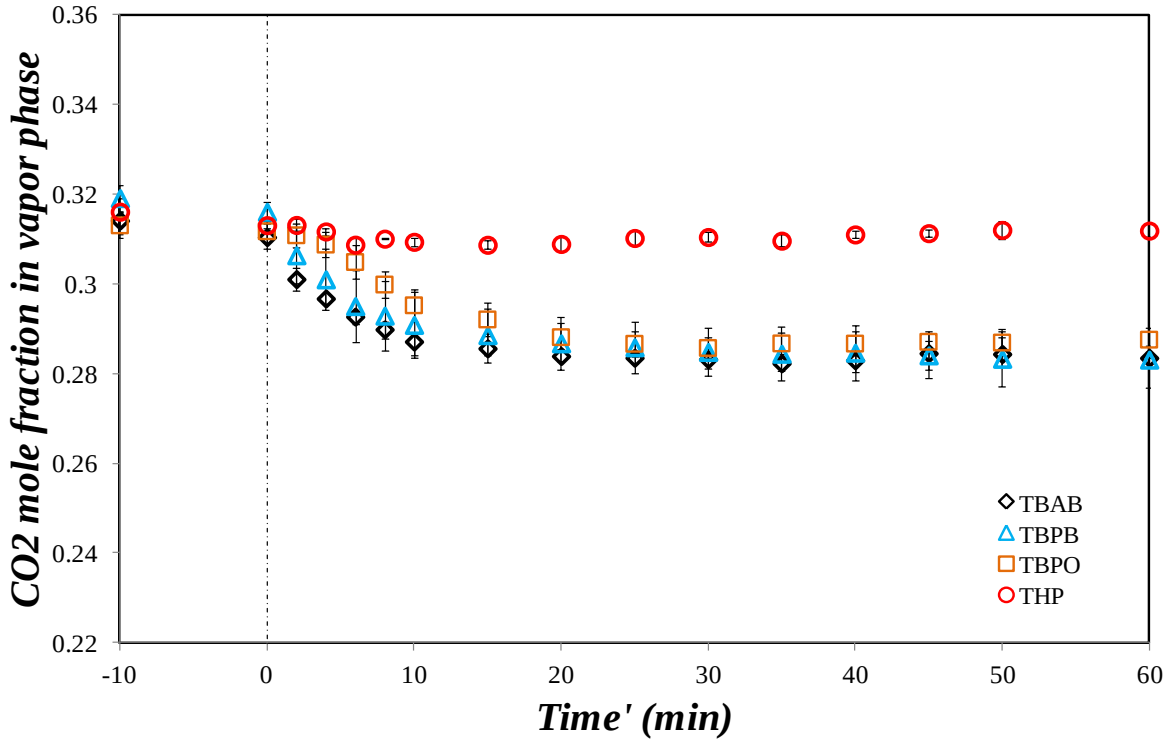

Figure 5.7. Main Crystallization results: evolution of CO_2 composition in gas phase after the crystallization (time' = 0).

The evolution of CO_2 composition in gas phase during hydrate formation in Main Crystallization is presented in *Figure 5.7*. In the first minutes, for TBAB, TBPB and TBPO CO_2 is preferably consumed to form the hydrate phase. Then, a competition with CH_4 appears and y_{CO2} tends to increase with time. For THP, y_{CO2} was practically stable, confirming the higher affinity of CH_4 for the hydrate phase in the presence of this promoter. The measured values of CO_2 capture rate are listed in *Table 5.4* and plotted in *Figure 5.8.*

Table 5.4. CO_2 capture rate during MC experiments; results expressed as fraction mole unit per minute.

	$-dy_{CO2}/dt \times 10^3$ (t = 10 min)	$-dy_{CO2}/dt \times 10^3$ (t = 20 min)	$-dy_{CO2}/dt \times 10^3$ (t = 30 min)
TBAB	2.33 ± 0.18^{a}	1.33 ± 0.10^{a}	0.91 ± 0.06^{a}
TBPB	$2.53 \pm 0.57^{a,b}$	$1.47 \pm 0.21^{a,b}$	$1.04 \pm 0.12^{a,b}$
TBPO	1.65 ± 0.24^{c}	1.18 ± 0.12^{c}	$0.87 \pm 0.08^{a,c}$
THP	0.37 ± 0.108^{d}	0.21 ± 0.04^{d}	0.09 ± 0.01^{d}

a, b, c and *d* Tukey-test with $p < 0.05$.

In *Table 5.4* and *Figure 5.8* we observe that TBAB and TBPB provided the highest CO_2 capture rates. There are no significant differences between these two additives. Comparing to the First Crystallization, CO_2 capture rate in Main Crystallization were generally smaller. This result was expected because the solubility of CO_2 is higher at lower temperature and this is an important parameter that limits the mass transfer phenomenon in vapor-liquid interface.

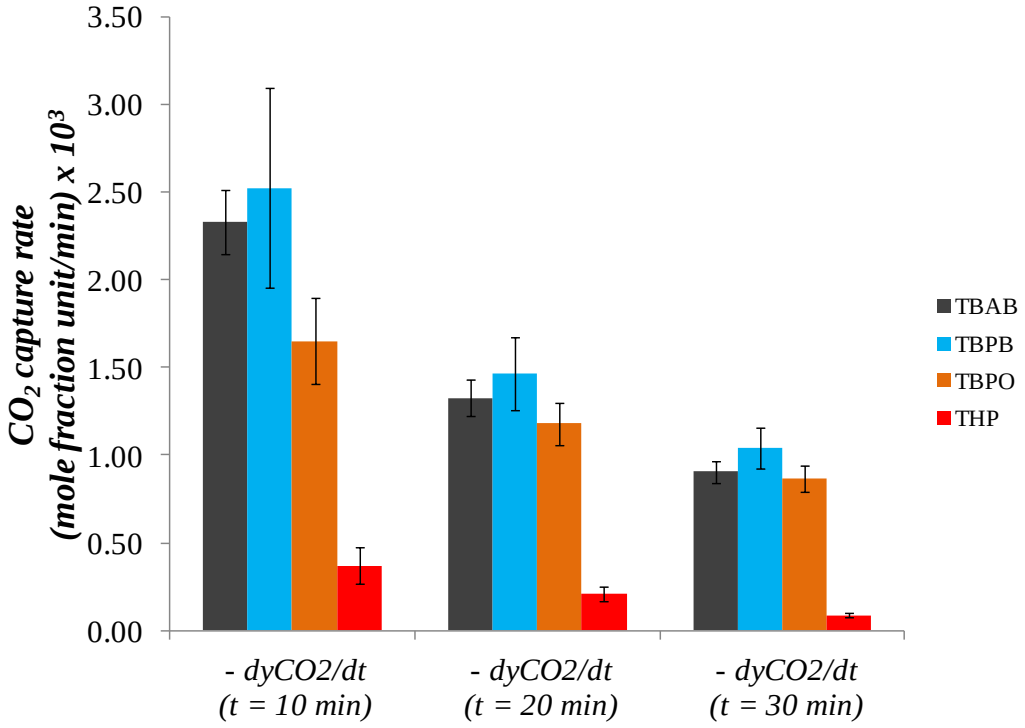

Figure 5.8. CO_2 capture rate for Main Crystallization.

5.4 Equilibrium state

After the hydrate formation in Main Crystallization step, we waited for 24 hours for the systems to reach the equilibrium state. At this point, liquid and gas sampling were performed and the phase compositions were measured. Then, we increased the set temperature up to 283.1 K and waited for 24 more hours for a new equilibrium. Once again the phase composition measurements were carried out. *Tables 5.5* and *5.6* present the characterization of the equilibrium state at the different set temperatures 281.K and 283.1 K, respectively.

We observe a good reproducibility of the results of run 1 and 2. Comparing the promoters in terms of equilibrium pressure the observed differences are mainly due to the amount of hydrate formed. This result can be considered as normal since a higher amount of hydrate phase indicates that more gas was trapped, thus lowering the pressure. The amount of hydrate formed depends on the initial promoter quantity and the hydration number of the hydrate it forms (see *Table 3.4* at *Chapter 3*). THP having the highest initial mole composition, more hydrate was formed.

TBAB and TBPB trapped more CO_2 in hydrate phase (n_{CO2}^{H}) confirming the tendency observed in phase equilibrium data at *Chapter 4* and in literature [123, 129, 137, 229-230]. The CO_2 vapor composition (y_{CO2}), being the smallest for these promoters, corroborated these results. TBPO and THP also confirmed the opposite tendency observed in *Chapter 4* by encaging more CH_4 than CO_2 in hydrate phase. It is interesting to notice that THP enclathrated almost the double amount of CH_4 than CO_2.

By increasing the set temperature some hydrates dissociated, which is evidenced by the decrease of n_H. This dissociation generally seemed to release mainly CO_2 since its vapor concentration was increased.

Table 5.5. Equilibrium state characterization at set temperature of 281.1 K; y_{CO2} is CO_2 vapor composition; n_H is the number of moles of hydrate; n_{CO2}^H, n_{CO2}^L and n_{CO2}^V are the number of moles of CO_2 in hydrate, liquid and gas phase, respectively; n_{CH4}^H, n_{CH4}^L and n_{CH}^V are the number of moles of CH_4 in hydrate, liquid and gas phase, respectively.

T = 281.1 K											
					Hydrate phase /moles			Liquid phase /moles		Gas phase /moles	
	run	*P /MPa*	$w_{promoter}$ /%	y_{CO2}	n_H $x10^{3*}$	n_{CO2}^H $x10^{3*}$	n_{CH4}^H $x10^{3*}$	n_{CO2}^L $x10^3$	n_{CH4}^L $x10^3$	n_{CO2}^G $x10^3$	n_{CH4}^G $x10^3$
TBAB	1	1.88	3.018	0.283	14.5 ± 0.5	16.2 ± 1.5	9.5 ± 1.6	13.0	1.1	35.4	89.6
	2	1.87	3.123	0.285	14.5 ± 0.5	16.1 ± 1.5	10.3 ± 1.6	13.0	1.1	35.4	88.8
TBPB	1	18.6	3.629	0.289	13.5 ± 0.7	15.5 ± 1.6	10.8 ± 1.8	13.4	1.1	35.7	87.9
	2	18.7	3.674	0.290	13.3 ± 0.7	15.0 ± 1.5	10.7 ± 1.8	13.4	1.1	36.1	88.4
TBPO	1	1.67	0.726	0.299	20.9 ± 0.6	20.5 ± 1.4	22.5 ± 1.7	11.6	0.9	32.9	77.2
	2	1.66	0.781	0.302	21.0 ± 0.6	20.1 ± 1.4	23.4 ± 1.7	11.7	0.9	33.0	76.2
THP	1	1.49	2.294	0.339	35.1 ± 1.1	18.6 ± 1.3	34.3 ± 1.5	12.7	0.8	33.5	65.3
	2	1.52	2.210	0.335	35.1 ± 1.1	18.5 ± 1.3	32.0 ± 1.6	12.7	0.8	33.8	67.0

***** calculated values ± expanded uncertainty calculated from uncertainty propagation method with 95 % coverage

Table 5.6. Equilibrium state characterization at set temperature of 283.1 K; y_{CO2} is CO_2 vapor composition; n_H is the number of moles of hydrate; n_{CO2}^H, n_{CO2}^L and n_{CO2}^V are the number of moles of CO_2 in hydrate, liquid and gas phase, respectively; n_{CH4}^H, n_{CH4}^L and n_{CH}^V are the number of moles of CH_4 in hydrate, liquid and gas phase, respectively.

T = 283.1 K											
					Hydrate phase /moles			Liquid phase /moles		Gas phase /moles	
	run	*P /MPa*	$w_{promoter}$ /%	y_{CO2}	n_H x10^{3} *	n_{CO2}^H x 10^{3} *	n_{CH4}^H x 10^{3} *	n_{CO2}^L x 10^{3}	n_{CH4}^L x 10^{3}	n_{CO2}^G x 10^{3}	n_{CH4}^G x 10^{3}
TBAB	1	1.94	4.158	0.292	12.8 ± 0.5	13.6 ± 1.5	7.9 ± 1.6	13.4	1.1	37.6	91.2
	2	1.95	4.343	0.294	12.3 ± 0.5	13.4 ± 1.4	8.6 ± 1.6	13.5	1.1	37.7	90.5
TBPB	1	1.95	4.826	0.301	11.5 ± 0.7	11.8 ± 1.5	8.6 ± 1.7	14.0	1.1	38.8	90.1
	2	1.95	4.888	0.304	11.3 ± 0.7	11.3 ± 1.5	9.2 ± 1.7	14.1	1.1	37.7	90.5
TBPO	1	1.71	2.045	0.309	18.1 ± 0.6	18.5 ± 1.4	21.8 ± 1.6	11.9	0.9	34.6	77.4
	2	1.72	2.063	0.312	18.2 ± 0.6	17.6 ± 1.4	22.1 ± 1.6	12.2	0.9	37.7	90.5
THP	1	1.57	2.628	0.349	32.9 ± 1.0	15.8 ± 1.2	32.4 ± 1.6	12.9	0.8	36.0	67.2
	2	1.56	2.585	0.346	32.8 ± 1.0	16.7 ± 1.3	31.8 ± 1.6	12.7	0.8	35.6	67.2

***** calculated values ± expanded uncertainty calculated from uncertainty propagation method with 95 % coverage

The relatively high uncertainties in *Tables 5.5* and 5.6 confirm the difficulty to accurately measure the phase composition in systems involving hydrates. This difficulty is in part related to the lack of experimental data, such as the density of aqueous solutions of promoters and the solubility of CO_2 and CH_4 in promoters' aqueous solutions. As a result, it was necessary to make some assumptions. To reduce the uncertainties in the final results, assumptions must be made carefully and the experimental uncertainties must be minimized at most.

Observing the results of TBPO and THP, especially for this last one, we notice that CH_4 has higher presence in hydrate phase while CO_2 is majority in liquid phase. Taking into account these results, a different gas separation process involving both the liquid and the hydrate phases can be imagined. In this new proposed process CH_4 could be trapped in hydrate phase while CO_2 would remain dissolved in the liquid phase. Moreover, the CH_4 content in hydrate phase between the two set temperatures is very close. This weak influence of the temperature suggests that the higher set temperature of 283.1 K can be used without losing efficiency. It may represent an energy gain for the process.

Experiments realized in the presence of TBAB presented the smallest CO_2 concentration in gas phase while those using THP showed the highest. In terms of separation efficiency of GSHF, this indicates that TBAB could be more appropriate for this process. *Figure 5.9* presents the calculated Separation Factor in terms of CO_2 removal of the process for each promoter at different set temperatures. Taking into account the uncertainties there are no meaningful differences between TBAB and TBPB and these promoters presented the best results. However, the small values of Separation Factor indicate a high difficulty to separate CO_2+CH_4 as well as confirm that CH_4 competes with CO_2 for occupying the cages in hydrate structure. Note that the Separation Factor is lower than 1 for THP which reinforces the idea that this promoter could be used to selectively trap CH_4 in hydrate phase instead of CO_2.

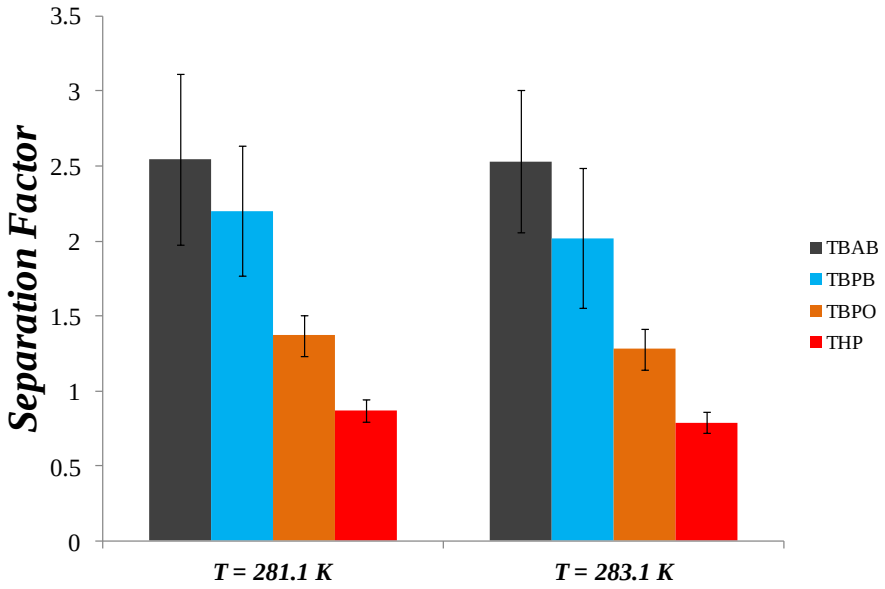

Figure 5.9. Separation factor with respect to CO_2 at equilibrium state.

Figure 5.10 shows the capacity of CO_2 removal of each hydrate phase, calculated as the contribution of CO_2 removal from the initial amount per mole of formed hydrate. For example, for TBAB, each mole of hydrate contributed to remove about (17.2 ± 2) % of total CO_2 in the feed gas. From this *Figure*, we can then see that there is practically no difference between TBAB and TBPB at set temperature of 281.1 K. At 283.1 K TBAB, TBPB and TBPO give very close results. In both conditions THP presented the smallest contribution for removing CO_2.

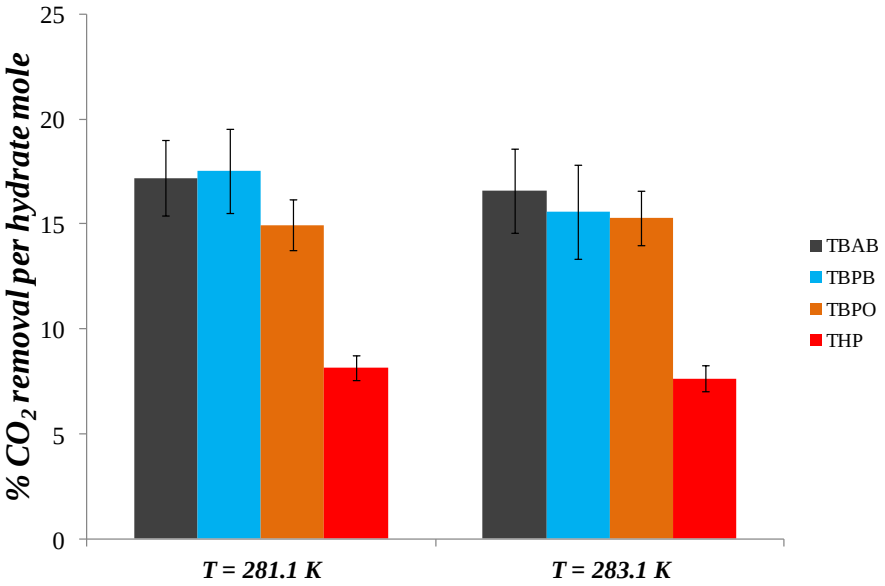

Figure 5.10. Contribution of each promoter in CO_2 removal.

Like in *Chapter 2*, we observed that one equilibrium stage crystallization is not enough to separate efficiently the gas mixture CO_2 + CH_4. However, the kinetics results are promising. We showed that generally CO_2 is preferentially capture at the first minutes of crystallization and we can considerably reduce the induction time under small driving force conditions by exploring the memory effect phenomenon.

CONCLUSIONS AND PERSPECTIVES

In this work we studied the gas separation by hydrate formation (GSHF) process as a new technique for biogas upgrade. Here, we are going to expose the main concluding remarks as well as some perspectives for hydrate-based process.

In the *Introduction* and *Chapter 1* we pointed out the importance of biogas as a renewable energy source and that hydrate-based process may be used to separate the two main constituents of biogas.

In *Chapter 2* the gas hydrate phase envelope diagrams were obtained by thermodynamic modeling for the couple CH_4/CO_2 in presence of water and low concentration of H_2S. These graphics show that the upgrading of biogas using gas hydrate process is possible, but requires a multi-stage process for high separation efficiency. A simulated biogas upgrading process via gas hydrate formation was therefore presented. The gas treated at the end of four stages of crystallization presented a methane concentration of about 87.7 %. The simulation showed a weak selectivity of the hydrate phase for the couple CH_4/CO_2. Moreover, the simulated process showed a high energy demand due to the high pressure and low temperature operation condition and important methane losses. The use of some hydrate promoters that reduce the induction time (kinetics) and the pressure required for the hydrate formation (thermodynamics) may improve the gas separation process. Therefore, a selection of chemical additives was carried out. Four thermodynamic promoters (TBAB, TBPB, THP and TBPO) were selected for their potential ability to improve biogas upgrading using hydrate formation.

Chapter 3 describes the experimental methods for the measurements of hydrate formation conditions and the study of GSHF process for biogas. The different DSC protocols used during the experiments for determining the hydrate phase transition properties are exposed. Moreover, a new experimental protocol exploring the memory effect was set up in order to verify the reduction of induction time under small driving force condition. A set of equations based on mass balance are presented for characterizing the equilibrium state in terms of phase composition.

The results of this research work are presented in two axis: the thermodynamic study (*Chapter 4*) and the process study (*Chapter 5*). In *Chapter 4* we present the measurements of the hydrate formation conditions for systems containing the selected promoters TBPB, TBPO and THP. Dynamic and/or stepwise DSC protocols were used for determining the phase

transition temperatures for each system. The measurements were carried out for promoter-water system and promoter-water-vapor system. The vapor phase being either pure CO_2 and CH_4 or CO_2 + CH_4 mixture in a composition close to most biogases, i.e., 40 mol% of CO_2.

In general, compared to the respective gas clathrates, the presence of promoters shifted the equilibrium curves toward lower pressures and higher temperatures, which confirms the capacity of these molecules to soften the conditions required by the process. The pressure/temperature limits of stability of thermodynamically promoted hydrates were explored in a wide range of promoter concentration.

The thermodynamic study involving aqueous solutions of TBPB in a range of mass fraction from 0.05 to 0.35 was carried out using DSC dynamic method. The phase diagrams of single TBPB semi-clathrate, mixed TBPB/CH_4 semi-clathrate (pressure ranging from 1 to 8 MPa) and mixed TBPB/CO_2+CH_4 semi-clathrate (pressure ranging from 1 to 2 MPa) was presented. For pressures below 4 MPa, TBPB/CH_4 semi-clathrate showed to be less stable than TBPB/CO_2 semi-clathrate for any additive concentration.

The phase behavior of single TBPO semi-clathrate was determined at ambient pressure for a TBPO mass fraction ranging from 0.05 to 0.4. From the analysis of DSC thermograms, the stoichiometric composition of TBPO hydrate was evaluated between w_{TBPO} = 0.26 and 0.30. For this system the phase transition temperatures varied from 278.1 to 281.0 K. The phase diagram of TBPO/CO_2, TBPO/CH_4 and TBPO/(CO_2+CH_4) semi-clathrates were obtained in a range of TBPO mass fraction from 0.05 to 0.30 and a pressure range from 1 to 3 MPa. In these systems the dissociation temperature varied from 284.4 K to 292.5 K. Furthermore, The TBPO/CH_4 semi-clathrate showed to be more stable than the TBPO/CO_2 semi-clathrate.

The *T*-*w* phase diagram of the binary system THP + water was obtained for THP mass fraction ranging from 0.025 to 0.500. This system presents an eutectic composition probably situated between w_{THP} = 0.101 and w_{THP} = 0.125. Moreover, above w_{THP} = 0.150 the system presents an invariant at 273.3 K delimiting the *liquid-liquid* and *hydrate-liquid* existing phase regions. The phase transition temperatures for THP/gas hydrates were measured at w_{THP} varying from 0.050 to 0.300 and gas pressure ranging from 1 to 3 MPa. The measured equilibrium temperatures varied from 281.6 to 293.6 K. Like TBPO, this promoter stabilizes more stable gas hydrates with CH_4 than with CO_2. The study of gas storage capacity showed that CH_4 occupies practically all available 5^{12} cages in the hydrate structure, while the cage occupancy rate for CO_2 was around 60 %.

The new data presented in this work represent the starting point for the conceptual design of a hydrate-based gas separation processes involving the studied promoters.

Finally, in *Chapter 5* we present the results of GSHF study for biogas upgrade with the selected thermodynamic promoters. These molecules were tested and evaluated in kinetics and thermodynamics aspects. The new protocol proposed for exploring memory effect shows excellent results. This phenomenon considerably reduced the induction time for hydrates crystallization under small driving force conditions.

In the first crystallization (FC) with set temperature of 275.1 K, THP presented the smallest induction time while TBPO exhibited the highest gas consumption rate and CO_2 capture rate. In the main crystallization (MC) with set temperature of 281.1 K TBPB showed the highest memory effect, characterized by the smallest induction time. The highest value of gas consumption rate was obtained with THP. For CO_2 capture rate, TBAB and TBPB presented the best results.

Hydrate phase compositions were estimated at equilibrium state, which allowed us to investigate the specific contribution of this phase in GSHF process. Therefore, from the results of phase composition, TBAB and TBPB presented best values of separation factor with respect to CO_2. However, the values obtained are small, since the CO_2 vapor mole fraction was reduced from 0.39 to 0.28. In terms of the capacity of CO_2 removal in hydrate phase, there is little difference between TBAB and TBPB at set temperate of 281.1 K. Each mole of TBAB or TBPB hydrate contributed to remove about 17.2 % of the total CO_2 in the feed gas.

Finally, we observed that CO_2 + CH_4 are poorly separated using GSHF in one equilibrium stage crystallization. However, the presence of thermodynamic promoters allowed to operate the experiments at relatively low pressure and high temperature. Furthermore, the feasibility to use the studied promoters in hydrate based process at small driving force by exploring the memory effect was stated.

Perspectives

In *Chapter 2* we observed that the hydrate phase condition is highly affected by the presence of hydrogen sulfide, which indicates that this gas is easily enclathrated in hydrate phase. Since this gas must be removed for upgrading biogas, GSHF could be used as a pre-treatment for H_2S removal.

The impressive results obtained with THP promoters in trapping CH_4 at full cage occupancy rate lead us to propose this promoter for methane storage and transport. Moreover, the results presented in *Chapter 4* and *5* show that the higher amount of CH_4 trapped into the THP hydrate phase and the weak solubility of this gas in the liquid phase are in contrast with CO_2. These differences of affinity could be proposed in a new two phase GSHF process, in which CH_4 could be trapped in hydrate phase while CO_2 would remain dissolved in the liquid phase.

The selected promoters showed some thermodynamic and kinetic gains on the GSHF process. It could be interesting to use these promoters for GSHF process for other systems, such CO_2 + N_2 from post-combustion flue gas or CO_2 + H_2 from syngas.

The obtained results by exploring the memory effect were very interesting. The possibility to control this phenomenon could be seen as a solution for the stochastic problem of hydrates nucleation. Further studies are then necessary to better understand and control this phenomenon.

Finally, using the data obtained in this work, it will be interesting to develop or improve existing thermodynamic and/or kinetic models. For example, the model proposed by Paricaud [133] that recently [47] showed good ability to describe *p*-*T* liquid-hydrate-vapor equilibrium data for semi-clathrates formed from gas mixtures, could be extended to represent and predict phase compositions as well.

REFERENCES

[1] AEBIOM. A Biogas Road Map for Europe. *Renewable Energy House Belgium: European Biomass Association*. **2009**.

[2] Hijazi O, Munro S, Zerhusen B, Effenberger M. Review of life cycle assessment for biogas production in Europe. *Renewable and Sustainable Energy Reviews*. **2016**, 54: 1291-1300.

[3] Sorda G, Sunak Y, Madlener R. An agent-based spatial simulation to evaluate the promotion of electricity from agricultural biogas plants in Germany. *Ecological Economics*. **2013**, 89: 43-60.

[4] van Foreest F. *Perspectives for Biogas in Europe*: OxfordI Istitute for Energy Studies; **2012**.

[5] Ward AJ, Hobbs PJ, Holliman PJ, Jones DL. Optimisation of the anaerobic digestion of agricultural resources. *Bioresource Technology*. **2008**, 99: 7928-7940.

[6] Suslov DY, Kushchev LA. Biogas technology – a contemporary method for processing organic wastes. *Chemical and Petroleum Engineering*. **2010**, 46: 308-311.

[7] Lombardi L, Carnevale E. Economic evaluations of an innovative biogas upgrading method with CO2 storage. *Energy*. **2013**, 62: 88-94.

[8] Persso M. *Report SGC 142 Evaluation of upgrading techniques for biogas. Swedish Gas Center (SGC)*. **2003**.

[9] SEAI. *Sustainable Energy Authority of Ireland. Fact Sheet Upgrading biogas to biomethane*. Fact Sheet Sustainable Energy Authority of Ireland.

[10] Wellinger A, Lindberg A. *Biogas upgrading and utilization*. In: Bioenergy, editor. IEA Bioenergy Task 24: Energy from biological conversion of organic waste.

[11] Muñoz R, Meier L, Diaz I, Jeison D. A review on the state-of-the-art of physical/chemical and biological technologies for biogas upgrading. *Reviews in Environmental Science and Bio/Technology*. **2015**, 14: 727-759.

[12] Wang Y, Lang X, Fan S. Hydrate capture CO2 from shifted synthesis gas, flue gas and sour natural gas or biogas. *Journal of Energy Chemistry*. **2013**, 22: 39-47.

[13] Dabrowski N, Windmeier C, Oellrich LR. Purification of Natural Gases with High CO2 Content Using Gas Hydrates. *Energy & Fuels*. **2009**, 23: 5603-5610.

[14] Sloan ED, Koh C. *Clathrate Hydrates of Natural Gases, Third Edition*: Taylor & Francis; **2007**.

[15] Merlin Christy P, Gopinath LR, Divya D. A review on anaerobic decomposition and enhancement of biogas production through enzymes and microorganisms. *Renewable and Sustainable Energy Reviews*. **2014**, 34: 167-173.

[16] Holm-Nielsen JB, Al Seadi T, Oleskowicz-Popiel P. The future of anaerobic digestion and biogas utilization. *Bioresource Technology*. **2009**, 100: 5478-5484.

[17] Petersson A, Wellinger A. Biogas upgrading technologies – developments and innovations. *IEA Bioenergy*. **2009**, Task 37 - Energy from biogas and landfill gas.

[18] Rasi S, Läntelä J, Rintala J. Trace compounds affecting biogas energy utilisation – A review. *Energy Conversion and Management*. **2011**, 52: 3369-3375.

[19] Sárvári Horváth I, Tabatabaei M, Karimi K, Kumar R. Recent updates on biogas production - a review. *Biofuel Research Journal*. **2016**, 3: 394-402.

[20] European-Union EU. Directive 2009/28/EC of the European parliament and of the council of 23 April 2009 on the promotion of the use of energy from renewable sources and amending and subsequently repealing directives. **2009**, 2001/77/EC and 2003/30/EC.

[21] Persson M, Jönsson O, Wellinger A. Biogas Upgrading to Vehicle Fuel Standards and Grid Injection. *IEA Bioenergy*. **2006**, Task 37 - Energy from Biogas and Landfill Gas.

[22] Rasi S, Veijanen A, Rintala J. Trace compounds of biogas from different biogas production plants. *Energy*. **2007**, 32: 1375-1380.

[23] Association Technique Energie Environomment ATEE. *Etat des Lieux de la Filière Biogaz en France*. **2015**. p. http://atee.fr/sites/default/files/2016-2011-2026_synthese_etude_etat_lieux_biogaz.pdf.

[24] El-Mashad HM, Zhang R. Biogas production from co-digestion of dairy manure and food waste. *Bioresource Technology*. **2010**, 101: 4021-4028.

[25] Cirne DG, Lehtomäki A, Björnsson L, Blackall LL. Hydrolysis and microbial community analyses in two-stage anaerobic digestion of energy crops. *Journal of Applied Microbiology*. **2007**, 103: 516-527.

[26] Lai TE, Nopharatana A, Pullammanappallil PC, Clarke WP. Cellulolytic activity in leachate during leach-bed anaerobic digestion of municipal solid waste. *Bioresource Technology*. **2001**, 80: 205-210.

[27] Mosey FE, Fernandes XA. Patterns of Hydrogen in Biogas from the Anaerobic Digestion of Milk-Sugars. *Water Science and Technology*. **1989**, 21: 187-196.

[28] Björnsson L, Murto M, Mattiasson B. Evaluation of parameters for monitoring an anaerobic co-digestion process. *Applied Microbiology and Biotechnology*. **2000**, 54: 844-849.

[29] Ferry JG. Enzymology of the fermentation of acetate to methane by Methanosarcina thermophila. *BioFactors*. **1997**, 6: 25-35.

[30] Shin H-C, Park J-W, Park K, Song H-C. Removal characteristics of trace compounds of landfill gas by activated carbon adsorption. *Environmental Pollution*. **2002**, 119: 227-236.

[31] Scano EA, Asquer C, Pistis A, Ortu L, Demontis V, Cocco D. Biogas from anaerobic digestion of fruit and vegetable wastes: Experimental results on pilot-scale and preliminary performance evaluation of a full-scale power plant. *Energy Conversion and Management*. **2014**, 77: 22-30.

[32] Chmielewski AG, Urbaniak A, Wawryniuk K. Membrane enrichment of biogas from two-stage pilot plant using agricultural waste as a substrate. *Biomass and Bioenergy*. **2013**, 58: 219-228.

[33] Dinuccio E, Balsari P, Gioelli F, Menardo S. Evaluation of the biogas productivity potential of some Italian agro-industrial biomasses. *Bioresource Technology*. **2010**, 101: 3780-3783.

[34] Koch K, Lübken M, Gehring T, Wichern M, Horn H. Biogas from grass silage – Measurements and modeling with ADM1. *Bioresource Technology*. **2010**, 101: 8158-8165.

[35] Skripsts E, Dubrovskis V, Zabarovskis E, V K. *Investigation of biogas production of cheese whey in processing with ozone before anaerobic digestion*. 12th International scientific conference engineering for rural development. Jelgava, Latvia, **2011**.

[36] Qiao W, Yan X, Ye J, Sun Y, Wang W, Zhang Z. Evaluation of biogas production from different biomass wastes with/without hydrothermal pretreatment. *Renewable Energy*. **2011**, 36: 3313-3318.

[37] Ryckebosch E, Drouillon M, Vervaeren H. Techniques for transformation of biogas to biomethane. *Biomass and Bioenergy*. **2011**, 35: 1633-1645.

[38] Sun Q, Li H, Yan J, Liu L, Yu Z, Yu X. Selection of appropriate biogas upgrading technology-a review of biogas cleaning, upgrading and utilisation. *Renewable and Sustainable Energy Reviews*. **2015**, 51: 521-532.

[39] Daniela Thrän, Tobias Persson, Jaqueline Daniel-Gromke, Jens Ponitka, Michael Seiffert, John Baldwin, et al. Biomethane – status and factors affecting market development and trade *IEA Task 40 and Task 37 Joint Study*. **2014**.

[40] Scholz M, Melin T, Wessling M. Transforming biogas into biomethane using membrane technology. *Renewable and Sustainable Energy Reviews*. **2013**, 17: 199-212.

[41] Patterson T, Esteves S, Dinsdale R, Guwy A. An evaluation of the policy and techno-economic factors affecting the potential for biogas upgrading for transport fuel use in the UK. *Energy Policy*. **2011**, 39: 1806-1816.

[42] Xu C-G, Li X-S. Research progress of hydrate-based CO2 separation and capture from gas mixtures. *RSC Advances*. **2014**, 4: 18301-18316.

[43] Xu C-G, Zhang S-H, Cai J, Chen Z-Y, Li X-S. CO2 (carbon dioxide) separation from CO2–H2 (hydrogen) gas mixtures by gas hydrates in TBAB (tetra-n-butyl ammonium bromide) solution and Raman spectroscopic analysis. *Energy*. **2013**, 59: 719-725.

[44] Park S, Lee S, Lee Y, Seo Y. CO2 Capture from Simulated Fuel Gas Mixtures Using Semiclathrate Hydrates Formed by Quaternary Ammonium Salts. *Environmental Science & Technology*. **2013**, 47: 7571-7577.

[45] Babu P, Linga P, Kumar R, Englezos P. A review of the hydrate based gas separation (HBGS) process for carbon dioxide pre-combustion capture. *Energy*. **2015**, 85: 261-279.

[46] Komatsu H, Ota M, Sato Y, Watanabe M, Smith RL. Hydrogen and carbon dioxide adsorption with tetra-n-butyl ammonium semi-clathrate hydrates for gas separations. *Aiche Journal*. **2015**, 61: 992-1003.

[47] Fukumoto A, Sales Silva LP, Paricaud P, Dalmazzone D, Fürst W. Modeling of the dissociation conditions of H2 + CO2 semiclathrate hydrate formed with TBAB, TBAC, TBAF, TBPB, and TBNO3 salts. Application to CO2 capture from syngas. *International Journal of Hydrogen Energy*. **2015**, 40: 9254-9266.

[48] Eslamimanesh A, Mohammadi AH, Richon D, Naidoo P, Ramjugernath D. Application of gas hydrate formation in separation processes: A review of experimental studies. *The Journal of Chemical Thermodynamics*. **2012**, 46: 62-71.

[49] Carroll JJ. Chapter one - Introduction. *Natural Gas Hydrates (Second Edition)*. Burlington: Gulf Professional Publishing; **2009**. p. 1-15.

[50] Jeffrey GA. Hydrate inclusion compounds. *Journal of inclusion phenomena*. **1984**, 1: 211-222.

[51] Dyadin YA, Udachin KA. Clathrate polyhydrates of peralkylonium salts and their analogs. *Journal of Structural Chemistry*. **1987**, 28: 394-432.

[52] Fowler DL, Loebenstein WV, Pall DB, Kraus CA. Some Unusual Hydrates of Quaternary Ammonium Salts. *Journal of the American Chemical Society*. **1940**, 62: 1140-1142.

[53] Dyadin YA, Udachin KA. Clathrate formation in water-peralkylonium salts systems. *Journal of inclusion phenomena*. **1984**, 2: 61-72.

[54] Feil D, Jeffrey GA. The Polyhedral Clathrate Hydrates, Part 2. Structure of the Hydrate of Tetra Iso-Amyl Ammonium Fluoride. *The Journal of Chemical Physics*. **1961**, 35: 1863-1873.

[55] Dyadin YA, Bondaryuk IV, Aladko LS. Stoichiometry of clathrates. *Journal of Structural Chemistry*. **1995**, 36: 995-1045.

[56] Shimada W, Shiro M, Kondo H, Takeya S, Oyama H, Ebinuma T, et al. Tetra-n-butylammonium bromide-water (1/38). *Acta Crystallographica Section C*. **2005**, 61: o65-o66.

[57] Muromachi S, Udachin KA, Shin K, Alavi S, Moudrakovski IL, Ohmura R, et al. Guest-induced symmetry lowering of an ionic clathrate material for carbon capture. *Chemical Communications*. **2014**, 50: 11476-11479.

[58] Kamata Y, Oyama H, Shimada W, Ebinuma T, Takeya S, Uchida T, et al. Gas Separation Method Using Tetra- n -butyl Ammonium Bromide Semi-Clathrate Hydrate. *Japanese Journal of Applied Physics*. **2004**, 43: 362.

[59] Demirbas A. Methane hydrates as potential energy resource: Part 1 – Importance, resource and recovery facilities. *Energy Conversion and Management*. **2010**, 51: 1547-1561.

[60] Demirbas A. Methane hydrates as potential energy resource: Part 2 – Methane production processes from gas hydrates. *Energy Conversion and Management*. **2010**,

51: 1562-1571.

[61] Makogon YF. Natural gas hydrates – A promising source of energy. *Journal of Natural Gas Science and Engineering*. **2010**, 2: 49-59.

[62] Lang X, Fan S, Wang Y. Intensification of methane and hydrogen storage in clathrate hydrate and future prospect. *Journal of Natural Gas Chemistry*. **2010**, 19: 203-209.

[63] Mori YH. Recent advances in hydrate-based technologies for natural gas storage-a review. *Journal of Chemical Industry and Engineering (CHINA)*. **2003**, 54: 1-17.

[64] Wang W, Carter BO, Bray CL, Steiner A, Bacsa J, Jones JTA, et al. Reversible Methane Storage in a Polymer-Supported Semi-Clathrate Hydrate at Ambient Temperature and Pressure. *Chemistry of Materials*. **2009**, 21: 3810-3815.

[65] Ogawa H, Imura N, Miyoshi T, Ohmura R, Mori YH. Thermodynamic Simulations of Isobaric Hydrate-Forming Operations for Natural Gas Storage. *Energy & Fuels*. **2009**, 23: 849-856.

[66] Babu P, Kumar R, Linga P. Pre-combustion capture of carbon dioxide in a fixed bed reactor using the clathrate hydrate process. *Energy*. **2013**, 50: 364-373.

[67] Komatsu H, Ota M, Smith Jr RL, Inomata H. Review of CO2–CH4 clathrate hydrate replacement reaction laboratory studies – Properties and kinetics. *Journal of the Taiwan Institute of Chemical Engineers*. **2013**, 44: 517-537.

[68] Sun Q, Kang YT. Review on CO2 hydrate formation/dissociation and its cold energy application. *Renewable and Sustainable Energy Reviews*. **2016**, 62: 478-494.

[69] Babu P, Chin WI, Kumar R, Linga P. Systematic Evaluation of Tetra-n-butyl Ammonium Bromide (TBAB) for Carbon Dioxide Capture Employing the Clathrate Process. *Industrial & Engineering Chemistry Research*. **2014**, 53: 4878-4887.

[70] Chatti I, Delahaye A, Fournaison L, Petitet J-P. Benefits and drawbacks of clathrate hydrates: a review of their areas of interest. *Energy Conversion and Management*. **2005**, 46: 1333-1343.

[71] Fukumoto A, Dalmazzone D, Paricaud P, Fürst W. Experimental Measurements and Modeling of the Dissociation Conditions of Tetrabutylammonium Chloride Semiclathrate Hydrates in the Presence of Hydrogen. *Journal of Chemical and Engineering Data*. **2015**, 60: 343-350.

[72] Karimi AA, Dolotko O, Dalmazzone D. Hydrate phase equilibria data and hydrogen storage capacity measurement of the system H2+tetrabutylammonium hydroxide+H2O. *Fluid Phase Equilibria*. **2014**, 361: 175-180.

[73] Deschamps J, Dalmazzone D. Hydrogen Storage in Semiclathrate Hydrates of Tetrabutyl Ammonium Chloride and Tetrabutyl Phosphonium Bromide. *Journal of Chemical & Engineering Data*. **2010**, 55: 3395-3399.

[74] Strobel TA, Taylor CJ, Hester KC, Steven F, Koh CA, Miller KT, et al. Molecular hydrogen storage in binary THF-H_2 clathrate hydrates. *The Journal of Physical Chemistry B*. **2006**, 110: 17121-17125.

[75] Tzirakis F, Stringari P, von Solms N, Coquelet C, Kontogeorgis G. Hydrate equilibrium data for the CO2 + N2 system with the use of tetra-n-butylammonium bromide (TBAB), cyclopentane (CP) and their mixture. *Fluid Phase Equilibria*. **2016**, 408: 240-247.

[76] Muromachi S, Hashimoto H, Maekawa T, Takeya S, Yamamoto Y. Phase equilibrium and characterization of ionic clathrate hydrates formed with tetra-n-butylammonium bromide and nitrogen gas. *Fluid Phase Equilibria*. **2016**, 413: 249-253.

[77] Du J, Wang L. Phase equilibrium measurements for clathrate hydrates of flue gas (CO2+N2+O2) in the presence of tetra-n-butyl ammonium bromide or tri-n-butylphosphine oxide. *The Journal of Chemical Thermodynamics*. **2015**, 88: 96-100.

[78] Kim S, Kang S-P, Seo Y. Semiclathrate-based CO2 capture from flue gas in the presence of tetra-n-butyl ammonium chloride (TBAC). *Chemical Engineering Journal*. **2015**, 276: 205-212.

[79] Linga P, Kumar R, Englezos P. The clathrate hydrate process for post and pre-combustion capture of carbon dioxide. *Journal of Hazardous Materials*. **2007**, 149: 625-629.

[80] Clain P, Delahaye A, Fournaison L, Jerbi S, Mayoufi N, Dalmazzone D, et al. *Characterization of mixed CO_2-TBPB hydrate for refrigeration applications* 7th International Conference on Gas Hydrates (ICGH) Edinburgh, Scotland, United Kingdom**. 2011**.

[81] Clain P, Ndoye FT, Delahaye A, Fournaison L, Lin W, Dalmazzone D. Particle size distribution of TBPB hydrates by focused beam reflectance measurement (FBRM) for secondary refrigeration application. *International Journal of Refrigeration*. **2015**, 50: 19-31.

[82] Clain P, Delahaye A, Fournaison L, Mayoufi N, Dalmazzone D, Fürst W. Rheological properties of tetra-n-butylphosphonium bromide hydrate slurry flow. *Chemical Engineering Journal*. **2012**, 193–194: 112-122.

[83] Martinez MC, Dalmazzone D, Fürst W, Delahaye A, Fournaison L. Thermodynamic Properties of THF + CO_2: Hydrates in Relation with Refrigeration Applications. *Aiche Journal*. **2008**, 54: 1088-1095.

[84] Ogawa T, Ito T, Watanabe K, Tahara K-i, Hiraoka R, Ochiai J-i, et al. Development of a novel hydrate-based refrigeration system: A preliminary overview. *Applied Thermal Engineering*. **2006**, 26: 2157-2167.

[85] Delahaye A, Fournaison L, Marinhas S, Chatti I, Petitet J-P, Dalmazzone D, et al. Effect of THF on Equilibrium Pressure and Dissociation Enthalpy of CO2 Hydrates Applied to Secondary Refrigeration. *Industrial & Engineering Chemistry Research*. **2006**, 45: 391-397.

[86] Marinhas S, Delahaye A, Fournaison L, Dalmazzone D, Fürst W, Petitet J-P. Modelling of the available latent heat of a CO2 hydrate slurry in an experimental loop applied to secondary refrigeration. *Chemical Engineering and Processing: Process Intensification*. **2006**, 45: 184-192.

[87] Xia Z-M, Li X-S, Chen Z-Y, Li G, Yan K-F, Xu C-G, et al. Hydrate-based CO2 capture

and CH4 purification from simulated biogas with synergic additives based on gas solvent. *Applied Energy*. **2015**, 162: 1153–1159.

[88] Castellani B, Rossi F, Filipponi M, Nicolini A. Hydrate-based removal of carbon dioxide and hydrogen sulphide from biogas mixtures: Experimental investigation and energy evaluations. *Biomass and Bioenergy*. **2014**, 70: 330-338.

[89] Tomita S, Akatsu S, Ohmura R. Experiments and thermodynamic simulations for continuous separation of CO2 from CH4+CO2 gas mixture utilizing hydrate formation. *Applied Energy*. **2015**, 146: 104-110.

[90] Zhong D-L, Li Z, Lu Y-Y, Wang J-L, Yan J. Evaluation of CO2 removal from a CO2 + CH4 gas mixture using gas hydrate formation in liquid water and THF solutions. *Applied Energy*. **2015**, 158: 133-141.

[91] Ricaurte M, Dicharry C, Broseta D, Renaud X, Torré J-P. CO2 Removal from a CO2–CH4 Gas Mixture by Clathrate Hydrate Formation Using THF and SDS as Water-Soluble Hydrate Promoters. *Industrial & Engineering Chemistry Research*. **2012**, 52: 899-910.

[92] Carroll JJ. Chapter two - Hydrate types and formers. *Natural Gas Hydrates (Second Edition)*. Burlington: Gulf Professional Publishing; **2009**. p. 17-50.

[93] Sloan ED, Fleyfel F. Hydrate dissociation enthalpy and guest size. *Fluid Phase Equilibria*. **1992**, 76: 123-140.

[94] de Deugd RM, Jager MD, de Swaan Arons J. Mixed hydrates of methane and water-soluble hydrocarbons modeling of empirical results. *Aiche Journal*. **2001**, 47: 693-704.

[95] Herslund PJ, Thomsen K, Abildskov J, von Solms N, Galfré A, Brântuas P, et al. Thermodynamic promotion of carbon dioxide–clathrate hydrate formation by tetrahydrofuran, cyclopentane and their mixtures. *International Journal of Greenhouse Gas Control*. **2013**, 17: 397-410.

[96] Komatsu H, Hayasaka A, Ota M, Sato Y, Watanabe M, Smith Jr RL. Measurement of pure hydrogen and pure carbon dioxide adsorption equilibria for THF clathrate hydrate and tetra-n-butyl ammonium bromide semi-clathrate hydrate. *Fluid Phase Equilibria*. **2013**, 357: 80-85.

[97] Lee Y-J, Kawamura T, Yamamoto Y, Yoon J-H. Phase Equilibrium Studies of Tetrahydrofuran (THF) + CH4, THF + CO2, CH4 + CO2, and THF + CO2 + CH4 Hydrates. *Journal of Chemical & Engineering Data*. **2012**, 57: 3543-3548.

[98] Mooijer-van den Heuvel MM, Peters CJ, de Swaan Arons J. Influence of water-insoluble organic components on the gas hydrate equilibrium conditions of methane. *Fluid Phase Equilibria*. **2000**, 172: 73-91.

[99] Lipkowski J, Komarov VY, Rodionova TV, Dyadin YA, Aladko LS. The Structure of Tetrabutylammonium Bromide Hydrate (C4H9)4NBr·21/3H2O. *Journal of Supramolecular Chemistry*. **2002**, 2: 435-439.

[100] Aladko LS, Dyadin YA, Rodionova TV, Terekhova IS. Clathrate Hydrates of Tetrabutylammonium and Tetraisoamylammonium Halides. *Journal of Structural*

Chemistry. **2002**, 43: 990-994.

[101] Oyama H, Shimada W, Ebinuma T, Kamata Y, Takeya S, Uchida T, et al. Phase diagram, latent heat, and specific heat of TBAB semiclathrate hydrate crystals. *Fluid Phase Equilibria*. **2005**, 234: 131-135.

[102] Chazallon B, Ziskind M, Carpentier Y, Focsa C. CO2 Capture Using Semi-Clathrates of Quaternary Ammonium Salt: Structure Change Induced by CO2 and N2 Enclathration. *The Journal of Physical Chemistry B*. **2014**, 118: 13440-13452.

[103] Wang X, Dennis M. Phase equilibrium and formation behaviour of CO2-TBAB semi-clathrate hydrate at low pressures for cold storage air conditioning applications. *Chemical Engineering Science*. **2016**, 155: 294-305.

[104] Lin W, Delahaye A, Fournaison L. Phase equilibrium and dissociation enthalpy for semi-clathrate hydrate of CO2+TBAB. *Fluid Phase Equilibria*. **2008**, 264: 220-227.

[105] Muromachi S, Takeya S, Yamamoto Y, Ohmura R. Characterization of tetra-n-butylphosphonium bromide semiclathrate hydrate by crystal structure analysis. *CrystEngComm*. **2014**, 16: 2056-2060.

[106] Alekseev VI, Gatilov YV, Polyanskaya TM, Bakakin VV, Dyadin YA, Gaponenko LA. Characteristic features of the production of the hydrate framework around the hydrophobic-hydrophilic unit in the crystal structure of the clathrate tri-n-butylphosphine oxide 34.5-hydrate. *Journal of Structural Chemistry*. **1982**, 23: 395-399.

[107] Goel N. In situ methane hydrate dissociation with carbon dioxide sequestration: Current knowledge and issues. *Journal of Petroleum Science and Engineering*. **2006**, 51: 169-184.

[108] Adisasmito S, Frank RJ, Sloan ED. Hydrates of carbon dioxide and methane mixtures. *Journal of Chemical & Engineering Data*. **1991**, 36: 68-71.

[109] Seo Y-T, Lee H, Yoon J-H. Hydrate Phase Equilibria of the Carbon Dioxide, Methane, and Water System. *Journal of Chemical & Engineering Data*. **2001**, 46: 381-384.

[110] Belandria V, Eslamimanesh A, Mohammadi AH, Théveneau P, Legendre H, Richon D. Compositional Analysis and Hydrate Dissociation Conditions Measurements for Carbon Dioxide + Methane + Water System. *Industrial & Engineering Chemistry Research*. **2011**, 50: 5783-5794.

[111] Herri JM, Bouchemoua A, Kwaterski M, Fezoua A, Ouabbas Y, Cameirao A. Gas hydrate equilibria for CO2–N2 and CO2–CH4 gas mixtures—Experimental studies and thermodynamic modelling. *Fluid Phase Equilibria*. **2011**, 301: 171-190.

[112] Suginaka T, Sakamoto H, Iino K, Takeya S, Nakajima M, Ohmura R. Thermodynamic properties of ionic semiclathrate hydrate formed with tetrabutylphosphonium bromide. *Fluid Phase Equilibria*. **2012**, 317: 25-28.

[113] Gaponenko LA, Solodovnikov SF, Dyadin YA, Aladko LS, Polyanskaya TM. Crystallographic study of tetra-n-butylammonium bromide polyhydrates. *Journal of Structural Chemistry*. **1984**, 25: 157-159.

[114] Shimada W, Ebinuma T, Oyama H, Kamata Y, Takeya S, Uchida T, et al. Separation of Gas Molecule Using Tetra- n -butyl Ammonium Bromide Semi-Clathrate Hydrate Crystals. *Japanese Journal of Applied Physics*. **2003**, 42: L129.

[115] Darbouret M. *Etude rheologique d'une suspension d'hydrates en tant fluide frifoporteur diphasique: resultats experimentaux et modelisation*. Saint-Etienne: Ecole National Supérieur des Mines de Saint-Etienne; **2005**.

[116] Ye N, Zhang P. Phase Equilibrium Conditions and Carbon Dioxide Separation Efficiency of Tetra-n-butylphosphonium Bromide Hydrate. *Journal of Chemical & Engineering Data*. **2014**.

[117] Suginaka T, Sakamoto H, Iino K, Sakakibara Y, Ohmura R. Phase equilibrium for ionic semiclathrate hydrate formed with CO2, CH4, or N2 plus tetrabutylphosphonium bromide. *Fluid Phase Equilibria*. **2013**, 344: 108-111.

[118] Pahlavanzadeh H, Khanlarkhani M, Mohammadi AH. Clathrate hydrate formation in (methane, carbon dioxide or nitrogen + tetrahydropyran or furan + water) system: Thermodynamic and kinetic study. *The Journal of Chemical Thermodynamics*. **2016**, 92: 168-174.

[119] Iino K, Takeya S, Ohmura R. Characterization of clathrate hydrates formed with CH4 or CO2 plus tetrahydropyran. *Fuel*. **2014**, 122: 270-276.

[120] Mooijer-van den Heuvel MM, Witteman R, Peters CJ. Phase behaviour of gas hydrates of carbon dioxide in the presence of tetrahydropyran, cyclobutanone, cyclohexane and methylcyclohexane. *Fluid Phase Equilibria*. **2001**, 182: 97-110.

[121] Cha J-H, Kim ES, Lee KS, Kang JW, Kim K-S. Phase Equilibria and Dissociation Enthalpies of Tri-n-butylphosphine Oxide Semiclathrate Hydrates Incorporated with CH4, CO2, and H2. *Journal of Chemical & Engineering Data*. **2013**, 58: 3494-3498.

[122] Du J, Wang L. Equilibrium Conditions for Semiclathrate Hydrates Formed with CO2, N2, or CH4 in the Presence of Tri-n-butylphosphine Oxide. *Industrial & Engineering Chemistry Research*. **2014**, 53: 1234-1241.

[123] Li D-L, Du J-W, Fan S-S, Liang D-Q, Li X-S, Huang N-S. Clathrate Dissociation Conditions for Methane + Tetra-n-butyl Ammonium Bromide (TBAB) + Water. *Journal of Chemical & Engineering Data*. **2007**, 52: 1916-1918.

[124] Kobori T, Muromachi S, Ohmura R. Phase Equilibrium for Ionic Semiclathrate Hydrates Formed in the System of Water + Tetra-n-butylammonium Bromide Pressurized with Carbon Dioxide. *Journal of Chemical & Engineering Data*. **2014**.

[125] Mohammadi AH, Eslamimanesh A, Belandria V, Richon D. Phase Equilibria of Semiclathrate Hydrates of CO2, N2, CH4, or H2 + Tetra-n-butylammonium Bromide Aqueous Solution. *Journal of Chemical & Engineering Data*. **2011**, 56: 3855-3865.

[126] Deschamps J, Dalmazzone D. Dissociation enthalpies and phase equilibrium for TBAB semi-clathrate hydrates of N2, CO2, N2 + CO2 and CH4 + CO2. *Journal of Thermal Analysis and Calorimetry*. **2009**, 98: 113-118.

[127] Li S, Fan S, Wang J, Lang X, Wang Y. Semiclathrate Hydrate Phase Equilibria for CO2 in the Presence of Tetra-n-butyl Ammonium Halide (Bromide, Chloride, or

Fluoride). *Journal of Chemical & Engineering Data*. **2010**, 55.

[128] Sun Z-G, Sun L. Equilibrium Conditions of Semi-Clathrate Hydrate Dissociation for Methane + Tetra-n-butyl Ammonium Bromide. *Journal of Chemical & Engineering Data*. **2010**, 55: 3538-3541.

[129] Arjmandi M, Chapoy A, Tohidi B. Equilibrium Data of Hydrogen, Methane, Nitrogen, Carbon Dioxide, and Natural Gas in Semi-Clathrate Hydrates of Tetrabutyl Ammonium Bromide. *Journal of Chemical & Engineering Data*. **2007**, 52: 2153-2158.

[130] Mayoufi N, Dalmazzone D, Fürst W, Elghoul L, Seguatni A, Delahaye A, et al. Phase behaviour of tri-n-butylmethylammonium chloride hydrates in the presence of carbon dioxide. *Journal of Thermal Analysis and Calorimetry*. **2012**, 109: 481-486.

[131] Sun Z-G, Liu C-G. Equilibrium Conditions of Methane in Semiclathrate Hydrates of Tetra-n-butylammonium Chloride. *Journal of Chemical & Engineering Data*. **2012**, 57: 978-981.

[132] Iino K, Sakakibara Y, Suginaka T, Ohmura R. Phase equilibria for the ionic semiclathrate hydrate formed with tetrabutylphosphonium chloride plus CO2, CH4, or N2. *The Journal of Chemical Thermodynamics*. **2014**, 71: 133-136.

[133] Paricaud P. Modeling the Dissociation Conditions of Salt Hydrates and Gas Semiclathrate Hydrates: Application to Lithium Bromide, Hydrogen Iodide, and Tetra-n-butylammonium Bromide + Carbon Dioxide Systems. *The Journal of Physical Chemistry B*. **2011**, 115: 288-299.

[134] Fukumoto A, Paricaud P, Dalmazzone D, Bouchafaa W, Ho TT-S, Fürst W. Modeling the Dissociation Conditions of Carbon Dioxide + TBAB, TBAC, TBAF, and TBPB Semiclathrate Hydrates. *Journal of Chemical & Engineering Data*. **2014**.

[135] Acosta HY, Bishnoi PR, Clarke MA. Experimental Measurements of the Thermodynamic Equilibrium Conditions of Tetra-n-butylammonium Bromide Semiclathrates Formed from Synthetic Landfill Gases. *Journal of Chemical & Engineering Data*. **2011**, 56: 69-73.

[136] Xia Z-M, Chen Z-Y, Li X-S, Zhang Y, Yan K-F, Lv Q-N, et al. Thermodynamic Equilibrium Conditions for Simulated Landfill Gas Hydrate Formation in Aqueous Solutions of Additives. *Journal of Chemical & Engineering Data*. **2012**, 57: 3290-3295.

[137] Fan S, Li Q, Nie J, Lang X, Wen Y, Wang Y. Semiclathrate Hydrate Phase Equilibrium for CO2/CH4 Gas Mixtures in the Presence of Tetrabutylammonium Halide (Bromide, Chloride, or Fluoride). *Journal of Chemical & Engineering Data*. **2013**, 58: 3137-3141.

[138] Long X, Wang Y, Lang X, Fan S, Chen J. Hydrate Equilibrium Measurements for CH4, CO2, and CH4 + CO2 in the Presence of Tetra-n-butyl Ammonium Bromide. *Journal of Chemical & Engineering Data*. **2016**.

[139] Englezos P, Kalogerakis N, Bishnoi PR. Formation and decomposition of gas hydrates of natural gas components. *Journal of inclusion phenomena and molecular recognition in chemistry*. **1990**, 8: 89-101.

[140] Kashchiev D, Firoozabadi A. Nucleation of gas hydrates. *Journal of Crystal Growth*. **2002**, 243: 476-489.

[141] Bishnoi PR, Natarajan V. Formation and decomposition of gas hydrates. *Fluid Phase Equilibria*. **1996**, 117: 168-177.

[142] Oshima M, Shimada W, Hashimoto S, Tani A, Ohgaki K. Memory effect on semi-clathrate hydrate formation: A case study of tetragonal tetra-n-butyl ammonium bromide hydrate. *Chemical Engineering Science*. **2010**, 65: 5442-5446.

[143] Buchanan P, Soper AK, Thompson H, Westacott RE, Creek JL, Hobson G, et al. Search for memory effects in methane hydrate: Structure of water before hydrate formation and after hydrate decomposition. *The Journal of Chemical Physics*. **2005**, 123: 164507.

[144] Takeya S, Hori A, Hondoh T, Uchida T. Freezing-Memory Effect of Water on Nucleation of CO2 Hydrate Crystals. *The Journal of Physical Chemistry B*. **2000**, 104: 4164-4168.

[145] Zhong D-L, Li Z, Lu Y-Y, Sun D-J. Phase Equilibrium Data of Gas Hydrates Formed from a CO2 + CH4 Gas Mixture in the Presence of Tetrahydrofuran. *Journal of Chemical & Engineering Data*. **2014**, 59: 4110-4117.

[146] Golombok M, Ineke E, Luzardo J-CR, He YY, Zitha P. Resolving CO2 and methane hydrate formation kinetics. *Environmental Chemistry Letters*. **2008**, 7: 325-330.

[147] van Denderen M, Ineke E, Golombok M. CO2 Removal from Contaminated Natural Gas Mixtures by Hydrate Formation. *Industrial & Engineering Chemistry Research*. **2009**, 48: 5802-5807.

[148] Horvat K, Kerkar P, Jones K, Mahajan D. Kinetics of the Formation and Dissociation of Gas Hydrates from CO_2-CH_4 Mixtures. *Energies*. **2012**, 5: 2248-2262.

[149] Ricaurte M, Dicharry C, Renaud X, Torré J-P. Combination of surfactants and organic compounds for boosting CO2 separation from natural gas by clathrate hydrate formation. *Fuel*. **2014**, 122: 206-217.

[150] Ricaurte M, Torré J-P, Diaz J, Dicharry C. In situ injection of THF to trigger gas hydrate crystallization: Application to the evaluation of a kinetic hydrate promoter. *Chemical Engineering Research and Design*. **2014**, 92: 1674-1680.

[151] Ricaurte M, Dicharry C, Broseta D, Renaud X, Torré J-P. CO2 Removal from a CO2–CH4 Gas Mixture by Clathrate Hydrate Formation Using THF and SDS as Water-Soluble Hydrate Promoters. *Industrial & Engineering Chemistry Research*. **2013**, 52: 899-910.

[152] Dartois E, Duret P, Marboeuf U, Schmitt B. Hydrogen sulfide clathrate hydrate FTIR spectroscopy: A help gas for clathrate formation in the Solar System? *Icarus*. **2012**, 220: 427-434.

[153] Arca S, Poletti L, Allessandre E. *Upgranding of biogas technology through the application of gas hydrates.* 7th International Conference on Gas Hydrates. Edinburgh **2011**.

[154] CSMGem. *Phase-equilibrium Calculation Program Package*. Accompanying the Following Book: Sloan ED, Koh CA, Clathrate Hydrates of Natural Gases, 3rd ed; Taylor & Francis Group: Boca Raton, **2008**.

[155] Ballard AL. *A non-ideal hydrate solid solution model for a multi-phase equilibria program.*: Ph.D. thesis at Colorado School of Mines; **2002**.

[156] NIST. *Thermophysical Properties of Fluid Systems. Acess data: 10/2012, URL: http://webbook.nist.gov/chemistry/fluid/*. **2012**.

[157] Sandler SI. *Chemical and Engineering Thermodynamics*. 3rd ed. New York: Wiley; **1998**.

[158] Duc NH, Chauvy F, Herri J-M. CO2 capture by hydrate crystallization – A potential solution for gas emission of steelmaking industry. *Energy Conversion and Management*. **2007**, 48: 1313-1322.

[159] Pertl A, Mostbauer P, Obersteiner G. Climate balance of biogas upgrading systems. *Waste Management*. **2010**, 30: 92-99.

[160] Hahn H, Krautkremer B, Hartmann K, Wachendorf M. Review of concepts for a demand-driven biogas supply for flexible power generation. *Renewable and Sustainable Energy Reviews*. **2014**, 29: 383-393.

[161] Torré J-P, Ricaurte M, Dicharry C, Broseta D. CO2 enclathration in the presence of water-soluble hydrate promoters: Hydrate phase equilibria and kinetic studies in quiescent conditions. *Chemical Engineering Science*. **2012**, 82: 1-13.

[162] Lirio CFdS, Pessoa FLP, Uller AMC. Storage capacity of carbon dioxide hydrates in the presence of sodium dodecyl sulfate (SDS) and tetrahydrofuran (THF). *Chemical Engineering Science*. **2013**, 96: 118-123.

[163] Shimada W, Ebinuma T, Oyama H, Kamata Y, Narita H. Free-growth forms and growth kinetics of tetra-n-butyl ammonium bromide semi-clathrate hydrate crystals. *Journal of Crystal Growth*. **2005**, 274: 246-250.

[164] Aladko LS, Dyadin YA, Rodionova TV, Terekhova IS. Effect of size and shape of cations and anions on clathrate formation in the system: Halogenides of quaterly ammonium bases and water. *Journal of Molecular Liquids*. **2003**, 106: 229-238.

[165] Du J, Wang L. Equilibrium Conditions for Semiclathrate Hydrates Formed with CO2, N2, or CH4 in the Presence of Tri-n-butylphosphine Oxide. *Industrial & Engineering Chemistry Research*. **2013**, 53: 1234-1241.

[166] van Ekeren PJ. Chapter 2 - Thermodynamic Background to Thermal Analysis and Calorimetry. In: Michael EB, editor. *Handbook of Thermal Analysis and Calorimetry*: Elsevier Science B.V.; **1998**. p. 75-145.

[167] Höhne GWH, Hemminger WF, Flammersheim HJ. Theoretical Fundamentals of Differential Scanning Calorimeters. *Differential Scanning Calorimetry*: Springer Berlin Heidelberg; **2003**. p. 31-63.

[168] Dalmazzone D., Dalmazzone C., B H. *Differential Scanning Calorimetry: A New Technique to Characterize Hydrate Formation in drilling Muds. SPE 63962*. **2000**.

[169] Kharrat M, Dalmazzone D. Experimental determination of stability conditions of methane hydrate in aqueous calcium chloride solutions using high pressure differential scanning calorimetry. *The Journal of Chemical Thermodynamics*. **2003**, 35: 1489-1505.

[170] Dalmazzone D, Kharrat M, Lachet V, Fouconnier B, Clausse D. DSC and PVT measurements: Methane and trichlorofluoromethane hydrate dissociation equilibria. *Journal of Thermal Analysis and Calorimetry*. **2002**, 70: 493-505.

[171] Lin W, Dalmazzone D, Fürst W, Delahaye A, Fournaison L, Clain P. Accurate DSC measurement of the phase transition temperature in the TBPB–water system. *The Journal of Chemical Thermodynamics*. **2013**, 61: 132-137.

[172] Mayoufi N, Dalmazzone D, Fürst W, Delahaye A, Fournaison L. CO2 Enclathration in Hydrates of Peralkyl-(Ammonium/Phosphonium) Salts: Stability Conditions and Dissociation Enthalpies. *Journal of Chemical & Engineering Data*. **2010**, 55: 1271-1275.

[173] Lin W, Dalmazzone D, Fürst W, Delahaye A, Fournaison L, Clain P. Thermodynamic properties of semiclathrate hydrates formed from the TBAB+TBPB+water and CO2+TBAB+TBPB+water systems. *Fluid Phase Equilibria*. **2014**, 372: 63-68.

[174] Höhne GWH, Cammenga HK, Eysel W, Gmelin E, Hemminger W. The temperature calibration of scanning calorimeters. *Thermochimica Acta*. **1990**, 160: 1-12.

[175] Kousksou T, Jamil A, Zeraouli Y, Dumas JP. Equilibrium liquidus temperatures of binary mixtures from differential scanning calorimetry. *Chemical Engineering Science*. **2007**, 62: 6516-6523.

[176] Richardson MJ. Quantitative aspects of differential scanning calorimetry. *Thermochimica Acta*. **1997**, 300: 15-28.

[177] Lafond PG, Olcott KA, Dendy Sloan E, Koh CA, Sum AK. Measurements of methane hydrate equilibrium in systems inhibited with NaCl and methanol. *The Journal of Chemical Thermodynamics*. **2012**, 48: 1-6.

[178] GUILBOT P, VALTZ A, LEGENDRE H, RICHON D. *Rapid on-line sampler-injector : a reliable tool for HT-HP sampling and on-line GC analysis*. Les Ulis, FRANCE: EDP Sciences; **2000**.

[179] LAUGIER S, RICHON D. *New apparatus to perform fast determinations of mixture vapor-liquid equilibria up to 10 MPa and 423 K*. Melville, NY, ETATS-UNIS: American Institute of Physics; **1986**.

[180] Belandria V, Mohammadi AH, Richon D. Compositional analysis of the gas phase for the CO2+N2+tetra-n-butylammonium bromide aqueous solution systems under hydrate stability conditions. *Chemical Engineering Science*. **2012**, 84: 40-47.

[181] Mayoufi N. *Caractérisation de coulis d'hydrates contenant du CO2 appliqués à des systèmes frigorifiques*. Palaiseau: Ecole Nationale Supérieur des Techniques Avancées; **2010**.

[182] Raal JD, Muûhlbauer AL. *Phase Equilibira: Measurement and Computation*: Taylor & Francis, PA; **1998**.

[183] Soave G. Equilibrium constants from a modified Redlich-Kwong equation of state. *Chemical Engineering Science*. **1972**, 27: 1197-1203.

[184] Thiam A. *Etude des conditions thermodynamques et cinétques du procédé de captage de CO2 par formation des hydrates de gaz: application au melange CO2-CH4*. Saint-Etienne: Ecole Nationale Supérieure des Mines de Saint-Etienne; **2008**.

[185] Belandria V, Mohammadi AH, Richon D. Volumetric properties of the (tetrahydrofuran + water) and (tetra-n-butyl ammonium bromide + water) systems Experimental measurements and correlations. *The Journal of Chemical Thermodynamics*. **2009**, 41: 1382-1386.

[186] Brantuas PF. *Captage du dioxide de carbone par semiclathrate hydrates: modélisation, experimentation et dimensionnment d'une unité pilote*. Saint-Étienne: École Nationale Supérieure des Mines de Saint-Étienne; **2013**.

[187] Higgins CE, Baldwin WH. Refractometric Determination of Mutual Solubility as Function of Temperature. Tributyl Phosphine Oxide and Water. *Analytical Chemistry*. **1960**, 32: 233-236.

[188] Ricaurte M, Torré J-P, Asbai A, Broseta D, Dicharry C. Experimental Data, Modeling, and Correlation of Carbon Dioxide Solubility in Aqueous Solutions Containing Low Concentrations of Clathrate Hydrate Promoters: Application to CO2–CH4 Gas Mixtures. *Industrial & Engineering Chemistry Research*. **2012**, 51: 3157-3169.

[189] Bouchemoua A. *Eude du captage du CO2 par la cristallisation des hydrates de gaz: appolcation au mélange CO_2-N_2*. Saint-Étienne: École Nationale Supérieure des Mines de Saint-Étienne; **2012**.

[190] Belandria V. *Hydrate Phase Equilibria Study of CO2 Containing Gases in Thermodynamic Promoter Aqueous Mixtures*. Fontainbleau: École Nationale Supérieure des Mines de Paris; **2012**.

[191] Lin W, Dalmazzone D, Fürst W, Delahaye A, Fournaison L, Clain P. Thermodynamic Studies of CO2 + TBAB + Water System: Experimental Measurements and Correlations. *Journal of Chemical & Engineering Data*. **2013**, 58: 2233-2239.

[192] Muromachi S, Shijima A, Miyamoto H, Ohmura R. Experimental measurements of carbon dioxide solubility in aqueous tetra-n-butylammonium bromide solutions. *The Journal of Chemical Thermodynamics*. **2015**, 85: 94-100.

[193] Diamond LW, Akinfiev NN. Solubility of CO2 in water from −1.5 to 100 °C and from 0.1 to 100 MPa: evaluation of literature data and thermodynamic modelling. *Fluid Phase Equilibria*. **2003**, 208: 265-290.

[194] Krichevsky IR, Kasarnovsky JS. Thermodynamical Calculations of Solubilities of Nitrogen and Hydrogen in Water at High Pressures. *Journal of the American Chemical Society*. **1935**, 57: 2168-2171.

[195] Holder GD, Corbin G, Papadopoulos KD. Thermodynamic and Molecular Properties of Gas Hydrates from Mixtures Containing Methane, Argon, and Krypton. *Industrial & Engineering Chemistry Fundamentals*. **1980**, 19: 282-286.

[196] Holder GD, Zetts SP, Pradhan N. Phase Behavior in Systems Containing Clathrate

Hydrates: A Review. *Reviews in Chemical Engineering*. **1988**, 5: 1-70.

[197] GUM. Evaluation of measurement data – Guide to the expression of uncertainty in measurement. *ISO - International Organization for Standardization*. **2008**, JCGM 100:2008.

[198] Gerd W, Peter MH, Maurice GC, Clemens E. A two-stage procedure for determining the number of trials in the application of a Monte Carlo method for uncertainty evaluation. *Metrologia*. **2010**, 47: 317.

[199] Maurice GC, Bernd RLS. The use of a Monte Carlo method for evaluating uncertainty and expanded uncertainty. *Metrologia*. **2006**, 43: S178.

[200] Harris PM, Cox MG. On a Monte Carlo method for measurement uncertainty evaluation and its implementation. *Metrologia*. **2014**, 51: S176.

[201] GUM. Evaluation of measurement data – Supplement 1 to the "Guide to the expression of uncertainty in measurement" – Propagation of distributions using a Monte Carlo method *ISO - International Organization for Standardization*. **2008**, JCGM 101:2008.

[202] Lucia B, Castellani B, Rossi F, Cotana F, Morini E, Nicolini A, et al. Experimental investigations on scaled-up methane hydrate production with surfactant promotion: Energy considerations. *Journal of Petroleum Science and Engineering*. **2014**, 120: 187-193.

[203] Zhang P, Ye N, Zhu H, Xiao X. Hydrate Equilibrium Conditions of Tetra-n-butylphosphonium Bromide + Carbon Dioxide and the Crystal Morphologies. *Journal of Chemical & Engineering Data*. **2013**, 58: 1781-1786.

[204] Sales Silva LP, Dalmazzone D, Stambouli M, Lesort A-L, Arpentinier P, Trueba A, et al. Phase equilibria of semi-clathrate hydrates of tetra-n-butyl phosphonium bromide at atmospheric pressure and in presence of CH4 and CO2 + CH4. *Fluid Phase Equilibria*. **2016**, 413: 28-35.

[205] Mayoufi N, Dalmazzone D, Delahaye A, Clain P, Fournaison L, Fürst W. Experimental Data on Phase Behavior of Simple Tetrabutylphosphonium Bromide (TBPB) and Mixed CO2 + TBPB Semiclathrate Hydrates. *Journal of Chemical & Engineering Data*. **2011**, 56: 2987-2993.

[206] Xia Z-M, Li X-S, Chen Z-Y, Lv Q-N, Xu C-G, Chen C. Hydrate-based Capture CO2 and Purification CH4 from Simulated Landfill Gas with Synergic Additives Based on Gas Solvent. *Energy Procedia*. **2014**, 61: 450-454.

[207] Sales Silva LP, Dalmazzone D, Stambouli M, Arpentinier P, Trueba A, Fürst W. Phase Behavior of Simple Tributylphosphine Oxide (TBPO) and Mixed Gas (CO2, CH4 and CO2+CH4) + TBPO Semiclathrate Hydrates. *The Journal of Chemical Thermodynamics*. **2016**, 102: 293 - 302.

[208] Kerr WL, Reid DS. The use of stepwise differential scanning calorimetry for thermal analysis of foods. *Thermochimica Acta*. **1994**, 246: 299-308.

[209] Zynger J. Automated, stepping differential calorimeter for the analysis of purity. *Analytical Chemistry*. **1975**, 47: 1380-1384.

[210] Maekawa T. Equilibrium conditions for gas hydrates of methane and ethane mixtures in pure water and sodium chloride solution. *Geochemical Journal*. **2001**, 35: 59 - 66.

[211] Shi L-L, Liang D-Q, Li D-L. Phase Equilibrium Data of Tetrabutylphosphonium Bromide Plus Carbon Dioxide or Nitrogen Semiclathrate Hydrates. *Journal of Chemical & Engineering Data*. **2013**, 58: 2125-2130.

[212] Anderson GK. Enthalpy of dissociation and hydration number of methane hydrate from the Clapeyron equation. *The Journal of Chemical Thermodynamics*. **2004**, 36: 1119-1127.

[213] Anderson GK. Enthalpy of dissociation and hydration number of carbon dioxide hydrate from the Clapeyron equation. *The Journal of Chemical Thermodynamics*. **2003**, 35: 1171-1183.

[214] Gupta A, Lachance J, Sloan Jr ED, Koh CA. Measurements of methane hydrate heat of dissociation using high pressure differential scanning calorimetry. *Chemical Engineering Science*. **2008**, 63: 5848-5853.

[215] A.V. Nikolaev, Yu.A. Dyadin, Yakovlev II. *Dokl Akad Nauk SSSR*. **1966**, 170: 110 (in Russian).

[216] Sales Silva LP, Dalmazzone D, Stambouli M, Lesort A-L, Arpentinier P, Trueba A, et al. Phase equilibria of semi-clathrate hydrates of tetra-n-butyl phosphonium bromide at atmospheric pressure and in presence of CH4 and CO2+CH4. *Fluid Phase Equilibria*. **2016**, 413: 28-35.

[217] Tumba K, Reddy P, Naidoo P, Ramjugernath D, Eslamimanesh A, Mohammadi AH, et al. Phase Equilibria of Methane and Carbon Dioxide Clathrate Hydrates in the Presence of Aqueous Solutions of Tributylmethylphosphonium Methylsulfate Ionic Liquid. *Journal of Chemical & Engineering Data*. **2011**, 56: 3620-3629.

[218] Stephenson RM. Mutual solubilities: water-ketones, water-ethers, and water-gasoline-alcohols. *Journal of Chemical & Engineering Data*. **1992**, 37: 80-95.

[219] Narayanan TM, Imasato K, Takeya S, Alavi S, Ohmura R. Structure and Guest Dynamics in Binary Clathrate Hydrates of Tetrahydropyran with Carbon Dioxide/Methane. *The Journal of Physical Chemistry C*. **2015**, 119: 25738-25746.

[220] Mohammadi AH, Richon D. Equilibrium data of (tetrahydropyran+hydrogen sulphide) and (tetrahydropyran+methane) clathrate hydrates. *The Journal of Chemical Thermodynamics*. **2012**, 48: 36-38.

[221] Kashchiev D, Firoozabadi A. Induction time in crystallization of gas hydrates. *Journal of Crystal Growth*. **2003**, 250: 499-515.

[222] Kashchiev D, Firoozabadi A. Driving force for crystallization of gas hydrates. *Journal of Crystal Growth*. **2002**, 241: 220-230.

[223] Najibi H, Momeni K, Sadeghi MT, Mohammadi AH. Experimental measurement and thermodynamic modelling of phase equilibria of semi-clathrate hydrates of (CO2+tetra-n-butyl-ammonium bromide) aqueous solution. *The Journal of Chemical Thermodynamics*. **2015**, 87: 122-128.

[224] Tajima H, Yamasaki A, Kiyono F. Energy consumption estimation for greenhouse gas separation processes by clathrate hydrate formation. *Energy*. **2004**, 29: 1713-1729.

[225] Babu P, Ho CY, Kumar R, Linga P. Enhanced kinetics for the clathrate process in a fixed bed reactor in the presence of liquid promoters for pre-combustion carbon dioxide capture. *Energy*. **2014**, 70: 664-673.

[226] Babu P, Kumar R, Linga P. Medium pressure hydrate based gas separation (HBGS) process for pre-combustion capture of carbon dioxide employing a novel fixed bed reactor. *International Journal of Greenhouse Gas Control*. **2013**, 17: 206-214.

[227] Babu P, Yao M, Datta S, Kumar R, Linga P. Thermodynamic and Kinetic Verification of Tetra-n-butyl Ammonium Nitrate (TBANO3) as a Promoter for the Clathrate Process Applicable to Precombustion Carbon Dioxide Capture. *Environmental Science & Technology*. **2014**, 48: 3550-3558.

[228] Sloan ED, Subramanian S, Matthews PN, Lederhos JP, Khokhar AA. Quantifying Hydrate Formation and Kinetic Inhibition. *Industrial & Engineering Chemistry Research*. **1998**, 37: 3124-3132.

[229] Ye N, Zhang P. Equilibrium Data and Morphology of Tetra-n-butyl Ammonium Bromide Semiclathrate Hydrate with Carbon Dioxide. *Journal of Chemical & Engineering Data*. **2012**, 57: 1557-1562.

[230] Sizikov AA, Manakov AY, Rodionova TV. Methane Capacity of Double Tetrabutylammonium Bromide + Methane Ionic Clathrate Hydrates. *Energy & Fuels*. **2012**, 26: 3711-3716.

[231] Bonnefoy O. *Influence des cristaux d'hydrates de gaz ou de glace sur la permeabilité d'un milieu poreux*. Saint-Étienne: École Nationale Supérieure des Mines de Saint-Étienne; **2005**.

[232] Jana AK. *Chemical Process Modelling and Computer Simulation* **2008**.

APPENDIX

To calculate important properties of gases, such as number of moles, compressibility factor and fugacity, the Equation of State of Soave-Redlich-Kwong (SRK) [183] were used:

$$p = \frac{RT}{v-b} - \frac{a(T)}{v(v+b)} \qquad (A.1)$$

where: p is the pressure; T is the temperature; v is the molar volume; R is the ideal gas constant; and $a(T)$ and b are coefficients depending on the nature of the gas:

$$a(T) = 0.42748\frac{R^2T_c^2}{p_c}\cdot\left[1+\left(0.48+1.574\omega-176\omega^2\right)\cdot\left(1-\sqrt{\frac{T}{T_c}}\right)\right]^2 \qquad (A.2)$$

$$b = 0.08664\frac{RT_c}{p_c} \qquad (A.3)$$

where: T_c is the critical temperature; p_c is the critical pressure; ω is the acentric factor. These parameters are constants for each gas. *Table A.1* present the values these parameter for some gases.

Table A.1. Constant properties of gases [157].

Gas	T_c /K	p_c /MPa	ω
CO_2	304.13	7.377	0.224
CH_4	190.56	4.599	0.011

The compressibility factor Z is calculated according to the *Equation A.4*

$$Z = \frac{Pv}{RT} \qquad (A.4)$$

After some arithmetic manipulations with *Equation A.1* and *Equation A.4* we can show that the compressibility factor Z is the solution for a cubic equation:

$$Z^3 - Z^2 + \left(A - B^2 - B\right)Z - AB = 0 \qquad (A.5)$$

The constants *A* and *B* are defined by:

$$A = \frac{a(T)p}{R^2T^2} \qquad (A.6)$$

$$B = \frac{bp}{RT} \qquad (A.7)$$

The *Equation A.5* can be solved iteratively or algebraically. In our calculations we used the second option by following Cardano's method described in Bonnefoy's thesis [231]. First we redefine the *Equation* A.5:

$$Z^3 + sZ^2 + cZ + q = 0 \qquad (A.8)$$

Then, we introduce other parameters:

$$r = c - \frac{s^2}{3} \qquad (A.9)$$

$$m = q + \frac{2s^3 - 9sc}{27} \qquad (A.10)$$

$$\Delta = \frac{m^2}{4} + \frac{r^3}{27} \qquad (A.11)$$

For the cases of $\Delta > 0$ the compressibility factor is calculated by:

$$Z = -\frac{s}{3} + \left(\sqrt{\Delta} - \frac{n}{2}\right)^{\frac{1}{3}} + \left(-\sqrt{\Delta} - \frac{n}{2}\right)^{\frac{1}{3}} \qquad (A.12)$$

On the other hand, if $\Delta < 0$ the compressibility factor is calculated by:

$$Z = -\frac{s}{3} + 2\sqrt{\frac{-r}{3}} \cdot \cos\left(\frac{\theta}{3}\right) \qquad (A.13)$$

with the angle θ defined by:

$$\cos\theta = -\frac{m}{|m|} \cdot \sqrt{\frac{-27m^2}{4r^3}} \qquad (A.14)$$

Finally, using this method is also possible to calculate the fugacity coefficient ϕ:

$$\ln\phi = -\frac{A}{B}\ln\left(1+\frac{B}{Z}\right) - \ln(Z-B) + Z - 1 \qquad (A.15)$$

And the fugacity *f* is then calculated by the *Equation A.16:*

$$f = \phi \cdot p \qquad (A.16)$$

In the case of gas mixture with *N* components the rule mixture is applied according to Soave [183]. The parameters of *Equations A.1* are now dependents to the composition of gas mixture (y_i).

$$a(T,\vec{y}) = \sum_{i=1}^{N}\sum_{j=1}^{N} y_i y_j a_{ij}(T) \qquad (A1.7)$$

where y_i is the mole fraction of gas *i* and is calculated by the *Equation A.18* where n_i is the number of moles of gas *i.*

$$y_i = \frac{n_i}{\sum_{j=1}^{N} nj} \qquad (A.18)$$

The parameter $a_{ij}(T)$ is calculated using the Equation *A.2* and knowing the value of the binary interaction parameter k_{ij}. For CO_2-CH_4 the binary interaction parameter k_{ij} is 0.12 [232].

$$a_{ij}(T) = \left(a_i(T)a_j(T)\right)^{1/2}(1-k_{ij}) \qquad (A.19)$$

It must be noted that in the *Equation A.19* if $i=j$ then $k_{ij}=0$.

Finally the parameter *b* is also dependent to the composition of the gas mixture.

$$b(\vec{y}) = \sum_{i=1}^{N} y_i b_i \qquad (A.20)$$

université PARIS-SACLAY
ÉCOLE DOCTORALE
Sciences mécaniques et énergétiques, matériaux et géosciences (SMEMAG)

Titre : *Procédé de Séparation par Formation Sélective d'Hydrates de Gaz pour la Valorisation du Biogaz*

Mots clés : Hydrate de gaz, séparation, biogaz, additives thermodynamques et Diagramme des phases

Résumé : Le biogaz, constitué essentiellement de méthane et de dioxyde de carbone, représente une voie alternative aux sources d'énergies fossiles. Pour être valorisé le mélange doit être séparé dans un procédé de séparation de gaz. Ces dernières années, un nouveau procédé basé sur la formation d'hydrates de gaz (GSHF) a suscité une attention particulière dans la communauté scientifique. Basé sur une transition de phase hydrate – liquide – vapeur conduite en présence de promoteurs thermodynamiques, la purification est supposée demander moins d'énergie et moins de réactifs dangereux pour l'environnement que les procédés chimiques traditionnels comme l'absorption dans des solutions d'amines. Une connaissance des équilibres de phase dans les systèmes eau + gaz + additifs est essentielle à la validation du procédé. Dans ce projet, nous avons étudié quatre promoteurs, le bromure de trétrabutylammonium (TBAB), le bromure de tétrabutylphosphonium (TBPB), l'oxyde de tributylphosphine (TBPO) et le tétrahydropyrane (THP), qui ont pour buts d'abaisser la consommation d'énergie et d'améliorer la cinétique et la sélectivité du procédé. Une partie de ce projet a été consacrée à déterminer les conditions d'équilibre d'hydrates de gaz en présence de ces promoteurs et différentes phases gaz (CO_2, CH_4 et biogaz simulé). Les méthodes de calorimétrie différentielle à balayage (DSC) ont été appliquées pour mesurer les températures de transition de phase. De nouvelles données d'équilibre de phases ont été déterminées pour les systèmes hydrates de gaz + promoteurs. Dans la deuxième partie du projet, nous avons effectué des mesures quantitatives dans un réacteur instrumenté afin d'évaluer le procédé GSFH pour la valorisation du biogaz. Chaque promoteur a été évalué tant sur le plan de la cinétique (temps, d'induction, vitesse de croissance cristalline) que sur celui de la thermodynamique (quantité de gaz piégé, sélectivité). L'optimisation du programme de formation / dissociation des hydrates a montré d'excellents résultats en termes de cinétique.

Titre : *Gas Separation by Gas Hydrate Selective Crystallization for the Valorization of Biogas*

Keywords : Gas hydrates, separation, biogas, thermodynamics promoters and phase diagrams

Abstract: Biogas represents an alternative path to fossil energies. It is composed mainly by methane and carbon dioxide. This couple must be separated in a gas separation process. In recent years, the new process based on gas hydrate formation (GSHF) has taken special attention in academic community. Besides, the use of thermodynamic promoters can increase the efficiency of the process. Since GSFH is based on phase transition phenomenon, knowledge about phase equilibria is essential. In this project, we have selected and studied four thermodynamic promoters (tretrabutylammonium bromide / TBAB; tetrabutylphosphonium bromide / TBPB; tributylphosphine oxide / TBPO; tetrahydropyran / THP) that have potential to improve GSFH process of biogas in terms of stability gain (less energy consumption), kinetics and selectivity. One part of this project consisted in determining the gas hydrate equilibrium conditions involving these promoters and the different gas phases (CO_2, CH_4 and simulated biogas). Differential scanning calorimetry (DSC) methods were applied to measure the phase transition temperatures. Therefore, new phase equilibrium data were determined for the promoter/gas hydrate systems. In the second part of the project, we carried out quantitative measurements in an instrumented reactor in order to evaluate the GSFH process for upgrading biogas. Each promoter was evaluated in kinetics and thermodynamics aspects, such as crystal growth rate, amount of gas trapped into the hydrate phase, and selectivity. The optimization of the hydrate formation / dissociation cycle showed excellent results in terms of kinetics improvement.

Université Paris-Saclay
Espace Technologique / Immeuble Discovery
Route de l'Orme aux Merisiers RD 128 / 91190 Saint-Aubin, France